The Hodge Centre for
Neuropsychiatric Immunology

Canolfan Hodge ar gyfer
Imiwnoleg Niwroseiciatrig

Investigating the effect of Maternal Obesity and Inflammation on Corpus Callosum associated Microglia during Perinatal Development

by

Jonathan Davis

A thesis submitted for the degree of

Doctor of Philosophy

September 2023

Summary

Microglia have important roles in supporting healthy brain development. Recent research uncovered many microglia populations in the developing brain. There is still much we do not know about developmental microglia. Microglia also form a vital part of the immune system, where they respond to inflammatory stimuli to protect the central nervous system. Inflammatory conditions such as maternal obesity and maternal immune activation are associated with neuropsychiatric and neurodevelopmental disorders, however the mechanisms mediating this relationship are not fully understood.

As central nervous system immune cells and important players in neurodevelopment, microglia are at a key position in the relationship between prenatal inflammation and pathological neurodevelopment. Studying the effect of inflammation on developmental microglia therefore provides an opportunity to investigate mechanisms involved in neuropsychiatric or neurodevelopmental disorder. This thesis characterised populations of microglia associated with the developing corpus callosum and investigated the impact of maternal obesity and maternal immune activation on corpus callosum associated microglia and brain development.

Microglia form dense clusters in close association with the developing corpus callosum reminiscent of developmental 'hotspots'. Analysis of expression profiles revealed more diverse microglial populations at the midline than the cortex (Chapter 2). Corpus callosum associated microglia also differed from cortical microglia with regard to birthdate, proliferation rate, ability to migrate and protein expression (Chapter 3).

High fat diet models of maternal obesity had variable impacts on offspring development. Corpus callosum organisation and associated microglia differentiation was unaffected by maternal high fat diet (Chapter 4). Models of maternal immune activation also produced variable effects on offspring development but somewhat affected corpus callosum organisation and associated microglia differentiation in addition (Chapter 5).

Novel insights into developmental microglia and interactions with maternal inflammation presented in this thesis may provide the basis for further investigations into intervention strategies for neuropsychiatric and neurodevelopmental disorders.

Acknowledgements

Thank you to the Hodge Foundation for funding this PhD.

I would like to thank Dr Erik Mire, my primary supervisor and main source of guidance throughout the PhD. Your knowledge and expertise has been invaluable in improving my scientific understanding and technical skills. I'd also like to thank Professor Jeremy Hall for your generous support and friendly, helpful advice.

I am grateful to Mayur Shetty and Ashmee Almeida for helping me to get through some of the large amount of practical work needed to produce meaningful results and for allowing me to understand how fun teaching can be, particularly when in collaboration with motivated and capable students.

I would like to thank the generous support of helpful collaborators and colleagues along the way. Mat Clement for very patient practical immunology support and advice, important parts of this project would not have worked without it. Cezar Tigaret for sharing your electrophysiology space, training, and support with bi-photon microscopy. Francesco Bedogni for helpful advice and maintaining a friendly working environment. Mark Bishop for practical cell sorting support. Angela Marchbank for single cell sequencing wet lab work. Tony Hayes for light sheet microscopy support. Laura Westacott for cryosectioning and perfusion training. Jack Reddaway for helping and allowing me to use your morphology analysis tools.

The technical team at NMHII, Emma Dalton, Olena Petter, Toni Watkins and Shane Wainwright, deserve a thank you for maintaining a productive work environment. The JBIOS team also deserve a big thank you for taking care of the many mice required for this project and for training and support with animal husbandry.

A huge thanks to my partner Ella for supporting me through some challenging times, many late nights, and working weekends. For creating a warm and stable home to return to. For always bringing a smile to my face when I needed it most.

A final thankyou to my Grandma, Margaret for always encouraging and motivating me to pursue my interests in scientific discovery. I wouldn't have come this far without you.

Contents

List of Figures

List of Tables

Abbreviations

ANOVA	Analysis of variance
ASD	Autism spectrum disorder
ATM	Axon Tract-associated Microglia
BAM	Border-Associated Macrophage
BrdU	Bromodeoxyuridine
CNS	Central nervous system
CPT1a	Carnitine Palmitoyltransferase 1A
CRP	C-reactive protein
DAM	Disease Associated Microglia
DAPI	4′,6-DiAmidino-2-PhenylIndole
DEPC	DiEthyl PyroCarbonate
E (for example E12.5)	Embryonic day
FDR	False Discovery Rate
GFP	Green Fluorescent Protein
GSEA	Gene Set Enrichment Analysis
IGF-1	Insulin-like growth factor 1
IL	Interleukin
LAMP2	Lysosomal-Associated Membrane Protein 2
LPS	Lipopolysaccharide
MCD	Maternal control diet
MEA	Manual Enrichment Analysis
MFG-E8	Milk-fat globule EGF factor-8
MHFD	Maternal high fat diet
MIA	Maternal Immune Activation
MOMI	Maternal Obesity Maternal Infection
MZG	Midline zipper glia
NES	Normalised Enrichment Score
NPCs	Neural progenitor cells
OCT	Optimal Cutting Temperature compound
ORA	Over Representation Analysis
P (for example P7)	Postnatal day

PAM	Proliferative-region-Associated Microglia
PBS	Phosphate Buffered Saline
PCA	Principal Component Analysis
PDGF-BB	Platelet derived growth factor BB
PFA	Paraformaldehyde
Poly I:C	Polyinosinic:polycytidylic acid
PUFAs	Poly Unsaturated Fatty Acids
SVZ	Sub-Ventricular Zone
TGF-β	Transforming Growth Factor β
TNF	Tumour necrosis factor
TUNEL	Deoxynucleotidyl transferase dUTP nick-end labelling
VEGF-A	Vascular endothelial growth factor A
VZ	Ventricular Zone

Chapter 1: Introduction

1.1. What are microglia?

As the resident macrophage immune cells of the central nervous system, microglia play an important role in neuro-immune interactions. However, microglia were not always known for their important immune functions. The term glia, Greek for glue, was coined by Rudolf Virchow in 1856 to describe the non-neuronal part of the central nervous system (CNS). At this time glia were thought to be a form of connective tissue. Building upon the work of Ramón y Cajal, microglia were recognised as a separate cell type by Pio del Rio-Hortega in 1919 through ammoniacal silver carbonate based histological analysis (Sierra et al. 2016). Throughout the following 100 years of microglia research, rather than being inert connective tissue, microglia were shown to actively participate in the CNS immunology (Prinz et al. 2019).

The shift in description of microglia from inert connective tissue to CNS based macrophage was due to findings demonstrating their ability to recognise pathogens through toll-like receptors, perform phagocytosis of pathogens and dying cells, and act as antigen-presenting cells (Streit and Kreutzberg 1988; Olson et al. 2001; Olson and Miller 2004). Microglia were shown to make up approximately 7% of non-neuronal cells across brain structures in mammalian species (Dos Santos et al. 2020). Recently, genome wide association studies have also identified many risk genes of CNS disorders expressed by microglia. These CNS disorders include Alzheimer's disease, Parkinson's disease, schizophrenia, autism spectrum disorder (ASD), and multiple sclerosis (Werling et al. 2016; Ma et al. 2018; Patsopoulos et al. 2019; Andersen et al. 2021; Bellenguez et al. 2022). Suspected involvement in these disorders makes microglia in the diseased brain an active area of research to this day.

1.1.1. The changing roles of microglia throughout brain development

The highly dynamic nature of microglia in the steady state was first visualised in 2005 (Davalos et al. 2005; Nimmerjahn et al. 2005). This finding indicated an active role for these macrophage cells under normal conditions and sparked a burgeoning of publications seeking to further our understanding of microglia within the diseased and healthy brain (Tremblay et al. 2015; Stratoulias et al. 2019). Such research interest has demonstrated that microglia support neurodevelopment in a number of important ways summarised in Figure 3.

Developmental processes carried out by microglia require cell-cell contact or short range signalling, with the minor exception of exosome signalling (Glebov et al. 2015). Microglia must therefore migrate to the structures which they support the formation of, during the relevant developmental time window. This leads to a complex pattern of spatio-temporal density shifts in microglia, some of which involve microglia forming 'hotspots' - tight clusters of high density around developing brain structures (Squarzoni et al. 2014). Microglial interaction with the developing CNS begins with the migration of early macrophage progenitors from the yolk sac.

1.1.2. Origin of microglia

Microglia derive from erythromyeloid progenitors present in the yolk-sac at embryonic day 8 (E8) in the mouse (Ginhoux et al. 2010a; Schulz et al. 2012). The first wave of hematopoiesis, termed primitive hematopoiesis, is initiated in the yolk sac around E7 with the appearance of early erythromyeloid progenitors (Utz et al. 2020).

Throughout differentiation into mature cells, microglia and their precursors express a range of markers at different stages. At around E8 erythromyeloid progenitors are $CD45^{-}$, $c\text{-}kit^{+}$, $CX3CR1^{+}$, $CD16/32^{+}$, $F4/80^{hi}$ and $CD11b^{lo}$ (Kierdorf et al. 2013; Utz et al. 2020). Through expression of the transcription factor Pu.1, amongst other transcription factors, these cells develop into $CD206^{-}$ $CD45^{+}$ $c\text{-}kit^{lo}$ $CX3CR1^{-}$ immature A1 cells. Continued differentiation through the Irf8 transcription factor produces $CD45^{+}$ $c\text{-}kit^{-}$ $CX3CR1^{+}$ A2 cells which will differentiate further to become mature microglia (Kierdorf et al. 2013). Interestingly, slightly later yolk sac populations at E9 show reduced differentiation into A1 and A2 cells suggesting

this stage of microglia development is confined to a short time-frame in the mouse (Utz et al. 2020).

1.1.2.1. Other brain macrophages

A second brain macrophage population, the Border-Associated Macrophages (BAMs), also arise from erythromyeloid progenitors in the yolk sac during primitive hematopoiesis through expression of Pu.1 and Irf8. These macrophages specifically colonise the borders of the CNS, including the choroid plexus, meninges and perivascular spaces. Despite their similar developmental origins, BAMs become transcriptionally distinct from microglia as early as E10.5 with a plethora of differentially expressed genes as well as increased CD206 and F4/80 expression (Utz et al. 2020).

Dependence on TGF-βR signalling is one key factor contrasting between microglial and BAM differentiation. Reduction in TGF-β signalling from E10.5 resulted in a decrease in microglial cell number from E14.5. These cells also had lower levels of microglia signature genes including *Sal1* and *P2y12*; higher levels of BAM markers including CD206 and F4/80; reduced proliferation and increased ameboid morphology at E14.5 and E18.5. BAMs on the other hand were slightly less proliferative at E14.5 but displayed no other alterations (Utz et al. 2020).

1.1.2.2. The Choroid Plexus

Construction of the cortical plate coincides with development of the choroid plexus, with the first evidence of the choroid plexus arising at approximately E12.5. This structure becomes extensive between E13.5 – E15.5 and fully formed by E16.5 (Chen et al. 2017). Colonisation of the choroid plexus is immediate as CD206+ BAMs predominantly reside here and in the meninges from E12.5. The few CD206+ BAMs not found within these regions were associated with blood vessels and assumed to be perivascular macrophages by Utz et al. (2020). Therefore, from E12.5 onward parenchymal brain macrophages can be more confidently considered microglia.

1.1.3. Central Nervous System Colonisation

Throughout the early stages of differentiation, brain macrophage progenitors begin their invasion of the CNS from the yolk sac. $CX3CR1^{+}$ macrophage progenitor CNS invasion is believed to occur in two waves in the mouse (Swinnen et al. 2013). The first wave occurring between E8.5 and E14.5, involves initial colonisation and a gradual increase in macrophage number (Alliot et al. 1999; Ginhoux et al. 2010a; Swinnen et al. 2013; Reemst et al. 2016). These macrophage progenitors will eventually go on to become microglia. It has been reported that during the first phase, microglial cells perform tangential migration to form a uniform layer across all CNS regions through migration along astrocyte foot processes and axonal bundles (Cuadros and Navascués 2001; Pont-Lezica et al. 2011; Mosser et al. 2017).

Underlying mechanisms of brain macrophage invasion at this stage are not fully understood. These cells may be attracted by cues secreted from apoptotic cells, such as lysophosphatidylcholine, as has been demonstrated in zebrafish (Casano et al. 2016; Xu et al. 2016). $CX3CR1^{+}$ brain macrophage co-localisation with apoptotic cells of the choroid plexus is an early indication of this mechanism in the mouse brain (Swinnen et al. 2013). Further studies on zebrafish indicate that recruitment of $CD45^{+}$ $CX3CR1^{+}$ brain macrophages is independent of most induced chemokine signals. However, the matrix metaloproteinases: MMP-8 and MMP-9 may be involved (Kierdorf et al. 2013).

Early brain macrophage migratory pathways are also yet to be described. Proposed colonisation routes are shown in Figure 1. Swinnen *et al.* (2013) suggest two routes of early $CX3CR1^{+}$ cell entry into the cortex: via the meninges by crossing the pial surface or via the ventricles by passing through the ventricle wall. This may change as development progresses with the majority of $CX3CR1^{+}$ cells near the pial surface at E12.5 changing to most $CX3CR1^{+}$ cells close to the ventricle at E17.5.

There is some evidence that brain macrophage precursors enter the brain parenchyma through blood vessels. For example, brain rudiments of E10-10.5 $Ncx\text{-}1^{-/-}$ mice that lack a heartbeat and functional blood circulation do not contain macrophage progenitors unlike wild-type controls (Ginhoux et al. 2010a). However, the first capillary sprouts do not fully invade the neuroepithelium until E9.5 after initial macrophage progenitor invasion around E8.5. Some suggest that these data indicate that macrophage progenitors may use, or need, pial

penetrating vessels to migrate along and into the brain parenchyma (Arnold and Betsholtz 2013; Reemst et al. 2016). Several studies have indicated that circulating macrophages can enter the brain through blood vessels in adult brains, at least under inflammatory conditions. However, these cells appear not to remain and integrate into the microglial population (Reemst et al. 2016).

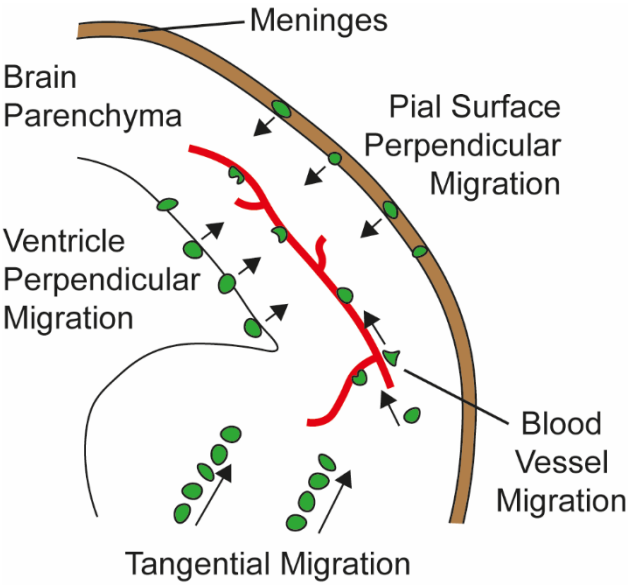

Figure 1: Microglia are thought to colonise the brain through a variety of pathways.
Diagram showing potential brain colonisation routes for microglia throughout development. Tangential migration is thought to occur during the first wave of invasion between E8.5-E14.5 in mouse. Perpendicular migration is thought to occur during the second wave of invasion after E14.5.

Proliferation may partially explain the first gradual increase in CX3CR1^{+} cells, as proliferating macrophage progenitors are more common earlier in development but decrease as a proportion of total CX3CR1^{+} cells as development progresses. Absolute number of proliferating macrophage progenitors remains low at the pial surface and cortex, suggesting that migration of progenitors also contributed towards the initial increase in CX3CR1^{+} cells. Macrophage progenitors are indeed highly motile during this phase (Swinnen et al. 2013).

At what stage microglia segregate from other macrophage populations is a topic requiring further research. Microglia were able to repopulate embryos by E17.5 following depletion from E10.5 to E14.5, suggesting either precursor invasion or proliferation of a few remaining microglia progenitors in the brain (Squarzoni et al. 2014). Recruitment of foetal monocytes was also noted at E14.5 in embryos depleted of microglia through anti CSF-1R antibody application (Hoeffel et al. 2015). Whether this process occurs absent of experimental manipulation such as microglia depletion is yet to be established.

As the second phase of microglial population increase begins, there is a tripling in cortical microglial cell number between E14.5-E15.5. This sharp increase cannot be explained by proliferation within the cortex alone which, as discussed, was shown to decrease proportionally throughout development. A new wave of progenitors have been proposed to enter the brain from the periphery during this time (Swinnen et al. 2013; Reemst et al. 2016). However, others suggest that microglial progenitors have become segregated from other macrophage populations at this time and remain so into adulthood (Waisman et al. 2015; Utz et al. 2020). After this stage, microglial numbers increase more slowly and begin to scatter throughout the brain (Reemst et al. 2016). Perpendicular migration occurs during this time, with microglia migrating to reach all brain layers (Mosser et al. 2017). In the developing cortex, microglia move toward the subcortical plate and accumulate in the junction of the cortical plate and pre-subplate (Monier et al., 2007). Invading brain macrophages interact with brain structures that are rapidly developing, beginning with rudimentary structures present during neurulation – the formation of the neural tube.

1.1.4. Neurulation

During neurulation, the neural plate develops as a thickened region of embryonic ectoderm (neuroectoderm) overlying the notochord and prechordal plate at approximately E7 in mouse (Rubenstein et al. 1998). The neural groove forms along the midline of this structure and the lateral edges of the neural plate elevate to form neural folds which become prominent by E8. Neurulation continues with neural folds meeting at the dorsal midline of the hindbrain-cervical boundary. Fusion begins here in a 'zipper-like' fashion rostrally to form the bulbous neural tube of the future brain and caudally to form the narrow neural tube of the future spine (Chen et al. 2017).

Closure of the future brain region at the rostral extremity (rostral neuropore) begins by E8.5 with fusion at the forebrain-midbrain boundary progressing bi-directionally to meet the caudally progressing fusion at the rostral forebrain by E9. Continued neural tube fusion results in closure of the hindbrain and spinal cord (caudal neuropore) between E9.5-E10. This process concludes with the separation of the neuroectoderm (future CNS) from the surface ectoderm (future skin) (Chen et al. 2017). Figure 2 shows a diagrammatic representation of these steps.

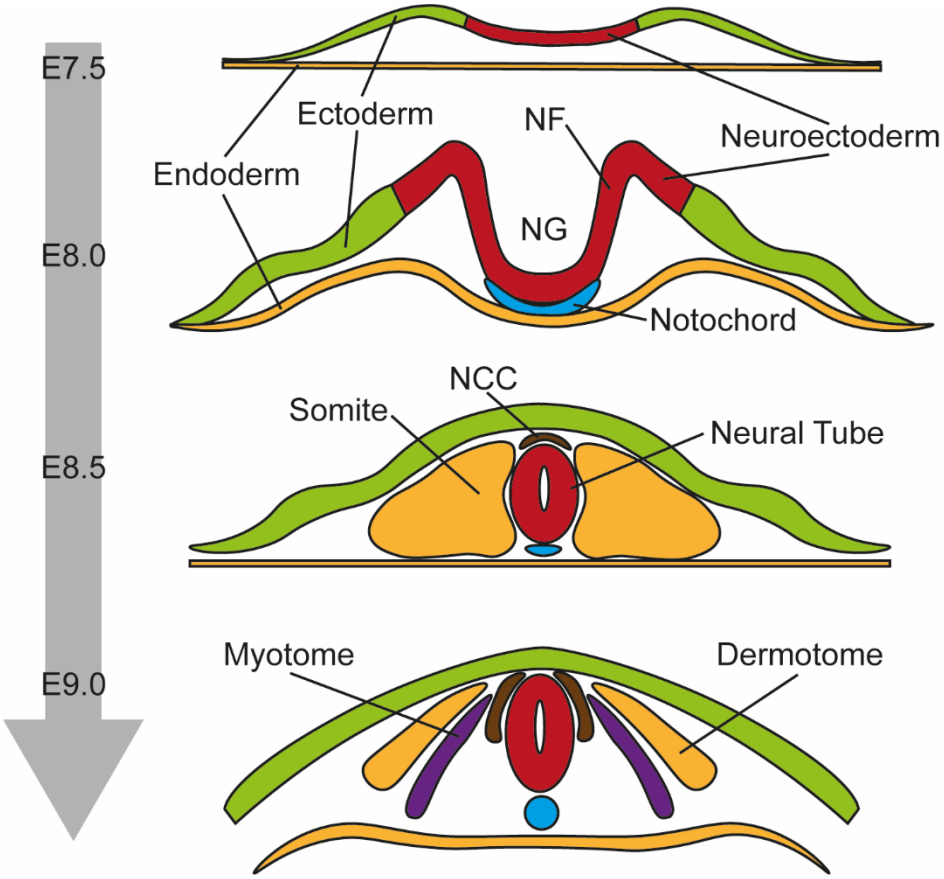

Figure 2: Early neurulation leads to formation of the neural tube.
Diagram showing key stages of neurulation in the developing mouse brain. The neural plate forms from the ectoderm before folding of the neural groove. This folding proceeds to closing of the neural tube alongside appearance of somite pairs and the notochord. During closing of the neural tube, neural crest cells separate. Somites later give rise to the dermatome and myotome (Chen et al. 2017). *NCC – Neural Crest Cells; NF – Neural Folds; NG – Neural Groove.*

As this occurs, early microglial progenitors expressing CX3CR1 begin to appear in the CNS. Round CX3CR1-GFP^{+} cells, not detected at E8, are found in the mesenchyme surrounding the nestin^{+} neural tube at E9 (Kierdorf et al. 2013). By E10.5, a small number of CX3CR1+ cells have entered the neuroepithelium of the neural tube. These cells will likely become microglia as most are CD206^{-}, in contrast to the CD206^{+} CX3CR1^{+} cells accumulating in the mesenchyme at this stage, which may yet become BAMs or microglia (Utz et al. 2020).

Beginning at E9.5, amoeboid microglial progenitors become more distinct from other macrophages as they enter the neural tube. Upon entry these cells begin losing expression of F4/80 and show signs of phagocytosis, with frequent uptake of 4′,6-diamidino-2-phenylindole (DAPI) -positive dying cells alongside strong Lysosomal-Associated Membrane Protein 2 (LAMP2) expression (Kierdorf et al. 2013). F4/80 is thought to be differentially expressed between microglia and peripheral brain macrophages, including BAMs, which express low or high levels respectively (Lund et al. 2018; Utz et al. 2020). F4/80 is one of the few markers with some evidence that it can be used to distinguish microglial precursors from other early macrophages. Further work is required to identify more markers with a greater distinction between early brain macrophages in order to better analyse the invasion and differentiation of developmental microglia.

1.1.5. Neurogenesis and Cortical Plate Formation

1.1.5.1. Neurogenesis

Brain development continues with the differentiation of the neuroectoderm, surrounding the central lumen of the neural tube, into 3 morphologically distinct layers: the innermost ventricular zone or ependymal layer; the intermediate zone or mantle layer; the outermost marginal zone or marginal layer (Kaufman and Bard 1999). Whereas the ependymal layer becomes distinct at E10, clear differentiation of the mantle and marginal layers as distinct zones begins around E10.5. The mantle and marginal layers will go on to form grey matter and white matter, respectively, of the brain and spinal cord. Later in development, around E14, mantle layer neuroblasts will migrate toward the periphery of the brain so that the grey matter becomes superficial to the white matter (Götz and Huttner 2005). The ependymal layer is composed of neuroepithelial progenitor cells that give rise to the vast majority of neurons, astrocytes and oligodendrocytes as well as ependymal cells of the ventricular lining (Tramontin et al. 2003). As ependymal cells only make up a small proportion of the ependymal layer, Ventricular Zone (VZ) may be more appropriate terminology for this region (Chen et al. 2017).

Proliferation of neural progenitor cells (NPCs) in the neuroectoderm is initially symmetrical, producing two identical daughter progenitors with every division to rapidly increase the NPC pool. This proliferative stage gradually transitions into a neurogenic stage between E10-E12, as differentiation of the neuroectoderm begins. Asymetric division involves NPCs in the

developing VZ producing one identical progenitor cell and a cell committed to differentiation into a neuron. The gradual shift in proliferation types proceeds from caudal to rostral regions. The transition from symmetrical to asymmetrical division marks the beginning of neurogenesis (Matsuzaki and Shitamukai 2015).

1.1.5.2. Cortical Plate Formation

Generally, each population of neurons is produced during a specific window of a few days, however regions with greater neuronal diversity, including the cerebral cortex, have longer neuron production. Complex cortical neurogenesis occurs between E11-E17 in mouse, with larger neurons generally being produced before shorter ones. In the cerebral cortex, the majority of neurons are organised within the cortical plate (Chen et al. 2017). The 6 layers of the cerebral cortex form in an 'inside-out' manner with earlier migrating neurons forming deeper layer 6 before later migrating neurons form successively more superficial layers up to layer 1 (Hicks and D'Amato 1968; Austin and Cepko 1990).

Early in neurogenesis, radial glial cells differentiate from neuroepithelial progenitors. Radial glia extend long processes across the early cortex and have the capacity to differentiate into neurons, astrocyte or oligodendrocytes (Malatesta and Götz 2013). The extension of radial glia processes across the entire thickness of the cerebral cortex, provides structure for the construction of the cortical plate, allowing neurons to migrate from the VZ to the mantle (Pinto and Götz 2007; Matsuzaki and Shitamukai 2015). The migration and differentiation of NPCs from the VZ into the marginal zone results in a bilaminar structure by E13 composed of the VZ and primitive pre-plate. As this process continues the marginal zone's pre-plate becomes divided into the nucleated regions of the cortical plate and subplate and the relatively anuclear intermediate zone, composed of cellular processes and transient migrating cells by E13.5-E14 (Molnár et al. 2006; Rash and Grove 2006).

As development progresses the cortical plate grows and becomes more dense with neuroblasts and eventually glioblasts entering from the VZ and Sub-Ventricular Zone (SVZ). Whilst most cortical neurons arise from the VZ via radial migration of neuroblasts forming excitatory glutamatergic projection neurons, neuroblasts from the ganglionic eminences migrate tangentially to form GABAergic inhibitory interneurons (Chen et al. 2017). Callosal projection neurons are born during various stages of development. Layer 6 callosal projection

neurons are born at approximately E12.5 along with corticothalamic projection neurons. Layer V cortical projection neurons are born around E13.5 with corticospinal motor neurons and layer II and III cortical projection neurons are born between E15.5-E17.5 (Fame et al. 2011).

Microglia, examined through Iba1 expression, were identified as being sparsely populated throughout the cerebral cortex during layer 6 neuron formation in the rhesus monkey (Cunningham et al. 2013). A monolayer of Iba1+ cells between the VZ and SVZ was found as well as a concentration of Iba1+ cells near blood vessels. By layer 4 neuron production, microglia had formed a dense band within the SVZ as found within human neocortex at 10 weeks gestation. The same study found dense microglial VZ/SVZ colonisation in the rat during peak layer 2 neurogenesis, suggesting some variation across species. In the mouse, microglia are clustered within the VZ/SVZ by E14.5 (Arnò et al. 2014). This increase in microglial ventricular zone density corresponds with the natural thinning of the proliferative VZ and inner SVZ in rats, and was contrasted with a sparse cortical distribution 2 days prior (Cunningham et al. 2013). Microglial migration into the VZ is mediated by neurogenesis and basal progenitor expression of Cxcl12 (Arnò et al. 2014).

1.1.6. The Maternal Immune Activation Model

Maternal Immune Activation (MIA) refers to the activation of maternal inflammatory pathways resulting in increased levels of inflammatory signalling molecules in maternal circulation. These inflammatory signalling molecules cross the placental and blood-brain barriers to influence foetal neurodevelopment (Bao et al. 2022a; Massarali et al. 2022). MIA is a frequently used model for the study of microglia. As such, an outline of this model will be presented here as context for the subsequent discussion of experimental results.

Under normal conditions, the immune system triggers an inflammatory response upon contact with pathogens in order to prevent infection. Characteristics of the inflammatory response depend upon the type of pathogen encountered, with differing arrays of cytokines and cell types triggered to respond to different pathogens (Verhoef et al. 2019). Pathogens are identified by the immune system through the binding of antigens to the receptors of immune cells (Charles A Janeway et al. 2001). These antigens can therefore be used in experimental models, such as MIA, to trigger an inflammatory response without the presence of the pathogen itself, inducing a ‘clean infection’.

Two commonly used antigens for MIA are the bacterial endotoxin lipopolysaccharide (LPS) and the synthetic viral RNA polyinosinic:polycytidylic acid (Poly I:C). LPS forms a large part of the outer membrane of gram-negative bacteria and is recognised by immune cells upon binding Toll-like receptor 4. Poly I:C is a synthetic analogue of double-stranded RNA which is typically found in some viruses and binds to Toll-like receptor 3 on immune cells (Maelfait et al. 2008). These two antigens trigger divergent immune responses leading to differing circulating maternal cytokine profiles and differing outcomes for offspring exposed to MIA (Bao et al. 2022a). As a side note, the coronavirus SARS-Cov-2 responsible for the COVID-19 respiratory illness and COVID-19 pandemic produces double-stranded RNA as part of its replication cycle (Gorbalenya et al. 2020; Bao et al. 2022a). Whether Poly I:C can act as a suitable model for COVID-19 infection requires more research.

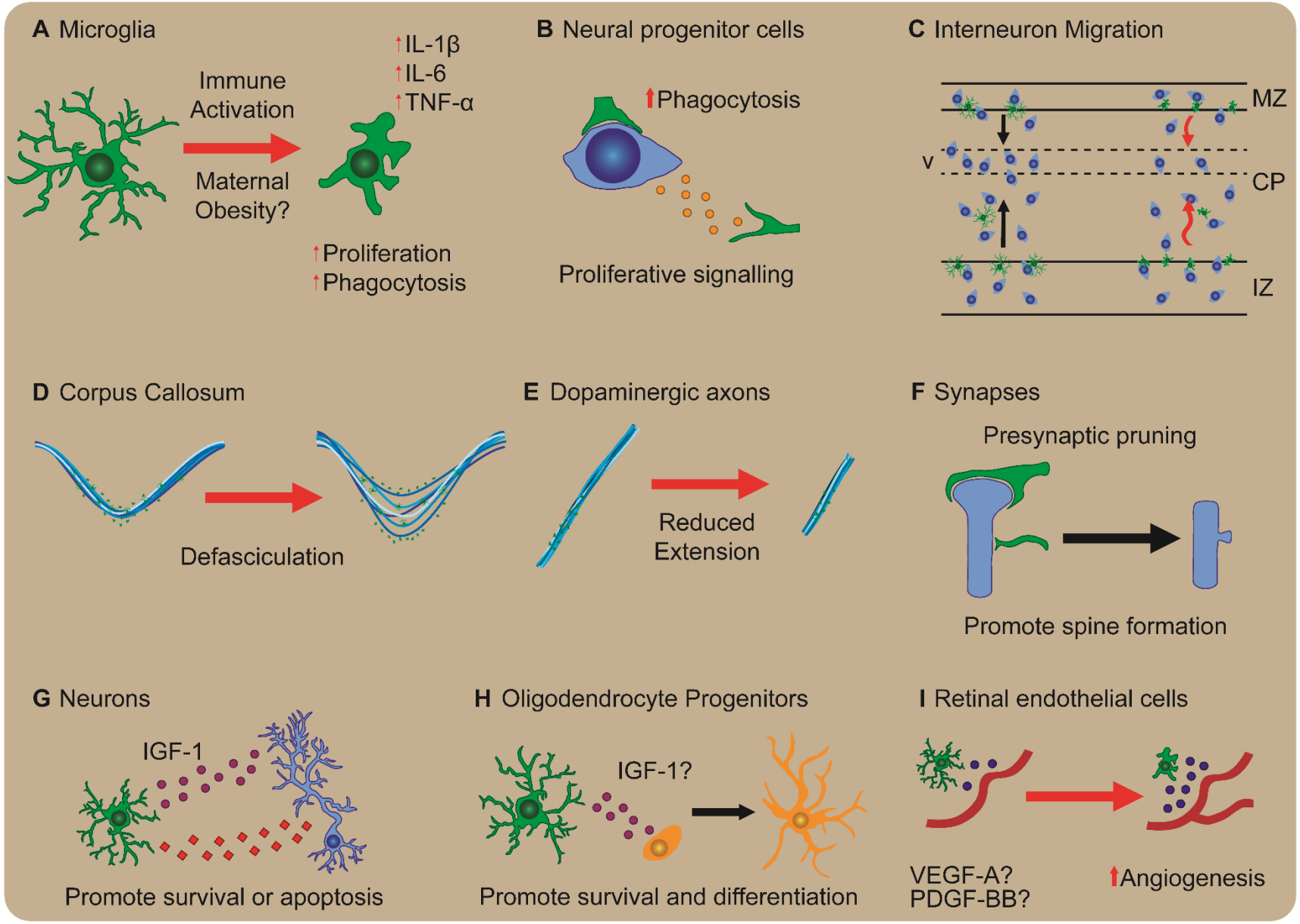
A Microglia
Immune Activation
Maternal Obesity?
↑IL-1β
↑IL-6
↑TNF-α
↑Proliferation
↑Phagocytosis
B Neural progenitor cells
↑Phagocytosis
Proliferative signalling
C Interneuron Migration
MZ
v
CP
IZ
D Corpus Callosum
Defasciculation
E Dopaminergic axons
Reduced Extension
F Synapses
Presynaptic pruning
Promote spine formation
G Neurons
IGF-1
Promote survival or apoptosis
H Oligodendrocyte Progenitors
IGF-1?
Promote survival and differentiation
I Retinal endothelial cells
VEGF-A?
PDGF-BB?
↑Angiogenesis

Figure 3: Developmental roles of microglia and how they are affected by maternal immune activation.

Maternal obesity primes microglial response to activation and is hypothesised to interfere with developmental functions of microglia. Some of the key functions of the role of microglia during brain development and the impact of immune activation are illustrated below. Upon interaction with pathogen-associated molecular patterns microglia become activated and increase expression of interleukin (IL) -1β, IL-6 and tumour necrosis factor-α (TNF-α). **A)** Postnatal cerebellar microglia show increased proliferation and phagocytosis and become ameboid in morphology upon LPS stimulation. **B)** Developmental functions of microglia start early in the brain where they regulate neural progenitor cell population size through phagocytosis and inducing proliferation in the prenatal cortex. Maternal immune activation reduces neural progenitor number likely through increased phagocytosis. **C)** Prenatal microglia are thought to regulate cortical interneuron migration. Microglia invade the developing cortical plate at the same time as Lhx6-expressing interneurons which accumulate in layer V. Maternal immune activation induces premature migration of Lhx6 interneurons into the cortical plate and reduced interneuron accumulation at layer V. **D)** Microglia associate closely with a subset of axonal tracts and play a critical role in their development. In the Corpus Callosum, both MIA and microglial depletion results in axon tract defasciculation. **E)** By contrast, MIA reduced the extension of dopaminergic axons into the subpallium, an effect opposite to microglial depletion. **F)** During postnatal development, microglia remove pre-synaptic structures through trogocytosis and induce spine head formation upon contact. **G)** They also support survival of postnatal layer V neurons through Insulin-like growth factor 1 (IGF-1) signalling and induce apotosis in post-natal cerebellar neurons. **H)** Similar trophic support for oligodendrocyte precursor survival and differentiation has been proposed within the postnatal corpus callosum. **I)** Lastly, immune activation increased microglial vascular endothelial growth factor A (VEGF-A) and platelet derived growth factor BB (PDGF-BB) expression and induced angiogenesis in retinal endothelial cells. *CP- Cortical plate. MZ- Marginal zone. IZ- Intermediate zone.*

This figure was adapted from Davis and Mire (2022)

1.1.7. Developmental Phagocytosis

Colonisation of the VZ/SVZ, where tbr2^{+}/pax6^{+} NPCs are located, allows microglia to influence cortical development. Here microglia contact, engulf and phagocytose healthy (non-apoptotic) Tbr2^{+} and Pax6^{+} NPCs throughout neurogenic and post neurogenic stages of cortical development (Arnò et al. 2014). The percentage of Tbr2+ cells contacted and likely later phagocytosed, as measured by live cell imaging, by microglia increased throughout development. Depletion of microglia through liposomal chlodronate injection – an inducer of cell death taken up by macrophages and microglia specifically (Rooijen and Sanders 1994), increased neural precursor number in organotypic brain slices. Furthermore, the reduced activation of microglia through doxycycline addition increased the number of NPCs pre- and postnatally, and increased the size of the SVZ postnatally as well as increased the number of NeuN+ neurons in the SVZ. The reverse treatment: activation of microglia via LPS injection, had the opposite effect on NPC number but not SVZ thickness (Cunningham et al. 2013). These findings are summarised in Figure 3B. Combined, these data demonstrate the need for the correct function and spatio-temporal distribution of this microglial population to assist with the progression of cortical development out of the neurogenic phase.

An increase in microglial density was also found within other proliferative zones of the developing brain including: the macaque medial wall telencephalon; the E80 macaque ganglionic eminence; the E100 macaque cerebellum; the E20 rat hippocampal formation; the P0 rat subpallial neurogenic zone of the hippocampal formation; the E20 ventricular zone of the rat third ventricle (Cunningham et al. 2013). This increase in density has been observed within the ventricular zone of the human neocortex at 10 weeks gestation. Microglia were shown to phagocytose progenitor cells at each of these sites, suggesting a widespread need for microglial localisation at proliferative zones during early brain development.

Some evidence supports the hypothesis that microglia phagocytose live differentiated neurons. This was shown initially under LPS induced neuro-inflammatory conditions through release of peroxynitrite and mediated by Milk-fat globule EGF factor-8 (MFG-E8) (Fricker et al. 2012) and later under control conditions in proliferative zones (Cunningham et al. 2013). MFG-E8 is also used by microglia for clearance of apoptotic cells, including neurons and NPCs, through interactions with the apoptotic marker phosphatidylserine (Fuller and Van Eldik 2008).

The overproduction of neocortical neurons in mouse through increased neural progenitor population size resulted in autism-like behavioural deficits (Fang et al. 2014). On the other hand, decreased cortical neuron number lead to memory deficits in mouse (Kim et al. 2019). Indeed, increased brain size and neuron number are often observed in children with ASD and reduced cortical neuron number is found in patients with schizophrenia (Courchesne et al. 2011; Gaus et al. 2022). These findings suggest that disruption to microglial regulation of NPC pool size, either through phagocytosis or other methods, could in part lead to neuropsychiatric or neurodevelopmental disorder. Further research is required to fully establish the relationship between microglial control of NPC pool size and neuropsychiatric or neurodevelopmental disorders in human.

1.1.8. Developmental Apoptosis

Apoptosis is a key component of cortical development, occurring in the ventricular zone, intermediate zone and the developing cortical plate between E12-E18. This allows removal of excess NPCs and temporary structures such as the pre-plate. Although the relative percentage of apoptotic cells is relatively low, estimated to be between 0.14 and 0.35% per day in the cortex (Deverman and Patterson 2009; Chen et al. 2017).

Microglial density increase, driven by invasion and local proliferation, in the zebrafish brain correlates with elevated neuronal apoptosis (Casano et al. 2016). Experimental modification to rates of apoptosis, either through UV laser irradiation or caspase-3 knockdown/inhibition, resulted in concomitant increase or decrease in microglial density. Additionally, ectopic apoptosis induction in the hindbrain, usually containing few microglia, increased microglial density in this region 24 hours later. Microglial attraction to sites of neuronal apoptosis was shown to be dependent upon nucleotide signalling through combined blockage of nucleotide release and receptor inhibition. This feature of embryonic brain development allows microglia to remove apoptotic debris (Mazaheri et al. 2014).

The choroid plexus undergoes high levels of apoptosis throughout concurrent waves of differentiation during formation (Currle et al. 2005). Microglia can be found at increased numbers within the mouse choroid plexus beginning at E11.5, peaking around E12.5-E13.5 before becoming no longer visible at E16.5 (Swinnen et al. 2013). This cluster of cells was

found within close proximity of cleaved caspase-3 labelled apoptotic choroid plexus cells, leading authors to propose that these 'activated' microglia are phagocytosing cellular debris.

Induction of apoptosis is another mechanism utilised by microglia for the removal of excess neural cells, as depicted in Figure 3G. During postnatal stages of developmental apoptosis, when cerebellar Purkinje cells are engaged in synaptogenesis, a significant number of developing neurons are removed. Microglia selectively remove Purkinje neurons within the cerebellum through the release of superoxide ions, inducing programmed cell death. This is followed by phagocytosis of cellular debris (Marín-Teva et al. 2004). The removal of apoptotic debris is known to be carried out by microglia even in the absence of microglial induction of apoptosis (Mazaheri et al. 2014).

1.1.9. Trophic Support

In opposition to decreases in NPC population size, microglia have also been shown to increase neuron number through the induction of proliferation in co-cultured NPCs (Yamamiya et al. 2019). In the early postnatal rat brain, inhibition of microglial activation through minocycline decreased proliferation of neural and oligodendrocyte progenitors. Blocking cytokine signalling in *in-vitro* microglial co-culture experiments also reduced neural and oligodendrocyte progenitor proliferation (Shigemoto-Mogami et al. 2014). These findings suggest microglial cytokine release – in particular IL-6 and IL-1β; enhances NPC proliferation in the developing rat brain. Microglial secretion of the cytokine osteopontin has also been shown to enhance NPC proliferation (Yamamiya et al. 2019). Further *in vitro* experiments suggest human microglia behave in a similar fashion, as human NPC microglial co-culture increased survival and proliferation of both cell types (Liu et al. 2013).

Adult IL-4 or IFN-γ activated microglia increased proliferation of co-cultured oligodendrocytes and NPCs in an IGF-1 dependent mechanism (Butovsky et al. 2006). Microglial secretion of IGF-1 is also required during early postnatal mouse brain development for survival of layer V cortical neurons (Postnatal day 3-7, P3-7) (Ueno et al. 2013) and oligodendrocytes (P4-7) (Wlodarczyk et al. 2017a). TNF-α secretion by LPS activated microglia on the other hand, blocked proliferation of co-cultured adult oligodendrocyte and NPCs (Butovsky et al. 2006). These contrasting findings highlight the vastly divergent effects of microglia found within differing environments or when exposed to specific cytokines.

Dense microglial populations also support white matter development. Increased density of iba1 immuno-labelled microglia have been observed within regions of mouse white matter postnatally (Ueno et al. 2013). Specifically, Green Fluorescent Protein (GFP) lentivirus labelled axons within the subcortical white matter, internal capsule, cerebral peduncle and corpus callosum with microglia increasing from P1-P3, peaking in number between P3-P7 before becoming diffuse after P14.

Neurons projecting to the corpus callosum and subcerebral regions can be found within layer V (Koester and O'Leary 1993). Interestingly, modifying microglial function through activation, suppression, transient ablation or genetic fractalkine receptor dysfunction increased terminal deoxynucleotidyl transferase dUTP nick-end labelling (TUNEL)-positive apoptotic cells within layer V (Ueno et al. 2013). Many of the apoptotic cells also labelled with cleaved caspase-3 co-expressed CTIP2, which is expressed by layer V subcerebral projecting neurons (Arlotta et al. 2005). Successive microglial-neuron co-culture experiments revealed microglial IGF1 release supports the survival of layer V neurons, depicted in Figure 3G. (Ueno et al. 2013). Whilst transient ablation decreased microglial number within white matter tracts, activation suppression or fractalkine receptor dysfunction models did not. This highlights the need for both correct microglial density and function around developing white matter tracts within the mouse. Given that, reduced interhemispheric connectivity is associated with social deficits in ASD, reduced microglial trophic support for layer V neurons could be involved in ASD development (Yao et al. 2021).

1.1.10. Interneuron migration

Microglia regulate the formation of neural structures at other time points through guidance of developing neurons (Figure 3C). Squarzoni *et al.* (2014) provide evidence of microglial involvement in the guidance of forebrain dopaminergic axons and laminar positioning of specific neocortical interneurons. In keeping with previous studies (Hoshiko et al. 2012; Cunningham et al. 2013), microglia were perturbed using mouse models either through depletion (*Pu.1*$^{-/-}$) or functional disruption (LPS MIA, *Cx3cr1*$^{-/-}$, *C3*$^{-/-}$, *DAP12*$^{-/-}$). Although cortical lamination and thalamic axon invasion was not disrupted at E18.5 in these models, as measured by immuno-labelling cortical neuron - Tbr1, Ctip2, Cux1; or thalamic and cortical axon markers – L1, neurofilament. Interneuron migration was disrupted. Specifically, the

Lhx6-expressing sub-population of cortical interneurons had less focal distribution around laver V in Pu.1$^{-/-}$, LPS MIA, *Cx3cr1*$^{-/-}$ and *DAP12*$^{-/-}$ mice compared with control animals at E18.5 and P7. This disruption persisted into early adolescence (P20) in Pu.1$^{-/-}$ and LPS MIA models with a parvalbumin expressing subset of these interneurons found at 10% increased level in layers III/IV relative to control mice.

As with other functions of microglia in development, correct positioning appears important for interneuron guidance. *Cx3cr1*^{GFP} labelled microglia appear mostly absent from the cortical plate until E16.5 when they begin progressively invading, beginning with deeper cortical layers (Squarzoni et al. 2014). This pattern mirrors the positioning of cortical inhibitory interneurons (Hevner et al. 2004). *Cx3cr1*$^{-/-}$ mutants had a slight shift in neocortical positioning which, as the authors suggest, could indicate that microglial misplacement contributed to observed altered *lhx6*$^{+}$ interneuron distribution at E18.5 and P7 (Squarzoni et al. 2014).

1.1.11. Corpus Callosum Formation

As the major interhemispheric commissure connecting both sides of the brain, corpus callosum formation is highly dependent on proper midline formation and fusion. This process requires glial cells – astrocytes, oligodendrocytes and microglia. Like all developmental processes, formation of the corpus callosum is best described in relation to earlier developmental structures.

At formation of the telencephalic hemispheres, rostral regions of the forebrain are joined but more dorsal regions, where the callosal axons will eventually cross the midline, must fuse for axons to cross the midline and the corpus callosum to form. This midline fusion occurs at approximately E14-E15 in mouse, although there is some variation in mouse strains (Richards et al. 2004b). The midline zipper glia (MZG), a population of early astrocytes, regulate this structural change through degradation of the interhemispheric leptomeninges, allowing fusion of the two hemispheres (Richards et al. 2004b; Fame et al. 2011; Gobius et al. 2016). MZG are thought to be guided by expression of sonic hedgehog and slit proteins (Lindwall et al. 2007). These cells provide a substrate for the subsequent migration of axons across the midline, guided by additional populations of early astrocytes that act as guidepost structures or axon guidance boundaries (Figure 4). These are induseum griseum glia and glial wedge glia (Shu et al. 2003b; Lindwall et al. 2007).

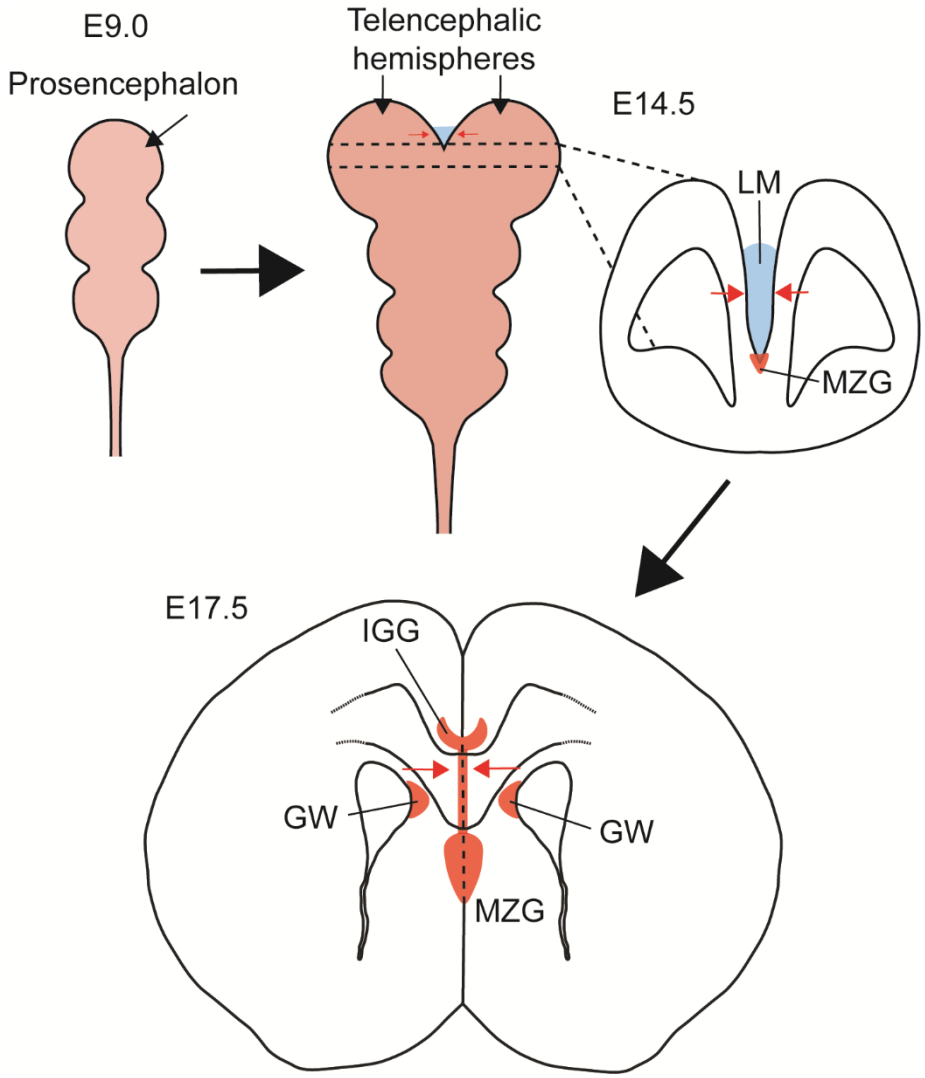

Figure 4: Fusion of developing mouse brain hemispheres involves midline zipper glia.

Diagram showing the fusion of mouse brain hemispheres. Telencephalic vesicles or hemispheres begin to develop as two buds from the prosencephalon around E9.5 (Chen et al. 2017). Around E14-E15, midline fusion occurs with degradation of the interhemispheric leptomeninges. The midline zipper glia are hypothesised to play an active role in this process (Richards et al. 2004). Following fusion of the developing hemispheres, glia are split into separate populations above and below the corpus callosum. Glial Wedge Microglia are also present at this time. *GW – Glial Wedge; IGG – Induseum Griseum Glia; LM – LeptoMeninges; MZG – Midline Zipper Glia.*

Gene expression data suggests glial wedge cells may also be involved in corpus callosum formation (Lindwall et al. 2007). Fibroblast growth factors are thought to be important for development of midline glial structures, particularly the induseum griseum (Lindwall et al. 2007). The nuclear factor 1 family of transcription factors, such as *Nfia* and *Nfib,* that act through GFAP and GAP43 to regulate radial glia differentiation into astrocytes are also known to be important for correct development of these glial structures (Lindwall et al. 2007).

The subcallosal sling, also referred to as the glial sling, is another important structure involved in corpus callosum development. Positioned just ventral to the corpus callosum and expected to provide guidance substrate for callosal fibres, these cells were initially described as glial precursors but many of the cells were found to be neurons (Shu et al. 2003b; Niquille et al. 2009). This forms between E15-E17 and nuclear factor transcription factors and JSAP1 are involved in its formation (Lindwall et al. 2007).

1.1.12. Axon development

1.1.12.1. Corpus Callosum Axon Tract Guidance

Corpus callosum development continues with axon migration across the midline occurring at E16.5 (Wahlsten et al. 2006). This process is outlined in Figure 5. Following axon growth through the intermediate zone, distinguishing from subcortically projecting axon by turning towards the midline and growing through the cingulate cortex, neocortical neurons reach the midline (Richards et al. 2004b). Correct positioning of callosal axons requires guidance molecule expression by guidepost glia and neurons in the glial wedges and induseum griseum (Shu et al. 2003b; Richards et al. 2004b; Niquille et al. 2009). This correct positioning within the corpus callosum is also necessary to innervate the relevant contralateral cortical area, meaning that incorrect positioning could result in cortical developmental abnormalities (Suárez et al. 2014).

Microglia accumulate at the site of the future corpus callosum at E15.5. The abundant presence of microglia during callogenesis make it an important region to understand in order to decipher the role of microglia in shaping developmental tracts (Pont-Lezica et al. 2014). Corpus callosum abnormalities are amongst the most common brain malformations detected prenatally and are often associated with neurodevelopmental disorders (Yeh et al. 2018; Bina et al. 2020). Furthermore, the demonstrated susceptibility of the corpus callosum to

developmental disruption through maternal immune activation make understanding the role of microglia important to assist in the creation of intervention strategies for neurodevelopmental disorders.

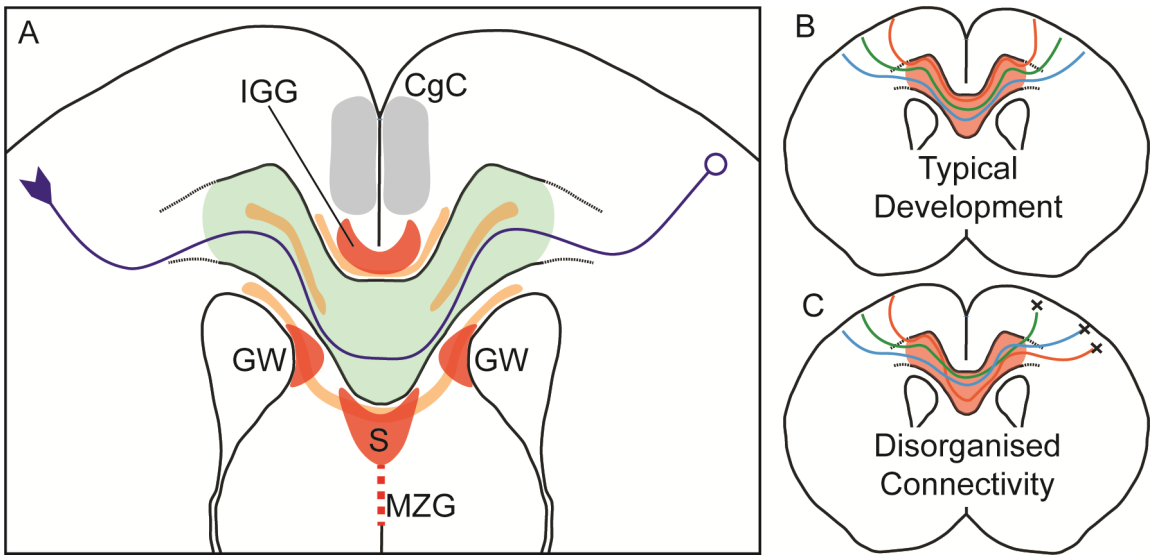

Figure 5: Several populations of different cell types guide developing corpus callosum axons across the midline.

A) Diagram of structures present around the developing corpus callosum, some of which are involved in guidance of axons across the midline. A neuron is shown in blue guided from left to right across the midline by guidepost structures to innervate the contralateral cortex. Populations of glia are shown in red. Glial wedge and induseum griseum glia have been shown to act as axon guideposts (Richards et al. 2004), but septal microglia have not. Guiding glutamatergic neurons are shown in orange as strips visible at E18.5 in mouse with guiding GABAergic neurons throughout the corpus callosum in green (Niquille et al. 2009). **B)** Diagram of correct corpus callosum positioning, for example with medial axons travelling through the dorsal corpus callosum to innervate the correct medial region of the contralateral cortex. **C)** Diagram of incorrect corpus callosum positioning, for example with medial axons travelling through the ventral corpus callosum to innervate the incorrect lateral region of the contralateral cortex. *CgC – Cingulate Cortex; GW – Glial Wedge; IGG – Induseum Griseum Glia; MZG – Midline Zipper Glia; S – Septal Microglia*

Callosal axons may be guided by a dense microglial population. At E15.5 Cx3xr1^{gfp} labelled microglia were shown to accumulate at the site of the future corpus callosum in the mouse (Pont-Lezica et al. 2014). This microglial population continues at least until E17.5 where a dense group of these cells was observed within the midline zipper (or septal) region and subcallosal sling, which extends to the ventricular aligned glial wedges. Microglia in these corpus callosum associated regions form two populations – round, CD68^{hi} cells mostly outside the tracts ventrally; ramified CD68^{lo} cells within the callosal tract.

MIA through LPS injection and mutation of *Dap12*, a microglia specific signalling molecule associated with white matter alterations, were selected as models of microglial dysfunction through which to analyse corpus callosum development. *Pu.1*$^{-/-}$ mice were also chosen to see the effects of microglial depletion on the developing corpus callosum. Whilst none of these models displayed changes in corpus callosum width or axon midline crossing, all three displayed defasciculation – the increased extension of NRP1 labelled axons ventrally into the L1CAM labelled corpus callosum (Pont-Lezica et al. 2014). Given that axon position within the corpus callosum determines contralateral target innervation, defasciculation could result in significant defects in cortical innervation (Zhou et al. 2013a; Suárez et al. 2014).

MIA and *Dap12*$^{-/-}$ mice did not show any changes in microglial distribution (Pont-Lezica et al. 2014). Microglia under these conditions did however show predominant down regulation of genes involved in neuritogenesis. This example suggests that normal microglial function, or developmental gene expression, is also required for corpus callosum development even with normal formation of the septal hotspot.

Microglia in corpus callosum associated regions are hypothesised to participate in axon growth and guidance through trophic support of formation pathways (Figure 3D). Alternatively, microglia may control the development of corpus callosum axon tracts through phagocytosis of guidepost glia and neurons, or by endocytosis of guidance molecules (Pont-Lezica et al. 2014). These hypotheses are based on gene expression data and understanding of the phagocytic function of microglia in development of other axon tracts. Further work is required to fully understand the role of microglia in corpus callosum development.

1.1.12.2. Dopaminergic Axon Tract Guidance

From E11.5 to E18.5 dopaminergic axons extend a long distance from the ventral mesencephalon to the telecephalon before innervating the striatal limbic system and neocortex (Prestoz et al. 2012). A key stage during this process is the halting of axon progression at E13.5 in the sub-pallium prior to extension into the striatum.

Microglia form a dense hotspot and assist with the guidance of striatal dopaminergic axon tracts (Figure 3E). This was demonstrated within the mouse brain where Cx3xr1^{gfp} labelled microglia were homogenously distributed at E12.5 and P20, in contrast to E14.5 where microglial hotspots were observed at the extremities of TH immuno-labelled midbrain dopaminergic axons (Squarzoni et al. 2014). Interestingly, the cortico-striatal notch (sub-pallial boundary) appears to contain, the basal progenitor expressed microglial attractant, Cxcl12 possibly explaining the increased density of microglia drawn to this region (Arnò et al. 2014).

In microglial depletion mouse models striatal TH-positive dopaminergic axons extended into the sub-pallium further than in control animals, in contrast to LPS MIA mice which exhibited a reduction in sub-pallial axon projection relative to controls (Squarzoni et al. 2014). Concurrent defects were observed at birth where an increased dorsal or ventral extension of dopaminergic axons were found in depleted or LPS MIA models respectively. Both models resulting in imbalanced striatal dopaminergic innervation. Whilst whole brain microglial depletion does not demonstrate that this specific hotspot is required for dopaminergic axon development, described TH-positive fragments found within the cytoplasm of hotspot microglia suggests that they are important for phagocytosis of these developing tracts.

1.1.13. Synapse regulation

During post-natal brain development microglia regulate synapse formation and removal. Contact of microglia on dendritic spines induces filopodia formation and increase in spine density (Miyamoto et al. 2016). Whilst later, during learning-dependant synapse formation, microglial BDNF secretion increases phosphorylation of a key mediator of synaptic plasticity (tropomyosin-related kinase receptor B) (Parkhurst et al. 2013). Presynaptic structures targeted for removal on the other hand are engulfed and trogocytosed by microglia in TREM2 and Complement 3 dependant mechanisms, removing them from the developing brain as shown in Figure 3F (Schafer et al. 2012; Filipello et al. 2018; Weinhard et al. 2018).

Microglia may also be involved in synapse maturation. Delayed recruitment of microglia to mouse thalamocortical barrel centres, usually occurring between P5-P9, also delayed functional maturation of postsynaptic glutamate receptors (Hoshiko et al. 2012). This delayed microglial recruitment was mediated by CX3CR1 deficiency. CX3CR1 is a fractalkine receptor able to bind neuronal CX3CL1 (fractalkine) and mediate microglial-neuronal interactions (Arnoux and Audinat 2015).

The CX3CL1-CX3CR1 axis has been shown to be involved in chemotaxis and adhesion of leukocyte populations and CX3CL1 can function as both a chemokine and an adhesion molecule (Cormican and Griffin 2021). CX3CL1 has also been shown to regulate microglial activation, with CX3CL1 expression either on the cell surface of neurons or released from neurons reducing activation of microglia (Biber et al. 2007; Paolicelli et al. 2014). Within the CNS, CX3CR1 is exclusively expressed by microglia (Jung et al. 2000; Hughes et al. 2002).

Reduction in mouse microglial synapse removal through *Cx3cr1* knockout, lead to increased hippocampal (CA1) pyramidal dendritic spine density. Single-cell electrophysiological recordings suggested immature connectivity and synapse function as well as a delay in brain circuit development at the whole-animal level (Paolicelli et al. 2011). These data demonstrate the necessity of microglia for healthy brain development in the mouse with defects observed in *Cx3cr1* knockout mice reminiscent of synaptic abnormalities seen in neurodevelopmental disorders such as ASD or Intellectual Disability (Pfeiffer et al. 2010).

1.1.14. Microglia in the Human Condition

The study of developmental microglia in the human brain is hindered by limitations not relevant to animal models. Human tissue can only be investigated through post-mortem studies. This limits the amount of tissue available to study, meaning that a single case is often used to generalise over an entire gestational age (Menassa and Gomez-Nicola 2018a). Furthermore, where tissue from spontaneous abortion is used, the lack of neuropathological abnormalities does not preclude the possibility of an underlying condition responsible for pregnancy loss that could also influence microglial behaviour.

Despite technical limitations, histopathological studies on human embryonic and foetal tissues produced similar results to animal models with regard to microglial distribution (Menassa and Gomez-Nicola 2018a). For example, early microglia cells, labelled with anti-IBA1 antibody, accumulate in the VZ during neurogenesis following entry from the meningeal or ventricular surface (Monier et al. 2006; Monier et al. 2007). Microglia also form dense clusters around the developing corpus callosum, as observed in mouse (Rezaie et al. 2005; Monier et al. 2007).

Although there is a lack of functional studies in human tissue, the distribution of microglia in the human brain suggests similarities in microglial function with animal studies. Microglia accumulate in association with specific areas of: neuronal migration; white matter tract formation; vasculogenesis; astrocyte formation; and synaptic pruning (Menassa and Gomez-Nicola 2018a).

1.2. Microglial Heterogeneity

Given such a broad range of tasks are performed by microglia throughout development, often in direct opposition to each other (promote spine formation/remove dendritic spines, induce NPC proliferation/induce neural apoptosis - Figure 3), it is likely that different populations of microglia exist within the developing brain. Indeed, many divergent microglial populations have now been identified and are beginning to be characterised. This feature of microglia was proposed from the outset with Rio-Hortega's original discovery of microglia in 1919, these cells were shown to vary by ramification (Stratoulias et al. 2019). Ameboid cells were referred to as 'activated' with ramified microglia termed 'resting' in reference to their immunological function, a distinction still used today. More recently, advances in single-cell sequencing have allowed systematic attempts to characterise microglial subtypes shedding more light on microglial heterogeneity throughout the lifespan.

Single-cell sequencing studies have consistently found highest transcriptional diversity during embryonic and early postnatal time points. This is despite variation in techniques used and number of cells analysed. In contrast, adult steady state conditions were found to have limited transcriptional heterogeneity (Matcovitch-Natan et al. 2016; Hammond et al. 2019; Li et al. 2019a; Masuda et al. 2019). Earlier microglia were also shown to differ from adult microglia in their decreased expression of canonical microglial signature genes such as *Tmem119* and *P2ry12* (Hammond et al. 2019; Masuda et al. 2019). Microglia are known to assume a variety of different morphologies and, as discussed, are distributed unevenly in the developing brain (Karperien et al. 2013). The power of single-cell sequencing in transcriptional profiling comes at the cost of morphological or density analysis, meaning features such as the morphology and density of many of the diverse developmental microglial populations are not yet known.

1.2.1. Early prenatal microglia

Examination of microglial transcription profile begins with precursors in the yolk sac and primitive brain at E10.5 (Matcovitch-Natan et al. 2016). These cells are described as 'early microglia', present at E10.5, E12.5 and E14.5, characterised by expression of cell cycling and differentiation associated genes *Mcm5* and *Dab2*. Despite spatial segregation between the yolk sac and brain, early microglia maintained transcriptional similarity. In the brain, early microglia transition into 'pre-microglia' which were present at E14.5, E16.5 and until after birth

at P3, P6 and P9. These cells are characterised by their expression of *Csf1* and *Cxcr2*, genes involved in neuronal development.

Li et al. (2019) describe a population of 'embryonic-like' microglia isolated from the E14.5 brain which segregate from P7 and P60 populations upon clustering, but show some similarity to a subset of proliferative P7 microglia. In contrast to the homogenous E14.5 embryonic-like population, Hammond et al. (2019) identify 3 distinct populations within the E14.5 brain. One of these populations share transcriptional similarities with BAMs, whilst the others transcriptionally similar to each other and enriched for genes involved in metabolism or proliferation. These metabolically active and proliferative microglia populations were also found in P4/P5 samples, perhaps explaining why E14.5 embryonic-like microglia were transcriptionally similar to P7 'primitive microglia' in Li et al. (2019). Proliferative microglia are characterised by their expression of *Mcm6* which, like *Mcm5* expressed by early microglia, is important for cell division and stimulated during growth (Ohtani et al. 1999). Metabolically active microglia were shown to upregulate transcripts associated with glycolysis (Hammond et al. 2019). Metabolically active and proliferative microglia are suggested to play a key role in expansion of microglial populations to populate the whole brain before giving rise to mature microglia. Postnatal-immature microglia, identified by Li et al. (2019) in the P7 brain, are suggested to fulfil a similar transitional role giving rise to either homeostatic adult microglia or Proliferative-region-Associated Microglia (PAM) populations which will be discussed in greater detail.

1.2.2. Late prenatal and postnatal microglia

Embryonic microglia isolated at E16.5 segregated into 6 distinct clusters characterised by expression of genes such as *Ctsb* and *Lamp1,* related to lysosomes, and *Apoe,* a myeloid cell activation marker (Masuda et al. 2019). $APOE^{+}$ cells were localised to the embryonic forebrain and cerebellum but, like other embryonic clusters, were not found in the juvenile P21 brain. Expression of *Apoe* was similarly observed in PAM and Axon Tract-associated Microglia (ATM) clusters isolated from P7 or P4/5 brains respectively (Hammond et al. 2019; Li et al. 2019a). These early postnatal clusters characterised by increased *Spp1* and *Gpnmb* expression, as well as *Clec7a* for PAM, were localised to the developing white matter tracts of the corpus callosum and cerebellum from P4-14. $CLEC7A^{+}$ PAM were also observed in the neurogenic niches of the lateral ventricles or ventricular zone at E17.5 as well as the

hippocampal dentate gyrus, sub-ventricular zone and rostral migratory stream from P14 onwards. In addition to increased *Apoe* expression, these white matter tract populations are similar to embryonic clusters isolated at E16.5 in their increased expression of *Lamp1*. PAM and ATM also show some similarity with 'pre-microglia' in that they upregulate neuronal development gene *Csf1.* The previously identified 'fountain of microglia' population was observed in the P7 corpus callosum and upregulates *Spp1, Gpnmb* and *Clec7a* (Hagemeyer et al. 2017). Given the high degree of transcriptional similarity between PAM, ATM and fountain microglia, isolated from overlapping brain regions at similar developmental time-points, it is likely that these are the same population of cells.

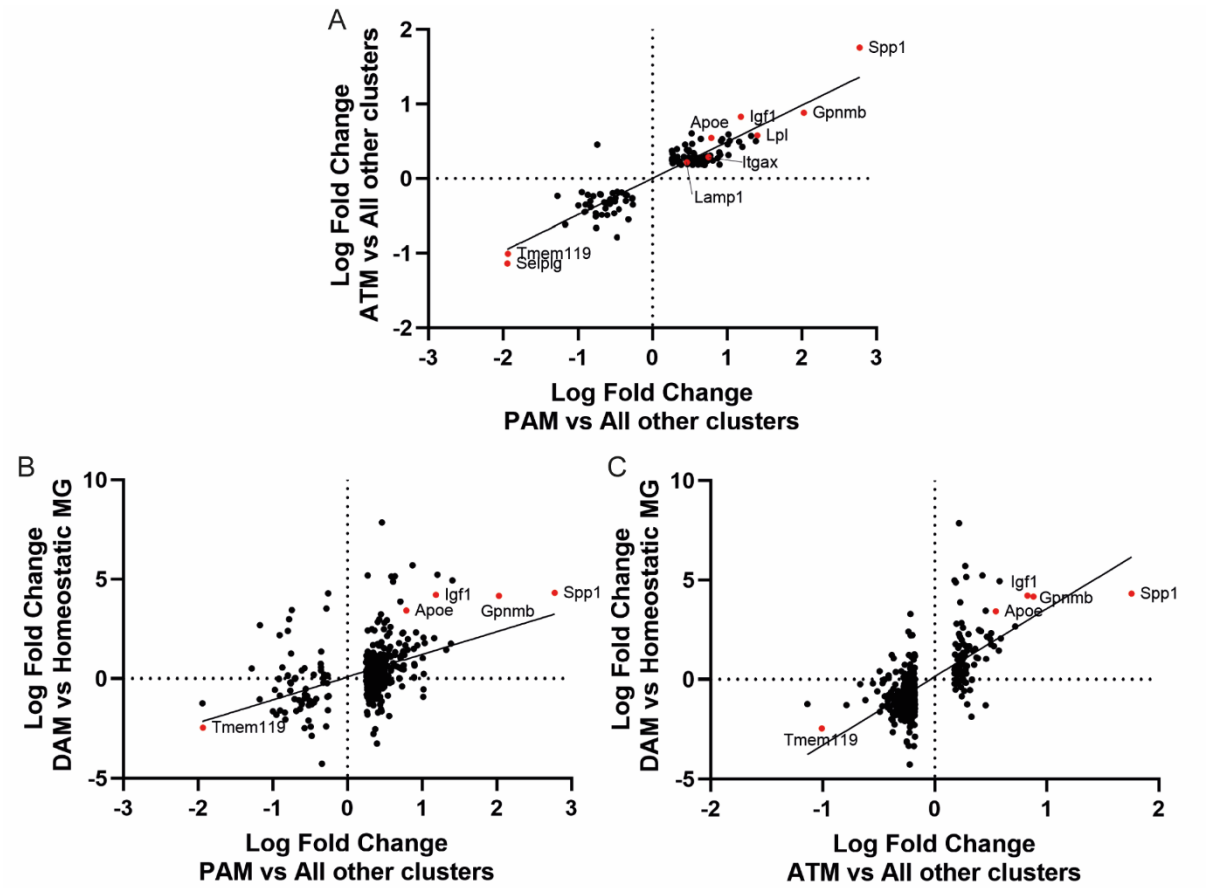

Figure 6: Expression profile of ATM and PAM microglia has similarities with DAM. **A)** Plots showing genes differentially expressed between PAM or ATM and other microglia plotted each other. **B-C)** Plots showing genes differentially expressed between PAM or ATM and other microglia plotted against genes differentially expressed between DAM and homeostatic microglia. Genes of interest are highlighted in red. Trend lines show a positive correlation suggesting similarities between these populations in differentially expressed genes. *ATM – Axon-Tract associated Microglia; DAM – Disease Associated Microglia; PAM – Proliferative region Associated Microglia*

Although the function of PAM, ATM and fountain microglia is not yet known, findings to date suggest PAM and ATM share some transcriptional similarity with prenatal microglia populations isolated at E16.5, as well as 'pre-microglia' and metabolically active microglia. This perhaps indicates an 'immature' or less differentiated state. Increased expression of myeloid cell activation marker *Apoe* could indicate similarities to an activated state. Increased PAM and ATM expression of glycolytic genes also suggests a shift from oxidative phosphorylation to glycolysis, which is a key metabolic alteration in inflammatory macrophages and an indication of an early, less differentiated state in other cell types (Hammond et al. 2019). Interestingly, as shown in Figure 6, PAM and ATM share many transcriptional similarities with Disease Associated Microglia (DAM), a subtype thought to restrict neurodegeneration in a genetic mouse model of Alzheimer's disease (Keren-Shaul et al. 2017). In addition to transcription profile, PAM displayed cytokine or chemokine secretion profiles, including Ccl3 and Ccl4, linked to microglia in aging and Alzheimer's disease models (Kang et al. 2018; Li et al. 2019a).

ATM were hypothesised to engulf material in the developing corpus callosum and cerebellum due to their enrichment of immune cell activation, lysosomal activity and phagocytosis associated genes as well as their ameboid morphology (Hammond et al. 2019). The similar ameboid morphology of PAM could lead to the same conclusion. In fact, $CLEC7A^{+}$ PAM were shown to contain cleaved caspase-3 and MBP^{+} positive particles in P7 brain slices suggesting recent phagocytosis of oligodendrocytes (Li et al. 2019a). These PAM were also shown to preferentially phagocytose pH-sensitive beads relative to other microglia. Microglia depletion was shown to reduce oligodendrocyte precursor survival and corpus callosum myelination, indicating a role for microglia in myelin formation (Hagemeyer et al. 2017).

Whilst the transcription profile of perinatal microglia has begun to be explored, further studies are required to resolve a number of outstanding questions. Transcriptional analysis of microglia at a range of perinatal time points is required to establish whether PAM, ATM and 'fountain of microglia' cells are the same developmental population. This analysis could also help to elucidate the relationship between these populations and other developmental microglia populations such as 'pre-microglia' or metabolically active microglia. Functional experiments are required to understand the role of these cells in the developing brain. Whilst initial experiments suggest PAM may be involved in developmental phagocytosis at P7, it is

not yet known whether, if present, they also carry out this function in the prenatal brain and if so, what structures they may phagocytose.

1.2.3. Postnatal and adult microglia

The region and time-point specific nature of P4- P7 clusters such as PAM and ATM populations is similarly reflected in clusters identified at P21. Masuda et al. (2019) found that P21 and adult P112 microglia expressed increased levels of *Sparc* and *Cst3*, a cysteine proteinase inhibitor that is involved in neurodegenerative diseases. $SPARC^{+}CST3^{+}$ microglia were primarily localised to the P21 cortex with less present in the P112 cortex. Approximately half of IBA1+ macrophages were $CST3^{+}SPARC^{+}$ in both the P21 and P112 cerebellum, whilst none were found in the forebrain. Clusters isolated from adult brains of other studies were also shown to express *Sparc*, or *Cst3* (Hammond et al. 2019; Li et al. 2019a).

In contrast to this reported adult microglial heterogeneity by brain region, Matcovitch-Natan et al. (2016) report only 76 genes differentially expressed between microglia isolated from different regions of the adult mouse brain with all adult microglia clustering together. A more recent study corroborated these results, finding less than 20 genes differentially expressed between different regions of the adult mouse brain and all adult microglia clustering into the same homeostatic cluster when controlling for experimental activation (Li et al. 2019a). Variation in microglial expression due to sex was also largely not observed, despite previous reports of sex-specific microglia differences (Thion et al. 2018a; Hammond et al. 2019). High levels of canonical microglia gene expression, such as *P2ry12*, *C1qa* and *Tmem119*, is repeatedly observed in homeostatic adult microglia (Matcovitch-Natan et al. 2016; Hammond et al. 2019; Li et al. 2019a; Masuda et al. 2019).

Despite seemingly similar single cell sequencing experiments performed on mouse microglia, studies presented throughout sections describing the various microglial populations differ in their findings. This likely reflects differences in experimental technique, with each study differing by: type of sequencing; sequencing depth; number of cells sequenced; and experimental activation controls used. Additionally, each study isolated microglia at slightly different time-points during the mouse lifespan using different mouse strains. Future studies should seek to unify divergent findings, perhaps through performing one experimental technique on a broad range of time-points or *vice-versa*.

1.2.4. Microglia and neuro-inflammation

Currently, little is known about the effect of acute inflammation on developmental microglia populations. In adulthood however, acute inflammation as induced by LPS injection leads to a global downregulation of microglial signature, homeostatic, phagocytic and anti-inflammatory genes in microglia (Sousa et al. 2018). Although microglia are relatively homogenous in adulthood, being composed almost entirely of homeostatic microglia, a small subset of these microglia showed transcriptional differences upon acute inflammation (Hammond et al. 2019; Li et al. 2019a). This subset expressed fewer genes associated with inflammation and more genes associated with DNA repair, suggesting a recovery from the inflammatory state. Both subsets of microglia influenced by acute inflammation differ from microglia isolated from models of neurodegeneration often associated with chronic neuro-inflammation, such as DAM (Sousa et al. 2018).

Similarly, little is known about the effect of states of chronic inflammation such as maternal obesity on developmental microglia. Through experiments on CD11b+ placental cells, which strongly correlated in inflammatory response with E17.5 microglia, placental macrophages were shown to be 'primed' by maternal obesity to produce an exaggerated response to LPS (Edlow et al. 2019). This effect was only observed in microglia from male offspring. Interestingly, other perturbations of the maternal environment, such as changes to the microbiome, have been shown to influence microglial transcription. Single-cell sequencing of developmental microglia revealed transcription changes in germ free mice lacking a microbiome (Matcovitch-Natan et al. 2016; Thion et al. 2018a). Differences in microglial brain colonisation were also observed in these mice (Thion et al. 2018a). The gut microbiome has also been shown to modulate microglial transcription profile in the adult mouse brain, towards transcription profiles associated with Alzheimer's disease and major depressive disorder (Huang et al. 2023).

1.3. How Maternal Obesity Influences Neuropsychiatric and Neurodevelopmental Disorders

Barker and Osmond's (1988) original work proposed that adult disease originates in foetal and developmental stages. This hypothesis was based on finding that geographical differences in mortality from cardiovascular issues such as stroke and ischaemia were closely related to maternal mortality, a more common issue in women with 'poor physique and health'. They also found that blood pressure in 10-year-old children was inversely related to birth weight. Since then, multiple large epidemiological studies have found an association between maternal obesity and increased risk for a broad range of neuropsychiatric disorders in offspring (Rodriguez et al. 2007; Heikura et al. 2008; Krakowiak et al. 2012). These neuropsychiatric disorders include schizophrenia and depression as well as neurodevelopmental conditions: ASDs; developmental delay; intellectual disability and attention deficit hyperactivity disorder (Edlow 2017). Such population based studies support extension of the developmental origin of health and disease hypothesis to brain disorders. They demonstrate that maternal obesity acts as a stressor, negatively influencing early development to prime the brain for later psychiatric disorder. This concept: environmental changes during the embryonic and foetal period leading to postnatal diseases, is often referred to as programming (Kwon and Kim 2017).

Global rates of obesity have increased rapidly in recent years, nearly tripling between 1975-2016 to reach record levels (WHO 2021). This presents a huge potential impact on future generations where neuropsychiatric disorders could accordingly become more common. Neuropsychiatric conditions have already increased within the past three decades, perhaps partially because of increased rates of obesity. However, more awareness and improved methods of diagnosis could also explain the increased prevalence of neuropsychiatric conditions. Such conditions make a significant contribution to the global burden of disease, with depression accounting for the second highest burden of disability worldwide (WHO 2011). Identification of the link between maternal obesity and neuropsychiatric disorder presents the opportunity to develop preventative intervention strategies to reduce levels of neuropsychiatric disorder. Given the high and increasing prevalence of these linked disorders, successful preventative intervention could have a huge global impact. In order to develop

such interventions, we must first gain a detailed understanding of the mechanisms behind the developmental programming of offspring under maternal obesity.

1.3.1. Preclinical Models of Maternal Obesity

Comparing studies on maternal obesity is challenging due to differences in methodology and study design with studies varying by high fat and/or high sugar diets used, different exposure periods and a range of behavioural testing setups. Whilst genetic models of obesity, such as the leptin deficient Lep^{ob}/Lep^{ob} mouse and leptin receptor mutated $Lep^{db}/+$, are frequently studied, these models are less similar to the human condition where the majority of cases of obesity are not as a result of genetic defect (Lutz and Woods 2012; Zhu et al. 2018).

Despite differences in study design, preclinical studies performed on a range of animal models support previously mentioned epidemiological data obtained from human studies (Davis and Mire 2021). For example, exposing non-human primates to a western-style diet: a high fat diet commonly used to induce obesity, resulted in more frequent behavioural deficits in offspring (Thompson et al. 2018). Some behavioural deficits were correlated with levels of maternal adiposity. In another study an association was identified between exposure to maternal high fat diet and anxiety related behavioural alterations (Thompson et al. 2017).

Despite some conflicting results, a common subset of behavioural alterations has been observed across studies on maternal obesity (Davis and Mire 2021). In mouse, maternal high fat diet resulted in decreased social interaction and communication (Kang et al. 2014; Buffington et al. 2016). Behavioural deficits such as these share similarities with human ASD. Interestingly, gut microbiota seem to play a crucial role in the emergence of social deficits (Buffington et al. 2016; Sgritta et al. 2019). Multiple studies have shown that anxiety-like behaviours, which continue to adulthood, are increased offspring exposed to maternal high fat diet (Yan et al. 2017; Abuaish et al. 2018; Manti et al. 2018). Conversely, some studies have found no effect or decreased anxiety in offspring, which could be explained by reduced exposure period and/or lesser enrichment in dietary fat (40% vs 60% of Kcal) (Balsevich et al. 2016; Hiramatsu et al. 2017). Further deficits frequently observed in maternal high fat diet offspring include cognitive defects such as impaired spatial learning and reduced learning rates (McKee et al. 2017; Park and Kim 2017; Sanguinetti et al. 2019). Similarly, offspring also displayed increased motor activity and heightened hedonic behaviour (Fernandes et al.

2012; Balsevich et al. 2016; Peleg-Raibstein et al. 2016; Hiramatsu et al. 2017). Combined, preclinical studies on the offspring of high fat diet fed animals demonstrate deficits in cognition, anxiety and social behavioural deficits. These deficits share similarities with the neuropsychiatric and neurodevelopmental conditions experienced by humans.

Human behavioural deficits associated with maternal obesity co-occur with alterations in brain structures. Reduction in measures of white matter integrity were observed in the 2-week old infants of obese mothers as well as in children aged 10 and 26 (Ou et al. 2015; Verdejo-Román et al. 2019). Defects in hippocampal development have also been reported in 7-11 year old children through reduced hippocampal volume (Alves et al. 2020). Interestingly, hippocampal defects were sex-linked. Although not entirely mapping on to human studies, animal studies involving high fat diets have also resulted in changes to brain structures. Alterations in prenatal hippocampal development were shown through increased NPC proliferation and decreased apoptosis (Niculescu and Lupu 2009a). Mouse models of maternal obesity also produced fewer oxytocin immuno-reactive neurons in the developing mouse hypothalamus and alterations in fatty acid metabolite profiles in the hippocampus and prefrontal cortex (Buffington et al. 2016; Zhu et al. 2018). Given the limited availability of evidence on structural brain changes in preclinical models of maternal obesity, further investigation is required on this topic.

1.3.2. Mechanisms by which Maternal Obesity acts on Offspring

Before birth, the developing foetus depends exclusively on maternal circulation for nutrient availability and signalling molecules, so any programming during in-utero development will be highly dependent on the maternal environment. Disease states and changes in nutrition status are known to negatively impact the maternal environment (O'Neil et al. 2014; Kwon and Kim 2017). Obesity involves the dysregulation of many homeostatic systems, as such there are a variety of different factors that may be involved in observed defects in brain structures and behavioural outcomes.

Establishing preclinical models has allowed some exploration of the mechanisms involved in eliciting behavioural and structural deficits in offspring. Several different factors have become apparent that can influence offspring programming, these include: maternal and foetal genetic

profile; nutrient availability; placental function; excess fatty acid circulation; and inflammation (Rivera et al. 2015a). The impact of metabolic dysfunction on neuro-inflammation, as mediated by microglia, may be another important element. Most of these factors interact with each other, painting a complicated picture of overlapping pathways that can affect programming (Jansson 2016). Given such a broad range of potential mechanisms for developmental disruption, only a subset of these will be covered in detail.

1.3.2.1. Lipid Profile

During obesity, accumulation of lipids causes the expansion of white adipose tissue. This white adipose tissue acts as an endocrine organ releasing adipokines and inflammatory mediators, in addition to chemokines that attract inflammatory immune cells. Increased lipolysis of white adipose tissue occurs releasing increased levels of free fatty acids into circulation (McArdle et al. 2013). In addition to increased circulating lipid levels, obese women show an altered lipid profile termed dyslipidaemia (Tu et al. 2019). This imbalance of lipid subtypes typically favours unhealthy lipids such as saturated fatty acids.

Since saturated fatty acids are elevated in obese versus lean pregnancies, these bioactive lipids could contribute towards developmental inflammation (Vidakovic et al. 2015; Davis and Mire 2021). The influence of saturated fatty acids on microglia has begun to be elucidated in adult mice through experiments that may also apply to foetal development. Saturated fatty acid gavage of adult mice increased expression of activation markers in microglia, including TNF-a, without increasing peripheral inflammatory cytokine levels (Valdearcos et al. 2014). Furthermore, depletion of microglia reduced hypothalamic inflammation and neuronal stress marker Hsp72, demonstrating microglia are responsible for saturated fatty acid mediated hypothalamic stress (Valdearcos et al. 2014). Metabolic changes may be responsible for this transition of microglia into a pro-inflammatory state, regulating activation state through modulation of plasma membrane properties (Köberlin et al. 2015; Divakaruni et al. 2018; Lancaster et al. 2018).

Poly Unsaturated Fatty Acids (PUFAs) are another lipid subtype often altered during obesity. The primary source of mammalian PUFAs is dietary, with meat containing high levels of n-6 PUFAs and fish containing elevated n-3 PUFA levels. PUFA precursors are also found in vegetable oils. These lipids have immuno-modulatory properties: n-6 PUFAs are converted

into pro-inflammatory eicosanoids and prostaglandins; n-3 (also termed omega-3) PUFAs have anti-inflammatory effect through conversion into pro-resolving mediators such as resolvins (Rey et al. 2019). An important aspect of maternal obesity is that manipulations of maternal dietary PUFA content causes changes to the lipid profile of the developing brain. Consuming a high n-6 and low n-3 PUFA diet resulted in corresponding changes in the foetal brain (Sakayori et al. 2016). Similar changes have been shown to influence microglial behaviour as maternal dietary n-3 PUFA deficiency impaired microglial process motility and regulated expression of inflammation related genes (Madore et al. 2014). Converse changes have been observed in foetal microglia, with low n-6/n-3 PUFA ratio resulting in higher n-3 PUFA membrane content, demonstrating the sensitivity of microglia to maternal dietary lipid content (Rey et al. 2018).

The majority of studies measuring impacts of dietary PUFA content on the developing brain have been done without the presence of obesity. These experimental designs do however relate to maternal obesity in that obese pregnant women consistently have an elevated n-6/n-3 PUFA ratio (Vidakovic et al. 2015; Benaim et al. 2018). Modern western diets, often involved in the cause of maternal obesity, mirror this lipid profile with a high n-6/n-3 PUFA ratio and elevated saturated fatty acid levels. As discussed, similar diets are therefore often used in animal models of obesity. Findings suggest diet supplementation with n-3 PUFAs represent a potential intervention strategy for maternal obesity; however, human studies on the topic have yielded controversial results regarding beneficial effects on offspring cognitive outcome (Davis and Mire 2021). Further investigations are needed to clarify the mechanisms involved.

1.3.2.2. Inflammation in Maternal Obesity

Meta-inflammation: the metabolically induced inflammatory response brought about by metabolic signals engaging inflammatory pathways in adipose tissues leading to increased immune cell infiltration, has a large impact on development (Davis and Mire 2021). In addition to adipokines, many inflammatory mediators are able to cross the placental barrier and influence the development of neural circuits (Rivera et al. 2015a). However, the inflammatory profile during maternal obesity is more complex than in obesity alone.

During pregnancy, the immune system must ensure protection from external pathogens as well as prevent rejection of the semi-allogenic foetus. Research has produced conflicting results which may in part be due to the use of a range of animal models with species-specific differences in immunology and placental anatomy (Ander et al. 2019). Comparison between human studies also has limitations resulting from study design variation including factors like: the period studied; cytokines measured; or biological variation between ethnic groups (Gillespie et al. 2016; Graham et al. 2017). Despite this, consensus has shifted away from a predominantly immune suppressant model to a more complex explanation, with changes in inflammatory condition throughout pregnancy. In early pregnancy, the blastocyst adheres to the uterine epithelium and begins to invade the endometrium. During this implantation stage, an inflammatory reaction occurs, associated with upregulated interleukin-6 (IL-6) and tumour necrosis factor (TNF) alongside other cytokines (Griffith et al. 2017). This inflammation assists with the repair of the uterine epithelium following blastocyst invasion (Yockey and Iwasaki 2018). Post implantation, a phase of upregulated anti-inflammatory cytokines occurs which promotes tolerance of foetal antigens (Graham et al. 2017). Following this, at the onset of parturition, pro-inflammatory signalling factors such as IL-6 and TNF increase, assisting with the progression of labour (Rinaldi et al. 2017).

In addition to assisting with pregnancy, IL-6 and TNF-α are classical immune mediators involved in acute inflammation which are upregulated after infection in both humans and animal models (Holub et al. 2013; Glass et al. 2019). C-reactive protein (CRP) is an example of another cytokine elevated after infection. CRP is predominantly increased after human microbial infection, although its role is limited in mouse (Holub et al. 2013; Torzewski et al. 2014). Obesity also has an impact on the immune system. As discussed, obesity induced meta-inflammation leads to pro-inflammatory cytokine production and further immune cell infiltration (Weisberg et al. 2003; Gregor and Hotamisligil 2011). Meta-inflammation differs from acute infection induced inflammation in that it's chronic and low-grade (Gregor and Hotamisligil 2011). Despite these differing inflammatory conditions, the same cytokines are involved. Early in the study of obese rodent models, elevated TNF-α levels were observed (Hotamisligil et al. 1993). Subsequent studies in both human and animal models identified other inflammatory mediators dysregulated by obesity, including IL-6, Transforming Growth Factor β (TGF-β) and CRP (Samad et al. 1997; Khaodhiar et al. 2004).

The inflammatory state becomes even more complicated when pregnancy and obesity occur together. This is reflected in scientific literature, where the inflammatory state during maternal obesity is somewhat controversial. Animal literature on maternal obesity produced conflicting findings: some papers found increases in pro-inflammatory cytokines (Kim et al. 2014); other papers found no change despite elevated foetal pro-inflammatory cytokines (Desai et al. 2013; Crew et al. 2016). As previously, these contrasting results could reflect study design differences involving inter-species variation or differences in diets since high fat and high sugar/high-fat diets are used to study obesity. Human studies are complicated by study design limitations and biological variation, as described for healthy pregnancy. IL-6, TNF-α and CRP are 3 frequently studied cytokines which report conflicting associations with BMI (Pendeloski et al. 2017; Sureshchandra et al. 2019). IL-6 was observed at consistently higher levels in obese pregnant women than lean counterparts and concentration varies with gestation (Friis et al. 2013; Christian and Porter 2014; Sen et al. 2014). Most studies also found an association between elevated CRP and maternal BMI (Christian and Porter 2014; Sen et al. 2014), however this was contrasted by a large longitudinal study (Friis et al. 2013). The association between TNF-α and maternal obesity is not well supported by human literature with some studies finding no correlation (Sen et al. 2014; Zembala-Szczerba et al. 2017). These findings highlight the complexity of the inflammatory state when obesity and pregnancy interact and point towards some level of immune dysregulation during maternal obesity (Davis and Mire 2021).

1.4. How Acute Maternal Immune Activation Influences Neuropsychiatric and Neurodevelopmental Disorders

Although many of the same inflammatory cytokines upregulated during obesity or modified throughout pregnancy are also involved in the inflammatory response to infection, there are differing inflammatory responses to infection. Bacterial antigens bind toll-like receptor 4, leading to a MyD88 dependant inflammatory response (Kawasaki and Kawai 2014). Viral antigens, on the other hand, bind to toll-like receptor 3 resulting in TRIF dependant inflammation. These two inflammatory pathways induce NFκB expression and downstream type 1 interferon and inflammatory cytokine expression. Whilst viral and bacterial vectors such as Poly I:C and LPS activate shared inflammatory pathways, each pathogen type elicits a slightly different cytokine profile (Bao et al. 2022a). These differences are reflected in the different outcomes of the offspring of maternal immune activation (Arsenault et al. 2014; Bao et al. 2022a).

Meta-inflammation, triggered by obesity, may also result in the activation of toll-like receptors 2 and 4 (Jialal et al. 2014). Although infection is can be somewhat similar to obesity with regard to the inflammatory cytokines upregulated, these conditions differ in terms of duration and scale of inflammation. Meta-inflammation involves chronic, low-grade upregulation of inflammatory cytokines whereas infection induces an acute, strong increase in inflammatory cytokines.

Despite some differences in inflammatory response, many of the behavioural impacts of maternal obesity are also observed following maternal immune activation, suggesting the inflammatory cytokines involved may act on similar neurodevelopmental pathways. Epidemiological studies have found an association between infection during pregnancy and increased risk for ASD, schizophrenia, childhood depression and bipolar disorders (Estes and McAllister 2016a; Brown and Meyer 2018). As mentioned, maternal obesity is also associated with increased risk for ASD and schizophrenia, although risks likely differ from maternal infection (Edlow 2017; Davis and Mire 2021).

Human outcomes have been replicated in behavioural measures of animal models. As for studies on maternal obesity, a variety of experimental methods have been used. Variation in pathogen mimetic used, often bacterial (LPS) or viral (Poly I:C), with variation in concentration and timing make study comparison challenging, however a common set of behavioural alterations are found as highlighted in Figure 7 (Davis and Mire 2021). Further more detailed comparison of MIA and high fat diet models are available at Bao et al. (2022) and Urbonaite et al. (2022). Mouse and rat models exhibited decreased communication and social interactions following either LPS or Poly I:C MIA (Gumusoglu and Stevens 2019).

Interestingly, as for studies on maternal high fat diet, gut microbiota seem to play an important role the emergence of social defects (Buffington et al. 2016; Kim et al. 2017). Rodent MIA models display core behavioural phenotypes related to schizophrenia, including sensorimotor gating deficits, attention impairments, increased anxiety and cognitive impairments (Brown and Meyer 2018; Gumusoglu and Stevens 2019). Maternal obesity models on the other hand have largely only been used to study anxiety and cognition, within this set of behavioural defects, possibly due to the lower association between schizophrenia and maternal obesity in epidemiological studies (Davis and Mire 2021).

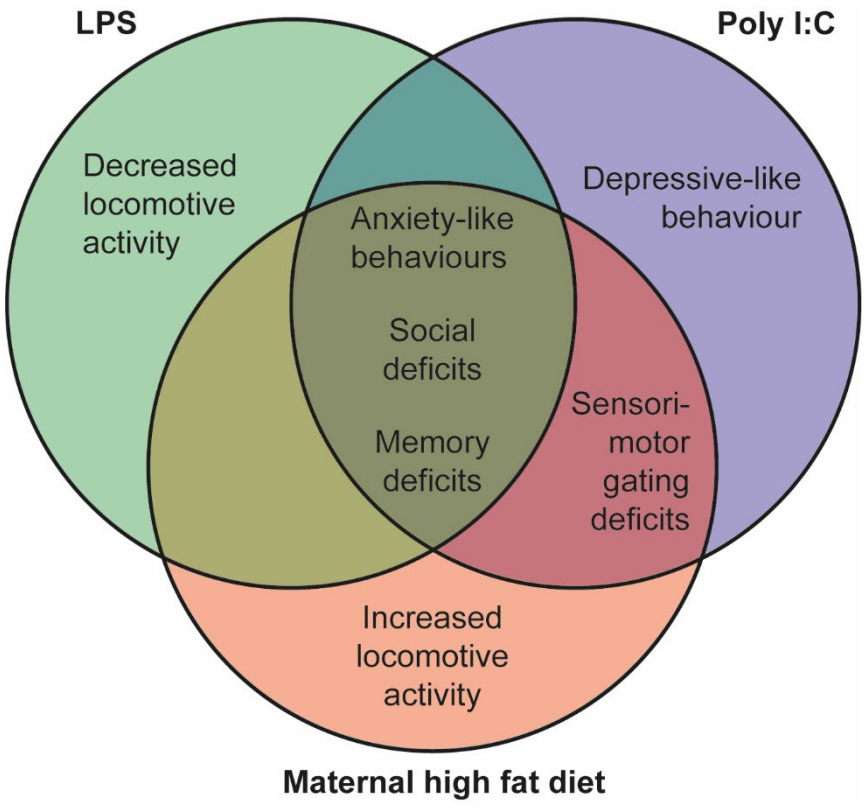

Figure 7: Offspring exposed to maternal immune activation and maternal high fat diet share behavioural deficits.

Venn diagram showing behavioural deficits observed in the offspring of rodents exposed to either maternal immune activation through LPS or Poly I:C and maternal high fat diet. *LPS – Lipopolysaccharide; Poly I:C – Polyinosinic:polycytidylic acid.*

1.5. Common Mechanisms between Maternal Obesity and Acute Maternal Immune Activation in Influencing Neuropsychiatric and Neurodevelopmental disorders

As discussed, maternal obesity and maternal infection are inflammatory states which share some common mechanisms. This is supported by the overlap in behavioural deficits observed in maternal obesity and maternal infection in both human and animal studies (Estes and McAllister 2016a; Edlow 2017; Brown and Meyer 2018; Davis and Mire 2021). Further investigations are required to clearly establish the similarities and differences between these two conditions and to uncover common and distinct mechanistic pathways involved. Common mechanisms likely involve inflammatory cytokines given many are upregulated in both conditions. Furthermore, since 'clean infection' such as LPS or Poly I:C MIA, without the presence of an active pathogen, is capable of producing said developmental defects, the maternal immune response itself is responsible for disrupting neurodevelopment rather than the pathogen. This further illustrates the vital role of cytokines in neurodevelopment.

1.5.1. Cytokines and Neurodevelopment

In addition to their roles in pregnancy, cytokines are involved in brain development (Davis and Mire 2021). Cytokines such as IL-6 and others belonging to TGF and TNF families regulate developmental processes from the initial CNS formation through to synaptogenesis. Studies have identified an association between genetic polymorphisms correlated with increased cytokine levels and increased risk for neuropsychiatric disorders. For example, the TNF-α variant -238 G>A, thought to increase circulating TNF-α levels, was correlated with schizophrenia in a Tunisian population (Inoubli et al. 2018) but not in Indian Bengalee patients (Debnath et al. 2013). There have also been conflicting results in studies on genetic variation related to IL-6. However, a single nucleotide polymorphism (rs2228145) influencing IL-6 receptor concentrations, was found to be significantly elevated in French early onset bipolar disorder patients and trending to increase in Indian Tamil patients (Sundaresh et al. 2019). This finding indicates a trans-ethnic association between bipolar disorder and this polymorphism. Given that there may be a link between alterations in cytokine levels and

neuropsychiatric disorders, dysregulation of cytokines through maternal obesity or maternal infection could increase the probability of developing neuropsychiatric disorders.

The importance of cytokines as signalling molecules in development also suggests that their disruption through maternal obesity or MIA may contribute to increased neurodevelopmental disorder susceptibility. IL-6 belongs to the neuropoietic cytokine family; This cytokine family regulates self-renewal of neuroepithelial cells (Deverman and Patterson 2009). *In vitro* experiments suggest that IL-6 is also involved in axon development, as outgrowth of neurites in cultured hypothalamic tissue was reduced. This finding relates to the *in vivo* environment where the newborn offspring of obese mice were shown to have increased circulating IL-6 levels in combination with reduced innervation of the hypothalamic paraventricular nucleus (Sanders et al. 2014). Dysregulated IL-6 levels as a result of maternal obesity may therefore impair formation of hypothalamic circuits (Sanders et al. 2014).

Neurite outgrowth is also influenced by the cytokine TNF-α. During a specific period of late embryonic and early postnatal development, soluble TNF-α reduced neurite outgrowth (Nolan et al. 2014). TNF exposure induced similar axon growth reduction in neuronal populations within the sympathetic nervous (Erice et al. 2019). Findings discussed here suggest that the increased expression of TNF-α as a result of maternal obesity could influence neurite outgrowth.

TGF-β signalling is involved in much of early CNS development (Meyers and Kessler 2017). TGF-β signalling is required for axon growth, differentiation and maintenance of dopaminergic neurons, as well as regulation of synaptic electrophysiology (Farkas et al. 2003; Luo et al. 2016). Dendritic spine morphology in midbrain neurons has also been shown to be regulated by TGF-β (Yoon et al. 2020).

Further studies provide an indication that disruption to TGF-β dependant developmental processes may influence the occurrence of neurodevelopmental disorders. For example, a study has identified an association between the common TGFB1 polymorphism, correlated with increased TGF-β production, and increased susceptibility to schizophrenia (Frydecka et al. 2013). Circulating monocytes of treatment free schizophrenia patients were also found to have elevated expression of TGF-β (Amoli et al. 2019).

Decreases in TGF-β expression may also impair development. Animal correlates of ASD such as repetitive behaviours and reduced measures of social interaction were observed in the male offspring of MIA rats with reduced hippocampal TGF-β expression (Fortunato et al. 2017). These findings are reflected in human where children with ASD had decreased TGF-β levels (El Gohary et al. 2015). Combined TGF- β results suggest that a fine balance of TGF-β levels appears to be required for typical neurodevelopment. This balance may be affected by maternal obesity and some evidence suggests disruption of this balance through MIA could lead to ASD-like behaviours. These limited studies could provide the basis for further research into the effects of altered TGF- β expression in development.

Microglia may be involved in the relationship between TGF-β signalling and neurodevelopmental disorder. This is because TGF-β signalling is required for the development and function of microglia (Butovsky et al. 2014; Lively et al. 2018). Modulation of microglia represents another mechanism by which inflammatory cytokines could affect brain development (Davis and Mire 2021).

1.5.2. Microglia and Neuro-inflammation

Microglia are heavily involved in brain development, as covered previously in this chapter. Microglia have also been implicated in the pathogenesis of many conditions including ASD, schizophrenia and major depressive disorder (Tay et al. 2018). The presence of microglia from the earliest stages of brain formation and the ability of these cells to sense their local environment place them at a key position to mediate the effects of maternal obesity and MIA (Davis and Mire 2021).

Signs of pathogen invasion, such as pathogen-associated molecular patterns, trigger a response from the resident immune cells of the CNS – microglia. The detection of pathogen-associated molecular patterns, LPS for example, leads to an acute systemic and CNS inflammatory response. This immune response is vital for the removal of pathogens, but can impair the developmental function of microglia, as covered in Figure 3.

Maternal obesity also influences microglial inflammatory state in that it can prime microglia towards a postnatal pro-inflammatory phenotype (Davis and Mire 2021). This was demonstrated in obese rats whose offspring had increased levels of microglial activation

marker CD11b within the hippocampus at birth (Bilbo and Tsang 2010). Subsequent LPS stimulus induced exaggerated hippocampal microglia activation and increased IL-1β production. These defects were accompanied by increased anxious behaviour among male offspring. Maldonado-Ruiz et al. (2019) demonstrated that maternal obesity exposed adult hypothalamic microglia become increasingly activated following grehlin mediated neuron activation. Less is known about the impact of maternal obesity on foetal microglial populations.

An important study found that, although maternal obesity did not induce a pro-inflammatory state, foetal microglia were 'primed' to produce more TNF-α upon LPS stimulation than controls (Edlow et al. 2019). Interestingly, placental macrophage populations strongly correlated with foetal microglia in LPS stimulated TNF-α production. Further examples of prenatal priming have been identified in relation to MIA (Mattei et al. 2017). Interactions with insults later in life may increase susceptibility to neuropsychiatric disorders. Evidence of this hypothesis is found in the synergistically increased risk for schizophrenia in males with MIA and later life psychological trauma (Debost et al. 2017).

The impact of maternal obesity on microglia may be mediated by a number of mechanisms. For example, microglial activation state was regulated by the adipose-derived hormone leptin in the rat hypothalamus. *In vitro* leptin or serum from high fat diet fed mice induced inflammatory cytokine production (Gao et al. 2014). Leptin receptor deficiency in myeloid cells, generated by Cre-Lox recombination, impaired microglial phagocytosis and decreased mouse hypothalamic neuron number (Gao et al. 2018). Leptin circulating levels are increased in the offspring of obese dams (Chen et al. 2008). This suggests that leptin signalling might regulate microglia phenotype in the developing brain of obese offspring (Davis and Mire 2021).

Microglial metabolism represents another mechanism by which maternal obesity may influence microglial behaviour. Gene expression associated with lipid metabolism increased in the microglia of obese rats, whilst there was a decrease in expression of glycolytic genes (Milanova et al. 2019). Metabolic reprogramming plays a key role in regulating macrophage phenotype and plasticity. Initially, glucose metabolism was thought to favour pro-inflammatory signalling, whilst fatty acid oxidation was associated with anti-inflammatory cytokine expression. The current view is that there is a more complex picture of metabolic flexibility

driving macrophage states (Van den Bossche et al. 2017). Recent work has begun to relate these findings to microglia.

Pro-inflammatory microglia have increased glucose metabolism that preferentially fuels the tricarboxylic acid (TCA) cycle, which is also fuelled by increased glutamine oxidation (Davis and Mire 2021). Glutamine is known to provide an alternative source of carbon upon acute hypoglycaemia to maintain microglia surveillance (Bernier et al. 2020). Anti-inflammatory polarised microglia had increased mitochondrial fatty acid oxidation and synthesis, where decreases were observed in inflammatory states. However, lipid droplets are often found in inflamed immune cells, including microglia, after LPS stimulation or in the aging brain (Marschallinger et al. 2020). Microglia containing lipid droplets have impaired phagocytic function and a pro-inflammatory secretome. Disruption to metabolism during maternal obesity could therefore affect microglial metabolic plasticity, leading to disruption in microglial activation state and behaviour, resulting in neurodevelopmental impairments.

1.6. Thesis Aims

Current data on microglia strongly suggests that several different microglia populations coexist within the perinatal developing brain (Hammond et al. 2019; Li et al. 2019a). Whilst work has begun on characterising these different populations, there is still much we do not know. Given that microglia accumulate around structures that they are supporting the development of, understanding clusters of developmental microglia is a priority when considering their potential involvement in neurodevelopmental disorders (Squarzoni et al. 2014). Microglia accumulating in the septal and glial wedge regions associated with the developing corpus callosum form dense clusters and are hypothesised to be involved in corpus callosum development, yet very little is known about the biology of these cells (Pont-Lezica et al. 2014). Characterisation of corpus callosum associated microglia was therefore the aim of chapters 2 and 3, with these cells studied further in chapters 4 and 5.

Despite clear association between maternal obesity or maternal immune activation and neuropsychiatric or neurodevelopmental disorders, the mechanisms involved in this relationship are not fully understood (Rivera et al. 2015a; Brown and Meyer 2018). Microglia are at a key position in the relationship between prenatal insult and neurodevelopmental disorder. This makes understanding the impact of inflammatory states on developmental microglia an important part in uncovering the mechanisms involved in neurodevelopmental disorders. Furthermore, very few studies have examined how heterogeneity in developmental microglia interacts with different prenatal inflammatory insults. These gaps in current understanding formed the basis of aims for chapters 4 and 5.

- Chapter 2: Demonstrate the formation of corpus callosum associated microglial hotspots and characterise the transcription profile of corpus callosum associated microglia.
- Chapter 3: Characterise the protein expression, birth date, proliferation rate and ability to migrate of corpus callosum associated microglia.
- Chapter 4: Explore the effects of maternal high fat diet on perinatal brain development and corpus callosum organisation as well as associated effects on the density, protein expression and birth date of corpus callosum associated microglia.

- Chapter 5: Explore the effects of maternal immune activation on perinatal brain development and corpus callosum organisation as well as associated effects on the density and expression profile of corpus callosum associated microglia.

Chapter 2: Transcription Profile of Corpus Callosum associated Microglia

2.1. Introduction

2.1.1. Corpus Callosum Microglia Hotspots

As discussed in chapter 1, microglia accumulate around structures which they are supporting the development of (Squarzoni et al. 2014). Microglia perform a variety of functions depending upon brain location (Tan et al. 2020). Given the broad range of functions carried out by microglia during development it is likely that various different microglial populations are carrying out these tasks. An example of an accumulation of microglia occurs during development of the corpus callosum. Pont-Lezica *et al.* (2014) identified a dense cluster of microglia ventral to the corpus callosum within the sub-callosal sling or septal region. Author's hypothesise that these microglia participate in axon growth and guidance either via: the modulation of neurite formation pathways; engulfment of guidepost glia and neurons; or endocytosis of guidance molecules. Whilst microglial depletion and functional disruption models have shown microglia as a whole are necessary for correct organisation of the corpus callosum, the function of this specific septal population is yet to be formally demonstrated.

Which subset of microglia may be present in the corpus callosum or involved in its formation is currently unknown. Understanding which specific subset of microglia may be involved in corpus callosum axon guidance could help to uncover mechanisms behind defects in corpus callosum formation, characteristic of neurodevelopmental disorders such as ASD (Paul et al. 2007). Differing susceptibility to physiological signals across heterogeneous microglial populations for example could explain the association of specific malformations with certain types of prenatal insults. For these reasons, I set out to identify which subset(s) of microglia colonise the developing corpus callosum region.

2.1.2. Candidate Populations

Identifying candidate populations was an initial step in mapping heterogeneous groups of microglia to the developing corpus callosum. Multiple studies have identified microglial populations found in close association with the corpus callosum during the later stages of its development, as discussed in the introduction. Briefly, Proliferative-region Associated Microglia (PAM) were identified within the Corpus Callosum from P4 to P14 with a peak at P7. The *Clec7a* gene coding for Dectin-1, a cell surface β-glucan receptor involved in antifungal immunity in phagocytes (Willment et al. 2005), was amongst the most upregulated in PAM relative to other microglia at P7. Dectin-1 and CX3CR1-GFP immunohistochemistry also located them at the neurogenic niches near the lateral ventricles at E17.5. Single-cell sequencing data suggested that these cells reduce expression of key microglia signature genes including *P2ry12* (Li et al. 2019b).

Axon Tract-associated Microglia (ATM) were predominantly found at P4/P5 (Hammond et al. 2019). Spp1 in-situ hybridisation, as for PAM, placed these cells in the corpus callosum and cerebellum P5. ATM have many other similarities with PAM with regard to expression profile (Table 1), as well as morphology – both clusters are ameboid. Their extremely similar expression profile, spatial and temporal localisation strongly suggest these are likely the same population of cells. Deviations in expression may be as a result of different sequencing techniques. These populations have been compared with Disease Associated Microglia (DAM) which also upregulate *Spp1*, *Gpnmb* and *Clec7a* (Keren-Shaul et al. 2017).

The 'Fountain of microglia' population also share many similarities with ATM and PAM. These ameboid cells have been identified forming clusters within the postnatal corpus callosum from around P1-P14 (Hagemeyer et al. 2017; Nemes-Baran et al. 2020). Like PAM, fountain microglia have been shown to phagocytose oligodendrocyte progenitors and express *Spp1*, *Gpnmb* and *Clec7a*. Additionally, fountain microglia support corpus callosum myelination during the early postnatal period and maintain oligodendrocyte precursor survival through to adulthood via *Igf1* expression (Hagemeyer et al. 2017; Wlodarczyk et al. 2017b).

As brain resident macrophages, microglia share many transcriptional similarities with Border-Associated Macrophages (BAMs) found within the meninges, choroid plexus and perivascular space (Goldmann et al. 2016; Utz et al. 2020). During early development

primitive macrophage precursors infiltrate the brain parenchyma and begin to form microglia (Ginhoux et al. 2010b). An intermediate population expressing both macrophage and microglial markers was found in close proximity to the brain borders at E14.5 (Hammond et al. 2019). Fusion of the brain hemispheres occurs shortly before axons cross the midline during corpus callosum formation, with midline zipper and induseum griseum glia bridging the fissure across the primitive meninge (Raybaud 2010; Fame et al. 2011). Septal cells could therefore be considered in close proximity to the meninges and so may contain brain border macrophages.

Table 1: Microglial populations potentially involved in corpus callosum formation

		Marker Expression					
Microglial Population	**Localisation**	Spp1	Gpnmb	Clec7a	P2ry12	Ms4a7	F13a1
PAM – Proliferative-region Associated Microglia (Li et al. 2019b)	Lateral Ventricles – E17.5 Corpus Callosum and Cerebellum – P4-P14	+	+	+	Low	-	-
ATM – Axon Tract-associated Microglia (Hammond et al. 2019)	Corpus Callosum and Cerebellum – P4/P5	+	+	-	Low	-	-
'Fountain of Microglia' (Hagemeyer et al. 2017)	Corpus Callosum and Cerebellum – P1-P14	+	+	+	+	?	?
Brain Border Microglia (Hammond et al. 2019)	Brain Borders – E14.5	-	-	-	+	+	-
Border-associated Macrophages (Utz et al. 2020)	Perivascular space, meninges, choroid plexus – E9.5 onwards	-	-	-	-	+	+

Some indication of septal microglia expression profile was provided when osteopontin, the protein expressed by *Spp1*, labelled microglia were identified in close proximity to the lateral ventricles, where the glial wedges are found, in the E18 rat brain (Choi et al. 2004). Although not discussed in the paper, figures also show osteopontin immuno-labelled septal microglia.

Osteopontin labelled microglia were shown to be phagocytic at P1 through engulfment of a fluorescent tracer.

2.1.3. Chapter Aims and Key Findings

The first aim of this chapter was a formal demonstration that an increased density of microglia is observed within septum during embryonic brain development, indicating the presence of a developmental hotspot. Indeed, microglia were found at a significantly higher density within the septum than surrounding regions at E18.5. Following on from this the expression of markers associated with PAM, ATM and fountain of microglia was identified within this dense septal microglial population through *in situ* hybridisation. Septal microglia appeared unique in the developing brain as they differed from other microglia associated with developing axon and those found within the cortex. Finally, a more in depth characterisation of microglial expression profile was carried out to more definitively answer which microglial populations are present in the developing brain. Homeostatic-like microglia were found to almost exclusively make up cortical regions whilst microglia with similar transcription profiles to metabolically active, proliferative, PAM and ATM populations colonise the midline region.

2.2. Materials and Methods

2.2.1. Animal Husbandry

Mice were kept in a climate-controlled environment and exposed to a 12hr light/dark cycle daily. All animal procedures were performed in accordance with the Animals (Scientific Procedures) Act 1986. Female mice were housed up to 4 per cage and had access to food and water *ad libitum* from acclimatisation to sacrifice. Male mice were held under the same conditions until breeding, when they were housed individually. The majority of mice were obtained from Charles River, with a small number of mice deemed excess stock obtained through internal transfer from other Cardiff University researchers. CX3CR1-GFP mice were kindly donated by Prof. Phillip Taylor and Elena Simonazzi. Upon transfer, animals were allowed to acclimatise for at least 1 week prior to breeding or any other manipulation. Some mice were ear clipped for identification purposes.

During breeding, up to 2 female mice were added to a cage containing a male mouse. The following morning, female mice were returned to their home cage or a new cage if pregnant without ear tags. Pregnancy was established by identification of a vaginal plug, at which point dams were considered to be at E0.5. Pregnant dams were sacrificed via cervical dislocation at the required stage of gestation, the uterus removed and kept on ice until dissection shortly thereafter.

Foetuses or embryos were dissected from the uterus and if E12.5 or younger, washed in Phosphate Buffered Saline (PBS) and fixed in 4% Paraformaldehyde (PFA) diluted in PBS for 24 hours at 4°C. Where older than E12.5, the brain was removed, washed in PBS and fixed in PFA for 24 hours at 4°C. After fixation, samples were washed in PBS at least 3 times and stored in PBS at 4°C. Placental, tail and foetal blood samples were also taken and stored at -20°C or -80°C for blood.

2.2.2. Immunohistochemistry

2.2.2.1. Fixed Tissue Sample Preparation

Brains were embedded in liquid 3% Agarose PBS solution, which was allowed to set before slicing. Brains were cut into 80µm thick coronal slices using a Leica vibratome and corpus callosum slices kept in PBS.

2.2.2.2. Fixed Tissue Immunohistochemistry

All immunostained slices were incubated in blocking solution (PBS, Triton 0.3%, Gelatin 0.02%) for 2 hours at room temperature followed by incubation in primary antibody solution for 48 hours at 4°C. To create primary antibodies solution, antibodies were diluted in antibody diluent (PBS Triton 0.3% Gelatine 0.02%) to concentrations shown in Annex Table 1. Slices were then washed 5 times for 20 minutes in PBS. After this, slices were incubated for 2 hours at room temperature in an appropriate secondary antibody, shown in Annex Table 2, diluted in antibody diluent. Slices were washed 3 times for 10 minutes in PBS, incubated in DAPI staining solution (VWR) for 10 minutes, washed 3 times in PBS and mounted onto glass slides in mounting medium (vectashield).

2.2.3. RNAscope in-situ Hybridisation

2.2.3.1. Sample Preparation

DiEthyl PyroCarbonate (DEPC) treated PBS was used in place of PBS at all stages of sample acquisition and processing, and will be referred to as PBS hereafter. Samples were incubated sequentially in 10, 20 and 30% PBS sucrose solution at 4°C until brains sank to the bottom of the container. Samples were then embedded in Optimal Cutting Temperature compound (OCT), frozen with dry ice and kept at -80°C until sectioning.

2.2.3.2. Slide Preparation

Frozen brain samples were sectioned coronally in 15µm slices using a Leica cryostat and corpus callosum slices fixed onto Superfrost Plus slides, ensuring that all slices fell within a central 19 by 32 mm area. Slides were then air-dried for approximately 2 hours before storage at -80°C until *in-situ* hybridisation following RNAscope multiplex protocols.

Slides were brought to room temperature and washed in PBS for 5 minutes to remove OCT. Slides were baked for 30 minutes at 60°C and then post-fixed by immersion in 4% PFA for 15 minutes at 4°C. Slides were then immersed for 5 minutes at room temperature in sequential ethanol solutions diluted in distilled water to 50%, 70% and 100% twice, before air-drying for 5 minutes at room temperature. The HybEZ RNAsope oven and humidity control tray with distilled water dampened paper was preheated to 40°C for 30 minutes.

2.2.3.3. Target Retrieval

RNAscope Target Retrieval Reagents were prepared by diluting 70ml 10x stock solution in 630ml distilled water. Target Retrieval Reagents were heated in a foil covered beaker to approximately 95°C for up to 15 minutes. Slides were placed in a slide rack and submerged in boiling Target Retrieval Reagents for 2 minutes if E18.5 or 1.5 minutes if E14.5; These target retrieval times were set following repeated optimisation experiments to balance background fluorescence levels and target visibility. Slide racks were then removed, placed in distilled water and moved up and down 3 times before washing in 100% alcohol and drying at 60°C for 5 minutes.

2.2.3.4. Protease Application

A hydrophobic barrier was drawn around tissue and allowed to dry for 5 minutes and slides were placed into the RNAscope EZ-Batch Slide Holder. Approximately 5 drops of RNAscope Protease III was applied for 10 minutes if E18.5 or 7.5 minutes if E14.5 under incubation at 40°C in the HybEZ RNAsope oven with humidity control tray; These timings were also determined by repeated optimisation experiments. Slides were then washed in distilled water.

2.2.3.5. Probe Hybridisation

RNAscope HiPlex probes and diluent were warmed to 40°C for 10 minutes and spun down. Probes were then diluted 1:50 in diluent, vortexed and cooled to room temperature. Approximately 6 drops of each probe outlined in Annex Table 1 were applied to each slide and incubated for 2 hours at 40°C in the HybEZ RNAsope oven following by slide washing in wash buffer for 2 minutes at room temperature.

2.2.3.6. Signal Amplification, Round 1 Fluorophore Binding and Counterstaining

Amplification solutions (RNAscope HiPlex Amp 1, 2 and 3) were sequentially applied to slides, incubated for 30 minutes at 40°C and washed in wash buffer twice. Approximately 6 drops of RNAscope HiPlex Fluoro T1-T4 were applied to slides and incubated for 15 minutes at 40°C followed by two washes in wash buffer. Slides were incubated for 30 seconds in DAPI before removing staining solution and mounting slides using ProLong Antifade Mountant.

2.2.3.7. Fluorophore Cleavage and Binding Round 2

Following round 1 imaging, coverslips were removed by soaking in 4x SSC at room temperature until coverslips came loose and slides washed in 4x SSC. Approximately 6 drops of 10% cleaving solution diluted with 4x SSC was applied to slides and incubated for 15 minutes at room temperature. Slides were then washed in PBST (0.5% Tween) twice for 2 minutes at room temperature. Cleaving solution and wash steps were then repeated. Approximately 6 drops of RNAscope HiPlex Fluoro T5-T8 was applied to slides, incubated for 15 minutes at 40°C and washed off twice in wash buffer for 2 minutes at room temperature. Slides were then mounted using ProLong Antifade Mountant before round 2 imaging.

2.2.3.8. Fluorophore Cleavage and Immunohistochemistry

Coverslips were removed and fluorophores cleaved as previously with 4x SSC and 10% cleaving solution. Immunohistochemistry was then performed as described, with samples incubated in blocking solution for 2 hours at room temperature followed by primary antibody solution for 48 hours at 4°C and secondary antibody solution for 2 hours at room temperature. Slides were then washed 3 times in PBS and mounted onto glass slides using ProLong Antifade Mountant before round 3 imaging.

2.2.4. Microscopy and Image Analysis

2.2.4.1. Microglia Density

Images were captured with a Zeiss LSM710 confocal microscope using a x20 lens. A tile-scan of 6 images in a z-stack of 6-10 images was taken per slice and cells were counted manually in each slice using FIJI cell counter plug-in. Microsoft Excel was used to store cell counting data and calculate average cell number per slice and cell density. GraphPad Prism 9 was used for statistical analysis and graph production.

2.2.4.2. RNAscope Imaging and Counting

Probes were visualised using a Leica epifluoresence microscope with x40 lens and stage position recorder. A z-stack of images were captured following round 1 of fluorophore binding, with the precise stage position recorded for rounds 2 and 3. During imaging rounds 2 and 3, a z-stack of images were captured at the same positon as round 1. Using FIJI, z-stacks were then compressed to a single slice via z-projection. RNAscope HiPlex Registration software was then used to combine RNAscope images into a single file composed of 6 channels.

Cell counting was performed in a semi-automated fashion. Adobe illustrator was used to place coloured semi-transparent circles over the DAPI labelled nucleus of Iba1 labelled microglia, with a different colour used for each marker. An ImageJ macro I created was then used to count the number of circles of all possible combinations of colours relating to all possible combinations of markers. Results were recorded in Microsoft excel and average cell number per slice for each marker combination, percentage of each marker combination and cell density calculated. GraphPad Prism 9 was used for statistical analysis and graph production.

2.2.5. Single-Cell RNA Sequencing

2.2.5.1. Sample Preparation

CD1 mice were bred and brains samples obtained as described in section 2.2.1, with the exception that following removal from the foetus, brains were taken immediately for further dissection as described below.

The following sample preparation and staining techniques were designed to minimise *ex vivo* gene expression changes based on protocols described in Marsh et al. (2022) and Ocañas et al. (2022). All procedures were carried out at pace, keeping all tools and reagents cold where possible. All tools and reagents were pre-chilled to 4°C or on ice. Following removal from the foetus, brains were dissected in ice-cold dissection buffer (HBSS, Actinomycin D 5µg/ml, Triptolide 3.6µg/ml, Anisomycin 10µg/ml). The meninges was removed and discarded then the cortices and a small area at the midline, as shown in Figure 8, were removed and kept in ice-cold dissection buffer. Cortical or midline tissue from half of each litter was considered 1 sample.

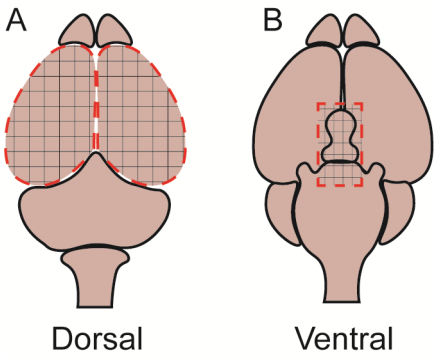

Figure 8: Regions dissected from E18.5 brains for single cell sequencing.
A) Dorsal view of the E18.5 mouse brain with cortical dissected regions highlighted. B) Ventral view of the E18.5 mouse brain with midline dissected region highlighted.

Each sample was dounce homogenised while rotating, on ice 5 times with a loose pestle and 5 times with a tight pestle in ice-cold dissection buffer. A 70µm nylon filter was pre-wet with HBSS and samples filtered into a 50ml tube. Samples were then spun down at 300g for 5 minutes at 4°C and supernatant discarded. Samples were re-suspended in 1ml sterile ice-cold PBS and 10µl taken and diluted 1:10 for automated cell counting. Samples were then spun down at 300g for 5 minutes at 4°C and supernatant discarded, then re-suspended in FACS buffer (0.25g Bovine-Serum Albumin in 50ml Sterile PBS) to approximately 1 million cells per 50µl.

2.2.5.2. Cell Staining

Cells suspended in FACS buffer were pipetted into conical 96 well plates at 25µl per well. All following incubation steps were performed at 4°C in the dark. Cells were incubated in 25µl live/dead marker (Live-or-dye 375/600 diluted 1:1000 in sterile PBS) for 15 minutes. A wash step was performed: 100µl FACS buffer added, plate spun down at 2000rpm for 3 minutes and supernatant flicked off. Cells were incubated with 25µl of Fc Block (Mouse BD Fc Block diluted 1:50 in sterile PBS) for 10 minutes followed by a wash step. Cells were incubated in 25µl cell surface marker mix (Annex Table 1), diluted in FACS buffer for 30 minutes followed by a wash step. Samples were then taken immediately on ice for FACS sorting.

2.2.5.3. FACS Sorting

Cells were sorted on Live-or-dye 375/600 negative (BV605), CD11b positive (FITC), CD45 mid (PE/Cy7) using a FACS Aria Fusion cell sorter operated by Mark Bishop. An example of the gating strategy used is shown below. Cells were sorted into a 1ml sample tube containing 10µl FACS buffer and passed on for single-cell sequencing.

2.2.5.4. Single-Cell RNA Sequencing: Wet Lab Work

The 10x genomics single-cell RNA sequencing protocol was selected for further analysis based on technician availability. All wet lab work was carried out by Angela Marchbank – Genome Hub Manager at Cardiff University. FACS purified microglia were sequenced using the Chromium single cell gene expression platform according to the Chromium Next GEM Single Cell 3' Reagent Kits v3.1 protocol, using Chromium Next GEM Single Cell 3' Kit v3.1 and Chromium Next GEM Chip G Single Cell Kit. Approximately 17500 cells were taken for sequencing from each of 12 samples – 4 samples from each MIA condition (PBS, LPS, Poly

I:C) half of which were isolated from the cortex and half from the midline. Sequencing steps were performed by 10x genomics to an average depth of approximately 34,000 reads using the Illumina NovaSeq 6000, resulting in 4 fastq files per sample used for further processing.

2.2.5.5. FASTQ file preparation

Barcode and Unique Molecular Identifier (UMI) fastq files were received at 29 base pairs (bp) in length, 1 base pair longer than expected as sequencing performed using the NovaSeq runs for an extra cycle. Trim Galore[1] (v0.6.5) was used to trim 1 base pair from the 3' end of the adapter/UMI sequence, leaving a 28bp sequence. FastQC[2] (v0.11.8) was used to perform quality control on fastq files. FastQC mean quality scores improve following trimming of additional base pair. Sequences failing duplication level tests and those with warnings for GC content were all from the barcode and UMI strand, with the exception of C_cortex_R1 and E_cortex_R1

2.2.5.6. Sequence Mapping

STAR (v2.7.9a) (Dobin et al. 2013) was used to create a genome index using *Mus Musculus* GRCm39 reference genome downloaded from Ensembl[3]. STARsolo (Kaminow et al. 2021) was selected as an open source alternative to CellRanger for the mapping of sequences to a reference genome. STARsolo[4] was run as described in documentation to match '10x Chromium scRNA-seq data' requirements. Output files were fed into Seurat[5] (v4.3.0) for further quantification, following the 'guided clustering tutorial' vignette.

2.2.5.7. Quality Control

Per cell, the total number of molecules detected (counts), the number of unique genes detected (features), and the percentage of mitochondrial DNA was recorded. Cells with low counts, features or high mitochondrial DNA were removed. Acceptable cells were defined as those with 20,000 – 400,000 counts, over 500 features and less than 10% mitochondrial DNA. Violin plots showing the number of cells in each sample for each of these quality control parameters are shown in Figure 9. Notably, the majority of cells from the dissected region of sample D did not pass this stage of quality control; this sample was therefore removed from further analysis. Although there were also few cells within sample E_cortex, all of these appeared to be high quality and so were included for further analysis.

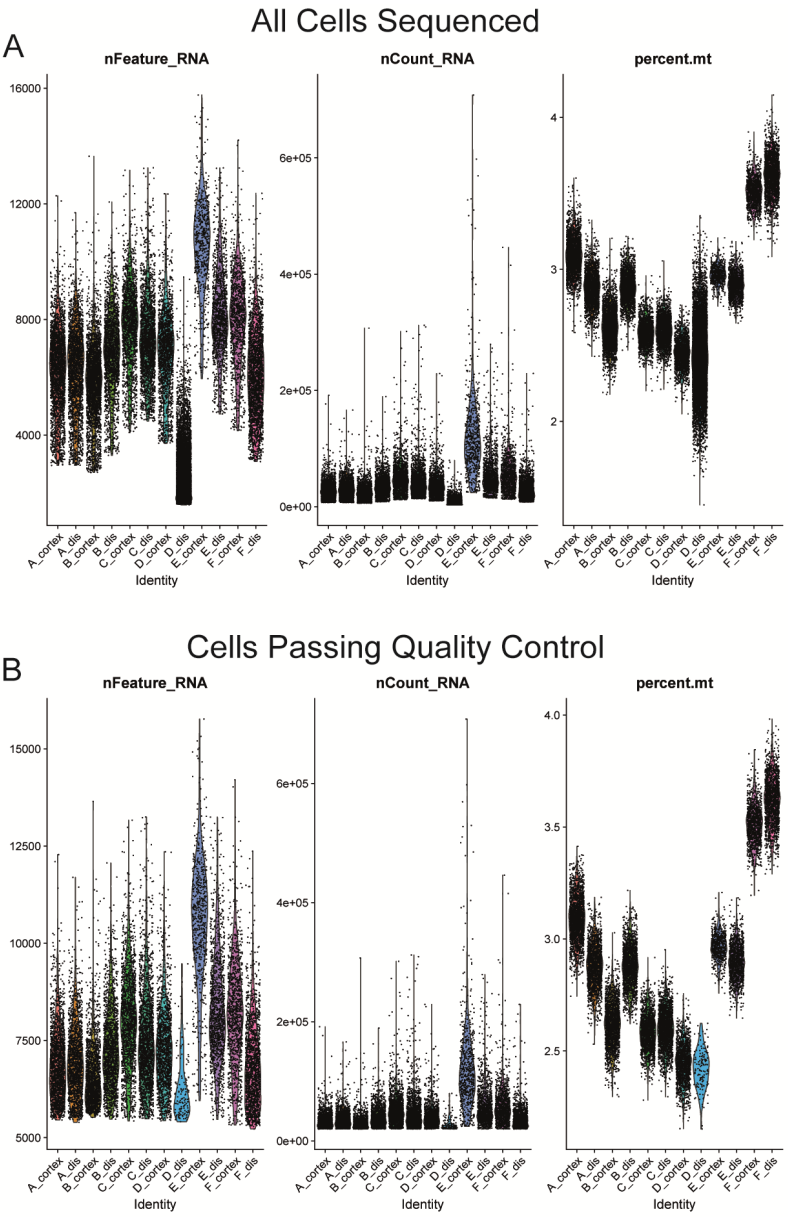

# cells	A_cortex	A_dis	B_cortex	B_dis	C_cortex	C_dis
Before	2666	2349	3156	2073	1817	2352
After	1929	1713	1892	1765	1682	2144

# cells	D_cortex	D_dis	E_cortex	E_dis	F_cortex	F_dis
Before	1832	11085	622	1370	1190	2413
After	1516	135	622	1316	1116	1609

Figure 9: Sample D and E were removed based on results of quality control analysis.

A) Per cell, the number of unique genes detected (features), the total number of molecules detected (counts), and the percentage of mitochondrial DNA was recorded in each sample.

B) Data as displayed in A with cells failing quality control removed. Acceptable cells were defined as those with 20,000 – 400,000 counts, over 500 features and less than 10% mitochondrial DNA. **Tables** showing total number of cells sequenced (before) and number of cells passing quality control (after) with removed samples highlighted. *Dis – Dissected midline region*

2.2.5.8. Normalisation, Scaling and Principal Component Analysis

Data was normalised and scaled as described in the 'guided clustering tutorial' vignette. Briefly, a global-scaling normalisation method was used by a scaling factor of 10,000 and the result log-transformed to normalise feature expression for each cell by total expression. Scaling was performed via linear transformation to ensure mean expression across cells falls at 0 and variance at 1. Dimensional reduction was performed via Principal Component Analysis (PCA). The number of components to include was chosen through plotting of an elbow plot, with cells clustered based on PCA score. Principal components were excluded at the point where the principal components only contribute 5% of standard deviation and the principal components cumulatively contribute 90% of the standard deviation. This resulted in 5 principal components in the final plot, produced through the following noise reduction steps.

2.2.5.9. Noise Reduction

Clustering was performed as described in the previously mentioned vignette and clusters identified through differential expression analysis. The effects of *ex vivo* activation or noise was then reduced. This process involved performing differential expression analysis between sample pairs. These sample pairs (for example A_cortex and B_cortex) correspond to cells isolated from the same litter and same region processed separately – different brains, kept in different containers, sorted separately, sequenced separately. With the exception of small differences occurring by chance, differences in expression between these samples can be attributed to the *ex vivo* environment. Significantly differentially expressed genes between sample pairs were therefore labelled as *ex vivo* activation genes and removed from the dataset. Previously described quality control steps were then performed, removing all cells not passing quality control after the removal of *ex vivo* activation gene expression levels. This process was repeated until there were no longer any *ex vivo* activation genes identified through differential expression analysis. Expression values for all genes removed from the dataset during this process were then re-introduced to remaining cells for further analysis.

A further noise reduction step was performed through Seurat[5] integration analysis, demonstrated in Figure 10 (Stuart et al. 2019). Through the identification of cross-dataset pairs of cells that are in a matched biological state, such as cells within sample pairs, this process performs batch effect corrections. Integration analysis was performed as described in the vignette.

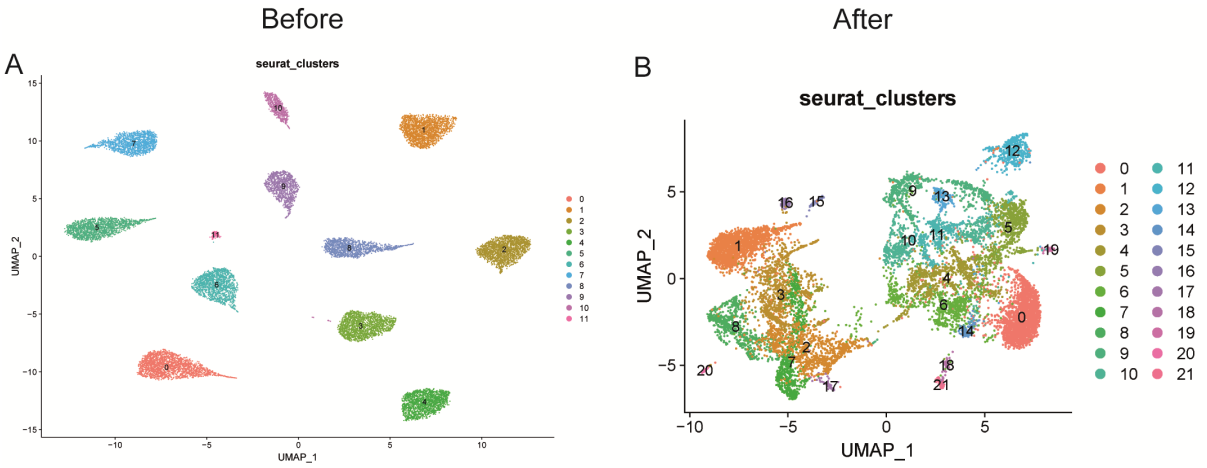

Figure 10: The noise reduction process reduced *ex vivo* activation.

A) UMAP plot showing seurat based clustering of cells before noise reduction steps.

B) UMAP plot showing seurat based clustering of cells after noise reduction steps.

2.2.5.10. Cluster Identification and Analysis

Data from ScType[6] (Ianevski et al. 2022) automated cell-type identification system was primarily used when labelling clusters, according to the associated vignette (Annex Table 3). This method took in gene expression data from clusters identified in Hammond et al. (2019) and Li et al. (2019a). Genes up or down-regulated in each of these previously identified clusters were compared with the transcription profile of clusters identified in data presented here and scores given dependant on how closely related transcription profiles for clusters are.

Cluster comparison was performed primarily using Seurat based differential expression analysis followed by WebGestalt (Liao et al. 2019) based Over Representation Analysis (ORA). ORA was necessary as very few significant markers, often 0, were identified for each cluster using Seurat. This is likely due to reduced variation between clusters following necessary noise reduction steps.

Clusters were further differentiated using pathway enrichment analysis performed by WebGestalt (Liao et al. 2019). Here, ORA was carried out on genes which reached an expression level of at least 5 units - log-transformed counts per 10,000 transcripts, as determined by Seurat (Butler et al. 2018). This method produced lists of GO terms, which were significantly over represented in genes expressed at the highest levels (above 5 units) across all clusters. The 5 unit cut off resulted in a manageable list of 230-290 genes out of a

possible 29664. Significance was calculated using hypergeometric testing and corrected for multiple testing using the Benjamini-Hochberg multiple test adjustment with a p-value of 0.05 or lower. Significant GO terms were then manually grouped into broad biological categories named: inflammatory, reactive, developmental, metabolic, migratory, and apoptotic. These groupings were selected due to the high prevalence of GO terms related to these biological processes amongst all clusters and their relevance to the hypotheses explored here. The level of enrichment of each of these categories, referring to the number of genes expressed over the number of genes expected from the Illumina *Mus musculus* reference set combined with the level of expression of each gene, was recorded for comparison between clusters. The manual grouping of GO terms and measuring of enrichment allowed approximate comparison of the ability of each cluster to perform the specific category of biological processes, providing some insight into the function of the cells within. This form of analysis will be termed Manual Enrichment Analysis (MEA). The results of this analysis can be seen in Annex Table 4.

ORA is effective at identifying genes where expression differences are large, making it a suitable tool to look at the most highly expressed genes; However, this approach is not effective where the difference is small but evidence suggests related genes perform in a coordinated way. Gene Set Enrichment Analysis (GSEA) addresses this limitation (Subramanian et al. 2005). Since GSEA aggregates per gene expression levels across genes within a gene set, small but coordinated changes can be detected. Therefore, when analysing differentially expressed genes between clusters, ORA was performed separately on up and downregulated gene lists and GSEA was also performed when there were 500 or more differentially expressed genes. Although there were few significantly altered GO terms identified, also likely due to noise removal reducing variation, these techniques improved understanding of the variation that remained. Enrichment ratio was used to report ORA, meaning the ratio of the number of observed genes divided by expected value. Normalised Enrichment Score (NES) was used to report GSEA, meaning the enrichment ratio normalised based on the number of genes in the gene set. Multiple testing correction was performed using False Discovery Rate (FDR) analysis.

Table 2: Tools used for Single-Cell RNA Sequencing Analysis.

#	Tool	Authors	Links
1	Trim Galore	Felix Krueger, Babraham Bioinformatics	Trim Galore
2	FastQC	Simon Andrews, Babraham Bioinformatics	FastQC
3	Ensembl	Rob Finn and Andy Yates, European Bioinformatics Institute	Ensembl
4	STARsolo	Alex Dobin, Cold Spring Harbor Laboratory	STARsolo
5	Seurat	Paul Hoffman, Satija Lab	Guided Clustering Integration
6	ScType	Aleksandr Ianevski, University of Helsinki	ScType
7	WebGestalt	Yuxing Liao, Baylor College of Medicine	WebGestalt

2.2.6. Statistical Analysis

Outside of RNA Sequencing analysis described previously, all statistical analysis was performed using Graphpad Prism. Like the majority of biological variables, data tested through statistical analysis was assumed to have been sampled from populations that follow a normal distribution.

For experiments involving the comparison of two groups, the unpaired t test was selected given that all experiments involved unmatched groups. For experiments involving more than two groups, one- or two-way ANOVAs were selected depending on whether the experiment involved measuring one or two independent variables.

For One-Way ANOVAs, the Brown-Forsythe test and Bartlett's test were used to test for equality of variance. Where variance differed significantly between groups, a Brown-Forsythe ANOVA was used to modify calculations of the F ratio and degrees of freedom to adjust for heterogeneity of within-group variances.

2.2.6.1. Replicates

Cell counts performed on brain slices, such as in figures 11, 12, and 13, were averaged between at least two brain slices from an individual brain to form one replicate. Brains were selected from at least two litters for each experiment.

2.3. Results

2.3.1. Identification of the Septal and Glial Wedge Microglial Hotspots

The presence of a microglial hotspot can be defined as a focal accumulation resulting in increased density of microglia in a developmental structure (Squarzoni et al. 2014). Microglia have been observed in close proximity to the corpus callosum and are thought to be involved in its formation (Pont-Lezica et al. 2014). Although shown adjacent to the corpus callosum the precise location of clusters of microglia was not shown, for example whether these cells predominantly cluster in the septum or glial wedges and how far along the rostro-caudal axis clusters stretch. These microglia are thought to be involved in formation of the corpus callosum and understanding the precise localisation of clusters may help shed light on their function. Demonstrating that these cells differ from other developmental microglia could also provide an initial indication that they are heterogeneous. Confirming the presence and localisation of microglial hotspots around the corpus callosum was therefore an initial aim of this project. In order to achieve this, immunohistochemistry and microglial cell counting was performed to estimate the density of cells within the septal region and surrounding areas. Microglia were observed accumulating in the late stages of prenatal corpus callosum development (Pont-Lezica et al. 2014). E18.5, at the end of mouse prenatal development, was therefore selected as a timepoint to study this cluster. Iba1 immuno-labelling was selected as a pan macrophage marker, however microglia are thought to be the only parenchymal macrophages during this developmental time window (Brioschi et al. 2020). It is therefore assumed that all labelled cells in this region are microglia.

Images shown in Figure 11 highlight the rostro-caudal extension of these dense microglial hotspots. Microglia populating the glial wedges can be seen at the genu level of the corpus callosum in Figure 11C. This level is rostral to the septal region, however more caudal in Figure 11D and E septal microglia can be seen forming a dense septal cluster as within the glial wedges. IBA1 labelled microglia in the fornix are similarly clustered in septal and glial wedge regions (Figure 11 F, G) which dissipate by more caudal regions, in Figure 11 I and J, where the hippocampal commissure can be seen. All levels displayed show a lack of dense iba1 staining in the corpus callosum as within the cortical region shown in Figure 11 H.

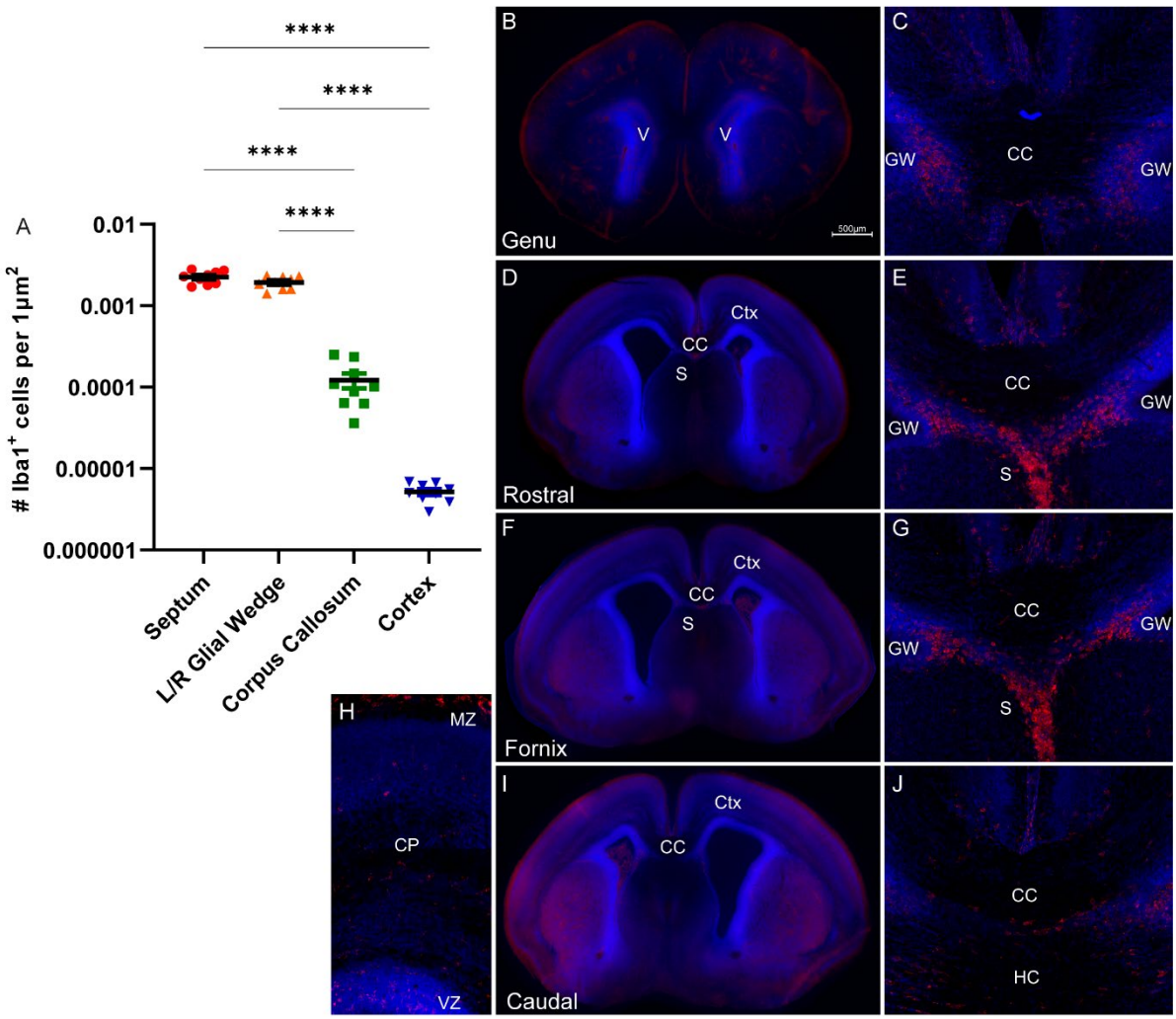

Figure 11: Microglia form a Dense Hotspot within the Prenatal Septum.

A) Mean (+/- SEM) number of Iba1^{+} cells per 1µm^{2} in rostral and fornix midline regions and cortical regions at E18.5. n=9 for all regions. (One-way ANOVA (F = 178.3, p < 0.0001), Tukey-Kramer post-hoc test, **** = p < 0.0001). **B, D, F, I)** Fluorescence microscope images of frontal E18.5 brain slices across the rostro-caudal axis with IBA1 immuno-labelled in red against Dapi in blue. **C, E, G, J)** Representative images of the midline region also covering genu, rostral, fornix and caudal regions respectively. **H)** Representative E18.5 cortical region image labelled as described previously. *CC – Corpus Callosum; CP – Cortical Plate; Ctx – Cortex; GW – Glial Wedge; HC – Hippocampal Commissure; MZ – Marginal Zone; S – Septum; V – Ventricle; VZ – Ventricular Zone.*

As the apparent location of the septal hotspot, rostral and fornix slices were therefore selected for density measurements shown in Figure 11A, with replicates defined here as the average cell count of one rostral and one fornix slice per brain. As expected, mean density of Iba1 labelled cells in the septum was significantly higher than within the corpus callosum ($p < 0.0001$) and cortex ($p < 0.0001$) by factors of 10 and 1000 respectively. Iba1 labelled cells in the glial wedges were comparably dense, with mean septal Iba1 density at 0.0022 cells per μm^2 relative to the glial wedge mean of 0.0019 cells per μm^2.

Data presented in this section show that corpus callosum associated microglial hotspots are present in both the septum and glial wedges at E18.5. These hotspot extend from the rostral to the fornix region of the corpus callosum. Other developmental microglia within the corpus callosum and cortex are less dense, highlighting that such high cell density is not a common feature developmental microglia.

2.3.2. Marker expression of septal microglia compared to other developmental microglia

2.3.2.1. Septal and Glial Wedge Microglia Expression Profile

Identifying which subset(s) of microglial cell colonises the developing corpus callosum region and how these differ from other populations could inform future work uncovering why particular defects, such as corpus callosum agenesis, are associated with particular developmental insults. RNAscope in-situ hybridisation combined with immunohistochemistry was therefore used to characterise septal microglia transcription profile for comparison with surrounding microglial cells and a reference population within the cortex. The number of $IBA1^+$ microglia, or macrophages, expressing all possible combinations of *Gpnmb, Clec7a, Spp1* and *F13a1* were counted and the proportion of each population recorded (Figure 12). Here, each replicate refers to the average cell count of 1-3 slices taken from an individual brain with three brains taken from each of two litters. Possible transcription factor expression was estimated based on developmental microglia populations previously identified in close proximity to the corpus callosum (Table 1).

The mean percentage of $IBA1^+$ cells expressing *Gpnmb* (38.3%) and *Spp1* (35.8%) within the septum was significantly higher than all cortical regions measured ($F = 18.31$, all $p < 0.0001$, Figure 12T). Glial wedges contained a similarly high proportion of *Gpnmb* and *Spp1*

expressing IBA1$^+$ cells, at 29.4% and 43.1% respectively. Although only 17.8% of septal microglia expressed *Clec7a*, this was significantly higher ($p < 0.05$) than within marginal zone or cortical plate regions where no IBA1$^+$*Clec7a*$^+$ cells were counted. This difference in expression proportion highlights the similarities in transcription profile between septal and glial wedge regions, whilst also demonstrating that cortical microglia differ from those within the septum and glial wedges.

F13a1 is uniquely expressed by non-microglial macrophages and monocytes (Hammond et al. 2019; Utz et al. 2020). A significantly higher proportion of IBA1$^+$*F13a1*$^+$ cells were counted within the marginal zone (44.3%) than all other regions measured ($p < 0.0001$, Figure 12T). This was expected given that *F13a1* expression was segregated to the meninges, as shown in Figure 1B. Parenchymal macrophages colonise the meninges but not the brain parenchyma (Utz et al. 2020). Interestingly, 12.4% of septal IBA1$^+$ cells expressed *F13a1* suggesting the presence of non-microglial macrophages in this region of the brain parenchyma, in contrast to previous reports (Brioschi et al. 2020).

Both the septum and glial wedges contain IBA1$^+$*Gpnmb*$^+$*Clec7a*$^+$*Spp1*$^+$ cells, as shown in Figure 2M and S, at 5.4% and 3.3% respectively. A further, 16.5% of septal IBA1$^+$ cells and 18.7% of glial wedge IBA1$^+$ cells express *Gpnmb*$^+$ with *Spp1*$^+$. Examples of these cells are marked by brown arrows in Figure 2I and K. Expression of these markers in combination indicates the presence of PAM or ATM within the septum and glial wedges (Table 1). Interestingly, a small proportion of IBA1$^+$*Gpnmb*$^+$*Clec7a*$^+$*Spp1*$^+$*F13a1*$^+$ cells (1.14%, Figure 12 – part of 'Other' group) were found within the septum. This suggests that either a small number of non-microglial macrophages transition into PAM or ATM or a small PAM/ATM like macrophages population exists within the septum.

Unlike corpus-callosum adjacent regions, cortical IBA1$^+$ cells did not express *Gpnmb*, *Clec7a* and *Spp1* in combination and only 0.48% of IBA1$^+$ cells expressed *Gpnmb* with *Spp1* within the ventricular zone (Figure 12C, E, G). A small population of IBA1$^+$*Clec7a*$^+$ cells were counted within the ventricular zone, in line with previous reports (Hammond et al. 2019). Cells expressing IBA1 alone without any other markers measured made up the majority of IBA1$^+$ cells in all areas of the cortex, whereas these cells are in the minority in both the septum and glial wedges (Figure 12C, E, G, M, S)

Clear differences in morphology were also observed within IBA1$^+$ cells. Strictly round, ameboid cells with no processes were labelled in the septum (Figure 12H) whilst highly branched, ramified cells with many processes were identified in the cortical plate (Figure 12D). IBA1$^+$ cell morphology was less extreme in other areas: ameboid cells were found in the marginal zone (Figure 12B), somewhat branched yet circular macrophages observed in the glial wedges (Figure 12N) and slightly more ramified cells visualised within the ventricular zone (Figure 12F).

In summary, glial wedge and septal macrophages share many similarities in both expression profile and morphology. These populations are reminiscent of previously identified PAM and ATM. Corpus callosum adjacent IBA1$^+$ cells differ from more distant populations found in the ventricular zone, cortical plate or marginal zone regions of the cortex. Here macrophages in deeper layers of the cortex differed from IBA1$^+$ cells in neighbouring regions closer to the meninges.

Figure 12: Corpus callosum adjacent microglia transcription profile differs from cortical microglia at E18.5.

A) IBA1 (green) immuno-labelled brain slice at E18.5. **B, D, F)** RNA *in-situ* (RNAscope) with iba1 immuno-labelling showing IBA1, *F13a1* and/or *Spp1* expression for MZ, CP and VZ regions respectively, n=6. **C, E, G, M, S)** Pie charts showing proportion of marker expression relative to total IBA1$^+$ cells within MZ, CP, VZ, S and GW regions respectively. **H)** RNA *in-situ* with iba1 immuno-labelling for S. **I-K)** Magnified region H-ii labelling *Gpnmb*, *Clec7a* and/or *Spp1* with Dapi. Brown arrow highlights IBA1$^+$*Gpnmb*$^+$*Spp1*$^+$ cell, red arrow depicts IBA1$^+$*Clec7a*$^+$ cell and yellow arrow indicates IBA1$^+$*F13a1*$^+$ cell. **L)** Magnified region H-i labelling *F13A1* and Dapi. **N)** RNA *in-situ* with iba1 immuno-labelling for GW. **O-Q)** Magnified region H-ii labelling *Gpnmb*, *Clec7a* and/or *Spp1* with Dapi. White arrow shows IBA1$^+$*Gpnmb*$^+$ cell, dark red arrow points out IBA1$^+$*Gpnmb*$^+$*Clec7a*$^+$*Spp1*$^+$ cell and yellow arrow highlights an IBA1$^+$*F13a1*$^+$ cell. **R)** Magnified region H-i labelling *F13a1* and Dapi. **T)** Mean (+/- SEM) percentage of IBA1$^+$ cells expressing *Gpnmb* (Purple), *Clec7a* (Red), *Spp1* (Orange) and *F13a1* (Yellow) within each region measured (One-way ANOVA, $F = 18.31$, $p < 0.0001$, Tukey-Kramer post-hoc test, *** = $p < 0.0001$, * = $p < 0.05$). *CC – Corpus Callosum; CP – Cortical Plate; GW – Glial Wedges; MZ – Marginal Zone; S – Septum; VZ – Ventricular Zone.*

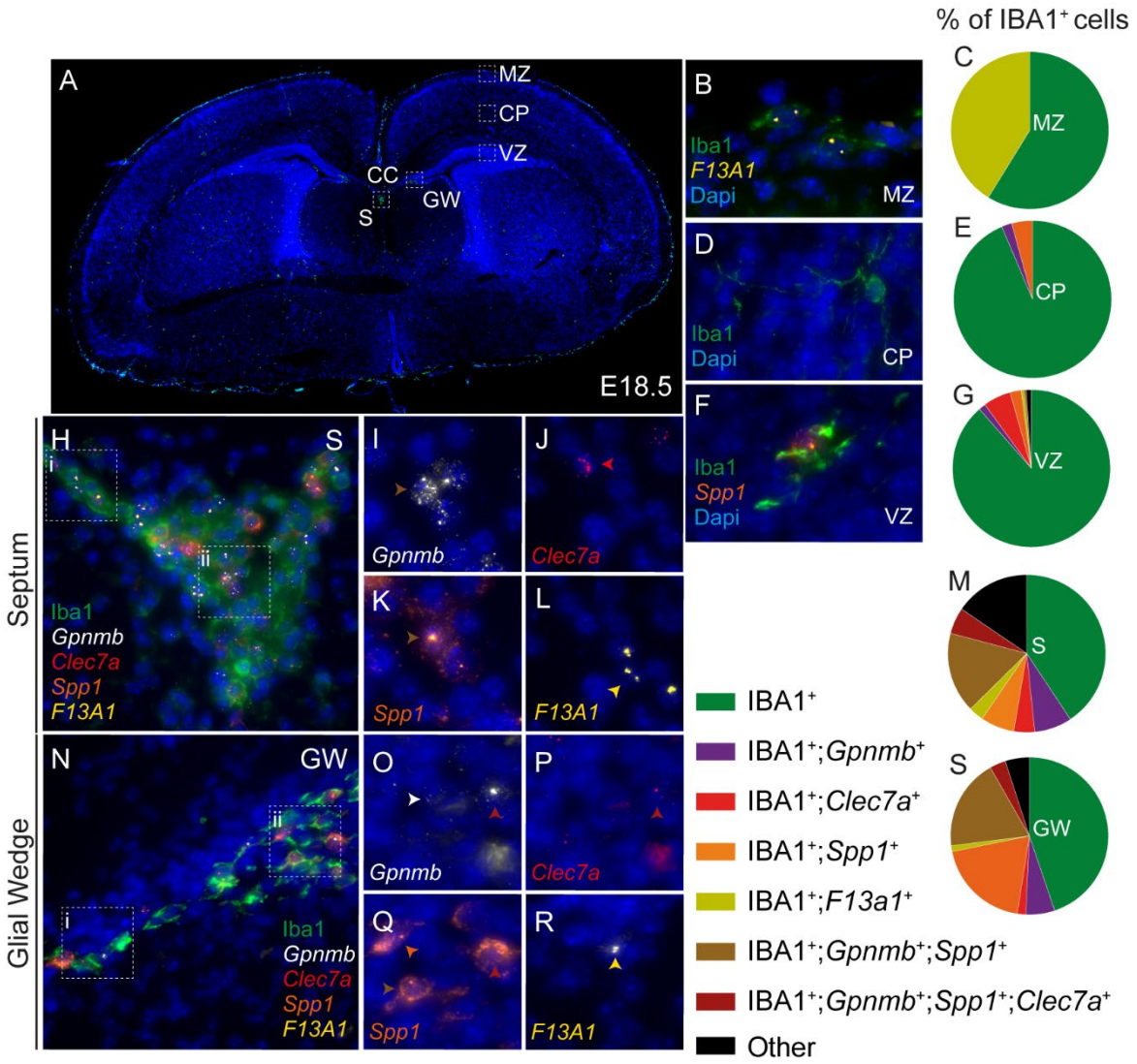
A
MZ
CP
VZ
CC
GW
S
E18.5
B
Iba1
F13A1
Dapi
MZ
D
Iba1
Dapi
CP
F
Iba1
Spp1
Dapi
VZ
% of IBA1⁺ cells
C
MZ
E
CP
G
VZ
M
S
S
GW
Septum
Glial Wedge
H
S
i
ii
Iba1
Gpnmb
Clec7a
Spp1
F13A1
I
Gpnmb
J
Clec7a
K
Spp1
L
F13A1
N
GW
ii
i
Iba1
Gpnmb
Clec7a
Spp1
F13A1
O
Gpnmb
P
Clec7a
Q
Spp1
R
F13A1
IBA1⁺
IBA1⁺;Gpnmb⁺
IBA1⁺;Clec7a⁺
IBA1⁺;Spp1⁺
IBA1⁺;F13a1⁺
IBA1⁺;Gpnmb⁺;Spp1⁺
IBA1⁺;Gpnmb⁺;Spp1⁺;Clec7a⁺
Other

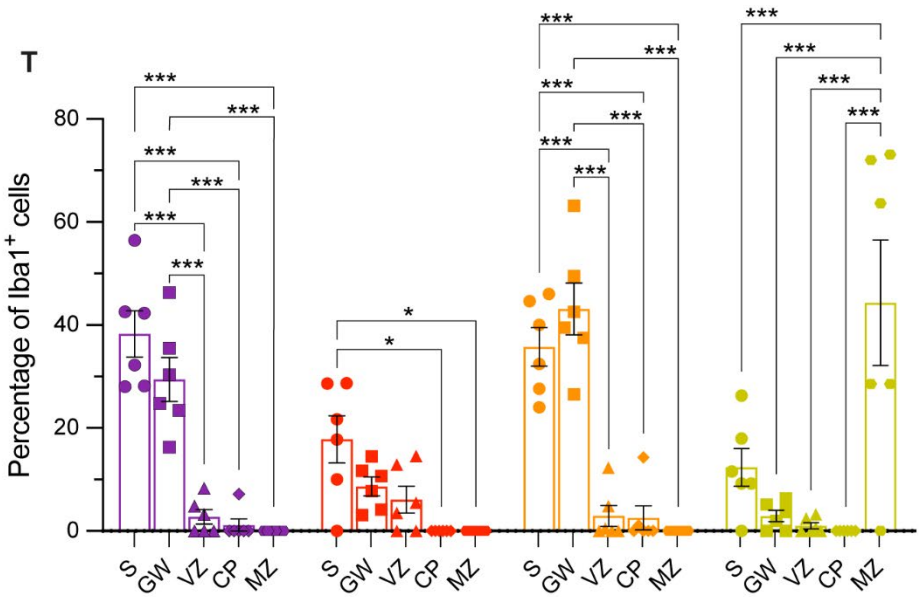
T
Percentage of Iba1⁺ cells
0
20
40
60
80
S
GW
VZ
CP
MZ

2.3.2.2. **Subpallial Dopaminergic Hotspot Microglia Expression Profile**

Exploration of the relationship between corpus callosum associated developmental microglia and microglia in contact with other developing axon tracts was the next objective. Having shown that microglia adjacent to the corpus callosum express markers associated with PAM and ATM, it was important to understand if this is a feature of all microglia associated with developing axon tracts. Again, this could help further understanding of the function of these cells and their involvement in neurodevelopmental disorder. Discrete microglial hotspots have been identified previously in the subpallial region surrounding dopaminergic axons at E14.5 (Squarzoni et al. 2014). The transcription profile of IBA1$^+$ cells surrounding dopaminergic axon tracts of the subpallium at E14.5 was therefore analysed through RNAscope in-situ hybridisation combined with immunohistochemistry, as in the previous section. Each brain was defined as a replicate formed of the average cell count of at least three slices.

Two microglial hotspots at the extremities of midbrain dopaminergic axons have been described: one at the site of dopaminergic axon entry into the subpalliam; the other at the subpallial boundary with the pallium (Squarzoni et al. 2014). IBA1$^+$ cells were therefore divided into two populations relating to these regions, the axonal entry and subpallial boundary regions respectively, and a further axon tract region acting as a reference population (Figure 13A). All three of these regions contain few cells expressing *Clec7a* and *F13a1* at less than 1% and less than 4% of IBA1$^+$ cells respectively (Figure 13E). Most of the few IBA1$^+$*F13a1*$^+$ cells were found within the axonal entry region. These are likely ventricular macrophages as they were almost exclusively found in close proximity to the ventricles (Figure 13I, K).

Axonal entry and subpallial boundary regions contained a small proportion of *Gpnmb* expressing IBA1 cells, at 4.3% and 7.4% respectively (Figure 13E). There was a slightly, although not significantly, higher proportion of *Gpnmb* expressing IBA1 cells than within the axon tracts where only 1.3% of IBA1$^+$ cells expressed *Gpnmb* (Figure 13C). Interestingly, almost all IBA1$^+$*Gpnmb*$^+$ cells also expressed *Spp1* with a maximum of 1.4% of cells expressing *Gpnmb* without *Spp1* in any region (Figure 13B-D). Brown arrows in Figure 13F-H, L, O and Q, indicate a few examples of these cells. *Spp1* expression more clearly differentiates axonal entry, subpallial boundary and axon tract IBA1$^+$ cells. The subpallial boundary contained a significantly higher mean proportion of IBA1$^+$*Spp1*$^+$ cells than within the

axonal entry ($F = 18.76$, $p = 0.0001$, Figure 13E) or axon tract ($p < 0.0001$) regions. Within both the subpallial boundary and axonal entry sites a large proportion of IBA1$^+$ cells expressed *Spp1 (*41.9% and 21.9% respectively) relative to the smaller 11.0% of IBA1$^+$ cells expressing *Spp1* along dopaminergic axon tracts.

Taken together this data suggests possible differences between groups of IBA1$^+$ cells localised to different regions of the developing subpallial dopaminergic axon tracts. The lack of IBA1, *Gpnmb, Clec7a* and *Spp1* co-expression shows PAM- and ATM-like cells are not localised to this developing axon tract region, unlike the corpus callosum region. Expression of *Spp1* at E14.5 suggests this marker is found in other developing microglial populations or that subpallial microglia are a premature stage of PAM or ATM. It is possible that these cells express more PAM and ATM later in development, although this subtype is known to be transient. Further *in situ* hybridisation experiments would be required to investigate this.

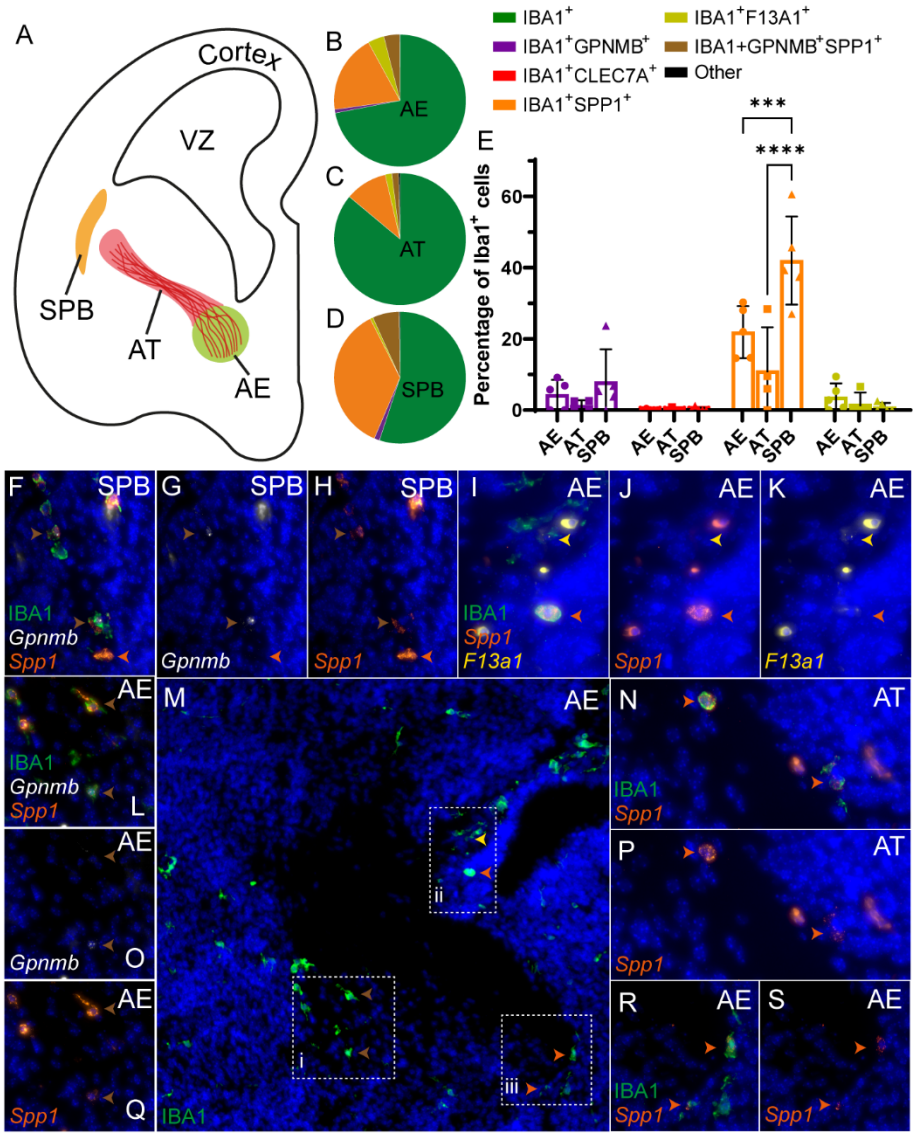
A
Cortex
VZ
SPB
AT
AE
B
AE
C
AT
D
SPB
IBA1+
IBA1+GPNMB+
IBA1+CLEC7A+
IBA1+SPP1+
IBA1+F13A1+
IBA1+GPNMB+SPP1+
Other
E
Percentage of Iba1+ cells
***
****
AE AT SPB AE AT SPB AE AT SPB AE AT SPB
F SPB IBA1 Gpnmb Spp1
G SPB Gpnmb
H SPB Spp1
I AE IBA1 Spp1 F13a1
J AE Spp1
K AE F13a1
L AE IBA1 Gpnmb Spp1
O AE Gpnmb
Q AE Spp1
M AE IBA1 i ii iii
N AT IBA1 Spp1
P AT Spp1
R AE IBA1 Spp1
S AE Spp1

Figure 13: Subpallial Dopaminergic Hotspot Microglia do not express PAM or ATM markers at E14.5

A) Diagram of the E14.5 brain labelling the regions analysed. **B, C, D)** Pie charts showing proportion of marker expression relative to total IBA1$^+$ cells within AE, AT and regions respectively. **E)** Mean (+/- SEM) percentage of IBA1$^+$ cells expressing *Gpnmb* (Purple), *Clec7a* (Red), *Spp1* (Orange) and *F13a1* (Yellow) within each region measured (One-way ANOVA, $F = 18.76$, $p < 0.0001$, Tukey-Kramer post-hoc test, **** = $p < 0.0001$, *** = $p = 0.0001$) Proportion of marker expression relative to total IBA1$^+$ cells within MZ, CP, VZ, S and GW regions respectively, n=5. **F, G, H)** RNA *in-situ* (RNAscope) with iba1 immuno-labelling showing IBA1, *Gpnmb* and/or *Spp1* expression for the SPB region with IBA1$^+$*Gpnmb*$^+$*Spp1*$^+$ and IBA1$^+$*Spp1*$^+$ cells marked by brown and orange arrows respectively. **I-K)** Magnified AE region M-ii labelling IBA1, *Spp1* and/or *F13a1*. IBA1$^+$*Spp1*$^+$ cell is marked by the orange arrow and IBA1$^+$*F13a1*$^+$ cell is indicated by the yellow arrow. **L, O, Q)** Magnified AE region M-i labelling IBA1, *Spp1* or *Gpnmb*. IBA1$^+$*Gpnmb*$^+$*Spp1*$^+$ cells are marked by brown arrows. **M)** IBA1 immuno-labelled image of the AE region with regions i-iii highlighted for magnification in surrounding images. **N, P)** RNA *in-situ* with iba1 immuno-labelling showing IBA1 and/or *Spp1* expression for the AT region with IBA1$^+$*Spp1*$^+$ cells marked by orange arrows. **R, S)** Magnified AE region M-iii labelling IBA1 and/or *Spp1* with IBA1$^+$*Spp1*$^+$ cells marked by orange arrows. *AE – Axonal Entry; AT – Axon Tract; SPB – SubPallial Boundary; VZ – Ventricular Zone.*

2.3.3. Single-cell Sequencing of Developmental Microglia

2.3.3.1. Sequencing method

As covered in the methods section, brains were harvested from embryos at E18.5 subjected to control or maternal immune activation conditions and dissected into two regions - the cortex and the septum. This method brought an element of cell localisation and regional differentiation into the technique, which is not possible when sequencing cells from whole brains. Regional differences are immediately apparent in Figure 14B where clusters largely self-segregate into cortical and septal populations. This trend can be viewed quantitatively in Figure 14D showing 15 of the 21 clusters identified are at least 90% composed of cells from one region. Maternal inflammatory state also appears to have a noticeable impact on clustering which will be covered in chapter 5. Results presented here will instead focus on data obtained from cells isolated from the control litter, highlighted in red in Figure 14B.

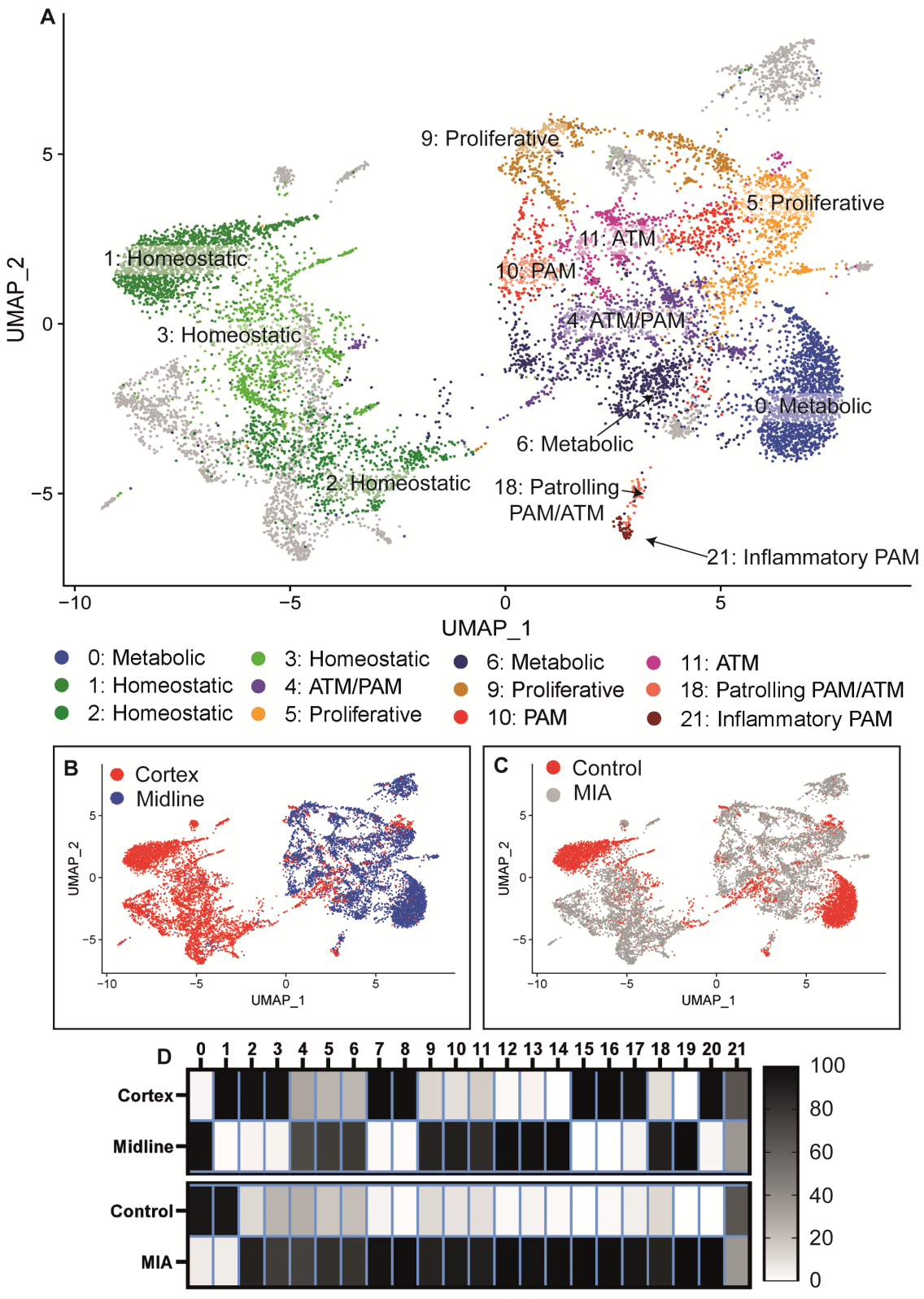
A
9: Proliferative
5: Proliferative
11: ATM
1: Homeostatic
10: PAM
4: ATM/PAM
3: Homeostatic
0: Metabolic
6: Metabolic
2: Homeostatic
18: Patrolling
PAM/ATM
21: Inflammatory PAM
UMAP_2
UMAP_1
0: Metabolic
1: Homeostatic
2: Homeostatic
3: Homeostatic
4: ATM/PAM
5: Proliferative
6: Metabolic
9: Proliferative
10: PAM
11: ATM
18: Patrolling PAM/ATM
21: Inflammatory PAM
B
Cortex
Midline
C
Control
MIA
D
Cortex
Midline
Control
MIA

Figure 14: A variety of different microglial clusters are present in the E18.5 brain. **A)** UMAP plot showing subset of 21 clusters identified through single cell sequencing of cells isolated from E18.5 brain samples. Clusters containing less than 5% of cells from control samples are greyed out. Clusters were labelled using ScType automated labelling system, previous single cell sequencing data and results of up-regulated gene over-representation analysis. **B)** UMAP plot from A highlighting cells taken from cortical (red) or dissected (blue) samples. **C)** UMAP plot from A highlighting cells taken from control (red) or MIA (grey) samples. **D)** Heatmap of the normalised percentage of cells assigned to each cluster from each sample type. ATM – Axon Tract associated Microglia; *PAM – Proliferative-region Associated Microglia*

2.3.3.2. Sequenced cells were almost exclusively microglia

All cells sequenced were isolated through flow assisted cell sorting (FACS) on $CD45^+$ and $CD11b^+$ gates. Although this gating strategy does not guarantee a pure population of microglia, analysis of transcription data strongly suggests that all but one of the identified clusters are indeed microglia. Firstly, despite limited expression of microglial markers in prenatal microglia populations (Hammond et al. 2019; Li et al. 2019b), all clusters identified express some level of previously identified microglia marker (Figure 15). Interestingly, C1qa and Tmem119 appear more highly expressed in cortical regions than dissected septal regions, whilst Trem2 is slightly more expressed in septal regions. More in depth analysis of marker expression revealed close similarities between microglial subpopulations. As discussed in the methods section, data from ScType (Ianevski et al. 2022) automated cell-type identification system was primarily used when labelling clusters (Annex Table 3). For 13 of the 22 clusters identified: all of the top 3 ScType label scores were microglia; 7 of the remaining 9 clusters had microglia clusters as the top ScType score; this strongly suggests that the majority of these cells are microglia. Whilst some of these clusters showed some resemblance to neutrophils, none of these clusters express canonical neutrophil markers making this possibility unlikely.

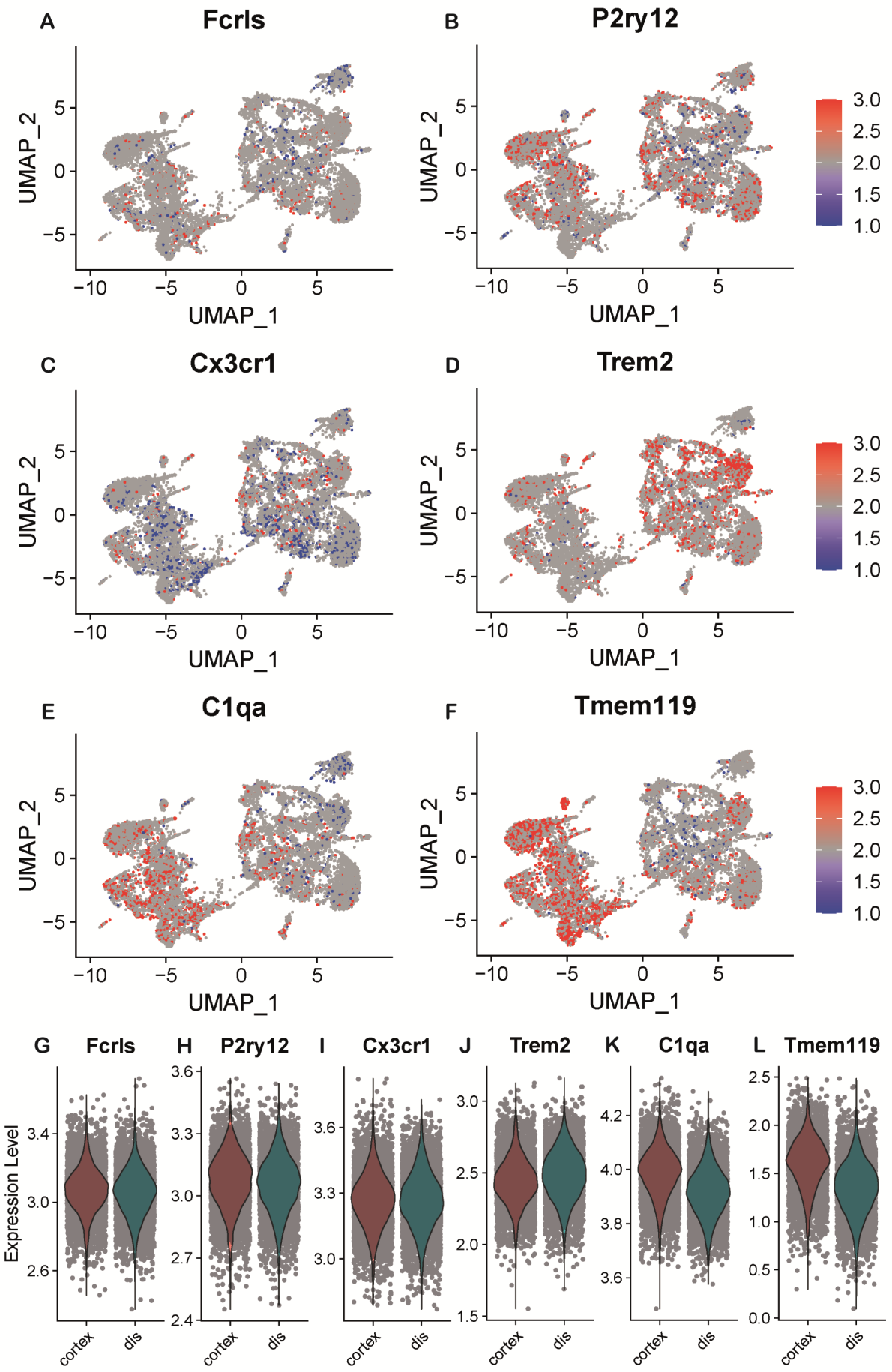
A
Fcrls
B
P2ry12
C
Cx3cr1
D
Trem2
E
C1qa
F
Tmem119
UMAP_1
UMAP_2
3.0
2.5
2.0
1.5
1.0
G
H
I
J
K
L
Expression Level
cortex
dis

Figure 15: Low level of canonical microglia gene expression in E18.5 macrophages.

A-F) UMAP plot coloured for expression of canonical microglial genes. Expression level in log-transformed counts per 10,000 transcripts. **G-H)** Expression of canonical microglia genes across cortical and dissected samples displayed in violin plots. Expression level in

2.3.3.3. Experimental Activation

WebGestalt (Liao et al. 2019) gene set analysis, described in the methods section, showed that all clusters expressed genes categorised under the response to alcohol GO term. This suggests cells may have reacted to alcohol exposure during the experimental technique, which may have influenced other elements of their transcription profile. Some evidence of technical artefacts on expression profile are seen under apoptosis regulation. Of the 21 clusters identified, 17 had some level of enrichment for genes categorised into GO terms relating to apoptosis (Annex Table 4). These GO terms: regulation of apoptotic signalling; intrinsic apoptotic signalling pathway; and myeloid cell differentiation – indicate some level of cell stress. Whilst this stress was not sufficient to induce apoptosis, as these cells were filtered out, it may have shifted expression profiles away from the *in vivo* environment. However, response to alcohol enrichment scores for all clusters ranged between 3.27-3.89; whilst apoptosis enrichment scores for all but 3 clusters fell below 5.72, suggesting these GO terms were mildly over represented within the most expressed genes. Furthermore, expression of genes associated with experimental activation of microglia, identified by Marsh et al. (2022), was low amongst all clusters. This is shown in Figure 16 where expression levels of this set of genes centres around 0 suggesting minimal experimental activation.

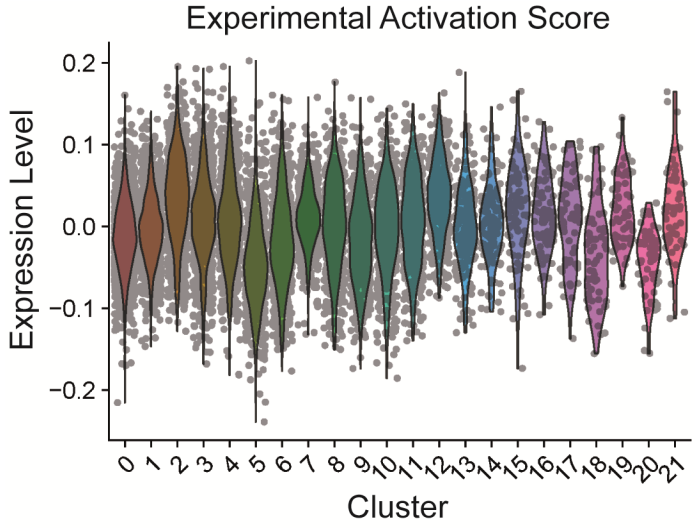

Figure 16: Low level of genes associated with experimental activation.

Expression of all genes associated with experimental activation in March et. al (2022) across all clusters displayed in violin plots. Expression level in log-transformed counts per 10,000 transcripts.

2.3.3.4. Cortical microglia expression profile

Focusing on microglia taken from control litters, the majority (69.93%) of microglia isolated from the cortex fall in to clusters 1, 2 and 3 - all of which are labelled as homeostatic microglia. This is visualised in Figure 14D. Homeostatic microglia, identified by both Hammond et al. (2019) and Li et al. (2019a) were primarily localised to adult mouse brains from P30 onwards or P60. Whilst these papers do not go on to analyse the behaviour or function of these cells, it is widely accepted that adult microglia are found in an 'active resting' state in which they actively scan their surroundings in preparation to respond to any pathogen or inflammatory stimulus (Hanisch and Kettenmann 2007). Based on the presence of this subtype in the adult mouse brain, it is assumed that the majority of cortical microglia have matured to an adult-like state by E18.5. In support of this, cortical microglia express increased levels of *Tmem119* (Figure 15) – a marker expressed by more mature microglia present from P6 to adulthood in the mouse brain (Bennett et al. 2016). Increased expression of complement cascade component *C1qa* in cortical microglia is also of note given the reported need for *C1q* expression during postnatal synaptic pruning (Stevens et al. 2007).

Cortical homeostatic cluster 1 is 94.76% composed of control cortical cells numbering 1518 (Figure 14D). Clusters 2 and 3 are 12.00% and 25.00% composed of control cortical cells at 111 and 229 cells respectively. A substantial proportion of cells from each MIA category make up the remainder of clusters 2 and 3. Cortical homeostatic clusters 7 and 8 on the other hand contain less than 22 control cells and are predominantly composed of cells from either PIC or LPS samples at 86.44% and 99.24% respectively.

Focusing on clusters containing at least 100 control cells, differential expression analysis revealed minor differences between homeostatic clusters 1, 2 and 3. Differentially expressed genes with a relative log fold change of over 0.25 between clusters were identified using Seurat (Ianevski et al. 2022). A total of 287 genes were differentially expressed in cluster 2 relative to cluster 1, with a maximum fold change of 0.576. Whilst only 31 genes were differentially expressed up to 0.284 fold change in cluster 3 relative to cluster 1. This is out of a total possible value of 29664 genes, highlighting the low level of differences between these populations. The small number of differentially expressed genes identified between these clusters makes GSEA unsuitable and ORA of differentially expressed genes unreliable in identifying specific differences between homeostatic populations. ORA of differentially expressed genes does suggest that cluster 2 expresses more genes associated with

inflammation than cluster 1. Specifically, cluster 2 shows increased expression of genes in GO terms for production of cytokines IL-10 and IL-12 through genes like *Cd47*, *Prkcd* and *Mapk14*. However, the broad ranging function of these genes makes assigning specific GO terms unreliable as established by the lack of significantly enriched GO terms identified. Focusing on the most highly expressed genes, MEA reveals high inflammatory enrichment scores for cluster 3 but low developmental enrichment scores relative to clusters 2 and 1 (Annex Table 4).

29.13% of control cortical cells do not cluster with homeostatic microglia; this amounts to 774 cells, which instead predominantly fall in to clusters 4, 5 and 6. Of these non-homeostatic cortical control cells: 214 are in ATM/PAM cluster 4; 143 belong to proliferative cluster 5; 164 fall in metabolic cluster 6. Non-homeostatic clusters are predominantly composed of cells from dissected samples so will be discussed further in subsequent paragraphs relating to dissected midline samples.

2.3.3.5. Midline microglia expression profile

Tissue dissected from the septal region tended to yield cells that made up clusters 4-6, 9-14, 18 and 19, as seen in Figure 14B. This broader range of clusters found in dissected midline samples highlights the increased diversity of microglial populations at the midline relative to the cortex. Cells from dissected samples were far less likely to cluster with cortical cells than vice versa, with only 1.29% of septal cells falling in homeostatic microglia clusters whilst 20.44% of cortex cells are found in metabolic, proliferative, ATM or PAM clusters. This perhaps reflects microglia in the septal region extending outside of the region dissected.

Clusters 9-14, 18 and 19 are at least 87% made up of cells from dissected midline samples (Figure 14D) and so will be referred to as dissected or septal region clusters. Clusters 4-6 are 69-77% composed of dissected sample cells and are included in this grouping. Septal region clusters share a close similarity to PAM and ATM populations previously identified by Hammond et al. (2019) and Li et al. (2019a) respectively. This is not entirely clear from *Gpnmb* and *Clec7a* expression shown in Figure 17 - marker genes for PAM and ATM. However, dissected region clusters showed a high degree of similarity in overall gene expression with ATM and PAM as demonstrated by expression of the top 10 ATM or PAM genes in Figure 17 E and F. ATM and PAM are known to share a close similarity with

metabolically active and proliferative microglia (Hammond et al. 2019; Li et al. 2019b). Similarity between ATM, PAM, metabolic and proliferative clusters is supported by the close grouping of these populations in the UMAP plot (Figure 14). The plot shown in Figure 17I further demonstrates the close similarity between PAM and ATM, where there is a clear positive correlation between genes differentially expressed by PAM and ATM.

The ScType cluster labelling method provided quantitative data to allow closely related septal microglia populations to be distinguished from one another. Metabolically active, proliferative, ATM and PAM were however, often amongst the top 3 scores for each dissected region cluster (Annex Table 3). The majority of cells isolated from control brains fell into metabolic, ATM/PAM and proliferative clusters 0, 4, 5 and 6 (Figure 14D).

The vast majority, 99.40%, of control dissected region microglia belong to metabolic cluster 0. This is in contrast with in-situ hybridisation data shown in Figure 12, suggesting that at least 20% of microglia in the septal region express markers associated with ATM and PAM. Control dissected region data is made up of 1 sample, as the other sample failed quality control checks (Figure 9). This technical limitation may have influenced results, as will be covered in the discussion.

Figure 17: Microglia from dissected samples express higher levels of PAM and ATM markers than cortical samples.
A-F) UMAP plot coloured for expression of: PAM and ATM markers Spp1, Gpnmb and Clec7a; macrophage marker F13a1; and top 10 genes expressed by PAM or ATM. Expression level in log-transformed counts per 10,000 transcripts. **G,H)** Expression of the 10 highest expressed PAM and ATM genes across cortical and dissected samples displayed in violin plots. Expression level in log-transformed counts per 10,000 transcripts. **I)** Plot showing genes differentially expressed between PAM or ATM and other microglial clusters with up- and down- regulated genes of interest highlighted in red and blue respectively. *ATM – Axon-Tract associated Microglia; Dis – Dissected; PAM – Proliferative-region Associated Microglia.*

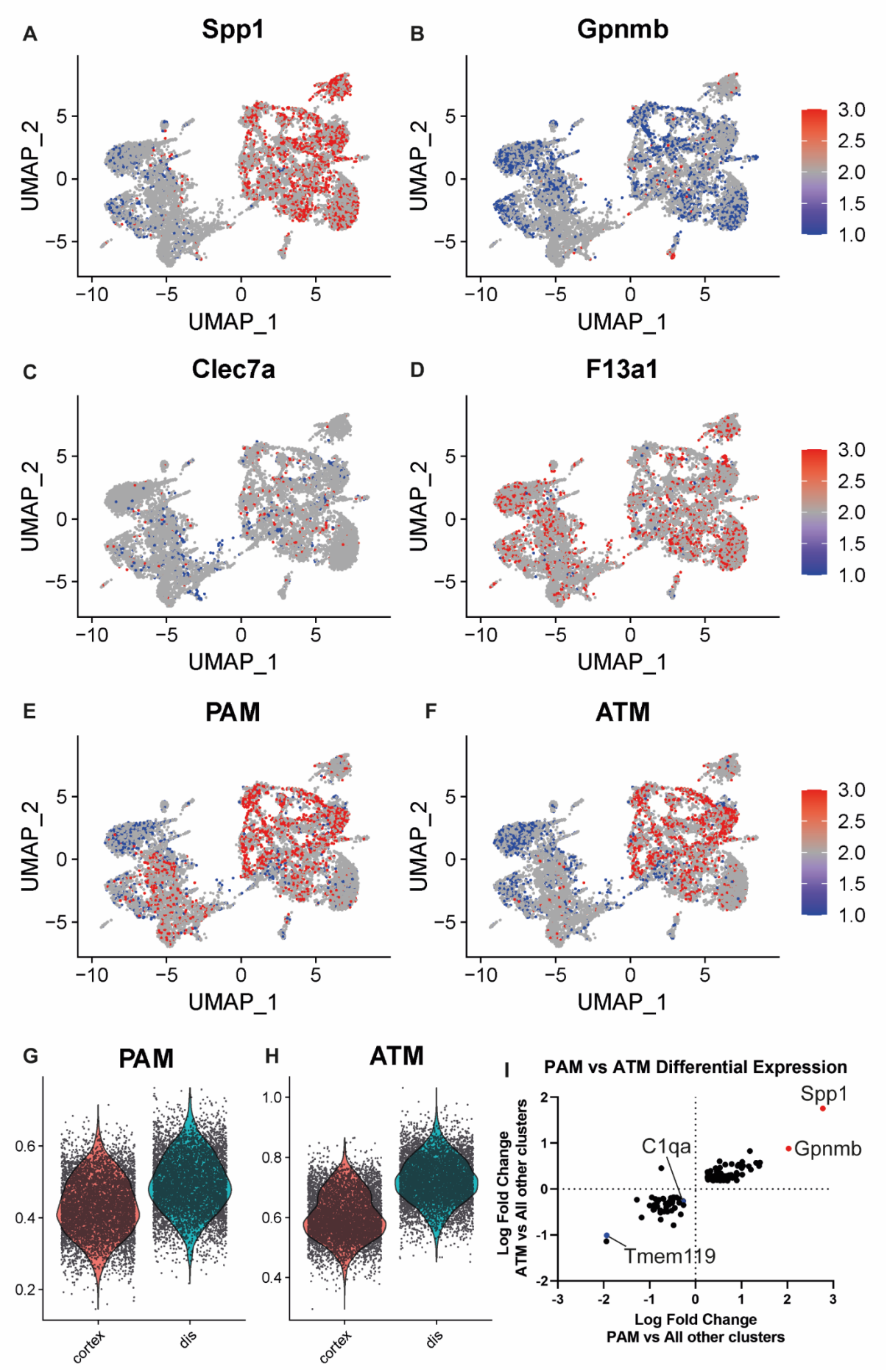
A
Spp1
B
Gpnmb
C
Clec7a
D
F13a1
E
PAM
F
ATM
UMAP_1
UMAP_2
3.0
2.5
2.0
1.5
1.0
G
PAM
H
ATM
cortex
dis
I
PAM vs ATM Differential Expression
Spp1
Gpnmb
C1qa
Tmem119
Log Fold Change
ATM vs All other clusters
Log Fold Change
PAM vs All other clusters

Clusters 4, 5, 6, 9, 10 and 11 contain at least 5% of cells from control samples. Of these, ATM/PAM cluster 4 contains the highest number of control cells, at 217, whilst related PAM cluster 10 and ATM cluster 11 contain 45 and 49 control cells respectively. ATM/PAM cluster 4 was so labelled as ScType identified a high degree of expression profile similarity between cluster 4 and both cluster 10 ATM and 11 PAM (Annex Table 3). Differential expression analysis found 644 genes differentially expressed by at least 0.25 log fold change between ATM/PAM cluster 4 and PAM cluster 10. ORA produced GO terms involved in transcription or translation such as RNA splicing, mRNA processing or protein exit from endoplasmic reticulum for both up and down regulated genes. Given that over 500 genes were differentially expressed by at least 0.25 log fold change, GSEA was performed. GSEA identified that 5 of the top 10 GO terms differentially expressed by cluster 10 contained the word 'response', such as response to oxidative stress or response to transforming growth factor beta. This suggests PAM cluster 10 is more reactive to external stimuli than ATM/PAM cluster 4.

714 genes were differentially expressed between ATM/PAM cluster 4 and ATM cluster 11. Within genes upregulated in cluster 11 ATM, according to ORA almost all are within substantially enriched inflammation related GO terms such as response to interferon-beta, response to type I interferon, response to interferon-gamma and response to virus. Genes involved include *IFI16, IFIT1, IRF1* and *CXCL10*. GSEA found that 'response to oxidative stress' was significantly (Hypergeometric testing, $p < 2.2e-16$,) differentially expressed by cells in cluster 11. The most differentially expressed GO term for cluster 4 cells was 'microtubule cytoskeleton organization involved in mitosis' suggesting higher levels of proliferation in cluster 11. Amongst the most highly expressed genes in MEA, cluster 11 appeared slightly more enriched for inflammatory GO terms than cluster 4, whilst both cluster 4 and 10 had low levels of inflammatory gene expression (Annex Table 4). Clusters 10 and 11 expressed slightly more migratory and developmental genes than cluster 4.

Proliferative microglia clusters 5 and 9 contain 144 and 74 cells respectively from control brains. As for ATM and PAM clusters, proliferative clusters have a high degree of similarity with metabolically active clusters, based on their presence within the top 3 results for sctype scores (Annex Table 3). This could also indicate a relationship between proliferative and metabolic clusters involving a fluid transition between these subtypes. Indeed, Hammond et al. (2019) suggest microglia may transition in and out of proliferative and metabolically active

states and show that they have considerable transcriptional overlap. Proliferative clusters 5 and 9 however, had a relatively high 1064 differentially expressed genes over 0.25 log fold change. ORA indicated a slightly increased expression of cytokine secretion related genes such as *Mapk14* and *Clec5a* in cluster 5. This corroborates over representation of highly expressed genes in MEA, which suggests cluster 5 is enriched for genes related to inflammatory GO terms (Annex Table 4). Cluster 9, on the other hand, expresses more genes, such as *Prkcd* and *Ccnd3,* related to the GO term: leukocyte proliferation. According to MEA, cluster 5 is more enriched for genes involved in metabolic GO terms. GSEA somewhat supports ORA results with 5 of the top 10 GO terms differentially expressed by cluster 5 containing the word 'metabolic'. Increased metabolic gene expression and decreased proliferative gene expression in cluster 5 could indicate the beginnings of a transition into a metabolically active state.

Cluster 21 contains 34 control sample cells, reaching 64.20% of cells in this small cluster. The expression profile of cells in this cluster is similar to PAM (Annex Table 3). MEA results show these cells are enriched for genes involved in inflammatory GO terms (Annex Table 4). Apoptotic GO terms are also somewhat enriched perhaps indicating that experimental manipulation has influenced the inflammatory state of cells in this cluster.

2.4. Discussion

2.4.1. Summary

This chapter distinguished a population of microglia located within the developing septum distinct from other developmental microglia populations. Microglia were shown to cluster in dense hotspots, in close proximity to the corpus callosum, within the septum and glial wedges at E18.5. The expression profile of microglia within these dense hotspots shared many similarities between glial wedges and the septal region as well as considerable contrast from developmental cortical microglia. In-situ hybridisation experiments also highlighted differences between septal microglia and another microglia population associated with developing axon tracts. Single cell sequencing data further differentiated cortical microglia from those around the mid-line, where the prevalence of microglial subtypes differed between regions analysed.

2.4.2. Microglial Hotspots

Septal and glial wedge microglia were shown to be significantly more dense than microglia found in other regions of the developing brain at E18.5. In annex figure 4 they were also shown to wrap around the corpus callosum. Whilst this does suggest the presence of a microglial hotspot, these cells appeared much more dense than earlier prenatal microglial populations supporting the development of brain structures. Microglia surrounding sub-pallial dopaminergic axon tracts, those associated with the layer V cortex and microglia clustered within the developing ventricular zone all appear more sparsely distributed (Cunningham et al. 2013; Ueno et al. 2013; Squarzoni et al. 2014). Post-natal 'fountain of microglia' cells are more comparable in density although still not reaching the level of E18.5 septal microglia (Wlodarczyk et al. 2017b; Nemes-Baran et al. 2020). This may be an initial indication that septal microglia carry out a different function than 'hotspots' supporting the development of a structure they are surrounding.

2.4.3. Corpus Callosum associated Microglia Subtypes

Septal and glial wedge microglia transcription profile resembled corpus callosum associated PAM, ATM and fountain of microglia cells. These populations differed from cortical microglia at E18.5 and sub-pallial axon tract associated microglia at E14.5. Septal microglia also share their ameboid morphology with PAM, ATM and fountain of microglia. These findings suggest septal microglia play some role in the formation of the corpus callosum, which appears to

require a unique microglial subtype during development. Further evidence of microglial involvement in corpus callosum development is presented in chapter 3.

In support of in-situ hybridisation data, single cell sequencing data showed $CD45^+$ $CD11b^+$ cells taken from the E18.5 midline were more likely to express genes associated with PAM and ATM than cortical samples (Figure 12G/H). Microglial subtypes with transcriptional similarities to PAM and ATM - metabolically active microglia and proliferative microglia, were also more prevalent at the midline than the cortex. Transcriptional similarity, as indicated by UMAP plot location in Figure 14, could indicate a relationship between these populations, perhaps meaning a developmental transition between proliferative microglia, metabolically active microglia and ATM or PAM. Microglia belonging to these subtypes in close proximity would provide further evidence of a transitional relationship between these populations. The many microglial cells not expressing PAM or ATM markers in glial wedges or the septum could be metabollically active or proliferative microglia. Further in-situ hybridisation or immunohistochemical experiments visualising markers associated with these microglia populations would test this. Analysing any transition in marker expression of microglia in cultured brain slices would be a useful further experiment.

The vast majority of cells isolated from the midline region of control brains were metabolically active microglia. ATM and PAM were, however, identified in samples exposed to LPS or Poly I:C MIA. These results could indicate that MIA induces a transition from metabolically active microglia to PAM or ATM. However, in-situ hybridisation results from control brains revealed 3.3-5.4% of microglia expressing 3 markers associated with ATM and PAM at the midline and up to 16.5-18.7% expressing 2 of these markers. Based on these results and dectin-1 expression data discussed in chapter 4, one would expect many more PAM or ATM cells. One explanation is that control dissected sample single cell results do not entirely reflect the typical *in vivo* environment. Notably, these cells were all taken from one sample as the second control brain sample failed quality control checks. It may be that errors were performed when dissecting brains for this sample meaning that septal and glial wedge hotspots were not included. A further possibility is that MIA does in fact induce an increase in PAM/ATM and proliferative microglia numbers relative to control and that at control levels the number of microglia in these clusters is too low to detect in the 1777 control midline region cells analysed. PAM or ATM marker expressing cells detected through *in-situ* hybridisation could in fact be metabolically active microglia, some of which Figure 17 shows do express

Spp1, Gpnmb or *Clec7a*. Expression of these markers could therefore suggest the process of transition from or to PAM/ATM is underway.

One feature that sets septal microglia apart from previously identified corpus callosum associated populations is the low level of *F13a1* expression. This indicates the presence of non-microglial macrophages (Hammond et al. 2019; Utz et al. 2020). Whether macrophages are able to enter the brain parenchyma and contribute towards the microglial pool during the late stages of embryogenesis is somewhat controversial, as discussed in the introduction (Reemst et al. 2016). The close proximity of the septum to the meninges may allow a small number of macrophages to enter this region, perhaps transitioning into microglia as suggested by their co-expression of PAM/ATM markers. Single cell sequencing data similarly showed that very few cells expressed markers associated with macrophages and those that did had a low level of expression for these genes. Surprisingly, these were found throughout cortical and midline clusters perhaps suggesting macrophages are also able to enter the cortex and transition into other microglial subtypes (Annex Figure 1).

A transition from macrophage to PAM/ATM-like microglia upon entry to the septum would demonstrate that signalling within the septal parenchyma is sufficient for the development of this microglial subtype. Indeed, microglia susceptibility to external signalling has been demonstrated through repeated cell culture and single cell sequencing experiments (Bohlen et al. 2017; Marsh et al. 2020). Experiments in which explants are taken from the septal region and transplanted to other brain regions and vice versa, accompanied by immunohistochemistry, could demonstrate whether septal brain parenchyma signalling is necessary and sufficient to induce development of this microglial subtype. If this were found to be a property of the septal region it could indicate the presence of a specific developmental niche for formation of the corpus callosum associated microglial subtype.

2.4.4. Cortical Microglia Subtypes

Developmental microglia in the cortex have consistently been shown to differ from corpus callosum adjacent microglia. These cells appear more ramified than corpus callosum adjacent microglia and also differ in expression profile. Cortical microglia were shown to be predominantly homeostatic populations not found at the midline. Microglia in the cortex are

likely to be performing developmental tasks distinct from microglia surrounding the corpus callosum. Such a phenotype has been identified in the early postnatal brain, P1 and P2, expressing high levels of *Csf1* and *Cxcr2* rather than Spp1, Dectin-1 or F13a1 (Matcovitch-Natan et al. 2016). These genes, amongst others expressed by 'pre-microglia', are associated with synaptic pruning and neural maturation. However, these are unlikely microglial functions in the cortex at E18.5 and single cell sequencing data showed no difference in expression of pre-microglia genes between the cortex and septum with both regions expressing a low number transcripts (Annex Figure 1). This population could therefore be exclusive to the postnatal brain or could be a later stage of microglial differentiation.

Cortical microglia at E18.5 may be in a surveillance and homeostatic phase characteristic of *Tmem119* expression (Bennett et al. 2016; Matcovitch-Natan et al. 2016). This is supported by single cell sequencing data showing increased prevalence of *Tmem119* expression amongst cortical microglia. Further cell behaviour experiments would be required to show whether these homeostatic microglia behave as adult microglia rather than carrying out developmental functions. Time-lapse microscopy experiments for example, could observe either developmental functions or 'resting state' like behaviour. Previous research has found unevenly distributed microglia in the E18.5 cortex which are suggested to be involved in the positioning of cortical inter-neurons (Squarzoni et al. 2014). Perhaps cluster 1 and 2 expression of genes categorised into developmental GO terms assist with this.

Although there were few differences in expression profile, cortical homeostatic populations were not uniform in their expression profile. Increased expression of genes involved in inflammation and decreased expression of developmental genes were detected in cluster 3. This could indicate these cells have entered an 'activated' state, which is less able to carry out developmental functions. The majority of cells in this cluster are from MIA samples. It is not known whether cells remain in an 'activated' state *in vivo* or if experimental manipulation is responsible for this shift.

29.13%, of cortical control cells clustered with predominantly midline sample based clusters. This could indicate that cortical microglia are not homogenously homeostatic. It may be that dissection resulted in small numbers of microglia from the midline region remaining with cortical samples. Such a technical error is supported by *in-situ* hybridisation data finding no

expression of ATM or PAM markers, although metabolic and proliferative clusters would not be detected. Gene expression measured through *in-situ* hybridisation only covers a small area of a thin slice of cortex containing very few cells. Single cell sequencing is therefore more likely to detect less common microglial populations within the cortex. Further experiments across larger portions of the brain, perhaps utilising immunohistochemistry to visualise metabolic or proliferative microglia markers in addition to PAM and ATM markers, would be required to further examine any cortical localisation of these populations.

2.4.5. Conclusion

Results discussed in this chapter demonstrate that developmental septal and glial wedge microglia form dense clusters which differ from all other prenatal microglia populations studied. Although the function of these cells is as yet unknown, similarities in expression profile and morphology with ATM and PAM populations associated with postnatal corpus callosum development provide a good basis for further exploration. Depletion experiments may in future help to confirm the function of these cells. The use of CD11c-targetted toxin regimes developed by Wlodarczyk et al. (2017) for example may be able to specifically deplete septal microglia if utilised prenatally. Subsequent defects in neonatal brain development could then be attributed to this population. Despite the similarity of PAM or ATM to fountain of microglia cells, related clusters identified here did not express elevated levels of this marker meaning that an alternative target will be required.

Chapter 3: Characterising Corpus Callosum associated Hotspot Microglia

3.1. Introduction

3.1.1. Corpus Callosum Microglia Function

Chapter 2 described the transcription profile of microglial populations forming clusters associated with the corpus callosum during prenatal development. However, little is known about the cell biology of microglia in this region. Further characterising corpus callosum associated microglia may help to identify what specific functions these cells are performing and in what way they may be influenced by developmental insults, possibly assisting with the development of treatments. Characterisation of developmental corpus callosum associated microglia was therefore an aim of this chapter.

Septal and glial wedge microglial populations are likely meaningful to embryonic brain development due to the apparent high density of these cells which, as discussed in the introduction, suggests they may be performing a key developmental function. Recent studies have successfully identified a broad range of developmental heterogeneous microglial sub-types (Hammond et al. 2019; Li et al. 2019a; Masuda et al. 2019). However, it is not yet known if microglial heterogeneity in distribution corresponds to microglial heterogeneity in microglial sub-type and function. These key gaps in our understanding also formed a second aim of this chapter.

3.1.2. Chapter Aims and Key Findings

Exploration of corpus-callosum associated microglia cell biology began by uncovering the specific time-point at which the septal hotspot begins to form in the mouse. Immunohistochemical staining of Dectin-1 uncovered the developmental time-course of differentiated microglia within the septum, suggesting roles for these cells in corpus callosum formation before and after birth. Where Dectin-1 is a marker associated with Proliferative region Associated Microglia (PAM). Additional aims involved characterising the birthdate and proliferation rate of corpus callosum associated microglia, as assessed via immunohistochemistry and cell counting. These experiments further differentiated septal microglia from other developmental microglia within the cortex. Similarly, microglial migratory ability differed between septal and cortical cultured explants. Birthdate, proliferation and migration results also hinted at the possibility of a microglial niche within the septum.

3.2. Material and Methods

3.2.1. Animal Husbandry

Animal husbandry was carried out as described in Chapter 2 (section 2.2.1)

3.2.2. BrdU Injection

Intraperitoneal injections were performed on pregnant dams at a specific stage of gestation as defined using methods described in chapter 2 (section 2.2.1). Injections were performed at 50µl per 10g of mouse using a 10mg/ml BrdU sterile PBS solution.

3.2.3. Immunohistochemistry

3.2.3.1. Fixed Frozen Tissue Sample Preparation

Samples were incubated sequentially in 10, 20 and 30% PBS sucrose solution at 4°C until brains sank to the bottom of the container. Samples were then embedded in Optimal Cutting Temperature compound (OCT), frozen with dry ice and kept at -80°C until sectioning. Frozen brain samples were sectioned coronally in 20µm slices using a Leica cryostat and corpus callosum slices fixed onto Superfrost Plus slides. Slides were then air-dried for approximately 2 hours before storage at -80°C until immunohistochemistry.

3.2.3.2. Fixed Frozen Tissue Immunohistochemistry

Immunohistochemistry was performed as in chapter 2 (section 2.2.2.2) with the exception that DAPI was incubated for 30 seconds rather than 10 minutes.

3.2.3.3. BrdU Immunohistochemistry

For Bromodeoxyuridine (BrdU) immunostained slices only: slices were incubated in PBS Triton 0.3% for 15 minutes followed by HCl at 1N for 10 minutes on ice, HCl at 2N for 10 minutes at room temperature then 20 minutes at 37°C and borate buffer for 12 minutes at room temperature. Slices were washed 3 times for 5 minutes in PBS before immunostaining was performed as described in chapter 2 (section 2.2.2.2).

3.2.4. Explant Culture

CX3CR1-GFP embryos were generated through animal husbandry techniques discussed in chapter 2 (section 2.2.1), with the exception that brains were not fixed. Instead of fixation, brain samples were immediately embedded in liquid low melting point 3% agarose PBS solution. Brains were then sliced using a Leica vibratome at 300µm in ice cold Krebs solution perfused with CO_2.

Corpus callosum slices were collected in sterile filtered HEPES medium and transferred onto polycarbonate culture membranes in culture dishes containing NTIC medium (Neurobasal containing 50µl penstrep, 1ml B-27 supplement, 500µl 50% Glucose, 500µl glutamine, 50µl N-acetyl cysteine, 25µl insulin, 100µl apo-transferrin, 50µl sodium selenite, 50µl human TGF-β2, 50µl murine IL-34, and 50µl ovine wool cholesterol – modified from Bohlen et al. (2017)) and incubated for 1 hour (37°C, 5% CO_2). Slices were then dissected, transplanted onto fresh polycarbonate culture membranes and incubated in 1 ml NTIC medium for 2 days before fixation in 4% PFA. Immunohistochemistry was carried out as has been described in chapter 2 (section 2.2.2.2).

3.2.5. Time-lapse Slice Culture

Brains were dissected from P0 CX3CR1-GFP following animal husbandry techniques described in the explant culture section (section 3.2.4). This same protocol was followed up until corpus callosum slices were collected. In this method, slices were collected in sterile filtered Krebs at 4°C before being mounted onto organotypic inserts in migration media (Neurobasal medium containing 2 mM L-glutamine, B27 supplement, 0.5% penicillin-streptomycin) and incubating for an hour at 37°C with 5% CO_2. Slices were then taken for imaging or incubated for up to 24 hours before imaging.

3.2.6. Microscopy and Image Analysis

3.2.6.1. Microglia Dectin-1 Expression

Slides were imaged using a Leica epifluorescence microscope with x20 lens, collecting a tile-scan across the corpus callosum. Cells were counted manually using the FIJI cell counter plug-in. Results were recorded in Microsoft Excel, which was also used to calculate average cell number per slice, cell density and proportion of cells expressing Dectin-1. GraphPad Prism 9 was used for statistical analysis and graph production.

3.2.6.2. Microglia BrdU and Ki-67 Labelling

Cell counting was performed as described in chapter 2 (section 2.2.4.1), with the exception that either BrdU or Ki-67 labelled cells were counted in addition to Iba1 labelled cells. GraphPad Prism 9 was used for statistical analysis and graph production.

3.2.6.3. Explant Migration

Explants were imaged using an inverted Leica epifluorescence microscope with x10 lens. Images were analysed using FIJI. Circles increasing in diameter by an arbitrary set value were drawn around each explant. The number of cells within each circle were counted and recorded in Microsoft Excel. GraphPad Prism 9 was used for statistical analysis and graph production.

3.2.6.4. Time-lapse bi-photon microscopy and Imaris image analysis

Brain slices were transferred on to a glass coverslip and held down onto the bi-photon microscope chamber using a nylon thread. Imaging was performed by collecting a z-stack, spanning 72 µm with serial optical sections every 8 µm, recorded every 10 min for 5 to 7 hours. During imaging, slices were kept at 37°C with 5% CO_2 and a constant flow of fresh migration media.

Image analysis was performed using Imaris. The original time-lapse is shown in the first third of Figure 18. Individual GFP expressing microglia were identified automatically using Imaris. The top 25% of those that migrated furthest and those that migrated fastest were labelled as mobile microglia and selected for further analysis, in order to eliminate any that cells that moved due to brain slice drift over time. All identified individual microglia can be seen in green in the second third of the Figure 18, with selected mobile cell paths highlighted in red. The glial wedge region is seen highlighted in white in the final third of Figure 18. Distance over time measurements were taken from the corner of the image contained within the glial wedge. These measurements were used to assess the direction of travel of mobile cells to produce data analysed in section 3.3.3.2.

Figure 18: A proportion of microglia were mobile in the postnatal corpus callosum region.

Time-lapse video taken from P0 CX3CR1-GFP brain slices, as shown in the first third, with subsequent Imaris analysis shown in the remainder of the video. Individual microglia are highlighted in green in the second third of the video with mobile microglia, controlling for brain slice drift, highlighted with red movement paths. The glial wedge region is highlighted in white in the final third of the video.

3.1.1. Statistical Analysis

Statistical analysis was performed as in chapter 2 (section 2.2.6).

3.1.1.1. Replicates

Replicates were defined for cell counting experiments as described previously in section 2.2.6.1.

Replicate definitions differed slightly regarding migration experiments. The total of all cells counted from at least 10 explants taken from the brain slices of one brain was used as an individual replicate for calculations shown in figure 22. Whereas for time-lapse data shown in figure 23, each mobile microglia, as defined in section 3.2.6.4, was defined as a replicate.

3.3. Results

3.3.1. Septal and Glial Wedge Dectin-1 Expression

An important feature of developmental microglia populations is the timepoints at which they are present. With this in mind, immunohistochemistry was performed labelling Dectin-1 and Iba1 as markers for PAM/ATM or microglia respectively. Analysis was focused on the midline region, where septal microglia are found, and the cortex, which acted as a reference population for comparison. Timepoints were selected at various stages during corpus callosum development: prior to midline fusion at E14.5; as axons cross the midline at E16.5; after formation and axon midline crossing at E18.5; during myelination at P7 (Shen et al. 2006).

3.3.1.1. Corpus Callosum Hotspot Formation

As covered previously the time-window during which microglial density shifts is hypothesised to be a key determinant of the effect on brain development. Establishing the as yet unknown time of formation and dissipation of septal and glial wedge hotspots was therefore an important objective explored through this set of immunohistochemistry.

Over the developmental time course measured, septal and glial wedge microglia localisation varies markedly. At E14.5 the septal region is yet to form as midline fusion has not yet occurred. As visible in Figure 19A and E, septal and glial wedge populations were not present as distinct populations at E14.5. By E16.5 Iba1 expressing microglia began to cluster into a 0.00045 cells per μm^2 dense hotspot within the septum (Figure 19M and F). By contrast, E16.5 glial wedge microglia were more diffuse at only 0.00013 cells per μm^2 and not yet a defined cluster, as shown in Figure 19F.

Later in development, at E18.5, a significantly more ($p = 0.0006$) dense cluster of microglia was identified in the glial wedges, visible in Figure 19I and N, where 0.00065 cells per μm^2 was recorded for this region. The septal cluster of microglia remained 0.0005 cells per μm^2 dense at E18.5 despite the expansion in the size of this region, visible when comparing Figure 19B and C. This high density of $Iba1^+$ cells within the septum remained postnatally (Figure 19N and K) whereas glial wedge microglia appear to migrate dorsally. The glial wedge itself has been shown to undergo a transition into a less wedge shaped ‘flatter’

structure consisting more of astrocytes than radial glia postnatally (Shu et al. 2003a). Figure 19K$_1$ highlights the Iba1 cells which appeared in focal clusters in the corpus callosum. The presence of microglial hotspots in the corpus callosum postnatally mirrors previous reports indicating 'fountain of microglia' cells (Hagemeyer et al. 2017; Staszewski and Hagemeyer 2019). The continued presence of dense microglial hotspots through to P7 suggests a developmental function of these cells after birth.

3.3.1.2. Dectin-1 Expression across Neurodevelopment

In addition to establishing the timecourse of microglial hotspot clustering, understanding when these cells begin to express ATM or PAM like markers could help to identify the role these cells are performing depending on those required during various stages of corpus callosum formation. Labelling Dectin-1 alongside microglial marker Iba1 was carried out to explore this, with replicates as the average of 2-4 slices from the rostral/fornix region of an individual brain.

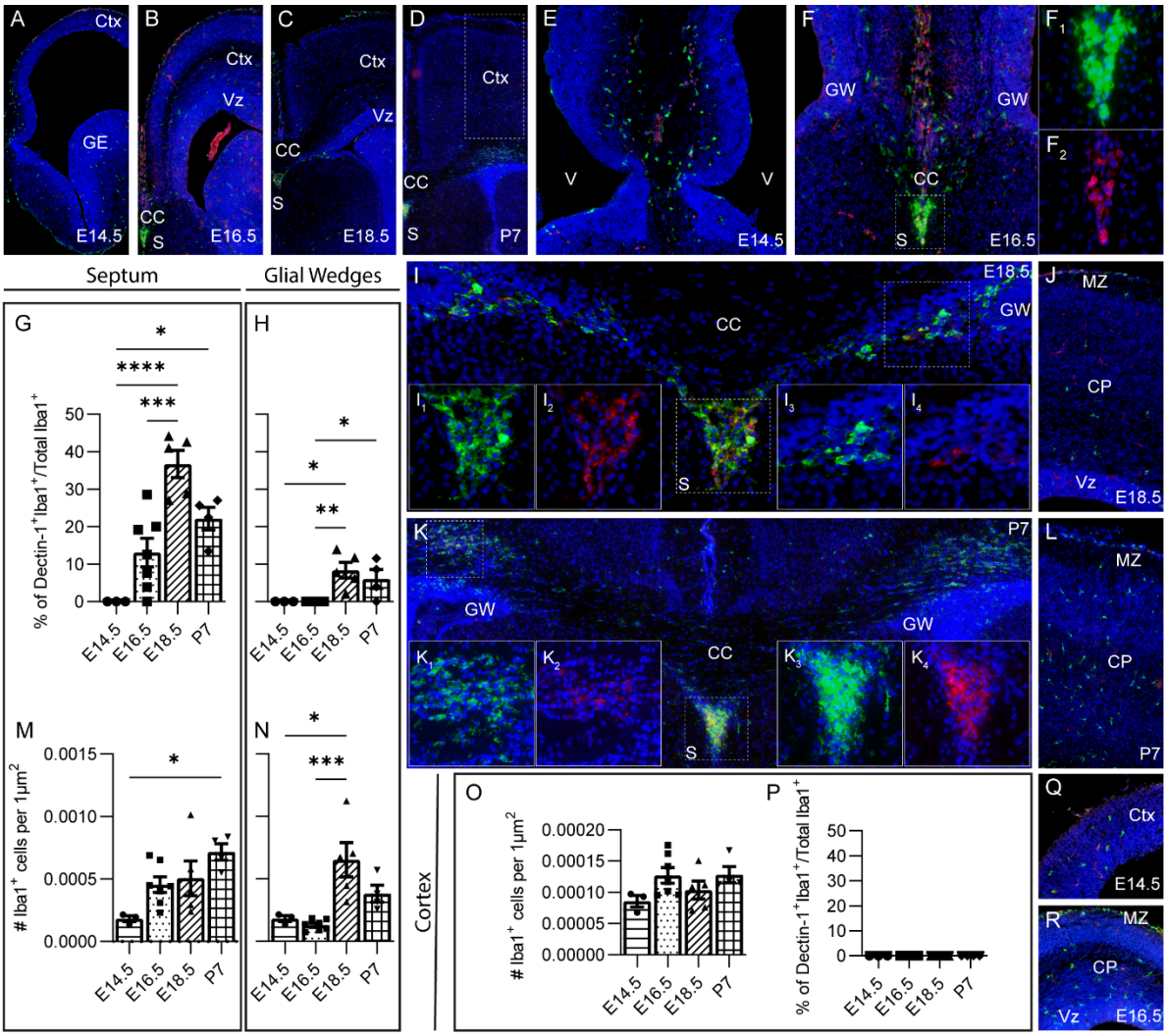

Figure 19: Microglial Dectin-1 expression peaks at E18.5 and extends postnatally. **A-D)** Fluorescence microscope images of E14.5, E16.5, E18.5 and P7 half brain slices with IBA1 and Dectin-1 immuno-labelling displayed in green and red respectively. Areas of interest are labelled and focused on throughout the figure**. E, F, I, K)** Images of the midline/corpus callosum region from E14.5, E16.5, E18.5 and P7 brains immuno-labelled for IBA1 (green) and Dectin-1 (red). F_1 and F_2 are magnified septal region F displaying either IBA1 (green) or Dectin-1 (red) respectively. I_1, I_2, I_3 and I_4 are magnified septal or glial wedge regions from I displaying either IBA1 (green) or Dectin-1 (red). K_1, K_2, K_3 and K_4 are magnified septal or glial wedge regions from K displaying either IBA1 (green) or Dectin-1 (red). **G, H, P)** Mean (+/- SEM) percentage of Dectin-1$^+$Iba1$^+$ cells as a proportion of total Iba1$^+$ cells at E14.5, E16.5, E18.5 and P7 in the septum, glial wedges or cortex (One-way ANOVA (G: $F = 14.88$, $p < 0.0001$, H: $F = 8.129$, $p = 0.0019$), Tukey-Kramer post-hoc test, **** = $p < 0.0001$, *** = $p < 0.001$, ** = $p < 0.01$, * = $p < 0.05$). **J, L, Q, R)** Images of the cortex region from E18.5, P7, E14.5 or E16.5 brains with immuno-labelled Iba1 in green and Dectin-1 in red. **M-O)** Mean (+/- SEM) number of Iba1$^+$ cells per μm^2 of brain region at E14.5, E16.5, E18.5 and P7 in the septum, glial wedges or cortex (One-way ANOVA (M: $F = 4.073$, $p = 0.0266$, N: $F = 9.715$, $p = 0.0008$) Tukey-Kramer post-hoc test, **** = $p < 0.0001$, *** = $p < 0.001$, ** = $p < 0.01$, * = $p < 0.05$). E14.5 – n=3; E16.5 – n=7; E18.5 – n=5; P7 – n=4; *CC – Corpus Callosum; CP – Cortical Plate; Ctx – Cortex; GE – Ganglionic Eminence; GW – Glial Wedge; MZ – Marginal Zone; S – Septum; V – Ventricle; Vz – Ventricular Zone.*

Mean proportion of Dectin-1 expressing microglia peaks with 36.7% of Iba1$^+$ cells at E18.5 in the septum (Figure 19G) and 8.4% of Iba1$^+$ cells in the glial wedges (Figure 19H). This was a significantly higher level than prior timepoints in both the septum ($p < 0.0001$ E14.5, $p = 0.0009$ E16.5) and glial wedges ($p = 0.0101$ E14.5, $p = 0.0006$ E16.5). Fewer Iba1$^+$ cells express Dectin-1 at P7 in the septum (22.1%) and glial wedges (6.0%), although not significantly. This pattern of expression suggests PAM/ATM-like cells may be more relevant to development at the end of the prenatal period or perhaps have begun to transition into another phenotype post-natally. Alternatively, Dectin-1 expressing cells may be migrating from this region at E18.5 to perform developmental functions postnatally or perhaps downregulate expression of Dectin-1, as will be discussed later.

Glial wedge and septal microglia share similarities in pattern of Dectin-1 expression. However, this expression begins sooner within the septum, being detected at E16.5 within the septum alone. Peak proportion of Dectin-1 expression is also 28.3% higher at E18.5 in the septum than the glial wedges. Such differences may indicate important differences between these populations.

Both septal and glial wedge Iba1^{+} cells are in complete contrast to cortical microglia which do not express Dectin-1 at any of the timepoints measured. Iba1 density also appears remarkably consistent at around 0.00010, less dense than the E16.5 or E18.5 septum by a factor of 5. This clearly highlights the differences between these two regions.

Results shown in this section continue to differentiate septal microglia from other developmental microglia populations within the cortex. Additionally, the presence of ATM or PAM like cells at P7 suggests a role for this cell type before and after birth.

3.3.2. Microglial Cell Division in Corpus Callosum Hotspots

Results so far have revealed the presence of a dense microglial hotspot that differs from many other microglial populations across development. Understanding the birthdate of septal microglia could help to uncover the function of these cells as well as provide tools to manipulate the septal hotspot through timed microglial depletion. Analysis of microglial proliferation after septum formation might also provide information on the function of septal microglia. For example, one would also expect this microglial population to be born at a different timepoint to cortical microglia where they are expected to perform a different function. If supporting hemisphere fusion, one might expect microglia to be born shortly before or during this process around E15 in mouse. A later birth date could indicate involvement in the guidance of pioneer axons or correct dorso-ventral positioning of axons within the corpus callosum. Proliferation following corpus callosum formation could indicate the presence of a dense niche providing microglia for the development of other structures. Immunohistochemistry experiments were therefore carried out in order to identify septal microglia birth date, through BrdU injection and immuno-labelling, and proliferation rate, with Ki-67 staining.

3.3.2.1. Birthdate of Septal and Glial Wedge Microglia

BrdU incorporates into the DNA of cells during the s-phase of mitosis, replacing thymidine (Perelson et al. 2000). Dividing cells can then be identified through immunohistochemical labelling. Pregnant dams were therefore injected with BrdU at various timepoints throughout neurodevelopment in order to label dividing microglia. 2-3 rostral/fornix region brain slices were taken at E18.5, when a dense population of septal microglia can be observed, and averaged to produce one replicate per brain from two different litters.

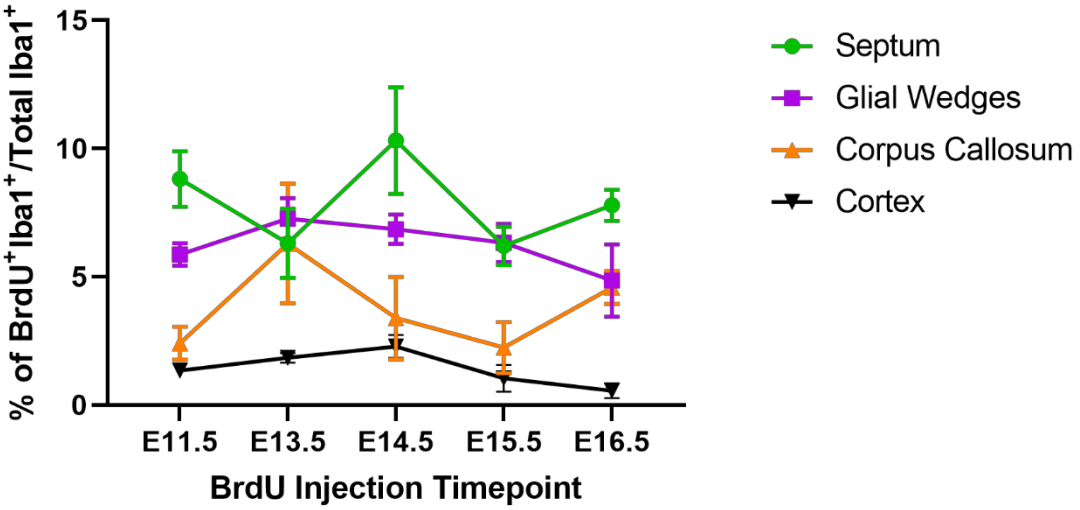

Figure 20: Septal and glial wedge microglia birthdate differs from cortical microglia. Mean (+/- SEM) percentage of $BrdU^+Iba1^+$ cells as a proportion of total $Iba1^+$ cells at E18.5 when BrdU was injected at E11.5, E13.5, E14.5, E15.5 or E16.5 - n=3 for each.

Microglia have contrasting birth date patterns in different regions of the developing brain as shown in Figure 20. These differences in microglial birthdates were significant (Two-way ANOVA, $p < 0.0001$, $F = 35.84$) with region of the brain accounting for 62.1% of variation in proportion of BrdU labelled Iba1 cells. Specifically, proportion of BrdU labelled Iba1 cells within the glial wedges and septum significantly differed from those within the cortex across all BrdU injection timepoints (Tukey's multiple comparisons post-hoc test, $p = 0.0001 \leq 0.316$). Septal, glial wedge and cortical mean percentage of BrdU labelled Iba1 cells varied around 7.91, 6.18 and 1.41 respectively. Proportion of BrdU labelled corpus callosum iba1 cells averaged between these two groups at 3.79% across all timepoints. Comparing this with other developmental populations, a population of GABAergic interneurons varied in BrdU labelling rate between 60.6% - 14.2% in the prenatal mouse brain (Inta et al. 2008).

Approximately 25% of a subset of dopaminergic neurons were $BrdU^+$ in the E12 mouse before declining below 5% from E13 onwards (Galliano et al. 2018).
BrdU injection timepoint only accounted for 4.3% of variation in proportion of BrdU labelled Iba1 cells and their interaction, 10.5% of variation. The low BrdU injection timepoint contribution towards variation, is visible in Figure 20 in the fairly consistent percentages of cells labelled with BrdU across timepoints injected. This is particularly the case for cortical microglia in a trend supported by previous literature describing consistent microglial proliferation rates within the cortex (Swinnen et al. 2013). Similarly, mean proportion of BrdU labelled glial wedge Iba1 cells varied by only 2.7%. Mean proportion of BrdU labelled Iba1 cells varied slightly more across timepoints within the septum and corpus callosum at 4% and 4.1% respectively.

Data presented here suggests a relatively consistent birth rate of new microglia cells across all regions measured with lower birth rate in the cortex than midline regions. However, corpus callosum and septal measurements were more variable both across and within time points than glial wedge and cortex measurements.

3.3.2.2. Proliferation Rate of Septal and Glial Wedge Microglia

Some work has been carried out to uncover the proliferation rate of microglia within the cortex and pia, with a decreasing proportion of microglia labelled with Ki-67 from E11.5 to E17.5 in the mouse despite a stable low total number of Ki-67 labelled microglia across this time-window (Swinnen et al. 2013). However, the proliferation rate of other developmental microglial populations, such as those within the septal hotspot, is unknown. In addition to shedding light on the function of septal microglia, differences in proliferation rate would further highlight the heterogeneity of developmental microglia.

As covered in the introduction, CD68 is a commonly used marker of microglia. There was a mean 23.81% and 29.56% of $CD68^+$ cells labelled with Ki-67 in the septum and glial wedges respectively. Figure 21 shows these values were significantly higher than within the cortex where only 14.79% of $CD68^+$ were labelled with Ki-67. In a similar trend to the birthdate patterns displayed in figure 5, septal and glial wedge microglia were comparable in Ki-67 measured proliferation rate but both populations differed from those within the cortex.

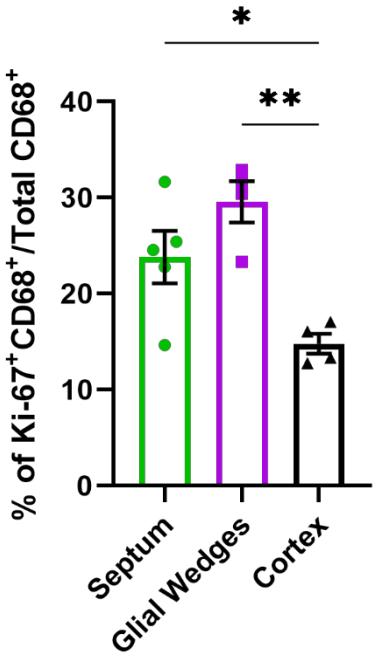

Figure 21: Septal and glial wedge microglia proliferation rate differs from cortical microglia at E16.5.

Mean (+/- SEM) percentage of Ki-67^{+}CD68^{+} cells as a proportion of total CD68^{+} cells at E16.5. (One-way ANOVA, $F = 10.20$, $p = 0.0039$, Tukey-Kramer post-hoc test, ** = $p = 0.0031$, * = $p = 0.040$) Septum/Glial Wedge – n=5; Cortex – n =4.

Taken together proliferation analysis and birth dating patterns revealed similarities between septal and glial wedge microglia. Both populations differed from cortical microglia. These findings echo previous results also showing similarities between the glial wedges and septum which differ from cortical microglia. Further comment on how this data relates to microglial function will be presented in the discussion.

3.3.3. Corpus Callosum Hotspot Microglia Migration

3.3.3.1. Septal Microglia Migration

A further important feature of microglial cell biology is their ability to migrate. Understanding the capacity of septal microglial to migrate could help provide insight into their function and site of action. Comparing this population to cortical microglia provides further features by which to differentiate these heterogeneous populations. Initial migration analysis experiments involved taking either septal or cortical explants from CX3CR1-GFP brain slices at E17.5. This timepoint was selected as a dense population of microglia can be found at this time. Explants were then cultured for 4 days and stained for GFP and TuJ1 - expressed by all CNS neurons. Areas of increasing distance from the explant were then marked allowing quantification of the number of microglia migrating at different distances from the explant.

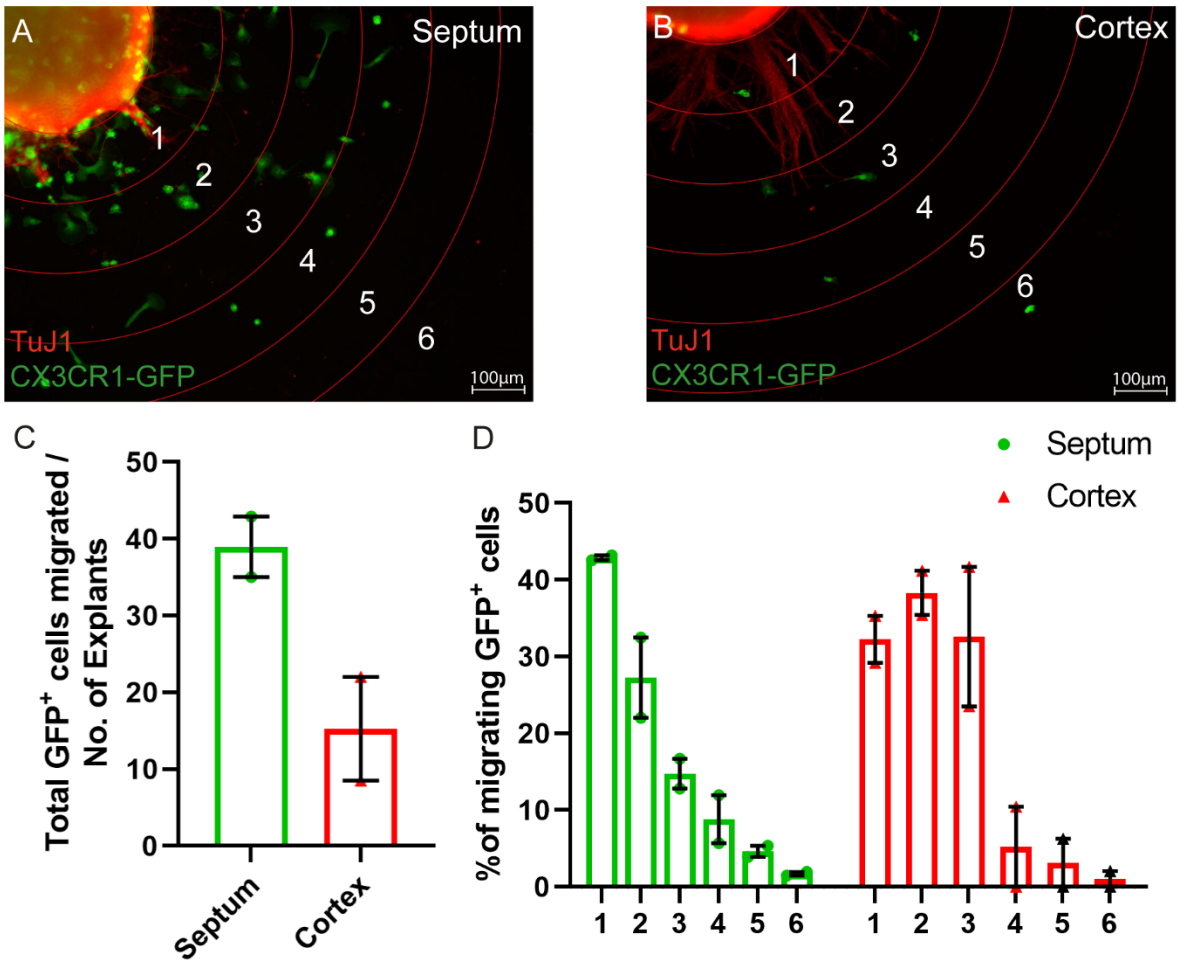

Figure 22: Septal microglial migration differs from cortical microglia.
A,B) Representative fluorescence microscope images of cultured explants immuno-labelled for Tuj1 in red and CX3CR1-GFP in green. Regions surrounding the explant used for quantification are labelled. **C)** Mean (+/- SEM) number of CX3CR1-GFP expressing cells which left the explant during culture, n=2. **D)** Mean (+/- SEM) percentage of CX3CR1-GFP expressing cells counted within each region around the explants, n=2.

The increased density of microglia within explants is reflected in the mean total number of microglia migrating from the explants which is higher in septal explants than cortical explants, at 38.95 and 15.25 cells respectively (Figure 22C). The majority of microglia from septal explants appear to migrate a shorter distance with 70.12% falling within areas 1 and 2 whilst a smaller proportion of microglia reach more distant areas with 6.32% reaching areas 5 and 6 (Figure 22D). Short septal migration distance suggests septal microglia may not reach the majority of the corpus callosum itself but perhaps reach the glial wedges. Cortical microglia migration pattern, is also similarly weighted towards nearer regions with 70.52% falling within areas 1 and 2 whilst 4.2% reach areas 5 and 6.

3.3.3.2. Glial Wedge Microglia Migration

Further experiments aimed at analysing the migration of corpus callosum hotspot microglia were performed to overcome technical limitations of explant experiments and provide further information on direction of travel and destination. Brain slices were taken from the corpus callosum region of early postnatal CX3CR1-GFP mouse brains. The glial wedge region of these slices was imaged via time-lapse bi-photon microscopy to check whether glial wedge hotspot microglia migrate towards the 'fountain of microglia'.

Mobile microglia were analysed as described in the materials and methods. This analysis found that the majority, 68.57% (Figure 23A), of mobile microglia moved towards the glial wedge hotspot. Further analysis showed that there was no clear relationship between distance from the glial wedge hotspot and direction of travel (Figure 23B).

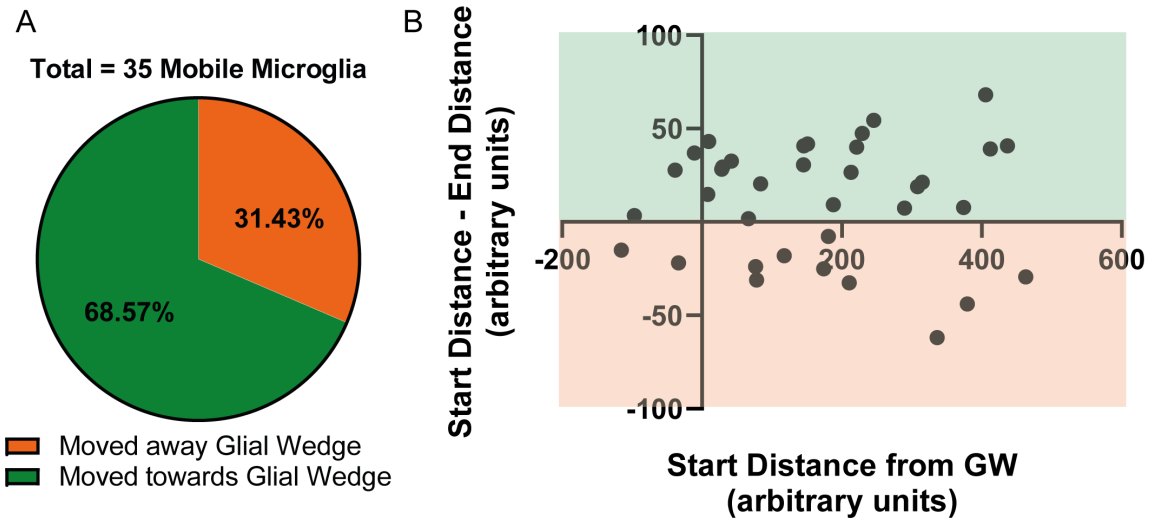

Figure 23: Postnatal microglia move towards glial wedge hotspots.

A) Pie chart showing the proportion of mobile microglia that moved towards or away from the glial wedge hotspot during time-lapse experiment. **B)** Scatter graph showing the relationship between distance form glial wedge hotspot and direction of travel, towards or away from the glial wedge hotspot, n=35.

3.4. Discussion

This chapter further distinguished a population of microglia found within the developing septum from other developmental microglia populations. Protein expression, birthdate pattern, proliferation rate and density measurements all show substantial similarities between developing septal and glial wedge microglia as well as considerable contrast from developmental cortical microglia. Understanding the differentiation time-course of microglia surrounding the corpus callosum, as well as their ability to proliferate, begins to shed light on their possible function.

3.4.1. Cell Biology of Septal and Glial Wedge Hotspot Microglia

Dectin-1 expressing microglia presence mirrors key milestones in formation of the corpus callosum, suggesting septal and glial wedge microglia play some role in the formation of the corpus callosum. Dectin-1 microglia appear at the start of corpus callosum formation as axons cross the midline around E16.5 and continue at least until P14 during corpus callosum myelination (Ozaki and Wahlsten 1992; Li et al. 2019c). Our current understanding of PAM, ATM and fountain of microglia-like cells, primarily localised to postnatal timepoints P4-P15, is that they are involved in oligodendrocyte progenitor survival and phagocytosis (Hagemeyer et al. 2017; Hammond et al. 2019; Li et al. 2019c). However, the prenatal septum and glial wedges are not known to contain particularly dense populations of oligodendrocyte progenitors which are fairly evenly distributed throughout the brain at E18.5 (Zheng et al. 2018). It may be that septal microglia act as a developmental niche providing reserve of this specific microglia subtype for the support of corpus callosum development postnatally. Initial migration experiments do not rule this out, given that at least a small proportion of septal microglia were able to migrate 500µm.

Observed explant migration patterns could reflect the majority of microglia reaching proximal structures such as the glial wedges, which express Dectin-1 at E18.5 only observed within the septum prior to this time-point. Alternatively, experimental limitations may have impacted migration distance. Cultured explants are not exposed to signalling molecules which may be present within the developing brain to guide microglia to their required locations. Microglia are known to respond to a chemoattractants such as ATP and C5a (Miller and Stella 2009). This

protocol also does not reproduce the 3D environment that these microglia are naturally found within. It may be that the high density of microglia increasingly inhibits migration when confined to a smaller 2D environment found within the culture dish. The culture medium provides a further complication in that it is currently unknown what signalling factors are required to maintain developmental microglia in an immature, non-activated state reflective of the in vivo environment. The use of a medium developed for adult microglia may also have influenced migration distance (Bohlen et al. 2017).

Time-lapse experiments in early postnatal brain slices were chosen to uncover whether glial wedge microglia enter travel towards the 'fountain of microglia' region, within the corpus callosum. Results from this experiment showed that the majority of microglia were stationary and most of those that were mobile moved towards the glial wedge hotspot. Further analysis attempted to understand whether microglia within the glial wedge were more likely to migrate towards the corpus callosum than those outside of it. This was found not to be the case as there was no obvious relationship between distance from glial wedge and direction of travel. These results suggest glial wedge hotspot microglia do not travel towards the 'fountain of microglia' within the postnatal corpus callosum. However, although closer to the *in vivo* state than explant experiments, brain slices still have many of the same limitations. Microglia were limited to a 2D environment, microglia may not be exposed to the same signalling molecules as *in vivo* following incubation, and the culture medium used differed from typical brain conditions. Furthermore, it may be that only certain subsets of microglia, such as PAM or ATM-like cells, were preferentially migrating towards the corpus callosum. An alternative model, such as the zebrafish, may be more suitable for these experiments as the translucent skin of these animals allows time-lapse experiments to be performed whilst keeping cells of interest closer to *in vivo* conditions.

High rates of proliferation measured in septal microglia at E16.5 provides a further indication that these cells form a developmental niche. This level of Ki-67 labelling in septal and glial wedge microglia differs from the proportion of microglia labelled with BrdU when injected at E16.5. A mean of 23.81% of septal and 29.56% of glial wedge microglia were labelled with Ki-67 at E16.5 compared to 7.80% of septal and 4.85% of glial wedge microglia labelled with BrdU injected at E16.5. This difference is unlikely to be as a result of the different microglial markers used, CD68 vs Iba1, given that most microglia express both of these markers (Jurga et al. 2020). Although CD68 has been associated with inflammation, septal microglia have an

'activated'-like phenotype similar to ATM which express CD68 (Hammond et al. 2019). One explanation is that Ki-67 labels cells during all active stages of cell division – G1, S, G2 and mitosis, whereas BrdU is only incorporated into cells during S phase (Scholzen and Gerdes 2000; Duque and Rakic 2015). Additionally, some microglia labelled with BrdU in septum at E16.5 may have migrated out of this region by E18.5, when slices were taken for this set of measurements. There was no increase in E16.5 injected BrdU labelled microglia in the glial wedges at E18.5 however there is a slight increase within the corpus callosum, perhaps indicating a small amount of migration here. Whilst initial migration experiments show that septal microglia are mobile, they also suggest microglia are more likely to reach the glial wedges than the corpus callosum. BrdU incorporation has, however, been shown to have some detrimental effects on cell proliferation and migration which may have reduced ability to detect corpus callosum migration (Duque and Rakic 2015).

BrdU birthdating patterns do not suggest a high level of involvement in early corpus callosum development involving fusion of the telencephalic hemispheres. Given that there was only a 4.01% increase in percentage of $BrdU^{+}Iba1^{+}$ cells at E14.5, with high levels of variation for this time point. Given that corpus callosum formation is underway at E16.5 with the migration of axons across the midline, one might expect an increase in the number of microglia born around this time to support this process. The reduction in septal BrdU labelling when injected at E15.5 and E16.5 could indicate that this population do not expand to support axon guidance across the corpus callosum. Alternatively, this reduction in BrdU signal may reflect a highly proliferative microglia population born at E15.5 or earlier. High rates of proliferation in these cells could result in decreased BrdU staining as BrdU signal decreases with each division (Perelson et al. 2000).

3.4.2. Cell Biology of E18.5 Cortical Microglia

An increased proportion of microglia migrated shorter distances from cortical explants. At this stage, cortical microglia begin to evenly distribute throughout the cortex (Swinnen et al. 2013; Squarzoni et al. 2014). One might therefore expect a more even distribution of microglia migration distances. Cortical explants were, however, affected by the same experimental limitations as septal explants. Despite these limitations, cortical migration pattern diverges from septal microglia migration pattern. This is further evidence that cortical and septal microglia are meaningfully different microglial populations

Cortical microglia appear to be born fairly consistently across time-points measured within the cortex. This is a trend supported by previous literature describing consistent numbers of microglia proliferating within the cortex, whilst percentage of proliferating microglia decreased (Swinnen et al. 2013). Cortical microglia had low levels of BrdU labelling when injected at any of the measured time-points. Rather than suggesting that these microglia were not born at any of the time-points measured, it is likely that low level BrdU signal represents a relationship with proliferation rate. As mentioned previously, BrdU signal diminishes with each division (Perelson et al. 2000). Therefore, low BrdU signal may indicate a high number of divisions or a low number of microglia born. For example, it may be that a sub-population of microglia proliferate at high enough rates to reduce BrdU labelling. Previous literature measuring proliferation rate through Ki-67 immunohistochemistry at earlier timepoints supports low numbers of proliferating microglia in the cortex (Swinnen et al. 2013). However, these results do not account for microglia migrating from the pia, where proliferation rates were shown to be slightly higher, or from ventricular regions. Indeed, this same research showed early microglia are primarily located at the pial surface and ventricular regions before populating the entirety of the brain, making identification of microglia which will eventually remain in the cortex difficult.

3.4.3. Conclusion

Results discussed in this chapter further demonstrate that septal and glial wedge microglia differ from cortical microglia. The expression profile and morphology of corpus callosum associated microglia is similar to previously described populations, perhaps suggesting a developmental phagocytosis role for these cells. As described in chapter 1, further experimentation would be required to demonstrate this, for which more genetic tools would be helpful.

Chapter 4: The Effects of Maternal High Fat Diet on Corpus Callosum Development

4.1. Introduction

4.1.1. Maternal Obesity and Neurodevelopmental Disorder

Epidemiological studies have found an association between maternal obesity and a wide variety of neuropsychiatric conditions including: Attention Deficit Hyperactivity Disorder (ADHD); autism spectrum disorders; anxiety; depression and schizophrenia (Schaefer et al. 2000; Van Lieshout et al. 2013; Chen et al. 2014; Rivera et al. 2015b). Defects in white matter structures and hippocampal volume have also been observed in children exposed to maternal obesity (Ou et al. 2015; Verdejo-Román et al. 2019; Alves et al. 2020). Animal studies involving high fat diets have produced comparable behavioural deficits in offspring accompanied by changes in a range of brain structures including the prefrontal cortex, hypothalamus and hippocampus (Niculescu and Lupu 2009b; Buffington et al. 2016; Zhu et al. 2018). The mechanisms behind this association between maternal obesity and behavioural deficits are not yet fully understood.

4.1.2. Mechanisms of Maternal Obesity

Obesity involves the dysregulation of many homeostatic systems; as such there are a variety of different factors which may be responsible for observed defects in brain structures and behavioural outcomes. Given that the developing foetus depends exclusively on maternal circulation for signalling molecules during development, changes to the maternal environment also affect offspring. The immune system is an example of one such system which is biased towards an inflammatory state under obesity (McArdle et al. 2013). Additional soluble signalling molecules such as leptin have been shown to be increased in the offspring of obese mice (Chen et al. 2008). Cytokines and adipokines such as this are able to influence microglial behaviour, either 'priming' them to a more inflammatory state postnatally or outright regulating activation state (Gao et al. 2014; Edlow et al. 2019). Furthermore, maternal high fat diet has been shown to induce microglial activation in offspring (Kang et al. 2014). Disruption to microglial behaviour during development is known to affect development of the forebrain

including the corpus callosum and cortical structures (Pont-Lezica et al. 2014; Squarzoni et al. 2014). Combined, these studies suggest cytokines and adipokines could be involved in mediating a relationship between maternal obesity and altered behaviour of developmental microglia.

In addition to increased levels of inflammatory cytokines, obese women show an altered profile of circulating metabolites, including fatty acids (Tu et al. 2019). Microglia are sensitive to metabolic changes with glycolysis associated with an inflammatory state and fatty acid oxidation or synthesis associated with anti-inflammatory behaviour (Bernier et al. 2020). As covered in the introduction, lipids differ in their immunomodulatory properties. In short, n-6 polyunsaturated fatty acids (PUFAs) produce pro-inflammatory effects and n-3 PUFAs have anti-inflammatory effects (Rey et al. 2019) . Based on this one would expect diets with high n6/n3 ratio to be more inflammatory than those with low n6/n3 ratio (Table 3). Importantly, dietary manipulations of PUFA content induce corresponding modifications in the lipid profile of the developing brain and the lipid membrane of microglia (Sakayori et al. 2016). These findings indicate a potential link between maternal dietary composition and microglial behaviour.

Table 3: High fat diets selected for diet induced obesity studies

Diet	MCD	MHFD	233HF	292HF	260HF
Fat Composition (% of kcal)	13.5%	60% - Lard	60% - Lard	60% - Lard	60% - Butter
N-3 PUFA level	Medium n-3	Low n-3	Low n-3	Low n-3	High n-3
N-6/N-3 PUFA ratio	6.3	13	9.16	9.16	5.33

Cytokines and metabolites are two examples of many factors influenced by obesity and potentially able to affect microglial behaviour. As established in chapter 1, microglia form heterogeneous populations during development, potentially with differing responses to developmental stressors such as maternal obesity. Such differing responses could reflect the wide variety of neurodevelopmental conditions associated with maternal obesity. Based on

findings discussed in chapter 3, septal microglia are suspected to play an important role in corpus callosum formation. Maternal obesity has been associated with defects in white matter tracts in human (Ou et al. 2015; Verdejo-Román et al. 2019). As the largest white matter tract in the brain, the corpus callosum is likely to be involved white matter associated abnormalities resulting from maternal obesity. A key aim was therefore to investigate the role of septal microglia in maternal obesity induced defects within the corpus callosum.

4.1.3. Chapter Aims and Key Findings

In order to investigate any relationship between maternal obesity and alterations in corpus callosum or septal microglia development a model system first had to be established, forming the initial aim of this project. Following on from the research presented in chapter 3, CD1 mice were selected for *in* vivo experiments. High fat diet was selected as a commonly used method to induce obesity in mice, which is more comparable to the human condition than genetic models (Christians et al. 2019). Since evidence supports the hypothesis that maternal dietary n6/n3 ratio may influence microglial behaviour; high fat diets of differing lipid composition were selected (**Table 3: High fat diets selected for diet induced obesity studies**). Establishing said model for maternal obesity proved challenging with inconsistent variation in maternal and foetal measurements across cohorts. Further aims involving characterisation of expected corpus callosum and microglial hotspot changes via immunohistochemistry revealed no impact of diet on these developmental features. Perhaps reflecting issues with the establishment of a model for maternal obesity.

4.2. Materials and Methods

4.2.1. High Fat Diet Feeding

CD1 female mice (6-8 weeks, Cardiff University) were randomly assigned into feeding groups in all 3 cohorts. Differences between diets are summarised in Table 3 and Table 4. In brief, cohort 1: maternal control diet (MCD) received a low fat diet (13.5% of calories from fat, LabDiet, 5001) and maternal high fat diet (MHFD) receiving a lard based high fat diet (60% calories from fat, Envigo, TD.06414). Cohort 2: MCD receiving a low fat diet (13.5% of calories from fat, LabDiet, 5001); 233HF receiving a lard based high fat diet (60% calories from fat, SafeDiets, 233HF); and 260HF receiving a butter based high fat diet (60% calories from fat, SafeDiets, 260HF). Cohort 3: MCD receiving a low fat diet (13.5% of calories from fat, LabDiet, 5001); 292HF receiving a lard based high fat diet (60% calories from fat, SafeDiets, 233HF); and 260HF receiving a butter based high fat diet (60% calories from fat, SafeDiets, 260HF). Mice had access *ad libitum* to each respective diet.

All other aspects of animal husbandry were as described in chapter 2 (section 2.2.1) with the exception that fat pads were also dissected, weighed and stored at -20°C. Blood samples were taken from each dam and all foetuses together then stored at -80°C. Notably, all dams had access to control diet in male mouse cages overnight during breeding. Body weight was measured at acclimatisation, 8 weeks on diet and sacrifice for cohort 1, every week for cohort 2 and twice per week for cohort 3. GraphPad Prism 9 was used for statistical analysis of weight differences and graph production.

4.2.2. Microscopy and Image Analysis

4.2.2.1. Foetal Measurements

Foetal brains at E18.5 were weighed following dissection. Cortices were imaged via digital camera on a light box. Cortex area was measured using FIJI by drawing around 1 cortex per brain, measuring in pixels and converting to mm^2 in Microsoft Excel. GraphPad Prism 9 was used for statistical analysis and graph production.

4.2.2.2. Corpus Callosum Measurements

Immunohistochemistry was performed as described in chapter 2 (section 2.2.2). Width of L1CAM and Nrp1 was measured using FIJI to draw a straight line at the midline from induseum griseum to the ventral extreme of marker expression. This was measured in pixels and converting to mm in Microsoft Excel. GraphPad Prism 9 was used for statistical analysis and graph production.

4.2.2.3. BrdU Cell Counting

For BrdU labelling data, immunohistochemistry was performed on vibrosliced brain samples as described in chapter 3 (section 3.2.2.3), alongside BrdU Injections as described in chapter 3 (section 3.2.1) and analysis as described in chapter 3 (section 3.2.4.2).

4.2.2.4. CPT1a Cell Counting

CPT1a expression data was produced using vibrosliced brain slices as described in chapter 2 (section 2.2.2) with analysis as described in chapter 3 (section 3.2.4.2) replacing BrdU or Ki-67 with CPT1a.

4.2.2.5. Dectin-1 and Spp1 Cell Counting

Dectin-1 and Spp1 expression data was produced using cryosliced brain slices as described in chapter 3 (section 3.2.2.2) with analysis as described in chapter 3 (section 3.2.4.1) adding Spp1 cell counting.

4.2.3. Statistical Analysis

Statistical analysis was performed as in chapter 2 (section 2.2.6).

4.2.3.1. Replicates

Replicates were defined for cell counting experiments as described previously in section 2.2.6.1.

For experiments involving the measurement of dams such as figure 24, each dam was considered a replicate. For experiments involving the measurement of number of embryos per litter such as figure 25, each litter was considered a replicate. For experiments involving the measurement of number of embryos such as figure 26, each embryo was considered a replicate.

4.3. Results

4.3.1. Establishing a Method for Diet Induced Obesity

Previous studies have successfully induced obesity by allowing mice *ad libitum* access to high fat diet for a variety of time windows, 8 weeks is frequently used (De Wilde et al. 2009; Christians et al. 2019). Although the majority of these studies were performed on C57BL/6 mice, the large litters often produced by CD1 mice make them an ideal strain for the developmental biology allowing fewer adult mice to be used. High fat diet consisting of 60% fat macronutrient levels has been shown to induce obesity in CD1 mice (Carpenter et al. 2013). In this project, initial studies were carried out using Envigo maternal high fat diet, hereafter referred to as MHFD, containing 60% of diet from fat (Envigo, TD.06414) with follow up cohorts using alternative diets 233HF, 292HF and 260HF (SafeDiets) for comparison against a control diet composed of 13.5% of calories from fat (LabDiet, 5001). These diets also differed in their polyunsaturated fatty acid (PUFA) level, as shown in Table 3. 292HF was an updated version of 233HF, differing only slightly in mineral levels discussed later alongside Table 4 and Table 5.

Unlike in human where Body Mass Index (BMI) is used to establish the onset of obesity, there is a lack of consensus on specific markers by which to determine obesity in rodents. Whilst some studies use various scanning techniques, tests for insulin resistance and lipid analysis, such techniques involve restraint and blood collection, adding stressors which may impact offspring (Montgomery et al. 2013; de Moura e Dias et al. 2021). A commonly used parameter is a weight difference of 15% above control (de Moura e Dias et al. 2021). A significant increase in weight relative to controls is also used to determine obesity (Carpenter et al. 2013). Both of these measures were considered in studies presented here.

4.3.2. High Fat Diet Cohort 1

4.3.2.1. Cohort 1 Dam Measurements

Female mice in cohort 1 were weighed after 8 weeks of *ad libitum* access to MHFD. At this point the anticipated significant difference (Unpaired t-test: $t(13)=3.025$, $p = 0.0098$) in dam weight between groups was observed, with MHFD mice weighing on average 13.3g more than their control diet counterparts (Figure 24A). These mice then underwent timed matings with control diet fed CD1 males. Due to technical limitations, this breeding phase began 13

weeks from the onset of MHFD feeding. Elevated MHFD group weight continued to breeding phase with a slight increase in average weight difference between groups but also an increase in MHFD dam weight variance. Weight measurements were again taken prior to culling of pregnant dams and collection of foetuses 18 days after impregnation – labelled sacrifice phase in Figure 24. After 18 days gestation, MHFD mean body weight was within 1.11g of control mice and no longer significantly heavier. Despite differences in body mass not being maintained throughout pregnancy, MHFD dams had on average a 2.18 percentage points higher proportion of weight attributed to fat pad weight at sacrifice (Figure 24B). This difference was not significant (Unpaired t-test: t(5)=2.280, p = 0.0715) although MHFD fat weight percentage was significantly more variable than MCD dams as measured by F-test of equality of variances (F test: F= 105.3, p=0.0188). At 82g, one dam was over 15% heavier than mean control weight at sacrifice, indicating obesity.

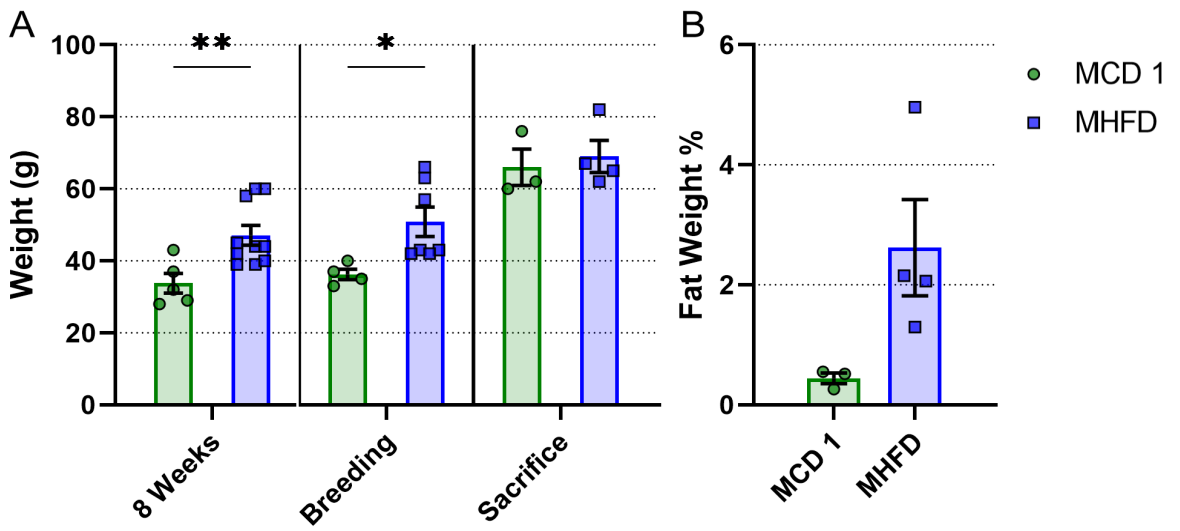

Figure 24: MHFD mice were significantly heavier than control mice until sacrifice. **A)** Mean (+/- SEM) weight of dams fed control diet (green) or high fat diet (blue) at 8 weeks after feeding start date (Unpaired t-test: t(13) = 3.025, p = 0.0098); at start of breeding (Unpaired t-test: t(9) = 2.603, p = 0.0286); and at sacrifice. 8 Weeks – MCD: n=5, MHFD – n=10; Breeding – MCD: n=4, MHFD – n=7; Sacrifice – MCD: n=3, MHFD: n=4. **B)** Mean (+/- SEM) dam fat weight as a proportion of total body weight. MCD: n=3, MHFD: n=4. *MCD 1 – Maternal Control Diet cohort 1; MHFD – Maternal High Fat Diet.*

4.3.2.2. Cohort 1 Foetal Gross Measurements

Having established an effect of high fat diet on pregnant dams, an important next step was to determine the consequences of these effects on the developing offspring. Counting the litter size and number of necrotic foetuses at E18.5 provides an estimate of the impact of MHFD exposure on foetal survival rate. Smaller litter size has been reported in mouse models of maternal obesity as embryos are increasingly reabsorbed (Luzzo et al. 2012).

Foetal body weight, brain weight and cortex area measurements establish approximate effects on overall development and brain growth respectively. Growth retardation and delayed cortical neurogenesis have been observed in mice exposed to maternal obesity (Luzzo et al. 2012; Rash et al. 2018). However, the effect of maternal high fat diet on body weight is somewhat unsettled with some studies reporting macrosomia - a newborn with an excessive birth weight (Hermann et al. 2010; Christians et al. 2019). Given that alterations in brain and body development are reported under maternal obesity, brain to body weight ratio is a useful tool for measuring neurodevelopmental abnormalities in relation to body development. Foetal brain, body and litter size measurements were therefore taken as initial indicators of the impact of high fat diet on offspring.

For cohort 1, average number of foetuses per litter at E18.5 was 14.33 in control diet fed mice and 12.75 in the high fat diet group. Although high fat diet mice had a slightly lower litter size on average this difference was not significant (Unpaired t-test: $t(5) = 1.372$, $p = 0.2284$). The lack of significance was unsurprising given that higher control group average litter size is skewed by 1 large litter of 17. This eliminates the possibility that equivalent overall body mass between groups at sacrifice (Figure 25A) was due to a reduction in litter size for MHFD dams.

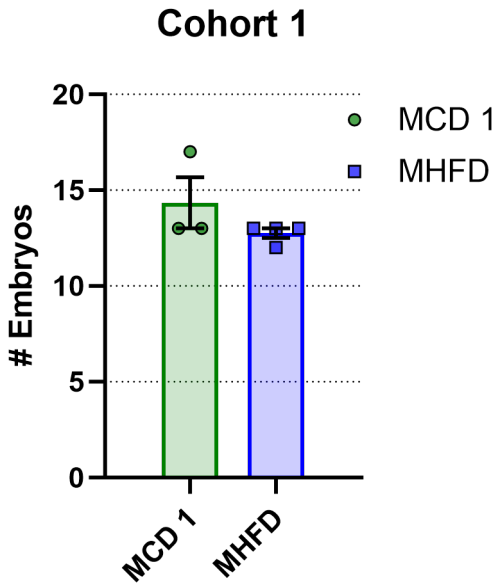

Figure 25: Cohort 1 litter size did not differ between groups.
Mean (+/- SEM) number of E18.5 foetuses per litter. MCD n=3; MHFD n=4. *MCD 1 – Maternal Control Diet cohort 1; MHFD – Maternal High Fat Diet cohort 1; MHFD – Maternal High Fat Diet.*

Body and brain measurements taken for cohort 1 E18.5 foetuses showed no significant differences across any of the measures taken (Figure 26). Control group body weight average was similar to high fat diet exposed offspring at 1.34g and 1.39g respectively. Average brain weight was even more similar with MCD brain average weight at 0.098g and MHFD average brain weight at 0.099g. Given similarities in these measures, the brain to body weight ratio was also comparable for control and high fat diet groups at 0.075 and 0.077 respectively. Finally, average cortex area for both cohort 1 groups differed by only 0.24mm^2 at 9.62mm^2 for control and 9.86mm^2 for high fat diet foetuses. Combined, these measures show no effect of MHFD exposure on offspring brain or body in-utero development.

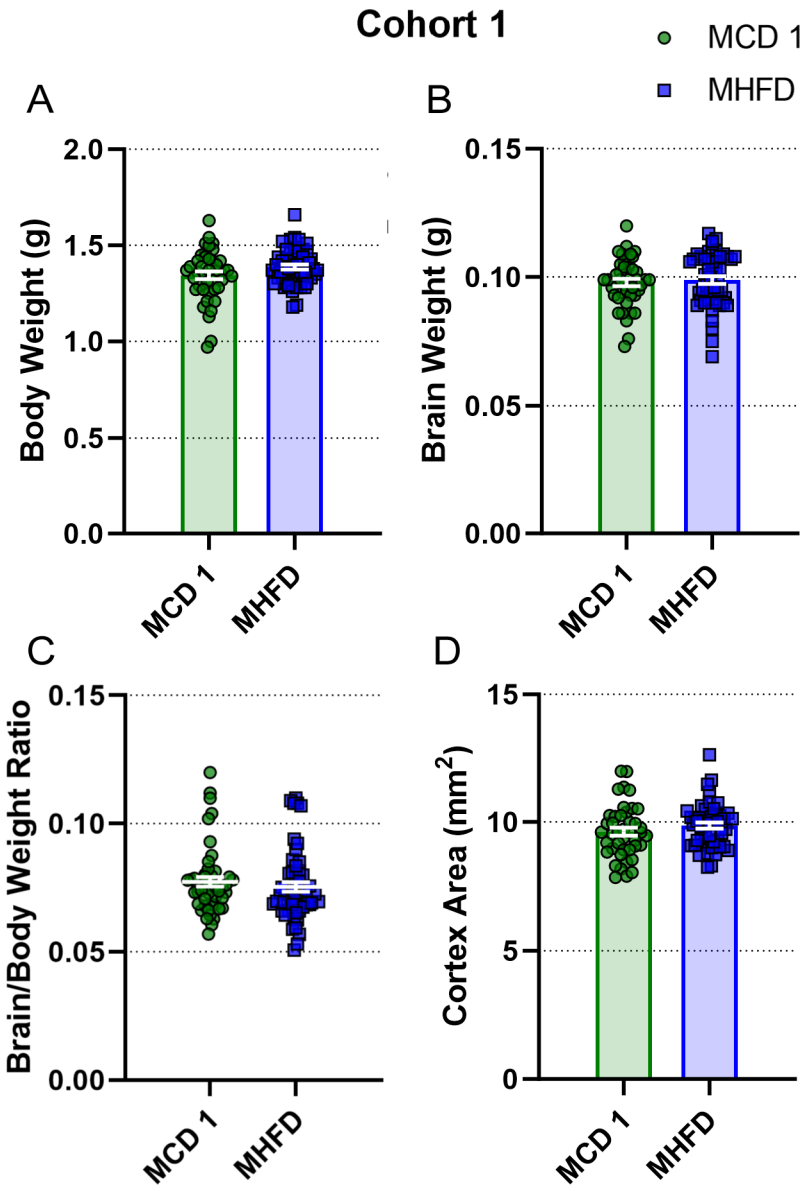

Figure 26: Cohort 1 foetus brain and body measurements do not differ between groups.

A) Mean (+/- SEM) E18.5 foetus body weight in grams. MCD1: n=43; MHFD: n=49. **B)** Mean (+/- SEM) E18.5 foetus brain weight in grams. **C)** Mean (+/- SEM) E18.5 foetus brain to body weight ratio. **D)** Mean (+/- SEM) E18.5 foetus cortex area in mm^2. *MCD 1 – Maternal Control Diet cohort 1; MHFD – Maternal High Fat Diet.*

4.3.2.3. Cohort 1 Corpus Callosum Defasciculation

Preliminary data (not shown) has indicated that embryos from obese dams fed a high fat diet have disorganised corpus callosum axons which become defasciculated, meaning usually tight axon bundles spread further into the entire width of the corpus callosum. Organisation of axons within the corpus callosum is tightly regulated and this organisation affects target innervation, disorganisation could therefore have a detrimental impact on cortical development and offspring health (Zhou et al. 2013a). Although no differences in brain growth were observed between control and MHFD foetuses, more subtle changes in brain structure could occur as a result of maternal high fat diet exposure.

In order to measure corpus callosum defasciculation immunofluorescence staining was carried out targeting L1 cell adhesion molecule (L1CAM) and Neuropillin 1 (Nrp1). L1CAM is a neuronal cell adhesion molecule expressed by all neurones passing through the corpus callosum, meaning that it can be used to measure corpus callosum width (Samatov et al. 2016). The membrane bound co-receptor Nrp1 on the other hand, is expressed only by a subset of corpus callosum axons (Piper et al. 2009). These axons usually pass through the dorsal side of the corpus callosum but extend further ventrally when defasciculated. Since brains were taken from E18.5 embryos, fascicular organisation of axons is visible within the corpus callosum.

The ratio of Nrp1 to L1CAM expression width at the midline was used as a measure of defasciculation. As shown in Figure 27, no significant difference in this ratio between MCD and MHFD embryos was found through unpaired t-tests. Nrp1 expression covered between 53-63% of L1CAM expression for rostral, fornix and caudal regions in the MCD group. In MHFD embryos, Nrp1 was expressed across 45% and 38% of the corpus callosum in rostral and fornix regions respectively before increasing to 70% in caudal slices. Ratio of Nrp1 to L1CAM width is similar across all levels of the corpus callosum showing no signs of defasciculation.

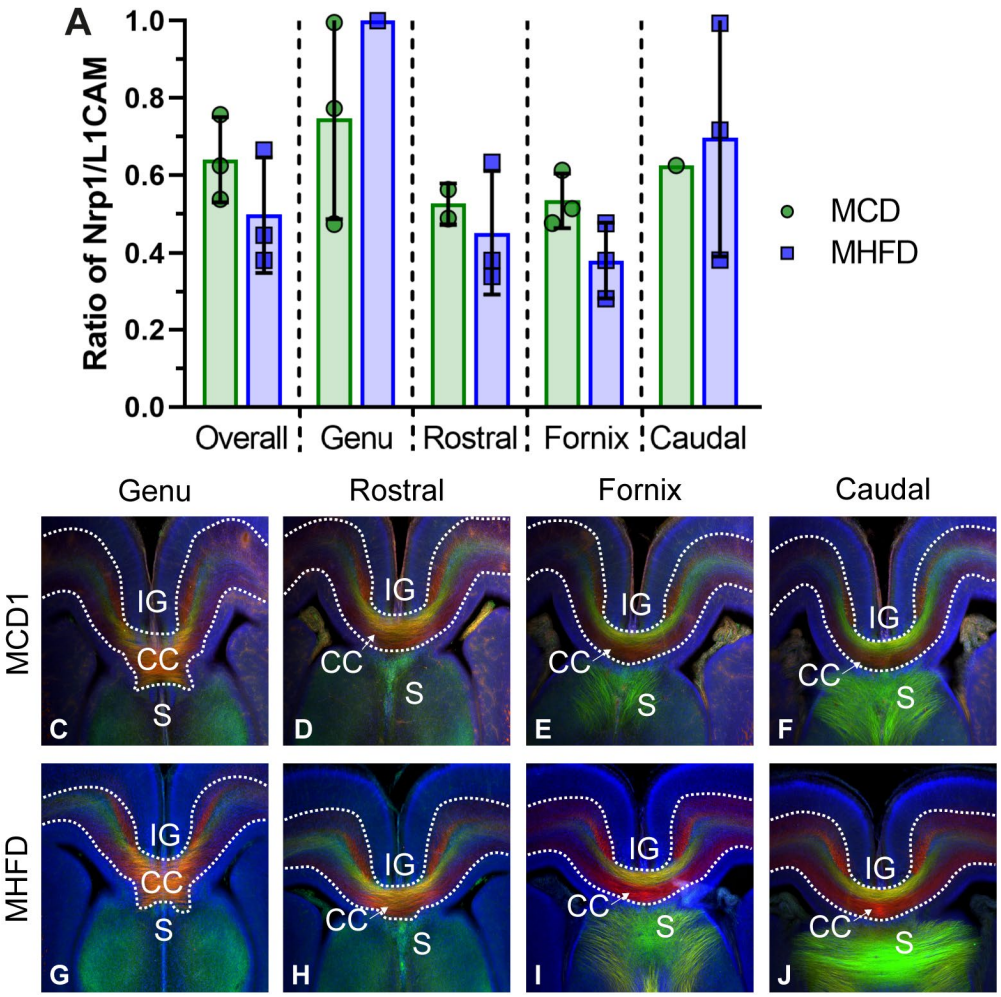

Figure 27: Corpus callosum axons did not become defasciculated when exposed to MHFD.

A) Mean (+/- SEM) ratio of Nrp1/ L1CAM width at E18.5 across all regions of the corpus callosum. n=3 for MCD genu, fornix and MHFD rostral,fornix caudal. n=1 for MHFD genu and MCD Caudal. n=2 for MCD rostral. **B/C)** Representative epifluorescence images of different corpus callosum regions across maternal diet groups. L1CAM labelled in red and Nrp1 labelled in green. *IG – Induseum Griseum; CC – Corpus Callosum; S – Septum.*

To summarise results for cohort 1, MHFD were significantly heavier than controls until E18.5. There were no changes in foetal brain weight, body weight, or cortex area when exposed to MHFD. Finally, there was no evidence of defasciculation within the corpus callosum under MHFD. A second cohort was therefore set up using different high fat diets in an attempt to produce consistent obesity in pregnant dams which may in turn have a stronger effect on foetal development.

4.3.3. High Fat Diet Cohort 2

4.3.3.1. Cohort 2 Dam Measurements

Two diets with differing n-6/n-3 PUFA levels were selected for high fat diet cohort 2. 260HF had higher levels of n-3 fatty acids and lower levels of n-6 fatty acids than control diet, biasing the lipid profile to an 'anti-inflammatory' supporting state. 233HF had higher n-6/n-3 fatty acid ratio providing a 'pro-inflammatory' metabolic profile. As before, mice were given access *ad libitum* to their respective diets and weighed after 8 weeks. Despite similar starting weights: within 1.25g of each other, dams fed either 260HF or 233HF diets did not significantly differ in weight from the control group or each other after 8 weeks (One-way ANOVA (F = 0.6594, p = 0.5349). The breeding phase was therefore delayed until 12 weeks after exposure to high fat diets. Despite high fat diet dams becoming on average 5.82g heavier than controls, this difference did not become significant by the breeding phase (One-way ANOVA (F = 1.715, p = 0.2212). By sacrifice, 260HF weight was 1g higher than control at 72.67g, whilst 292HF weight was 5.67g lower than control at 66g and all dams within 15% of control (Figure 28A).

Fat weight proportions, however, did differ significantly with 260HF dam fat weight 3.32 percentage points higher than control (One-way ANOVA (F = 27.67, p = 0.0009), Tukey-Kramer post-hoc test p = 0.0007) and 233HF dam fat weight 1.75 percentage points higher than control (One-way ANOVA (F = 27.67, p = 0.0009), Tukey-Kramer post-hoc test p = 0.0182). Interestingly, 260HF fed dams had a significantly higher fat proportion than 233HF fed dams (One-way ANOVA (F = 27.67, p = 0.0009), Tukey-Kramer post-hoc test p = 0.0293). More so than cohort 1, such drastic differences in fat weight as a proportion of body weight suggest more severely altered metabolism in 260HF dams than 233HF, which also appears disrupted relative to control mice. In contrast to cohort 1, high fat diet mice were not significantly heavier than control at any time point. Therefore, any disruption to foetal development cannot be considered as a result of obesity but due to high fat diet exposure alone.

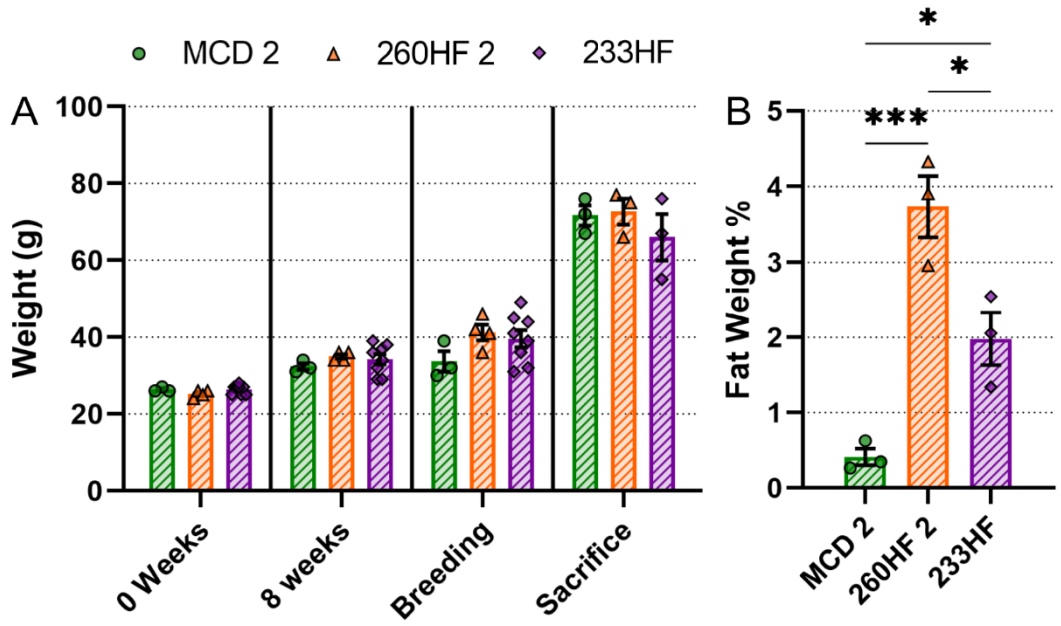

Figure 28: 260HF and 233HF mice were not significantly heavier than control mice despite heavier fat pads

A) Mean (+/- SEM) weight of dams fed control (green), 260HF (orange) or 233HF (purple) diets at start of feeding; 8 weeks after feeding start date; at start of breeding; and at sacrifice. Pre-sacrifice MCD2 n=3, 260HF2 n=4, 233HF n=8. Post-sacrifice n=3 for all. **B)** Mean (+/- SEM) dam fat weight as a proportion of total body weight (One-way ANOVA (F = 27.67, p = 0.0009), Tukey-Kramer post-hoc test, * = p < 0.03, **** = p = 0.0007). *MCD 2 – Maternal Control Diet cohort 2; 260HF – High Fat diet 260 cohort 2; 233HF – High Fat diet 233.*

4.3.3.2. Cohort 2 Foetal Gross Measurements

Cohort 2 average litter size was very similar between all groups, varying by only 1.66 (Figure 29). 260HF mice had significantly more fat mass, indicating other contributors to overall dam body mass must be decreased in these mice. Within group variation for both 260HF and 233HF high fat diet groups was, however, higher than the control group with standard deviations of 2.08, 3.06 and 0.58 respectively. This could suggest some level of developmental disruption differing dependant on individual dam responses to high fat diet.

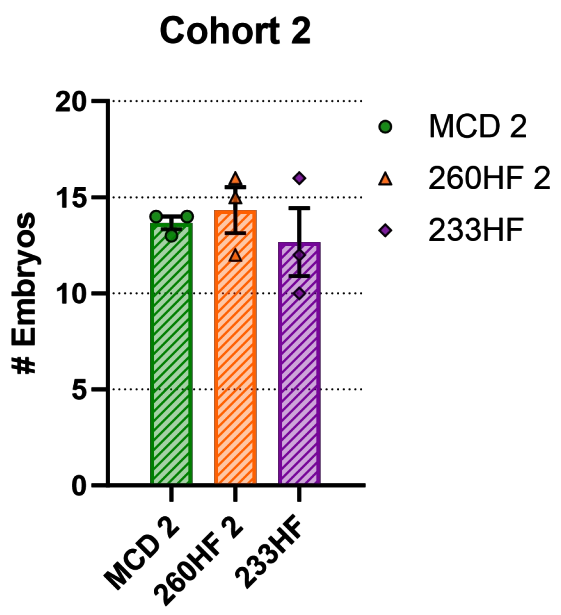

Figure 29: Cohort 2 litter size did not vary between groups.
Mean (+/- SEM) number of E18.5 foetuses per litter, n=3. *MCD 2 – Maternal Control Diet cohort 2; 260HF – High Fat diet 260 cohort 2; 233HF – High Fat diet 233.*

With regard to foetal body and brain measurements, the second cohort of maternal high fat diet exposed mice portrayed significant differences across all foetus measures shown in Figure 30. Foetuses in the 233HF group had an average body weight of 1.12g which was significantly lower than both control and 260HF groups at 1.57g and 1.50g respectively (One-way ANOVA (F = 111.7, p <0.0001), Tukey-Kramer post-hoc test, p <0.0001). This suggests disruption to overall foetal development under exposure to 233HF diet, which is barely detectable in 260HF mice.

A comparable pattern is carried through to brain measurements; where the average brain weight (Figure 30B) for the 233HF group was significantly lower by 0.018g compared to control and 260HF groups (One-way ANOVA (F = 44.20, p <0.0001), Tukey-Kramer post-hoc test, p <0.0001). This suggests changes to foetal development were carried through to the brain, an organ homeostaticly protected from developmental abnormalities where possible (Dennis et al. 2013). These differences are reflected in the brain to body weight ratios of cohort 2 offspring where 233HF mice were 0.082, significantly higher than 0.068 in control and 0.072 in 260HF mice (One-way ANOVA (F = 39.60, p <0.0001), Tukey-Kramer post-hoc test, p <0.0001). The 0.04 difference between control and 260HF brain to body weight ratio was also significant (One-way ANOVA (F = 39.60, p <0.0001), Tukey-Kramer post-hoc test, p = 0.0355). This significant increase in ratio acts as an indication of the protection afforded to the brain against developmental disruption, since brain weight was proportionally not as severely affected by 233HF diet as the entire foetal body. The difference observed between 260HF and control groups suggests that whilst some delayed development occurred in the foetal body as a whole, the brain was protected from this delay in growth. This is evident in identical brain weights for these groups.

Cortex area mirrors (Figure 30) brain weight in that 233HF cortices are lowest at 8.66mm^2, significantly lower than control cortices by 1.79mm^2 and 260HF cortices by 1.61mm^2 (One-way ANOVA (F = 60.2, p <0.0001), Tukey-Kramer post-hoc test, p <0.0001). Control and 260HF groups only differ by 0.18mm^2. Brain weight and cortex area measurements therefore suggest brain growth was reduced in the 233HF group but to a much smaller extent, if at all in 260HF foetuses.

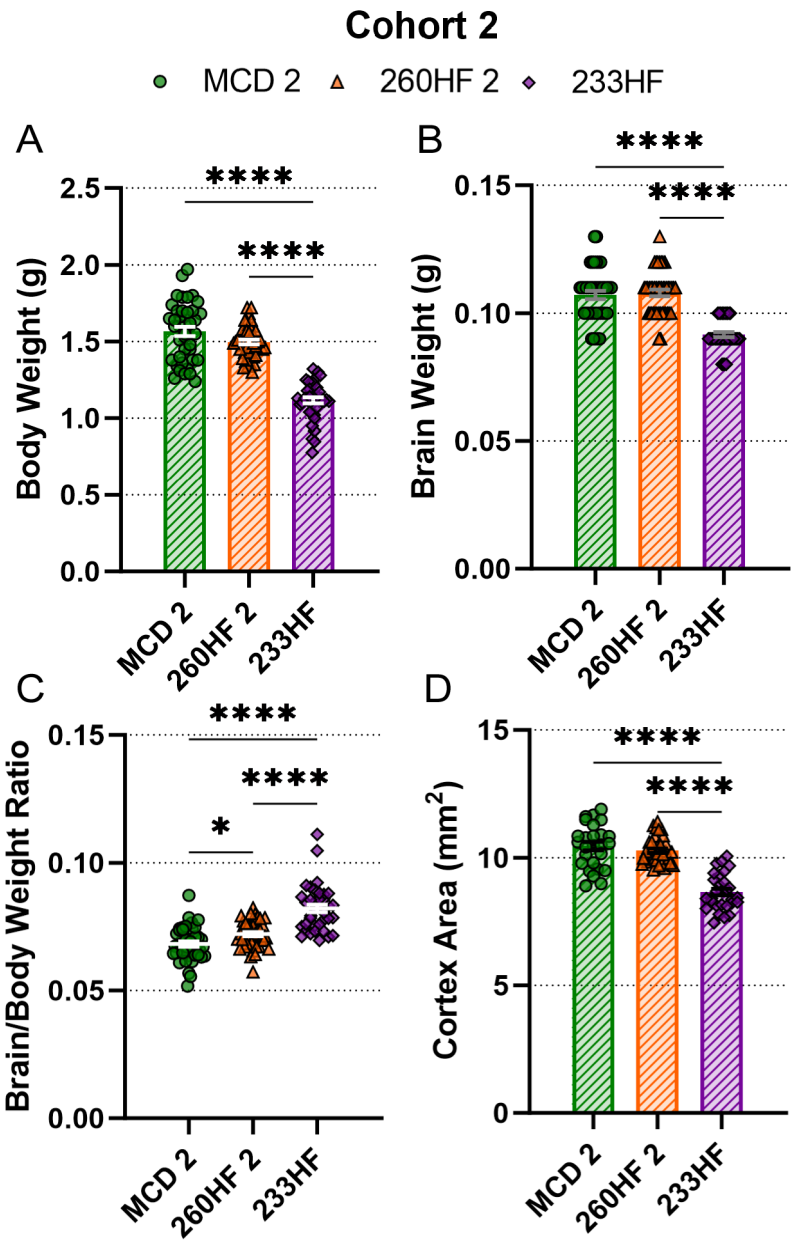

Figure 30: Cohort 2 foetus brain and body measurements were decreased in high fat diet groups compared to control.

A) Mean (+/- SEM) E18.5 foetus body weight in grams (**** = One-way ANOVA (F = 111.7, p <0.0001), Tukey-Kramer post-hoc test, p <0.0001) MCD2: n=41; 260HF2: n=43; 233HF: n=38. **B)** Mean (+/- SEM) E18.5 foetus brain weight in grams. (**** = One-way ANOVA (F = 44.20, p <0.0001), Tukey-Kramer post-hoc test, p <0.0001) **C)** Mean (+/- SEM) E18.5 foetus brain to body weight ratio. (One-way ANOVA (F = 39.60, p <0.0001), Tukey-Kramer post-hoc test, **** = p <0.0001, * = 0.0355) **D)** Mean (+/- SEM) E18.5 foetus cortex area in mm^2. (**** = One-way ANOVA (F = 60.2, p <0.0001), Tukey-Kramer post-hoc test, p <0.0001). *MCD 2 – Maternal Control Diet cohort 2; 260HF 2 – High Fat diet 260 cohort 2; 233HF – High Fat diet 233.*

4.3.3.3. Cohort 2 Corpus Callosum Defasciculation

Given the presence of changes to gross foetal measurements not observed in cohort 1, more subtle defects in corpus callosum organisation were expected for cohort 2. However, this was not the case with foetuses of cohort 2 following a similar pattern to those in cohort 1. No significant differences were found between high fat diet or control conditions, as measured through one-way ANOVA. Figure 31 shows a high level of similarity between groups within each region of the corpus callosum measured. There are some changes in variation in the rostral region with standard deviation for: MCD at 0.037; 260HF at 0.082 and 233HF at 0.21 whilst caudal standard deviations reach: 0.050 for MCD; 0.16 for 260HF and 0.069 for 233HF. Such increased intra-group variation could indicate differences between individual foetuses or dams in response to high fat diet exposure. A much higher number of repeats would be required to uncover any such differences.

In total, data gathered from mice in cohort 2 suggested diets 233HF and 260HF were not sufficient to induce obesity after 12 weeks of feeding. They were, however, sufficient to induce decreases in foetal body and brain weight measurements, particularly in 'inflammatory' 233HF exposed mice. Such disruption was not sufficient to induce corpus callosum defasciculation. This model was repeated in an additional cohort in an attempt to replicate and build upon results.

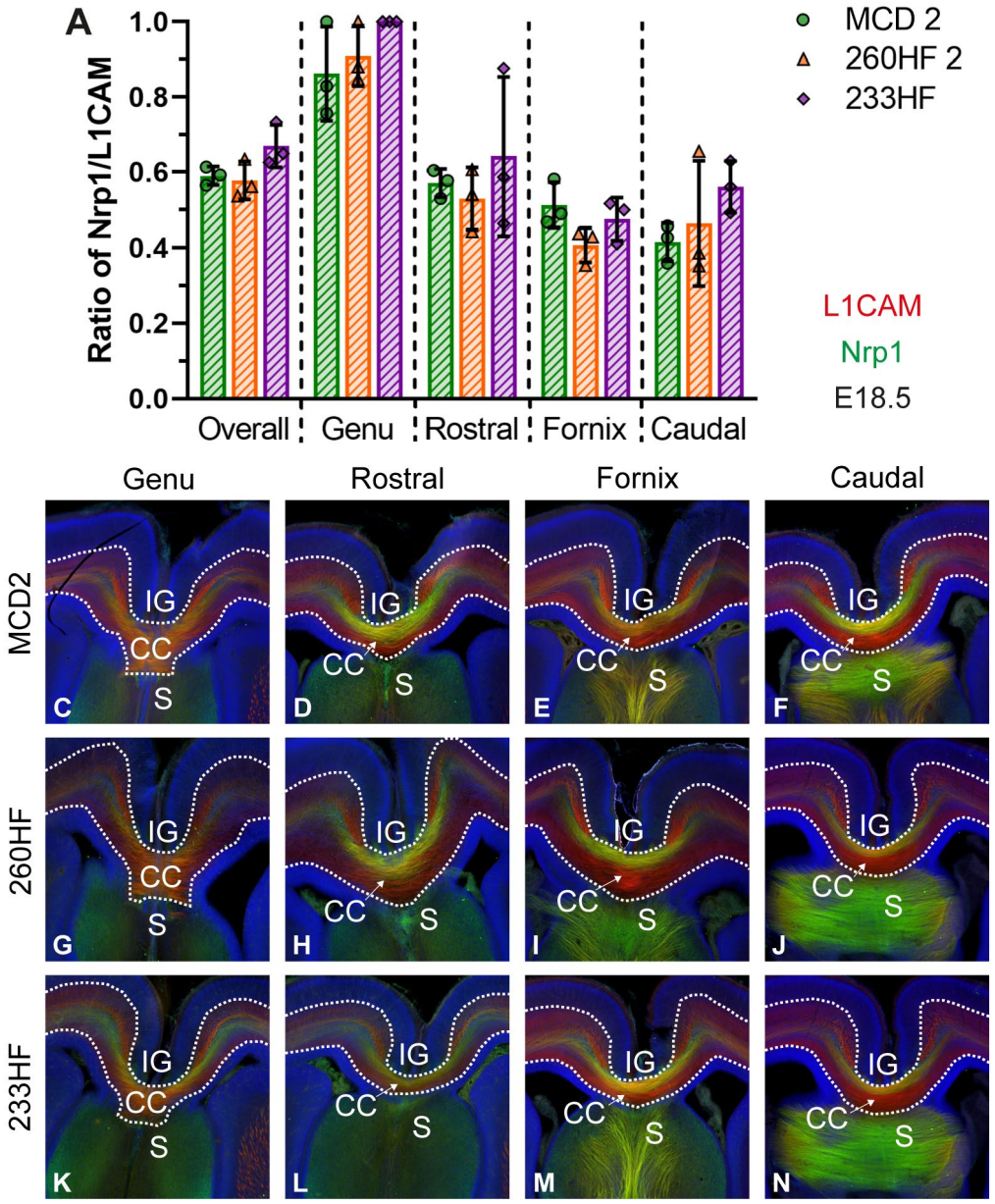

Figure 31: Corpus callosum axons did not become defasciculated when exposed to high fat diet.

A) Mean (+/- SEM) ratio of Nrp1/ L1CAM width at E18.5 across all regions of the corpus callosum. n=3 for all groups. **B-M)** Representative epifluorescence images of different corpus callosum regions across maternal diet groups. L1CAM labelled in red and Nrp1 labelled in green. *IG – Induseum Griseum; CC – Corpus Callosum; S – Septum. MCD 2 – Maternal Control Diet cohort 2; 260HF 2 – High Fat diet 260 cohort 2; 233HF – High Fat diet 233.*

4.3.4. High Fat Diet Cohort 3

4.3.4.1. Cohort 3 Dam Measurements

Producing an additional cohort of high fat diet fed dams provided the opportunity to repeat findings and demonstrate consistency of effect of each high fat diet. Identical diets to cohort 2 were requested for cohort 3, however 233HF had been updated by the supplier (SafeDiets) to 292HF. Differences between these diets were subtle; overall nutrient levels were comparable with the exception of amino acid levels, although this was compensated with increased overall protein levels (Table 4).

Table 4: Nutrient composition of 233HF vs 292HF

Nutrient (% mass)	233HF	292HF	Difference
Protein	22.4	25.8	3.4
Vitamins & Minerals	4.4	7.1	2.7
Fibre	4.6	6.5	1.9
Amino Acids	13.7	0.39	-13.31
Carbohydrates	29.6	24.95	-4.65
Fat	35.3	35.3	0

Mineral and vitamin level comparison between 233HF and 292HF in Table 5 shows slight adjustments of up to 2mg/kg of diet. Although precise levels of mineral and nutrient levels are not known for optimal mouse development and function in the wild, previous studies have established levels suitable for ‘acceptable performance’ - supporting growth and reproduction. Such studies identified: 5g/kg for calcium; 0.5g/kg for sodium and chlorine; 2g/kg for potassium; 4000IU/kg for vitamin A, as achieving acceptable performance (Nutrition 1995). Furthermore, up to 8.9g/kg potassium supported good growth and reproduction. Given that in both diets mineral levels exceed or are within 100mg of recommended levels, both diets are likely to support typical neurodevelopment. However, differences in mineral and vitamin concentrations may still influence results.

Table 5: Mineral and vitamin comparison between 233HF vs 292HF where difference over 500mg/Ul per kg

Minerals (mg)	233HF	292HF	Difference
Calcium	8699.9	7322	-1377.9
Sodium	416.9	1050	633.1
Potassium	9583.5	7572	-2011.5
Chlorine	539.7	1429	889.3
Vitamins (Ul)			
Vit A	5200.6	5783	582.4

As previously, all groups began with comparable weights varying by only 0.5g (Figure 32A). By 8 weeks of high fat diet feeding 292HF fed dams were significantly heavier than controls by 8.33g (One-way ANOVA (F = 4.287, p = 0.0262), Tukey-Kramer post-hoc test, p = 0.0215), whilst 260HF mice were only 5.32g heavier than controls. This trend continued through to breeding at 11 weeks after diet exposure with 292HF mice still significantly heavier than controls by 11.11g (One-way ANOVA (F = 8.150, p = 0.0021), Tukey-Kramer post-hoc test, p = 0.0015) and 260HF mice now 6.74g heavier than controls.

By sacrifice, there were no longer any significant differences between groups (One-way ANOVA (F = 0.5379, p = 0.6063). Groups differed by only 3.66g and all high fat diet dams were within 15% of mean control weight. MCD and 292HF also had relatively high variance, with standard deviations of 7.57 and 9.43 respectively compared to 3.51 for 260HF. High variance in control mice may be explained by random differences in litter size. Mean fat weight as a proportion of total body weight did not differ significantly between groups despite differences between 260HF or 292HF and control groups of 3.01% and 4.45% respectively (Figure 32B). This likely reflects the high variance in HFD groups with 260HF standard deviation at 2.00 and 292HF at 1.94. As discussed for cohort 2, this perhaps indicates individual variation in metabolism.

Figure 32: 292HF mice are significantly heavier than control mice until sacrifice. **A)** Mean (+/- SEM) weight of dams fed control (green), 260HF (orange) or 292HF (purple) diets at start of feeding; 8 weeks after feeding start date; at start of breeding; and at sacrifice (One-way ANOVA: * = (F = 4.287, p = 0.0262), Tukey-Kramer post-hoc test, p = 0.0215; ** = (F = 8.150, p = 0.0021), Tukey-Kramer post-hoc test, p = 0.0015). Pre-sacrifice: MCD3 n=9, 260HF3 n=8, 292HF n=9. Post-sacrifice: MCD3 and 260HF n =3, 292HF n=4. **B)** Mean (+/- SEM) dam fat weight as a proportion of total body weight. *MCD 3 – Maternal Control Diet cohort 3; 260HF – High Fat diet 260 cohort 3; 292HF – High Fat diet 292.*

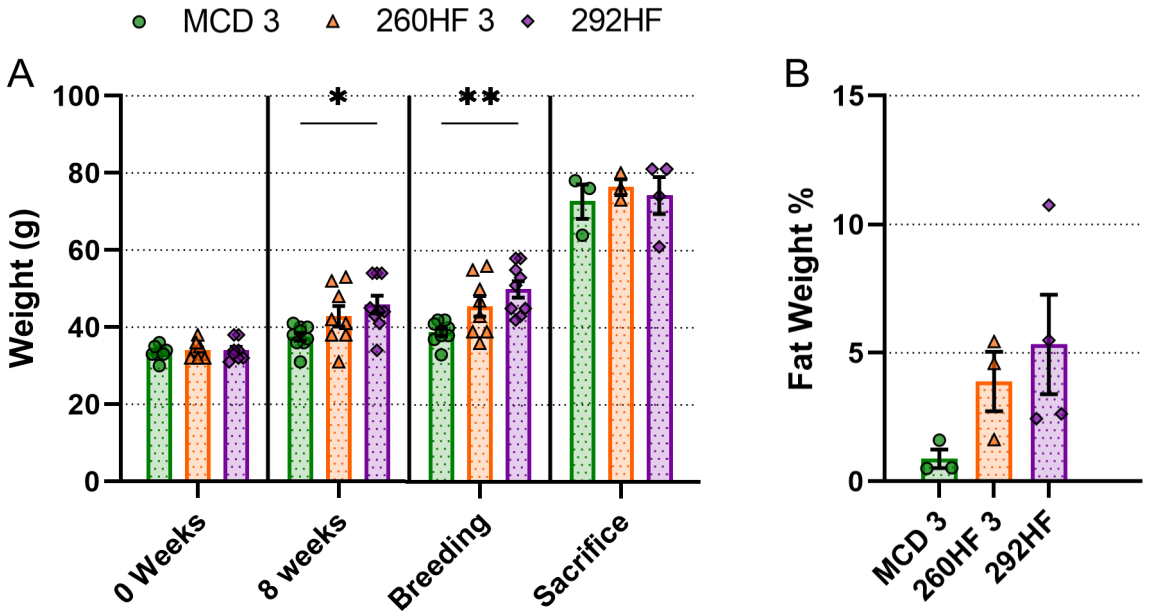

4.3.4.2. Cohort 3 Foetal Gross Measurements

In contrast to previous cohorts, average litter size in cohort 3 did differ significantly between groups, with 292HF litter size significantly lower than control (* = One-way ANOVA (F = 7.746, p = 0.0168), Tukey-Kramer post-hoc test, p = 0.0141). As shown in Figure 33, the 260HF litters form an intermediate group at 14.67 foetuses per litter compared to 12.75 for 292HF and 16.33 for MCD. This pattern of highest detrimental impact of diet in 292HF followed by 260HF mirrors fat weight and overall dam weight at breeding, suggesting a possible dose effect in cohort 3 with less inflammatory 260HF representing an intermediate. The number of necrotic foetuses at E18.5 was also measured for this cohort. Necrotic embryos were those judged by eye to be clearly non-viable: often discoloured, partially reabsorbed and always much smaller than littermates. Whilst no significant differences were found for necrotic foetuses, there were on average more 292HF necrotic foetuses than in other cohorts, again suggesting this diet was most detrimental to development.

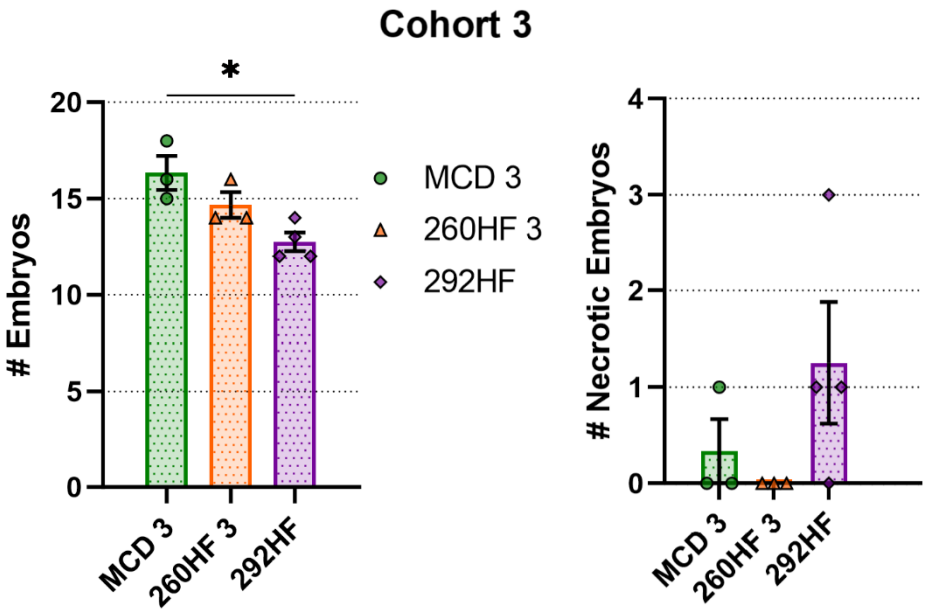

Figure 33: Cohort 3 high fat diet litter size is lower than control groups.
A) Mean (+/- SEM) number of E18.5 foetuses per litter. (* = One-way ANOVA (F = 7.746, p = 0.0168), Tukey-Kramer post-hoc test, p = 0.0141) MCD3 and 260HF n =3, 292HF n=4. **B)** Mean (+/- SEM) number of necrotic foetuses per litter. *MCD 3 – Maternal Control Diet cohort 3; 260HF 3 – High Fat diet 260 cohort 3; 292HF – High Fat diet 292.*

Unlike cohort 2, mean foetus body weight for both high fat diet groups was significantly lower than control mice by 0.15g (One-way ANOVA (F = 16.04, p <0.0001), Tukey-Kramer post-hoc test, p <0.0001). Brain weight did not differ significantly between groups, varying by only 0.007g or 0.006 respectively (One-way ANOVA (F = 2.877, p =0.0598). This may be as a result of high fat diet exposed foetuses successfully preventing impaired development observed in the body as a whole from affecting brain growth. In line with this theory, brain to body weight ratio visible in Figure 34C was increased in high fat diet groups, although not significantly (One-way ANOVA (F = 2.099, p =0.1266). Both high fat diet groups did however display lower mean cortex areas than control mice. 260HF mean cortex area was 8.30mm^2, significantly lower than the 9.48mm^2 control group (One-way ANOVA (F = 10.36, p <0.0001), Tukey-Kramer post-hoc test, **** = p <0.0001). Likewise, 292HF mean cortex area was significantly lower than control mice at 9.01mm^2 (One-way ANOVA (F = 10.36, p <0.0001), Tukey-Kramer post-hoc test, * = 0.0194). This suggests that cortical brain growth was in fact affected by both high fat diets which was highly unexpected given there was no accompanied decrease in overall brain weight.

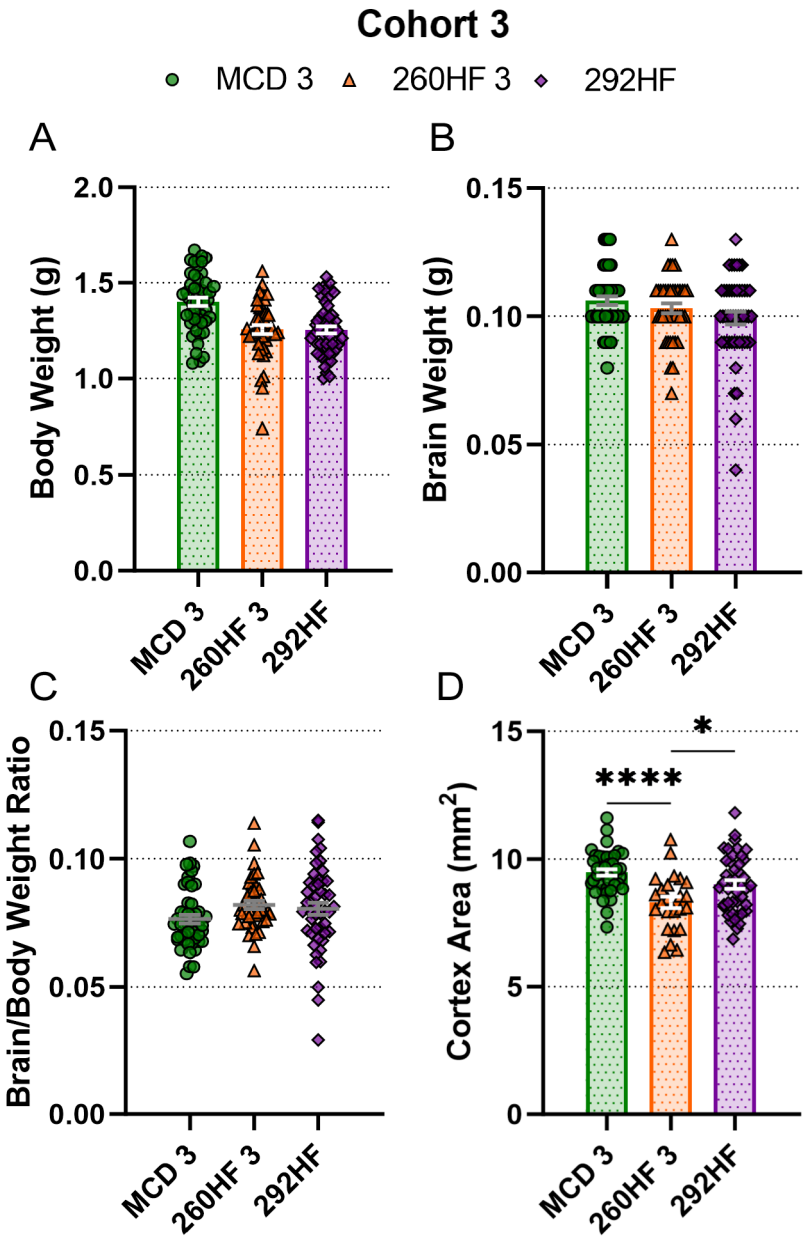

Figure 34: Cohort 3 foetus body weight and cortex area was decreased in high fat diet groups compared to control.

A) Mean (+/- SEM) E18.5 foetus body weight in grams (**** = One-way ANOVA (*F* = 16.04, *p* <0.0001), Tukey-Kramer post-hoc test, *p* <0.0001) MCD3: n=49; 260HF3: n=43; 292HF: n=51. **B)** Mean (+/- SEM) E18.5 foetus brain weight in grams. **C)** Mean (+/- SEM) E18.5 foetus brain to body weight ratio. **D)** Mean (+/- SEM) E18.5 foetus cortex area in mm^2. (One-way ANOVA (*F* = 10.36, *p* <0.0001), Tukey-Kramer post-hoc test, **** = *p* <0.0001, * = 0.0194) *MCD 3 – Maternal Control Diet cohort 3; 260HF 3 – High Fat diet 260 cohort 3; 233HF – High Fat diet 233.*

All data for this figure was produced by Ashmee Almeida and Mayur Shetty.

4.3.4.3. Cohort 3 Pup Gross Measurements

A subset of mice in cohort 3 were allowed to develop until postnatal day 7, when measurements were taken as previously for E18.5 foetuses. Figure 35A shows that at P7 pup body weight varied by only 0.42g, however all other measurements differed significantly between groups. Mean brain weight was 0.044g significantly lower for 260HF pups (One-way ANOVA (F = 10.95, p =0.0003), Tukey-Kramer post-hoc test, p = 0.0345) and significantly higher by 0.044g for 292HF pups (p =0.0002). Brain to body weight ratio therefore followed the same pattern with control pups at 0.074, 260HF pups at 0.065 and the 292HF group at 0.077. These differences can perhaps be explained by differing effects of the diet once supplied via maternal milk rather than through the bloodstream via the placenta. Alternatively, pups may have modified rates of development in an attempt to correct in-utero under or over development. This hypothesis is explored further in Figure 36.

Reversing the decreased 260HF brain weight trend, cortex area was highest for 260HF pups at 28.19mm^2, significantly higher than control mice by 3.02g (One-way ANOVA (F = 3.511, p =0.0493), Tukey-Kramer post-hoc test, p = 0.0463). 292HF mean cortex area was only 0.79mm^2 higher. These findings were again surprising given cortex area and brain weight were both used as approximate measures of developmental brain growth. Increased cortex size relative to weight can, however, be explained by increased ventricular area. This would expand cortex area visible from the outside whilst not contributing much to overall brain weight.

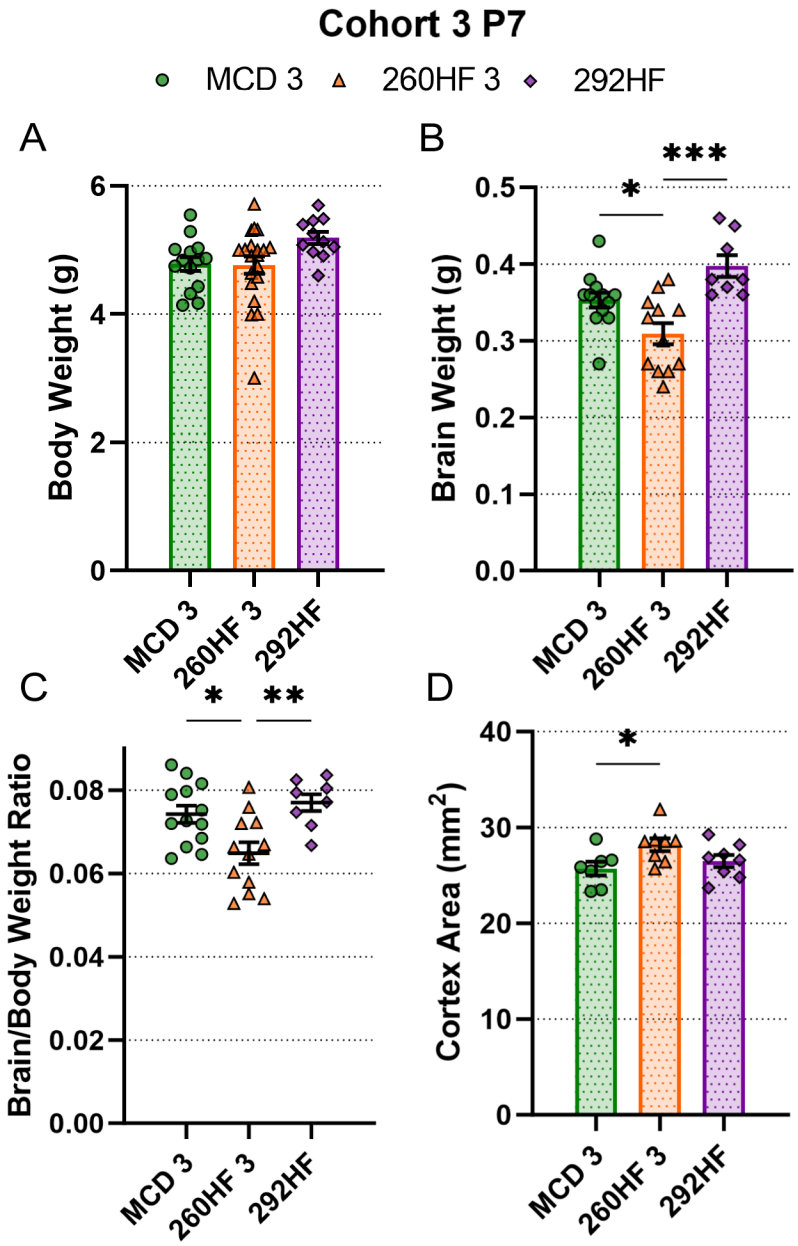

Figure 35: Cohort 3 postnatal brain measurements differed between high fat diet groups and control groups.

A) Mean (+/- SEM) P7 pup body weight in grams. MCD3: n=14; 260HF3: n=20; 292HF: n=11. **B)** Mean (+/- SEM) P7 pup brain weight in grams. (One-way ANOVA (F = 10.95, p =0.0003), Tukey-Kramer post-hoc test, **** = p =0.0002, * = 0.0345) **C)** Mean (+/- SEM) P7 pup brain to body weight ratio. (F = 7.198, p =0.0028), Tukey-Kramer post-hoc test, ** = p =0.0049, * = 0.0141) **D)** Mean (+/- SEM) P7 pup cortex area in mm^2. (* = One-way ANOVA (F = 3.511, p =0.0493), Tukey-Kramer post-hoc test, p = 0.0463) *MCD 3 – Maternal Control Diet cohort 3; 260HF 3 – High Fat diet 260 cohort 3; 233HF – High Fat diet 233.* **Ashmee Almeida and Mayur Shetty contributed towards data in this figure.**

A notable pattern becomes clear when comparing E18.5 mice with P7 mice, as shown in Figure 36. Measurements were normalised to control conditions, making differences in rate of change between time points more apparent. Body weight of high fat diet exposed offspring was 90% of control levels before birth at E18.5, but this underdevelopment was corrected for in 260HF mice and overcorrected for 292HF mice, reaching 108% of control by P7. During typical development multiple homeostatic mechanisms ensure all organs of the body develop to an expected size relative to overall body size and at a set rate (Turrigiano and Nelson 2004; Boulan and Léopold 2021). It may be that such mechanisms succeeded for 260HF mice but overcorrected for 260HF mice perhaps as a result of altered metabolic state. Indeed, similar data has been reported previously where offspring showed decreased body weight under maternal high fat diet prenatally leading to overcompensation postnatally (Jungheim et al. 2010). Such overcompensation has been termed 'catch-up growth' in humans and rodent models and is associated with metabolic dysfunction in offspring (Tang et al. 2018; Moon et al. 2022). This state is often induced through reduction in nutrition during pregnancy that may reflect the lack of suitable nutrition under high fat diet in this case.

Rates of brain growth as measured by brain weight and cortex area also differ between high fat diet groups. Brain weight is similar for all groups prenatally; however as previously 292HF mice overcorrected for this difference by reaching 112% of control mean brain weight by P7. For 260HF-exposed offspring, brain weight increased at a slower rate than control mice and did not meet control levels at P7. This pattern may indicate that some developmental compensation is required to prevent falling behind expected levels due to irregular availability of metabolites. Surprisingly, the alternate measure of brain growth – cortex area, did not match brain weight. 260HF mean cortex area began much lower than control mice at 88% of this level, but increased rapidly to exceed control levels by P7. Mean cortex area of 292HF mice was at 95% of control prenatally and again overcompensated for this difference by increasing to 103% of control levels by P7. Both of these measures could represent an overshoot of compensatory developmental mechanisms anticipated by their in-utero starting points. Differing changes in brain weight and cortex area could indicate regional specificity in brain growth under 260HF, with the cortex appearing to grow more than other regions of the brain.

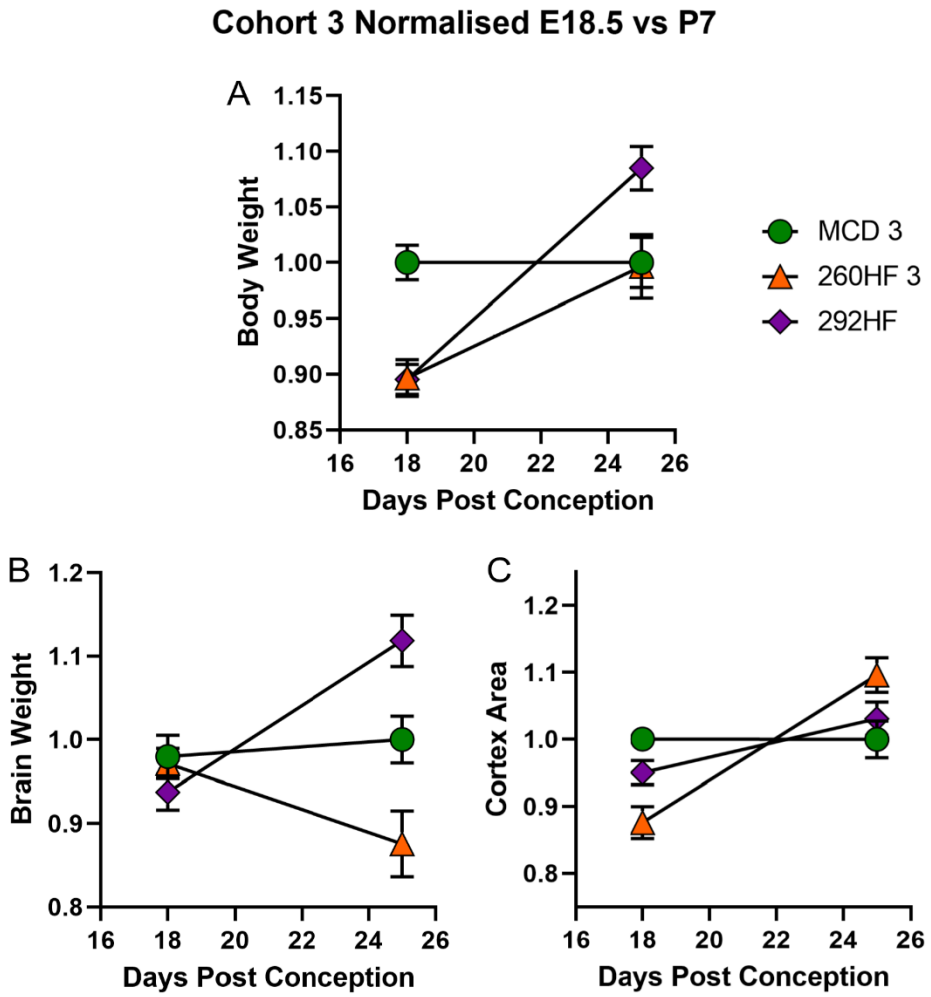

Figure 36: Brain measurement and body weight rate of change differed between high fat diet and control groups.

A) Mean (+/- SEM) normalised E18.5 foetus and P7 pup body weight in arbitrary units plotted against days post conception. E18.5 - MCD3: n=49; 260HF3: n=43; 292HF: n=51. P7 - MCD3: n=14; 260HF3: n=20; 292HF: n=11. **B)** Mean (+/- SEM) E18.5 foetus and P7 pup brain weight in arbitrary units plotted against days post conception. **C)** Mean (+/- SEM) E18.5 foetus and P7 pup cortex area in arbitrary units plotted against days post conception. *MCD 3 – Maternal Control Diet cohort 3; 260HF 3 – High Fat diet 260 cohort 3; 233HF – High Fat diet 292.*

Ashmee Almeida and Mayur Shetty contributed towards data in this figure.

4.3.4.4. Cohort 3 Corpus Callosum Defasciculation

Given that previous data (not shown) suggested defasciculation would most likely be found towards the caudal end of the corpus callosum, measurements for cohort 3 foetuses were taken only for the fornix region. As for previous cohorts there were no significant differences

between any groups measured (Figure 37). Here replicates were defined as the average of two brain slices taken from an individual brain.

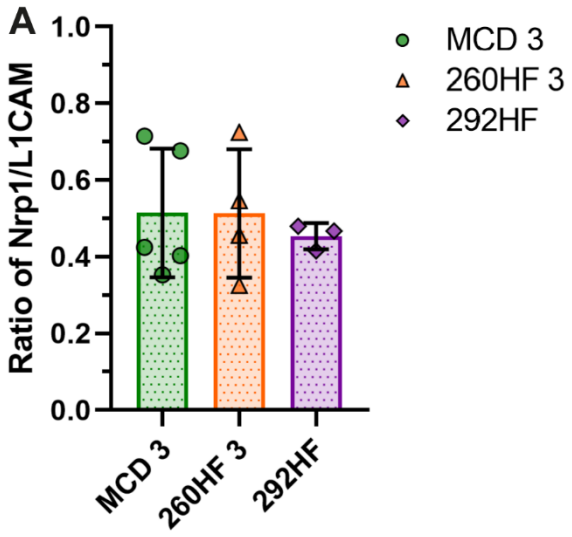

Figure 37: Corpus callosum axons did not become defasciculated when exposed to high fat diet.

Ratio of fornix Nrp1 expression width at the midline relative to midline L1CAM expression. MCD3 n=5, 260HF3 n =4, 292HF n=3. *MCD 3 – Maternal Control Diet cohort 3; 260HF 3 – High Fat diet 260 cohort 3; 233HF – High Fat diet 292.*

All data for this figure was produced by Ashmee Almeida and Mayur Shetty.

4.3.5. Cross-cohort Comparison

4.3.5.1. All Cohort Dam Weight

The generation of three distinct cohorts of high fat diet mice allows insights to be gained when comparing within diet groups across cohorts. Whilst every attempt was made to keep conditions consistent between cohorts, inevitably variations will have occurred. One example of this is that cohorts were produced at different times of year – cohort 1 in summer/autumn; cohort 2 in autumn/winter; cohort 3 in spring/summer. Although animal houses are kept under control conditions, it has been noted that some believe animals may behave differently based on seasons despite this (Ferguson and Maier 2013). If found a lack of difference between cohorts could have presented the opportunity to combine diet groups to increase statistical power.

When comparing dam weight in Figure 38, each group in cohort 3 was significantly higher than the corresponding group in cohort 2 at 0 weeks on diet (One-way ANOVA (F = 31.08, p < 0.0001), Tukey-Kramer post-hoc test, p < 0.0001). This may be due to age differences between cohorts, with cohort 2 mice at 45 days old upon diet exposure and cohort 3 mice 81 days when receiving diet. Cohort 1 mice were 130 days old when fed high fat diet.

At 8 weeks on their respective diet deviation between cohorts reduced with control groups differing by up to 5.22g compared to 7.17g at 0 weeks. Cohort 3 260HF mice were 7.88g heavier than those in cohort 2 at 8 weeks reduced from 8.75g at 0 weeks. Cohort 3 292HF mice, however, remained significantly heavier than cohort 2 counterparts at 11.64g (One-way ANOVA (F = 6.315, p < 0.0001), Tukey-Kramer post-hoc test, p = 0.0067) increased from 7.63g at 0 weeks. The significant difference between 292HF mice and 233HF mice remained (One-way ANOVA (F = 5.385, p = 0.0002), Tukey-Kramer post-hoc test, p = 0.0418) but shrank to 10.38g. Difference between control cohorts remained constant at 5.22g during breeding measurements whilst 260HF cohort differences decreased to 4.38g. These findings may indicate differing effects of each diet on mice because of initial body mass or age, with 260HF inducing less weight gain in higher body mass dams and 233HF/292HF causing more. Of course contrasting cross cohort results from 233HF and 292HF diets could also be due to minor diet improvements perhaps being more palatable to dams, random variation between mice or seasonal effects.

Finally, at sacrifice there were no significant differences (One-way ANOVA (F = 0.7099, p = 0.6645) between cohorts for corresponding diet groups with differences between groups decreasing for 260HF and 233HF/292HF to 0.08g and 3.14g respectively. Control group cross cohort mean body weight had a range of 6.67g, increasing slightly from breeding phase. Such unifying of cross cohort dam body weight at sacrifice shows that body mass changes occurring during pregnancy overcome all other influences of body mass. It appears as though during pregnancy dams are able to correct being under or over weight irrespective of diet or any differences present between cohorts.

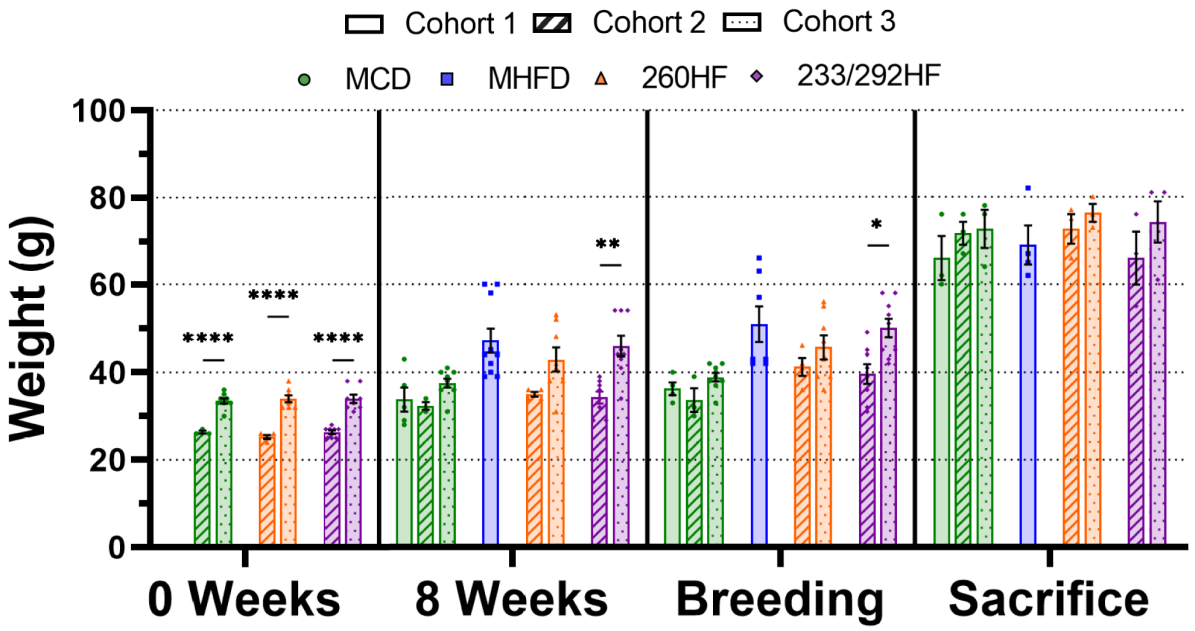

Figure 38: Dam weight differs by cohort differ despite consistent diet.
Mean (+/- SEM) weight of dams fed control (green), 260HF (orange) or 292HF (purple) diets across 3 cohorts with weight measured at start of feeding; 8 weeks after feeding start date; at start of breeding; and at sacrifice (One-way ANOVA, Tukey-Kramer post-hoc test (PH) **** = (F = 31.08, p < 0.0001), PH p < 0.0001; ** = (F = 6.315, p < 0.0001), PH p = 0.0067; * = (F = 5.385, p = 0.0002), PH p = 0.0418). n numbers are as recorded in previous dam weight figures. *MCD 3 – Maternal Control Diet cohort 3; 260HF – High Fat diet 260 cohort 3; 233HF – High Fat diet 233; 292HF – High Fat diet 292.*

4.3.5.2. All Cohort Fat Weight

In contrast to dam weight, mean dam fat weight as a proportion of body weight remained consistent across cohorts differing by only 0.43% and 0.15% for control and 260HF groups respectively (Figure 39). 233HF/292HF groups differed by 3.35% with cohort 3 292HF having much higher standard deviation to cohort 2 233HF at 3.876 and 0.6072 respectively. This could mean that inter cohort differences did not affect maternal metabolism, at least with regard to regulation of fat storage in fat pads. Variation between 233HF and 292HF without concomitant 260HF 2 and 260HF 3 changes provides some evidence that diet composition alterations affected fat metabolism, rather than other factors varying by cohort.

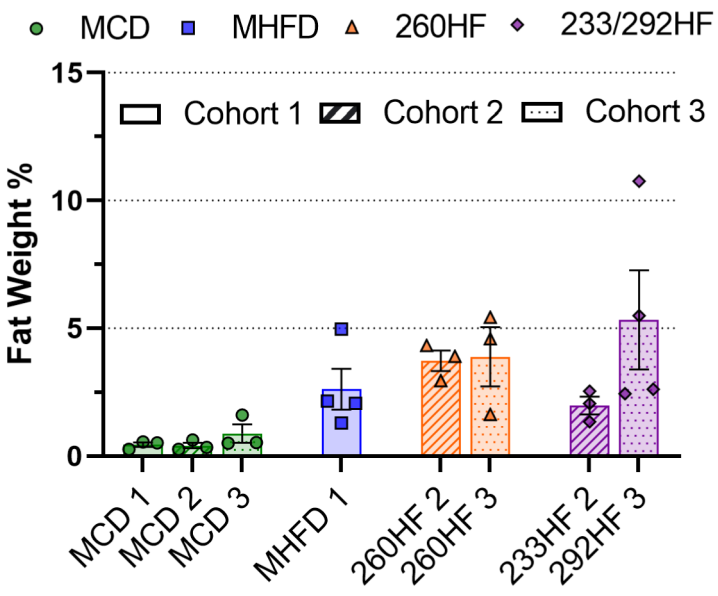

Figure 39: Fat weight does not differ across cohorts within diet groups.
Mean (+/- SEM) dam fat weight as a proportion of total body weight. n numbers are as recorded in previous fat weight figures. *MCD 3 – Maternal Control Diet cohort 3; 260HF – High Fat diet 260 cohort 3; 233HF – High Fat diet 233; 292HF – High Fat diet 292.*

4.3.5.3. All Cohort Foetal Gross Measurements

Comparing average litter size between cohorts in Figure 40 revealed highest variability between control diet groups, with groups differing by 2.67 although not significantly (One-way ANOVA (F = 2.167, p = 0.1958). In contrast, high fat diet groups vary by less than 0.4. Taking all cohorts together, control groups average at 14.78 foetuses per litter which is approximately 2 foetuses more on average than MHFD and 233HF groups but less than 0.5 foetuses more than 260HF groups. Assuming differences between cohort litter sizes are due to random variation, one could conclude an effect of 'inflammatory' MHFD and 233/292HF diets on litter size and therefore offspring survival, which may be too subtle to detect without a high number of repeats. On the other hand, the significant decrease in litter size (Figure 33A) for cohort 3 292HF mice may be as a result of unusually high litter sizes in the cohort 3 control group.

Mean foetal body weight varied significantly between all cohorts. Control E18.5 foetuses in cohort 1 had mean body weight of 1.34g compared to 1.4g in cohort 3. Cohort 2 control foetuses, however, weighed on average 1.57g which was significantly higher than cohorts 1 and 2 (MCD: **** = One-way ANOVA (F = 22.17, p <0.0001), Tukey-Kramer post-hoc test, p <0.0001). 260HF exposed foetuses had a mean body weight of 1.50g in cohort 2 but significantly less by 0.24g, 19% of body weight, in cohort 3 (Unpaired t-test: t(8.63) = 84, p < 0.0001). In contrast, 233HF or 292HF exposed foetuses had mean body weight of 1.12g in cohort 2 increasing significantly to 1.25g in cohort 3 (Unpaired t-test: t(2.73) = 84, p = 0.0078).

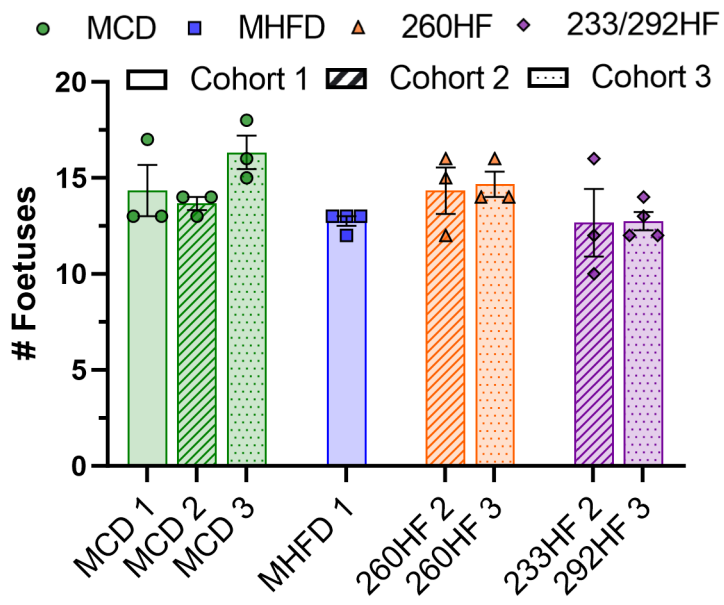

Figure 40: Within group litter size does not vary significantly across cohorts.

Mean (+/- SEM) number of E18.5 foetuses per litter across all cohorts. n numbers are as recorded in previous litter size figures. *MCD 1 – Maternal Control Diet cohort 1; MHFD – Maternal High Fat Diet; MCD 2 – Maternal Control Diet cohort 2; 260HF 2 – High Fat diet 260 cohort 2; 233HF – High Fat diet 233; MCD 3 – Maternal Control Diet cohort 3; 260HF 3 – High Fat diet 260 cohort 3; 292HF – High Fat diet 292.*

There are multiple explanations for this unexpected cross cohort variation. One is that time of year affected foetal development. This cohort also had smallest litter size, although only marginally (Figure 40), perhaps allowing individual foetuses to grow larger due to higher resource allocation. Dam age is another factor which is further explored in Figure 48.

As shown in Figure 41, high fat diet group brain weight mirrored body weight between cohorts with 260HF brain weight decreasing significantly from cohort 2 to cohort 3 (Unpaired t-test: $t(2.13) = 81$, $p = 0.0366$) and increasing significantly from cohort 2 to cohort 3 for 233HF/292HF groups (Unpaired t-test: $t(2.73) = 84$, $p = 0.0078$). In control groups both cohorts 2 and 3 had significantly heavier mean brain weight, at 0.11g, than cohort 1 mean brain weight at 0.098g (One-way ANOVA ($F = 9.887$, $p = 0.0001$), Tukey-Kramer post-hoc test, $p < 0.001$). Given neurodevelopment is affected by similar forces to overall development; the same explanations are viable for these differences between cohorts.

Brain to body weight ratio also varied between cohorts. Control groups in cohorts 1 and 3 shared brain/body ratios of 0.077, with cohort 2 significantly lower at 0.068 (One-way ANOVA ($F = 9.272$, $p = 0.0002$), Tukey-Kramer post-hoc test, $p < 0.0015$). Cohorts 2 and 3 also varied in 260HF group brain to body weight ratio, with cohort 3 significantly higher (Unpaired t-test: $t(5.57) = 81$, $p < 0.0001$). The 233HF/292HF groups on the other hand remained constant between cohorts at 0.082 and 0.081 respectively.

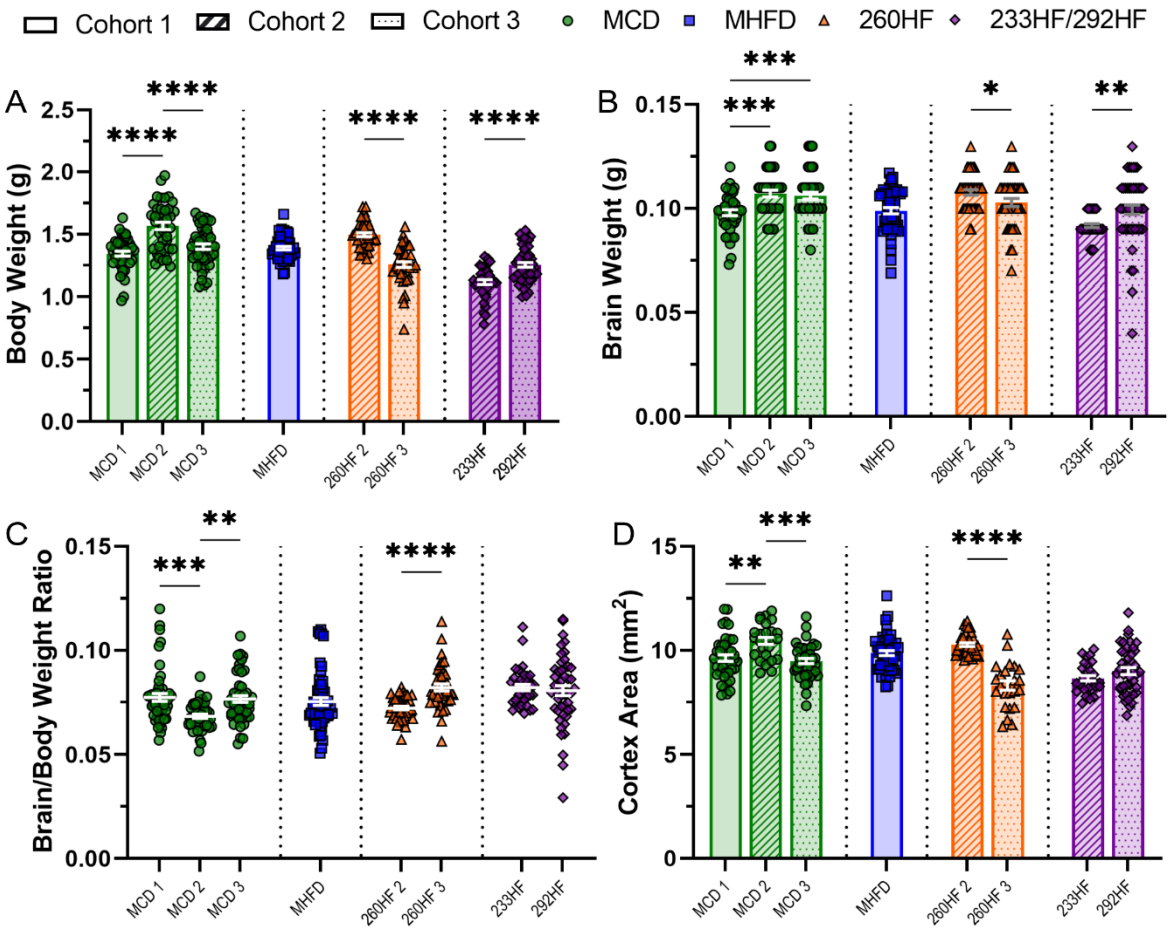

Figure 41: Body and brain mass varied between cohorts for both control and high fat diet groups.

A) Mean (+/- SEM) E18.5 foetus body weight in grams between cohorts (MCD: **** = One-way ANOVA (F = 22.17, p <0.0001), Tukey-Kramer post-hoc test, p <0.0001) (260HF: Unpaired t-test: t(8.63) = 84, p < 0.0001) (233HF/292HF: Unpaired t-test: t(4.98) = 87, p < 0.0001). **B)** Mean (+/- SEM) E18.5 foetus brain weight in grams between cohorts (MCD: **** = One-way ANOVA (F = 9.887, p = 0.0001), Tukey-Kramer post-hoc test, p <0.001) (260HF: Unpaired t-test: t(2.13) = 81, p = 0.0366) (233HF/292HF: Unpaired t-test: t(2.73) = 84, p = 0.0078). **C)** Mean (+/- SEM) E18.5 foetal brain to body weight ratio (MCD: One-way ANOVA (F = 9.272, p = 0.0002), Tukey-Kramer post-hoc test, *** = p = 0.0004, ** = 0.0013) (260HF: Unpaired t-test: t(5.57) = 81, p < 0.0001). **D)** Mean (+/- SEM) E18.5 foetus cortex area in mm^2 (One-way ANOVA (F = 10.11, p <0.0001), Tukey-Kramer post-hoc test, *** = p =0.0001, ** = 0.001) (260HF: Unpaired t-test: t(9.19) = 57, p < 0.0001). *MCD 1/2/3 – Maternal Control Diet cohort 1/2/3; MHFD – Maternal High Fat Diet. 260HF 2/3 – High Fat diet 260 cohort 2/3; 233HF – High Fat diet 233; 292HF – High Fat diet 292.*

Ashmee Almeida and Mayur Shetty contributed towards data in this figure.

Cortex area was elevated significantly in cohort 2 control foetuses relative to cohorts 1 and 3 (One-way ANOVA ($F = 10.11$, $p < 0.0001$), Tukey-Kramer post-hoc test, $p \leq 0.001$). 260HF exposed offspring had significantly lower mean cortex area in cohort 3 compared with cohort 2 by 1.97mm^2 (Unpaired t-test: $t(9.19) = 57$, $p < 0.0001$). Mean cortex area did not differ significantly between cohorts for 233HF and 292HF groups (Unpaired t-test: $t(1.495) = 71$, $p = 0.1393$). Inter-cohort variation across all foetal measures highlights the lack of scientific basis to combine groups between cohorts for increased statistical power.

4.3.5.4. All Cohort Defasciculation

Looking across cohorts the Nrp1/L1CAM ratio fluctuates around 0.5 across all regions despite changes in variation across groups. In total, results clearly show no differences in defasciculation between high fat diet and control maternal diets across all cohorts produced. This finding clarifies that more severe prenatal stressors than high fat diet alone are required to induce defects in corpus callosum organisation.

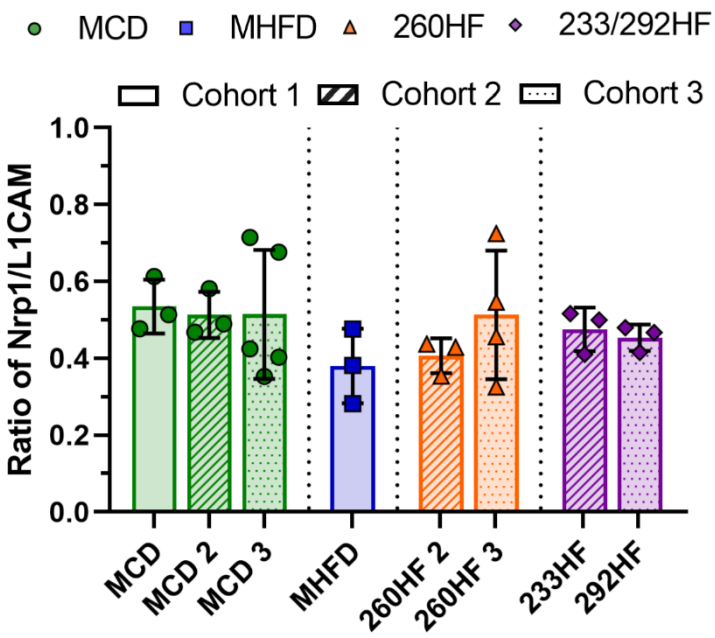

Figure 42: Corpus callosum axons did not become defasciculated across all cohorts.

Cross-cohort comparison of ratio of Nrp1 expression width at the midline relative to midline L1CAM expression within the fornix region of the corpus callosum. n numbers are as recorded in previous defasciculation figures.

Ashmee Almeida and Mayur Shetty contributed towards data in this figure.

4.3.6. Effect of Maternal High Fat Diet on Microglia

Microglia are known to be involved in maintaining the organised pattern within the corpus callosum and disruption in their behaviour could explain the previously observed maternal inflammation associated defasciculation (Pont-Lezica et al. 2014). Supporting this hypothesis, preliminary data also found an increase in the number of microglia invading the corpus callosum in more caudal regions (data not shown). As discussed, corpus callosum defasciculation was not observed here, so any changes to microglial behaviour under these conditions would suggest that microglia were not responsible for corpus callosum defasciculation. Alternatively, corpus callosum microglia may have been disrupted to an extent not able to induce corpus callosum defasciculation. Given the broad range of functions carried out by developmental microglia, there are other elements of corpus callosum development that could be disrupted by maternal obesity induced alterations to microglia that were not detected in this study. It is therefore important to uncover such alterations in order to guide further studies analysing the impact of maternal obesity on the corpus callosum. As important players in cortical neurogenesis, changes to cortical microglia behaviour could have been responsible for reductions in cortex area in the current study.

Developmental microglia behaviour were therefore examined, initially through the measurement of microglial density within the corpus callosum for cohort 1 and in the corpus callosum and cortex regions for cohort 2. This was carried out through Iba1 immunofluoresence staining in E18.5 brain slices taken from the offspring of mice fed either control, MHFD, 233HF or 260HF diets. The number of Iba1 cells were then counted from confocal images. Microglial birthdating was investigated in parallel through the injection of bromodeoxyuridine (BrdU) at various timepoints throughout development, as described previously under control conditions. Finally, expression of markers associated with septal microglia and metabolism were analysed through immunofluorescence staining.

4.3.6.1. Microglial Density under Maternal High Fat Diet

Data displayed in Figure 43 shows microglial density was unaffected by any of the high fat diets tested within the cortex or corpus callosum surrounding regions. In cohort 1, density of Iba1 labelled microglia was marginally higher in MHFD exposed foetuses across all regions; however, this did not reach significance for the t-tests performed for each region. Relatively high levels of within group variation may have influenced this, with standard deviation in

control groups ranging from a maximum of 0.0024 in cohort 1 to 0.00040 at most in cohort 2. Interestingly, cohort 2 high fat diet groups appear marginally lower than control for microglia density although again not enough to reach significance for one-way ANOVA tests performed. Taken together these results clearly indicate no effect of diet on microglial density within the cortex or corpus callosum associated regions.

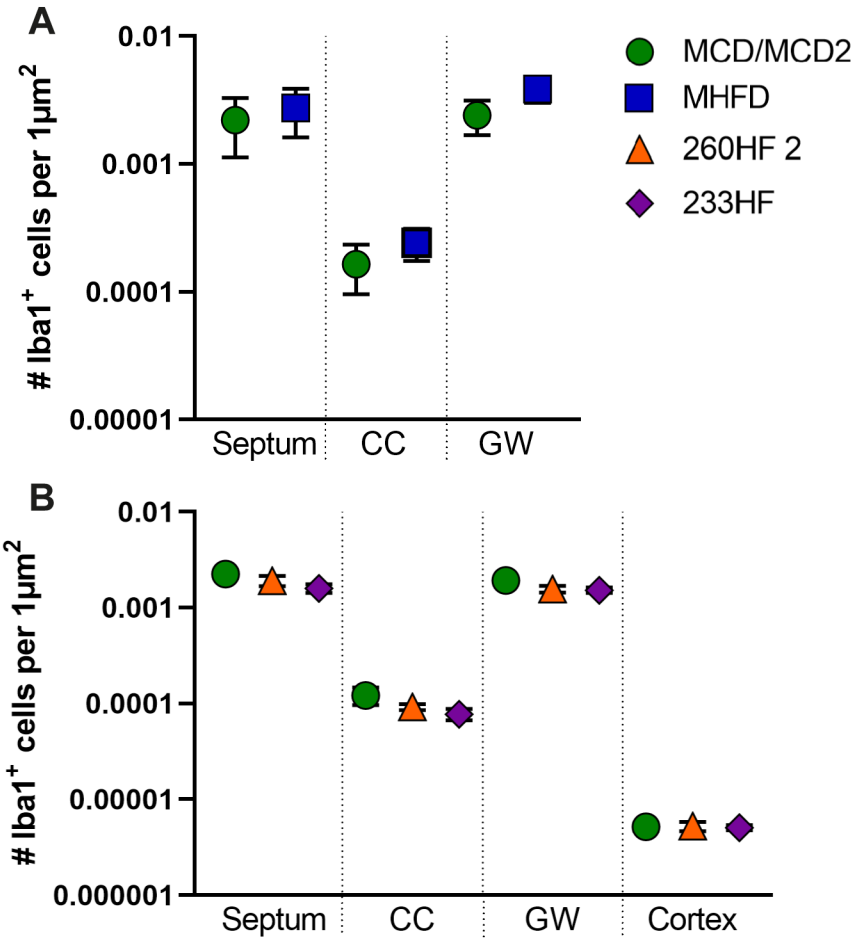

Figure 43: Microglial density did not differ between diet groups for any regions measured.

A) Mean (+/- SEM) number of Iba1$^+$ cells per 1µm^2 in the corpus callosum and surrounding regions in cohort 1. **B)** Mean (+/- SEM) number of Iba1$^+$ cells per 1µm^2 in the cortex, corpus callosum and surrounding regions in cohort 2. MCD/MCD2 n=16; MHFD n=5; 260HF n=9; 233HF n=9. *MCD 1/2 – Maternal Control Diet cohort 1/2; MHFD – Maternal High Fat Diet. 260HF – High Fat diet 260; 233HF – High Fat diet 233.*

4.3.6.2. Microglial Birthdate under Maternal High Fat Diet

Similarly, the proportion of microglia labelled with BrdU did not change across diet groups in regions surrounding the corpus callosum (Figure 44). Two-way ANOVAs were performed for each region measured, revealing no significant effect of diet on percentage of BrdU labelling. Timepoint was a significant source of variation in the cortex (37.26% of variation, p=0.0018, two-way ANOVA) and the septum (27.20% of variation, p=0.0127, two-way ANOVA), suggesting variation in birth dates across regions as discussed in the previous chapter. Interaction could not be measured for data shown in Figure 44 due to missing data for timepoints 13.5-15.5 in the MHFD group; however, separating each cohort and repeating statistical tests revealed no significant interaction between diet and time-point in any region. These data suggest that although there is some variation in proportion of BrdU labelled Iba1 cells, for example within the septum at E13.5, high fat diet exposure did not influence microglial birth date. It may be that increasing number of repeats would reveal differences of up to 0.5% at some time-points; however, such subtle differences are unlikely to be biologically significant.

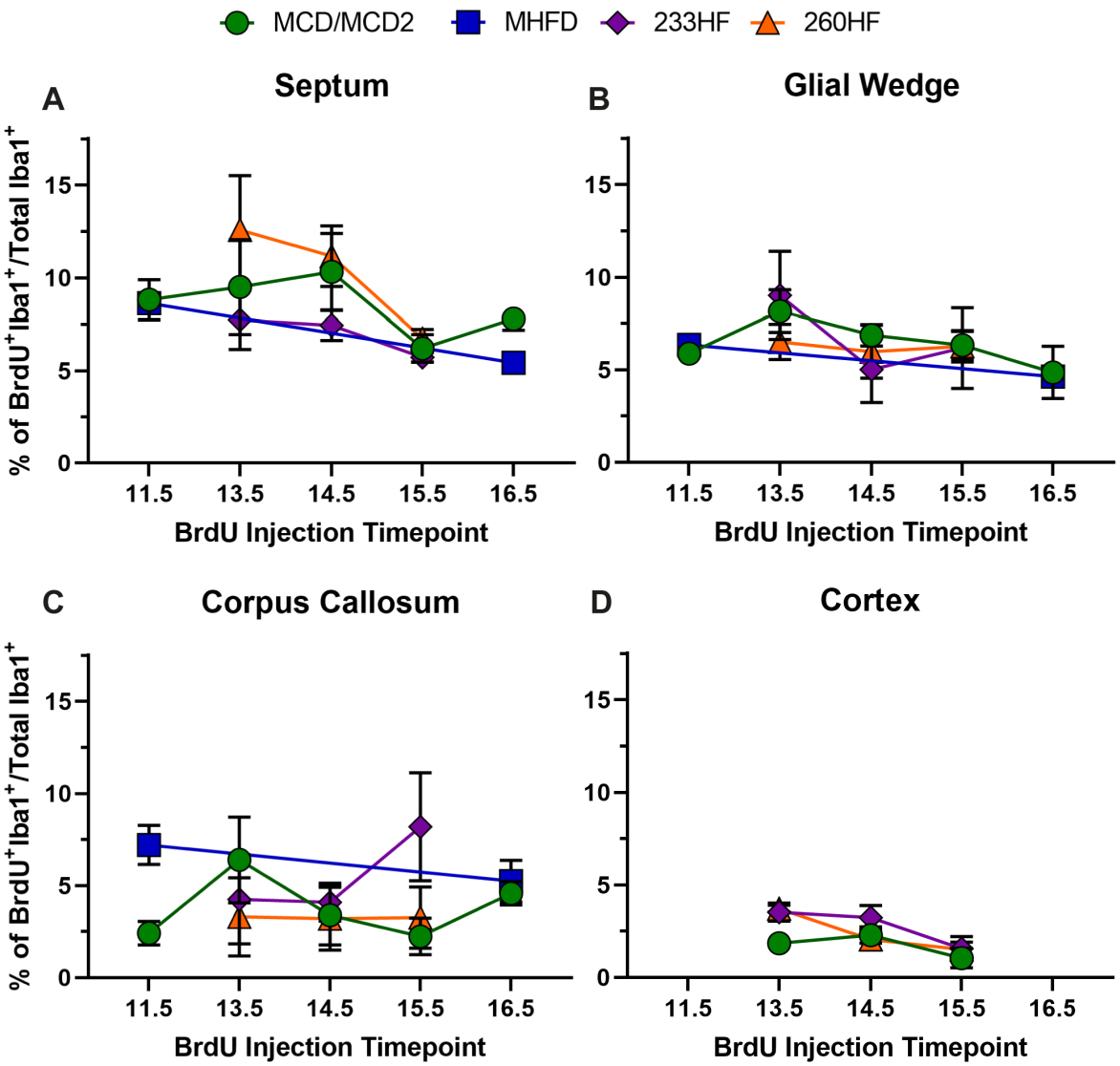

Figure 44: Microglial birthdate did not differ between diet groups for any regions measured.

A-D) Mean (+/- SEM) percentage of $BrdU^+$ $Iba1^+$ cells for each time-point of BrdU injection across respective brain regions and diets. MCD/MCD2 E11.5 n=3, E13.5 n=3, E14.5 n=3, E15.5 n=3, E16.5 n=3; MHFD E11.5 n=2, E16.5 n=3; 233HF E13.5 n=3, E14.5 n=3, E15.5 n=3; 260HF E13.5 n=3, E14.5 n=3, E15.5 n=3. *MCD 1/2 – Maternal Control Diet cohort 1/2; 260HF – High Fat diet 260; 233HF – High Fat diet 233.*

4.3.6.3. Expression of Microglial Markers under Maternal High Fat Diet

Density and birthdate of component cells are important biological features of the septal developmental hotspot. Changes in microglial subtype present within the septal hotspot is another feature which could influence foetal development and may be affected by high fat diet exposure. With this in mind, foetuses from cohort 3 were cryopreserved, sectioned and immuno-labelled for Iba1, Dectin-1 and Spp1 – markers identified in chapter 3 as associated with septal microglia. Changes in number of cells expressing these markers was measured to establish any shift in microglial subtype under high fat diet exposure.

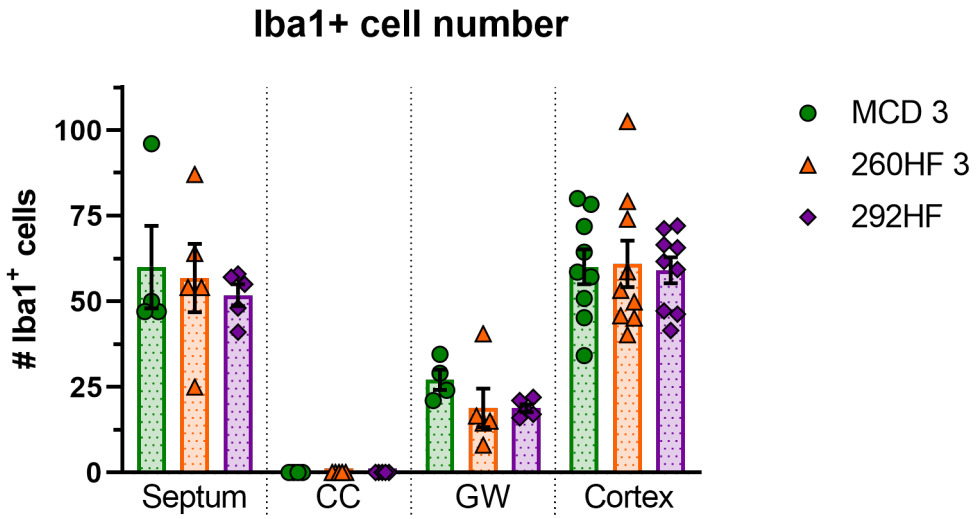

Figure 45: Number of microglial cells did not differ between diet groups for any regions measured.

Mean (+/- SEM) number of Iba1⁺ cells in the corpus callosum and surrounding regions in cohort 3. MCD3 n=4, cortex n=9; 260HF n=5, cortex n=9; 292HF n=5, cortex n=9. *MCD 3 – Maternal Control Diet cohort 3; 260HF 3 – High Fat diet 260 cohort 3; 292HF – High Fat diet 292.* **All data for this figure was produced by Ashmee Almeida and Mayur Shetty.**

Cohort 3 samples were cryosectioned into much thinner slices than those cut via vibratome for cohorts 1 and 2. Therefore, inevitably much fewer cells were detected under these conditions making comparison of microglial density between cohorts more difficult. For example, no cells were detected within the corpus callosum. Overall number of Iba1⁺ cells is therefore shown in Figure 45, where there was no significant variation between diet groups for any regions measured according to the one-way ANOVAs performed.

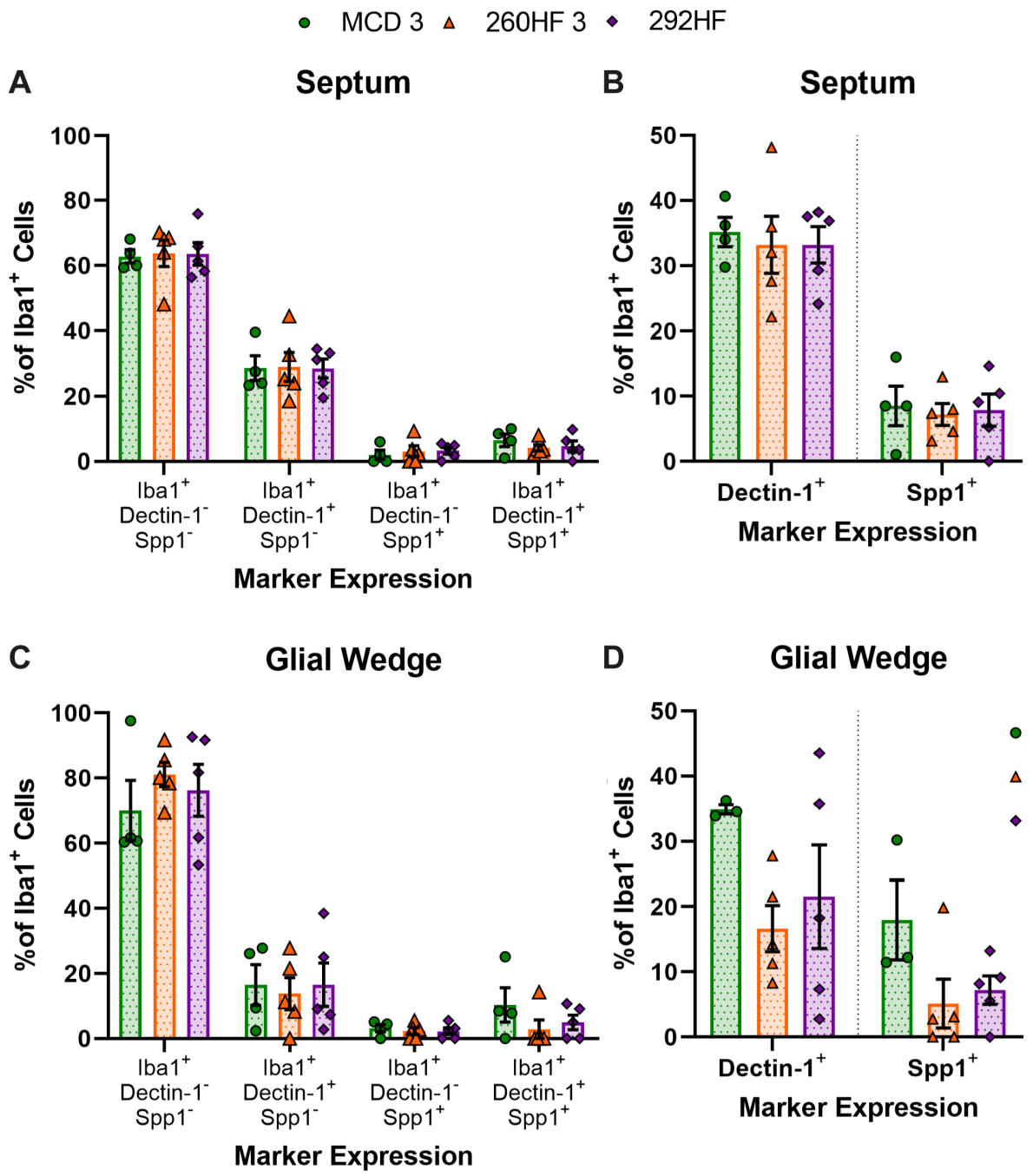

Figure 46: Proportion of microglial cells expressing septal microglia markers did not differ between diet groups in the septum or glial wedges.

A-D) Mean (+/- SEM) Percentage of Iba1+ cells expressing respective septal microglia markers in the septum or glial wedges. MCD3 n=4; 260HF n=5; 292HF n=5. *MCD 3 – Maternal Control Diet cohort 3; 260HF 3 – High Fat diet 260 cohort 3; 292HF – High Fat diet 292.* **All data for this figure was produced by Ashmee Almeida and Mayur Shetty.**

Figure 46 shows septal expression of markers associated with septal microglia was remarkably consistent between diet groups. Each expression pattern as a proportion of total Iba1$^+$ cells fell within 2% of the corresponding group exposed to a different diet. Comparing this to the glial wedges, although not as consistent, there was still minimal variation between diet groups. This is corroborated by less than 1% variation attributed to diet (<0.01% of variation, p>0.999, two-way ANOVA) or diet cell type interaction (0.7576% of variation, p=0.7181, two-way ANOVA) for septal and glial wedge regions.

Dividing cells by those that express individual markers, rather than in combination, as in Figure 46D makes what variation there is more visible. Mean HFD expression of both dectin-1 and spp1 appears lower than control foetuses with 260HF the lowest. This difference was not significant however, likely in part due to the high in-group variation seen in high fat diet groups particularly for the glial wedge region. Such variation could reflect technical differences more apparent when cryosectioning as variation in cutting angle between slices can lead to more or less of the glial wedge, and different levels within the glial wedge, being visible. This effect may be less apparent in the septal region due to its position at the midline. Alternatively, it may be that high fat diet has induced variability in marker expression given that there is higher variability in proportion of dectin-1$^+$iba1$^+$ HFD cells. Taken together these results build upon previous findings suggesting that application of different high fat diets did not affect microglial behaviour in developing offspring.

4.3.6.4. Microglial CPT1a Expression under Maternal High Fat Diet

The metabolic disruption associated with maternal obesity could have a range of effects on microglia which are not picked up by changes in density, birthdating or septal marker expression. Expression of key metabolic enzymes, for example, could be altered as microglia attempt to adapt to chronic elevation of circulating free fatty acids (Vidakovic et al. 2015). Carnitine Palmitoyltransferase 1A (CPT1a) is the key rate limiting enzyme of mitochondrial fatty acid oxidation – the process by which fatty acids are fed into the tricarboxylic acid cycle for the release of energy (Schlaepfer and Joshi 2020). This enzyme was described as absent from microglia in the developing rat brain (Jernberg et al. 2017) and only in astrocytes in mouse (Bernier et al. 2020), however this was not the case for septal microglia. As shown in Figure 47, 54.01% of Iba1 labelled control microglia expressed CPT1a within the septum compared to 3.97% and 13.89% in the corpus callosum and glial wedges respectively. Cortical microglia, on the other hand, follow previously described data in their lack of CPT1a expression. These findings lend further support to the hypothesis that septal microglia form a population that is transcriptionally distinct from other microglia within the cortex or nearby structures, discussed in chapter 3.

Alterations in expression of CPT1a could lead to changes in microglial behaviour. Aside from affecting the availability of ATP, changes to microglial metabolic status are known to influence activation state (Van den Bossche et al. 2017). The inhibition of CPT1a function has been shown to reduce microglial ramification and motility (Bernier et al. 2020), as well as reduce fatty acid induced increase in pro-inflammatory cytokine expression for other macrophages (Malandrino et al. 2015). The expression of CPT1a was therefore investigated through immuno-fluorescence staining in E18.5 embryos exposed to maternal high fat diet.

Expression of CPT1a was not significantly different within any region between any of the groups measured according the one-way ANOVA tests performed. This is despite the apparent decrease in the proportion of MHFD septal microglia expressing CPT1a visible in Figure 47. Parity between high fat diet groups could be expected based on the lack of disruption to the corpus callosum under these conditions (Figure 42).

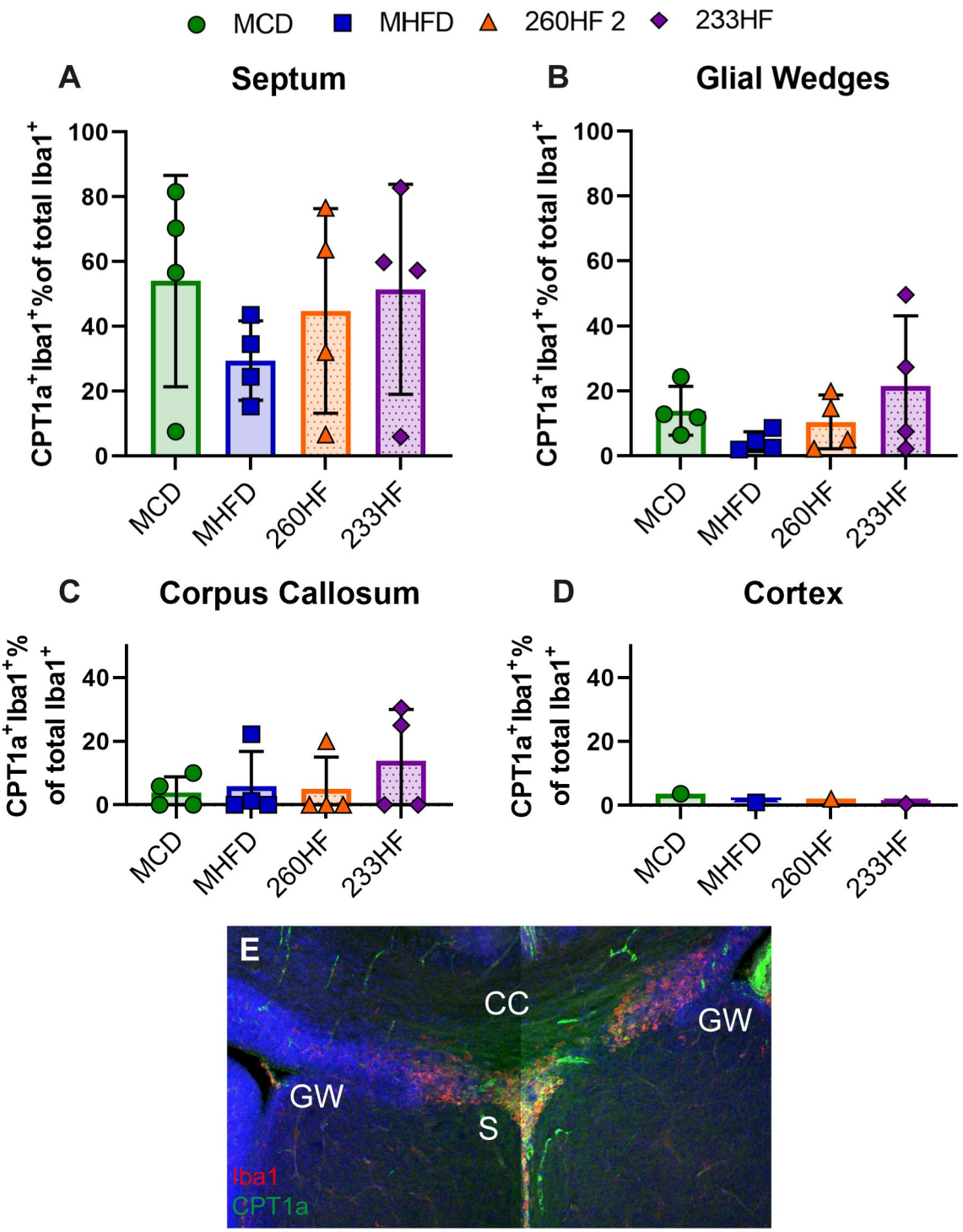

Figure 47: Microglial CPT1a expression did not differ between diet groups.

A-D) Mean (+/- SEM) Percentage of Iba1$^+$ cells expressing CPT1a in respective region. **E)** Representative image of CPT1a immunofluorescence staining with Iba1 in red and CPT1a in green. MCD n=4; MHFD n=4; 260HF2 n=4; 233HF n=4. *MCD – Maternal Control Diet cohort 1 & 3 combined; 260HF 2 – High Fat diet 260 cohort 2; 233HF – High Fat diet 233; CC – Corpus Callosum; S – Septum; GW – Glial Wedge*

4.4. Discussion

4.4.1. Summary of Key Findings

Initial experiments presented in this chapter set out to establish the effects of various high fat diets on: maternal metabolism through body weight and fat composition measurements; or foetal development through body weight, brain weight, cortex area and defasciculation measurements. No significant effect of MHFD was found on foetal development, but it did increase maternal body weight until E18.5. 233HF and 260HF diets did not induce a significant change in maternal body weight for cohort 2, but did decrease foetal body and brain weight measurements – particularly for 233HF. In cohort 3, 292HF dams alone were significantly heavier than control until E18.5 and had significantly smaller litters. Foetal body weight and cortex area measurements were also decreased for both high fat diet groups in cohort 3, however at P7 only 260HF pups had significantly decreased brain weight but increased cortex area. Comparing cohorts against each other revealed heavier starting dam weights in cohort 3 vs cohort 2 and differences in gross foetal measurements across control and high fat diet groups between all 3 cohorts. Maternal high fat diet exposure showed no effect on any measures taken of microglia density, birthdate, septal microglia marker expression or CPT1a expression.

4.4.2. Limitations

Obesity, here defined as a significant increase in weight from control group, was successfully induced in the first and third cohort of high fat diet fed mice (Figure 24, Figure 32). Decrease in litter size under maternal high fat diet has been reported by some groups (Niculescu and Lupu 2009a; King et al. 2013a). Such litter size reduction did not account for the reduction in weight difference between control and high fat diet groups since there was no significant effect on litter size in cohort 1 and cohort 3 litter size differences account for approximately 3.75g at most. One potential explanation for the lack of weight difference at sacrifice in cohorts 1 and 3 is that high fat diet groups reduced consumption of their diet. Over time cohort 3 high fat diet mice reduced their total diet consumption (data not included), presumably the same trend applied to cohorts 2 and 1. After 13 weeks on the diet, mice were subjected to timed matings. During this time, high fat diet mice had access to control diet, perhaps contributing to weight loss. Due to difficulties in breeding, some mice had access to this diet for a prolonged period. Perhaps during this time mice reduced high fat diet consumption and therefore reduced weight gain relative MCD mice. Use of diets with

increased rodent palatability was a potential solution to reduction in diet consumption before breeding, however many of these diets contain high carbohydrate levels (Higa et al. 2014; Fernandes et al. 2016). High carbohydrate levels could act as a confounding factor when attempting to examine the role of fatty acids in prenatal development and microglial behaviour. Whilst genetic mouse models of obesity are available, diet induced obesity is thought to better mimic human obesity (Lutz and Woods 2012).

The second cohort of high fat diet mice did not show a significant difference between MCD and either high fat diet group at 8 weeks or at breeding onset for their respective diets. This result differs from literature, where many studies have used a high fat diet to induce obesity in mice (Carpenter et al. 2013; Fernandes et al. 2016; Speakman 2019). There are many potential environmental factors that could explain this difference as housing conditions are not entirely consistent between animal facilities. For example, the surrounding bacterial milieu is likely to differ significantly between facilities. This could impact the gut microbiome which is emerging as an important player in the development of obesity (Davis 2016; Lai et al. 2018). Factors such as the ambient noise level, handling frequency, cage change frequency and variation in experimental procedures could influence stress levels, which may increase or decrease diet consumption depending on the stressor (Ellacott et al. 2010). With this in mind, an alternative frequently used mouse supplier (Charles River) was used as an attempt to modify the gut microbiome for cohort 3. Indeed, source of animals is known to be a key contributor to gut microbiome composition (Stough et al. 2016; Ericsson and Franklin 2021). However, it may be that gut microbiome began to transition during acclimatisation to the animal. Measures were also taken to reduce stress, such as more frequent handling prior to diet exposure to habituate mice to required experimental manipulations.

Despite measures taken to influence weight gain, maternal obesity was not maintained throughout pregnancy to E18.5 in cohort 3. This is in contrast to some studies (King et al. 2013a; Edlow et al. 2016; Panchenko et al. 2016), but each of these studies reported that obese dams gained less weight than controls during pregnancy. King *et al.* (2013) found that obese dams reduced food intake when pregnant and during pregnancy fat and liver weight decreased. However, obese dams remained significantly heavier than control through to E18, possibly due to their use of high sugar high fat ‘cafeteria diet’. Upon repetition of this protocol researchers found this significant weight difference was not maintained through to E18 (King et al. 2013b). These contrasting findings further demonstrate the difficulty of using diet to

induce maternal obesity. Interestingly, control and high fat diet dam weight became even closer upon removal of the uterus, perhaps suggesting obesity particularly affects this organ (King et al. 2013b; King et al. 2013a). Reportedly, obesity can impact the oocyte prior to conception leading to defects arising prior to the blastocyst stage (Luzzo et al. 2012). One might therefore expect developmental defects despite obesity not being maintained through to the collection of embryos at E18.5 in each of the 3 cohorts presented here.

4.4.3. High Fat Diet impact on Foetal Development

In cohort 1, reduction in weight difference between MHFD and control groups by sacrifice prevented MHFD mice being classified as obese when foetuses were collected. However, given that MHFD dams were significantly heavier upon breeding, offspring did spend a portion of their in-utero development under conditions of maternal obesity. Given that obesity has been shown to have an impact on mouse development from the blastocyst stage, one might still expect developmental defects in this cohort (Luzzo et al. 2012). Differences in proportion of fat mass also indicated disruption to metabolism in MHFD mice, despite similar overall weight at sacrifice. Higher variation in MHFD dams relative to MCD in overall weight and fat weight percentage indicate differing responses between dams to the high fat diet. Reduction in inter-group weight differences between breeding and sacrifice may be explained by differences in dam behaviour or metabolism between the two groups during pregnancy. Despite MHFD fed dams being significantly heavier than controls after feeding until E18.5, this appeared not to be a significant enough stressor to induce developmental defects in offspring. The metabolic disruption evident from increased maternal fat as a proportion of weight did not cause any changes in foetal brain or body development as measured by weight. Cortex area remained consistent between groups indicating no effect on brain growth. Finally, there was no evidence disorganisation within the corpus callosum under MHFD. This lack of an impact on foetal development suggests a more severe stressor, such as maintained obesity throughout pregnancy may be required to induce expected defects in offspring.

For cohorts 2 and 3, although dams were not technically obese at E18.5, increased fat mass amongst high fat diet dams does suggest disruption to metabolism. This state perhaps represents ‘normal weight obesity’ – a high percentage of body fat despite normal body mass index; more closely than obesity itself (Maejima et al. 2020). Slight reduction in litter size within

the cohort 2 260HF group, whose relative fat mass differed most significantly from control, hints at a potential impact of diet on offspring development. However, growth retardation was not observed in these foetuses and delayed cortical brain growth did not appear significant, as measured by cortex area and brain weight. Such defects have been observed in some mice exposed to maternal obesity previously, but not all (Luzzo et al. 2012; Rash et al. 2018; Christians et al. 2019).

Combined, cohort 2 offspring data suggest that 233HF diet was disruptive enough to induce growth retardation and affect brain growth despite not occurring during maternal obesity. Increase in brain body ratio may reflect the embryo's homeostatic mechanisms protecting the brain from metabolic defects inducing body wide growth retardation. This measure suggests 260HF offspring may form an intermediate step with reduced impact on overall growth and brain growth. 260HF dam body weight ratio nicely follows this pattern with an intermediate effect size. It is unsurprising that 233HF was more detrimental to development as it contains a lower proportion of n-3 PUFAs which is predominantly obtained through diet and often reduced in western diets. This key micronutrient is vital for neurogenesis, grey matter expansion and cell differentiation (Morgese and Trabace 2016).

Findings from cohort 3 somewhat corroborate trends identified in cohort 2. Litter size in the 292HF group, comparable to cohort 2 233HF, was significantly lower than control with 260HF forming an intermediate group. Mean within high fat diet group litter size was almost equivalent between cohorts. This suggests 292HF/233HF was more detrimental to offspring in-utero survival than 260HF. This is matched by increased numbers of necrotic foetuses in 292HF litters. Differences occur when comparing brain and body weight measurements. 260HF foetuses appear more affected by high fat diet exposure in cohort 3 than in cohort 2 whilst cohort 3 292HF offspring are less affected than cohort 2 233HF foetuses. Importantly, differences in body weight and cortex area were also noted between control groups suggesting that confounding environmental factors were at play. A combination of factors may have accumulated to result in these differences. Alternatively, an unmeasured factor such as microbiome-diet interactions may have differed between cohorts 2 and 3. These results demonstrate the difficulty in using environmental manipulations to measure effects on in-utero development and highlight the importance of tightly controlling all possible variables.

4.4.4. High Fat Diet and Metabolism

Results discussed so far lead to the conclusion that high fat diet consumption has a variable impact on litter size, brain growth and overall growth retardation. This is supported by many conflicting findings in the rodent literature (Christians et al. 2019). Variable dietary impact may be, as discussed, because many other factors are interacting to influence offspring outcome. Alternatively, it may be that the maintenance of obesity throughout in-utero development is required to induce consistent defects in gross foetal development measures. This may explain why no effect of high fat diet was observed for corpus callosum organisation, microglial density or marker expression. Aside from preliminary experiments, published data has shown defasciculation can be induced by LPS maternal immune activation (Pont-Lezica et al. 2014). Under such conditions cytokine profile is acutely altered (Glass et al. 2019). Whilst obesity results in more subtle but chronically modified cytokine profile, the metabolic defects induced in this study are unlikely to come close to the cytokine modifications occurring as a result of infection or even obesity (Gregor and Hotamisligil 2011).

Few studies have explored the effect of maternal obesity on microglial behaviour. Those that have find subtle shifts in mouse microglial activation state and increase in microglial density in the juvenile primate amygdala (Edlow et al. 2019; Dunn et al. 2022). Whilst changes such as this may not have been picked up in experiments performed, metabolic disruption more subtle than obesity in this study may not have induced such defects anyway. For example, any possible elevation in circulating free fatty acids under increased fat accumulation may not be sufficient to impact cortical development alone. This may instead require one of the many other features of obesity, such as increased adipokine or inflammatory cytokine levels (McArdle et al. 2013). Alternatively, more extreme high levels of circulating free fatty acids found in obesity due to increased lipolysis of white adipose tissue may be required to have any effect on microglia or corpus callosum defasciculation (McArdle et al. 2013). Additional data on the lipid profile of the high fat diet mice could have helped to uncover the role of high fat diet as opposed to obesity.

4.4.5. Individual Metabolic Variation

Increased in-group variation in weight was observed in high fat diet groups of all 3 cohorts (Figure 38). This may be due to the high genetic variation in CD1 mice interacting with perturbations in homeostasis induced by excessive fat consumption (Aldinger et al. 2009).

This strain was selected over more genetically homogenous strains due to the closer resemblance to obesity development in humans, which are themselves highly genetically diverse. Despite variation during feeding and breeding phases, at sacrifice high fat diet mice weight variation was similar to control groups. It may be that development of offspring from individual dams with a more strongly altered metabolism was more deranged. To explore this a correlation matrix was produced, as number of repeats was not sufficient for multiple linear regression. The correlation matrix shown in Figure 48 excluded control groups to explore altered metabolism, as measured by fat weight, exclusively in high fat diet exposed dams. Interestingly, there was a slight negative correlation between total fat mass or proportional fat mass and litter average body weight at -0.47 and -0.54 respectively. This perhaps suggests that level of metabolic state is in fact modulating offspring outcome, with some dams 'responding' to high fat diet exposure and others not. An increased number of dams per group would be required to explore this further. Weight at 8 weeks and at sacrifice did not correlate strongly with litter measurements. However, total number of days on diet was somewhat positively correlated with average brain to body weight ratio. This may however, be explained by inter-cohort differences in days on diet with MHFD dams spending on average 44 days less than other high fat diet groups. Figure 48 also shows age was not a significant confounding factor since age at study start or end did not correlation strongly with any litter measurements taken.

4.4.6. Conclusion

Data discussed in this chapter shows a limited effect of maternal high fat diet exposure on in-utero development. Maternal diet alteration also had no discernible impact on developmental microglia behaviour or corpus callosum development. As a more acute stressor with inflammatory implications, maternal immune activation formed an alternative method to induce defects in developmental microglia, as will be discussed in the next chapter.

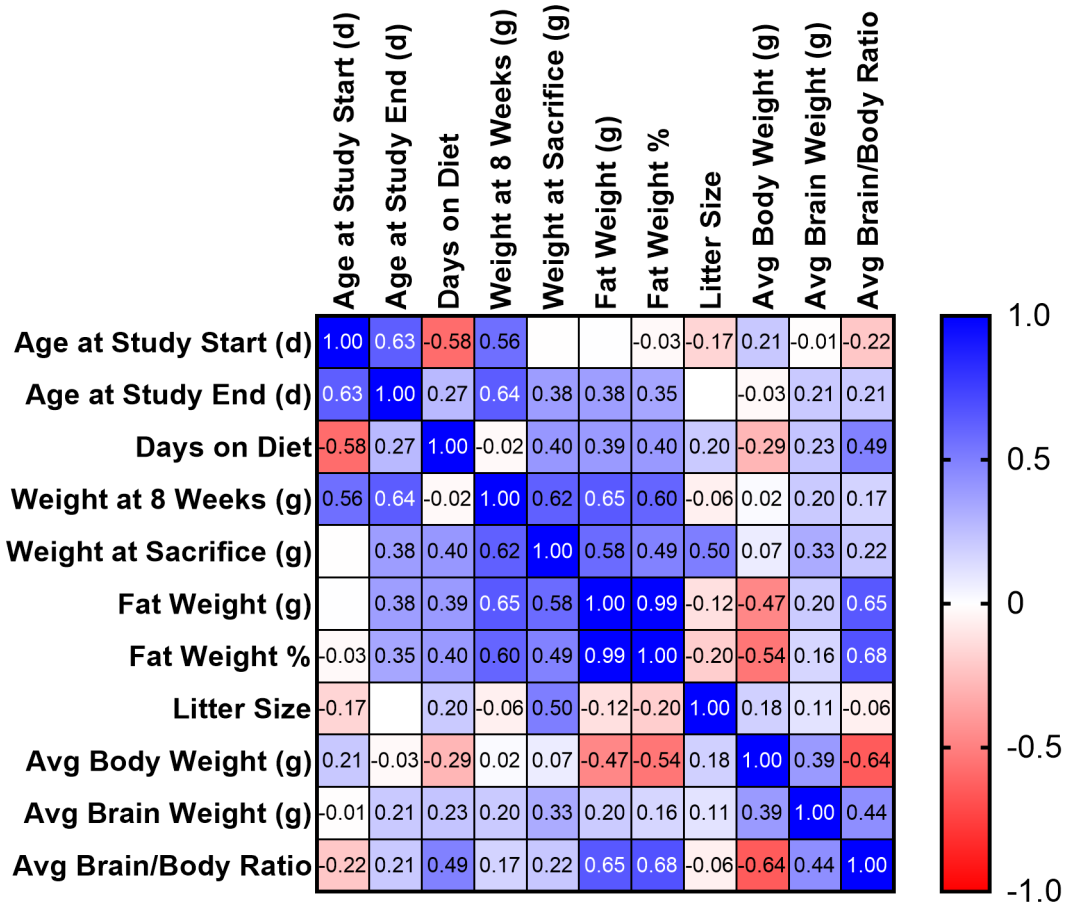

Figure 48: Maternal fat weight somewhat negatively correlates with litter average body weight. Heat map showing Pearson r correlation coefficients for comparisons between relevant experimental measures.

Chapter 5: The Effect of Maternal Immune Activation on Corpus Callosum Development

5.1. Introduction

5.1.1. Maternal Immune Activation and Neurodevelopmental Disorder

The immune system plays a vital role during the progression of pregnancy, carefully regulating cytokine levels to assist with each stage of early development. Disruption to this process, for example through the necessary acute inflammatory response to infection, can therefore interfere with neurodevelopmental processes. Accordingly, studies have shown infection during pregnancy is associated with increased risk for ASD, schizophrenia, bipolar disorders and childhood depression (Estes and McAllister 2016b; Brown and Meyer 2018). Corroborating animal studies find behavioural alterations thought to be representative of schizophrenia and ASD (Brown and Meyer 2018; Gumusoglu and Stevens 2019)

5.1.2. Mechanisms of Maternal Immune Activation

The acute inflammatory response associated with infection involves upregulation of classical immune mediators IL-6 and TNF-α amongst other inflammatory cytokines (Holub et al. 2013; Glass et al. 2019). Despite complex alterations in cytokine profile occurring during pregnancy, the impact of pathogen induced immune activation on cytokine levels is largely the same as in non-gravid humans and animals (Fricke et al. 2018; Singh et al. 2018; Davis and Mire 2021). In order to fulfil their roles protecting from external pathogens and assisting with key events during pregnancy, cytokines act as broad signalling molecules interacting with a variety of cell types and inducing a range of responses. IL-6, for example, is known to regulate self-renewal of neuroepithelial cells (Deverman and Patterson 2009) and TNF-α is involved in modifying neurite outgrowth during late embryonic and early postnatal development (Nolan et al. 2014). Unsurprisingly, inducing MIA during pregnancy, in addition to inducing behavioural deficits, has resulted in alterations to the structure and make-up of the developing mouse brain (Cunningham et al. 2013; Pont-Lezica et al. 2014; Squarzoni et al. 2014).

Perhaps most sensitive to changes in cytokine profile, as the brain's resident and highly reactive macrophage immune cell, microglia are likely to be impacted by MIA during pregnancy. Indeed, changes in microglial phagocytic capacity (Cunningham et al. 2013; Mattei et al. 2017), motility (Ozaki et al. 2020) and expression of a range of genes (Pont-Lezica et al. 2014; Matcovitch-Natan et al. 2016; Mattei et al. 2017; Ben-Yehuda et al. 2019) have been reported under the influence of MIA. As described previously, the involvement of microglia in brain development implicate them in the development of MIA associated behavioural and brain defects. Further evidence for their mechanistic involvement in MIA associated defects comes from studies finding microglial depletion associated brain and behavioural defects often mirror those found in MIA (Pont-Lezica et al. 2014; Squarzoni et al. 2014). Aims based on these findings form the backbone of this chapter, which centres around: establishing a model of MIA; measuring the impact of MIA on overall foetal development; measuring the impact of MIA on corpus callosum formation and associated microglia.

Following on from Barker and Osmond's (1988) original work demonstrating the foetal and developmental origins of adult disease, a "three-hit hypothesis of disease vulnerability and resilience" was proposed (Daskalakis et al. 2013; Kim et al. 2015). This well supported hypothesis suggests that genetic predisposition forms "hit 1," the prenatal environment is described as "hit 2," which alters gene expression and leads to phenotypes with differing susceptibility to later life experiences and exposures, or "hit 3" (Kim et al. 2015). It therefore follows that multiple "hits" in the prenatal environment may also predispose one to detrimental phenotypes in later life. Relating this to the current study, maternal high fat diet exposure outlined in chapter 4 was insufficient to consistently induce neurodevelopmental defects particularly within the corpus callosum. However, given that there was some disruption to markers of early development, such as brain and body weight, it may be that this model induced a mildly detrimental environment or "hit" to neurodevelopment. With this in mind, a further aim of this chapter was to investigate whether an additional maternal stressor was sufficient to induce more consistent and extreme developmental defects. As previously the focus of study was on development of the corpus callosum and associated microglia.

5.1.3. Chapter Aims and Key Findings

Similar to the influence of mild chronic inflammation during maternal high fat diet, MIA resulted in alterations to gross foetal measurements used to establish an overall effect on development. Unlike previous work however, these defects were carried through to the corpus callosum where defasciculation was observed under some conditions as well as changes to glial wedge hotspot microglia. Whilst combining maternal stressors through maternal high fat diet and MIA produced interesting effects on dam and foetal gross measurement, impact on the corpus callosum and associated microglia was more limited.

5.2. Materials and Methods

5.2.1. Maternal Immune Activation

CD1 female mice (6-8 weeks, Charles River) for MIA cohorts or C57BL/6 female mice (6-8 weeks, Charles River) for were randomly assigned into groups relating to MIA injection protocol and/or feeding groups. For MIA cohorts, the PBS group received an intraperitoneal (i.p.) injection of PBS at 5µl per gram body weight (5µl/g) at E15.5. The Poly I:C group received an i.p. injection of Poly I:C diluted to 4 mg/ml at 5µl/g at E15.5. The LPS group received an i.p. injection of LPS diluted to 0.024mg/ml at 5µl/g at E15.5. Time point and concentration of LPS injection was selected based on previous research which found corpus callosum defasciculation following LPS injection as described above (Pont-Lezica et al. 2014). Poly I:C concentration was selected based on previous unpublished data suggesting concentrations higher than 20mg/kg caused high rates of necrotic foetuses at E18.5. Microglia were also found to begin accumulating in the septal region at E15.5 in chapter 3 (section 3.3.1.2) suggesting that MIA during this time may affect septal microglia. For Maternal Obesity Maternal Infection (MOMI) cohorts, the PBS group received an i.p. injection of PBS at 5µl/g at E12.5. The MIA group received an i.p. injection of Poly I:C diluted to 4 mg/ml at 5µl/g at E12.5. The MCD group received *ad libitum* access to a low fat diet (13.5% of calories from fat, LabDiet, 5001). The 260HF group received *ad libitum* access to the butter based high fat diet described in chapter 4 (60% calories from fat, SafeDiets, 260HF).

For the MOMI cohort, mice were treated as described in chapter 4 (section 4.2.1.). For MIA and MOMI cohorts, dam temperature was recorded using a laser thermometer pointed under the tail immediately before and 3 hours after injection. Blood samples were taken from each dam and all foetuses together then stored at -80°C. Dam weight was also recorded immediately before and 24 hours after injection. GraphPad Prism 9 was used for statistical analysis of weight and temperature differences and graph production.

5.2.2. Microscopy and Image Analysis

5.2.2.1. Foetal Measurements

Foetal measurements were taken as described in chapter 4 (section 4.2.2.1).

5.2.2.2. Corpus Callosum Measurements

Corpus callosum measurements were taken as described in chapter 4 (section 4.2.2.2).

5.2.2.3. Dectin-1 Cell Counting

Dectin-1 expression data was produced as described in chapter 4 (section 4.2.2.5).

5.2.3. Microscopy and Image Analysis

Single cell sequencing results follow on from those presented in chapter 2 (section 2.3.3), therefore all methods are as described in chapter 2 (section 2.2.5).

5.2.4. Statistical Analysis

Statistical analysis was performed as in chapter 2 (section 2.2.6).

5.2.4.1. Replicates

Replicates were defined for cell counting experiments as described previously in section 2.2.6.1.

For experiments involving the measurement of dams, embryos per litter and number of embryos replicates were defined as in section 4.2.3.1.

5.3. Results

5.3.1. Establishing a Model for Maternal Immune Activation

There are two substances commonly used to induce an immune response: lipopolysaccharide (LPS) – a bacterial cell wall protein used to simulate bacterial infection; Polyinosinic:polycytidylic acid (Poly I:C) – a chemically synthesised mimic of viral double stranded RNA used as a proxy for viral infection (Chow et al. 2016; Bertani and Ruiz 2018). Given that each of these molecules simulates different types of infection, with LPS binding toll-like receptor 4 and Poly I:C binding toll-like receptor 3, they each produce divergent cytokine responses in the recipient (Bao et al. 2022b). They also each have differing effects on offspring behaviour and development (Arsenault et al. 2014). In this study both LPS and Poly I:C were used in order to compare the differing effects of bacterial and viral infection on foetal development, corpus callosum formation and developmental microglia.

Additional variation in cytokine response and offspring outcome is brought about by different doses and batches of LPS and Poly I:C, the injection day and administration route for mice undergoing MIA (Bao et al. 2022b). This study is centred around the involvement septal and glial wedge hotspot microglia in corpus callosum development. Given that these microglia begin to accumulate and differentiate to express their respective markers from E15.5 onwards, this time-point was selected for MIA induction. Furthermore, this is a crucial time-point for corpus callosum formation as axons are beginning to cross the midline and establish correct positioning. Inflaming the maternal environment at this time, via LPS IP injection, was previously shown to induce corpus callosum defasciculation (Pont-Lezica et al. 2014). LPS dose size and administration route was matched to this study since this was evidently sufficient to affect corpus callosum development. Poly I:C dose size was selected by comparing a range of previous studies and carrying out some preliminary experiments to ensure dosage was not lethal to offspring. PBS injection is frequently used as a control to correct for any effects of the injection itself.

When mounting an immune response to infection, like humans, mice undergo changes in body temperature. This is therefore a useful tool to measure whether an immune response was successfully induced. Although initially the MIA model was associated with a period of increased temperature followed by a decrease in temperature, many studies since have

observed a decrease in dam temperature 3-4 hours post injection (Smith et al. 2007; Estes et al. 2020). It may be that differing sources of poly I:C are responsible for this variation as has been reported previously (Estes et al. 2019). In addition to a decrease in maternal temperature, pregnant rodents also often fail to gain the usual amount of weight 24 hours post-injection (Lins et al. 2019; Estes et al. 2020). This is thought to be due to reduced food consumption, possibly as a result of sickness behaviour (Bronson et al. 2011). Maternal temperature change 3 hours post-injection and weight change 24 hours post-injection were therefore measured to establish the effectiveness of poly I:C or LPS administration.

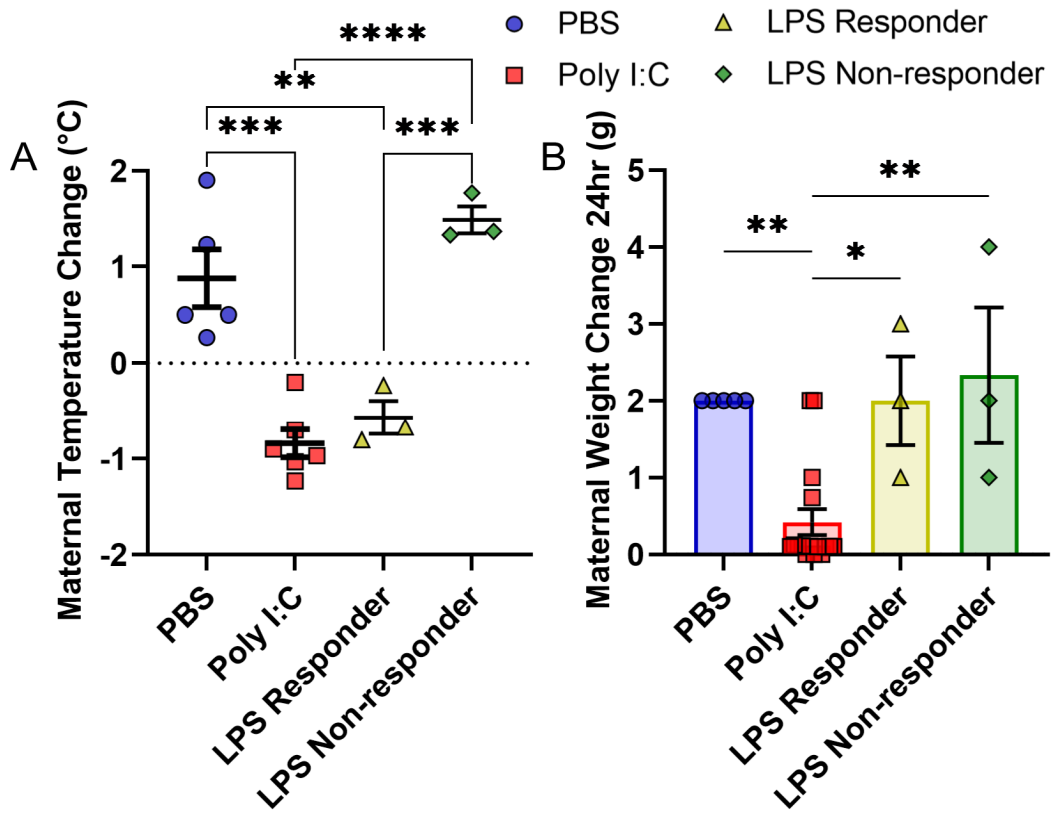

Figure 49: Maternal immune activation effected maternal temperature and weight gain.

A) Mean (+/- SEM) maternal temperature change 3 hours post injection. (One-way ANOVA (F = 24.22, p <0.0001), Tukey-Kramer post-hoc test, **** = p <0.0001, *** = p <0.0006, ** p =0.0042). **B)** Mean (+/- SEM) maternal weight change 24 hours post injection (One-way ANOVA (F = 10.48, p =0.0002), Tukey-Kramer post-hoc test, ** = p <0.0032, * = p =0.0162). PBS n=5; Poly I:C n=6; LPS responder/non-responder n=3.

Following injection with PBS, dams had a mean increase in temperature of 0.88°C. This was significantly higher (One-way ANOVA (F = 24.22, p <0.0001), Tukey-Kramer post-hoc test, p =0.0006) than Poly I:C injected dams which decreased in temperature by on average 0.84°C. Interestingly, half of the dams injected with LPS increased in temperature similar to PBS injected dams whilst the other half decreased to a similar level to Poly I:C injected dams. Such divergent response to LPS injection has been reported previously in the literature, with some mice having differing levels of immune response to pathogen challenge.

Maternal weight change measures also suggested some disruption to the maternal environment. PBS injected dams each gained 2g 24 hours after injection whilst Poly I:C dams gained significantly less (One-way ANOVA (F = 10.48, p =0.0002), Tukey-Kramer post-hoc test, p =0.0028), averaging at 0.42g. This time both LPS groups had mean values comparable to PBS injected dams, reaching almost exactly 2g. These LPS injected dams had a higher in group variance, as clear from Figure 49B, although standard deviations did not differ significantly (Brown-Forsythe test (F = 1.798, p =0.1757)). This perhaps suggests some more mild or highly variable effect on the maternal condition in LPS groups. These findings are in contrast to previous reports which found reduced weight increase in LPS injected pregnant dams but not those injected with Poly I:C (Arsenault et al. 2014). These were however performed on C57BL/6 mice rather than CD1 mice used here and an alternative administration route was used.

Combined, these readings demonstrate the effectiveness of Poly I:C injection in inducing MIA and that LPS injection, whilst able to induce an possible inflammatory response in some mice was more dependent on individual variation. Even in LPS responders it can be suggested that the immune response was less strong than Poly I:C since no reduction in maternal weight gain was observed.

5.3.2. MIA Offspring Gross Measurements

Initial results suggested that MIA was successfully induced both through the injection of Poly I:C and through LPS injection. Gross foetal measurements taken from E18.5 foetuses of MIA dams allowed the investigation of any concomitant impacts on offspring development. Measurements were taken as described in the previous chapter to establish any impact on foetal survival to term, overall development and neurogenesis.

Interestingly, the mean litter size of PBS injected dams was significantly smaller than poly I:C and LPS responder groups (One-way ANOVA (F = 6.210, p = 0.0075), Tukey-Kramer post-hoc test, p < 0.024) by 4.87 and 5.2 respectively (Figure 50). This was unexpected given that reduced litter size has been observed in previous studies of both Poly I:C and LPS MIA (Bao et al. 2022b). Decreased PBS litter size perhaps indicates some impact of the injection itself on offspring. With IP injections coming in close proximity to developing foetuses in the uterus. This is somewhat corroborated by the elevated number of necrotic foetuses relative those observed without injection in chapter 4. Aside from this, mean litter size remained consistent between groups at around 13.5 foetuses. Each MIA groups had a greater than 0 number of nectroic foetuses, again suggesting some disruption to in-utero development. Highest individual numbers of necrotic foetuses were both found in the Poly I:C group, perhaps suggesting maximal disruption to foetal survival within this group.

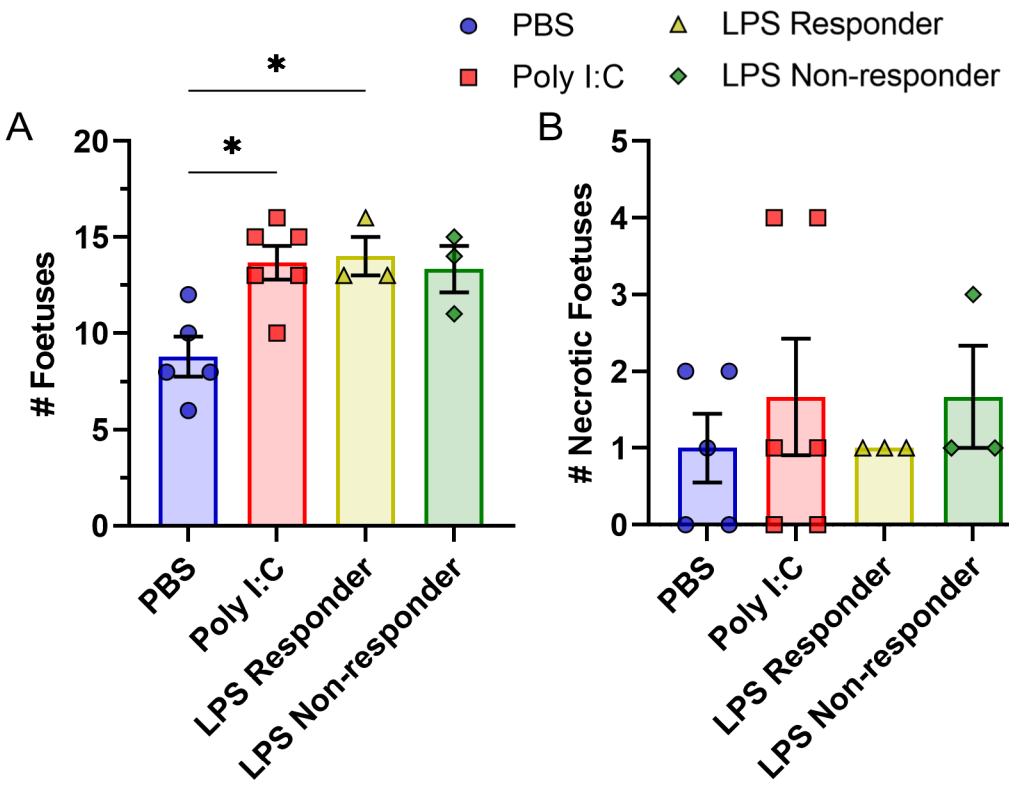

Figure 50: PBS injected dams had a smaller litter size than MIA groups without affecting number of necrotic foetuses.

A) Mean (+/- SEM) number of E18.5 foetuses per litter. (* = One-way ANOVA (F = 6.210, p = 0.0075), Tukey-Kramer post-hoc test, p < 0.024) **B)** Mean (+/- SEM) number of necrotic foetuses per litter. PBS n=5; Poly I:C n=6; LPS responder/non-responder n=3.

Overall foetal development, as measured by foetal body weight, showed significant variation between most groups (Figure 51). PBS group mean body weight was 1.393g, significantly higher (One-way ANOVA (F = 59.72, p <0.0001), Tukey-Kramer post-hoc test, p <0.0001) than Poly I:C exposed foetuses at 1.247g and significantly lower (One-way ANOVA (F = 59.72, p <0.0001), Tukey-Kramer post-hoc test, p = 0.0015) than LPS responder and non-responder groups at 1.525g and 1.491g respectively. Whilst offspring body weight decrease has been repeatedly reported in the literature (Arsenault et al. 2014; Li et al. 2018; Bao et al. 2022b), an increase in offspring body weight has not been reported as a result of LPS MIA. This increase in body weight is difficult to interpret due to its presence in both responder and non-responder groups. It may be that the PBS group itself is in fact unusually low. This is somewhat corroborated by the previously described decrease in mean litter size indicating some defect within these mice.

In a reversal of the foetal body weight pattern, Poly I:C group mean brain weight is significantly higher (One-way ANOVA (F = 22.72, p <0.0001), Tukey-Kramer post-hoc test, p <0.0001) than all other groups at 0.1172g (Figure 51B). This is 0.0126g higher than PBS, 0.087g higher than LPS responder and 0.0102g higher than LPS non-responder groups. This reflects the possibility that neurodevelopment was protected from the detrimental impact of Poly I:C on development as a whole, perhaps overcorrecting in allocation of resources to increase brain weight. These findings are in contrast to an MIA study performed in rats which produced reduced offspring brain weight, however this has not been measured in mouse (Kowash et al. 2019). Reflecting the described differences in body and brain weight, mean brain to body weight ratio was unsurprisingly significantly higher (One-way ANOVA (F = 73.05, p <0.0001), Tukey-Kramer post-hoc test, p <0.0001) in Poly I:C exposed foetuses relative to all other groups. This again reflects the developmental protection afforded to the brain from more extreme detrimental conditions found thin the poly I:C group.

Interestingly, in Figure 51D LPS groups both display higher mean cortex areas than the PBS group by approximately 0.9mm^2. This is surprising given that brain weights were highly comparable between these groups. Rodent cortical neurogenesis, like human neurogenesis, occurs across a caudo-dorsal gradient with caudal regions forming first. In rodents the first cortical regions initiate neurogenesis around E12 and cease by E16, whilst more dorsal regions such as the occipital cortex start at a similar time but neurogenesis proceed over a longer period (Chen et al. 2017). Oligodendrogenesis on the other hand occurs in three

waves in the mouse. The second wave begins at approximately E15 in dorsal regions of the forebrain (Chen et al. 2017). It was recently reported that Poly I:C MIA induced an increase in oligodendrocyte precursor numbers (Canales et al. 2021). It may be that in this study LPS MIA induced an increase in oligodendrocyte numbers, which in turn increased forebrain size.

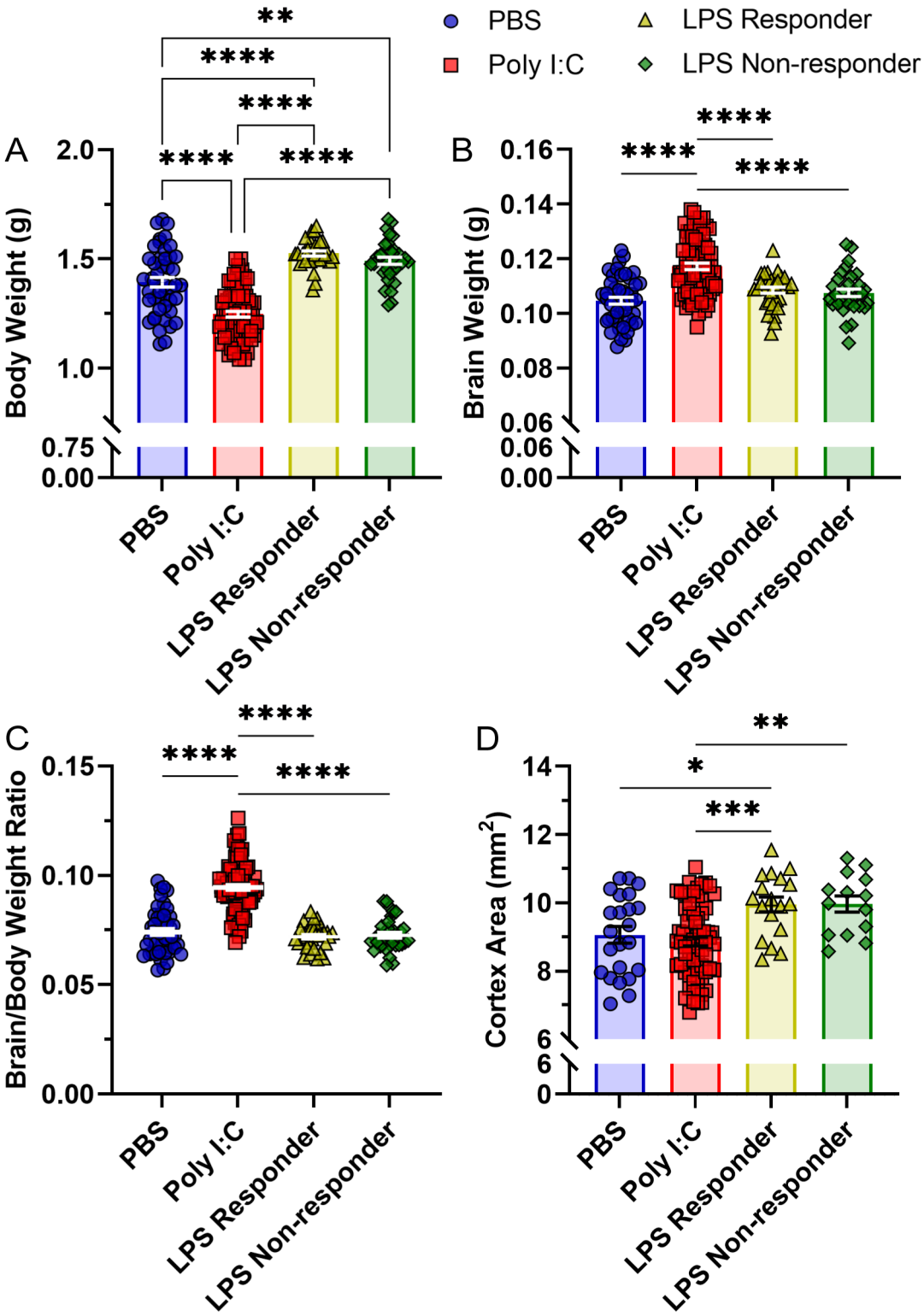

Figure 51: Brain and body measurements were affected by maternal immune activation.

A) Mean (+/- SEM) E18.5 foetus body weight in grams (One-way ANOVA (F = 59.72, p <0.0001), Tukey-Kramer post-hoc test, **** = p <0.0001, ** = p = 0.0015). **B)** Mean (+/- SEM) E18.5 foetus brain weight in grams (**** = One-way ANOVA (F = 22.72, p <0.0001), Tukey-Kramer post-hoc test, p <0.0001). **C)** Mean (+/- SEM) E18.5 foetus brain to body weight ratio (**** = One-way ANOVA (F = 73.05, p <0.0001), Tukey-Kramer post-hoc test, p <0.0001). **D)** Mean (+/- SEM) E18.5 foetus cortex area in mm^2. (One-way ANOVA (F = 7.934, p <0.0001), Tukey-Kramer post-hoc test, *** = p =0.0009, ** =0.0031, * =0.0404) PBS n=68; Poly I:C n=82; LPS responder n=34; LPS non-responder n=34.

LPS data for this figure was produced by Ashmee Almeida and Mayur Shetty.

5.3.3. MIA Offspring Corpus Callosum Defasciculation

Corpus callosum defasciculation was previously reported in C57BL/6 offspring exposed to MIA through LPS injection at E15.5 (Pont-Lezica et al. 2014). Data shown in Figure 52A replicates these findings, with LPS responder mean Nrp1/L1cam ratio reaching 0.58 compared to approximately 0.57 previously (Pont-Lezica et al. 2014). This was significantly higher than the PBS group (One-way ANOVA (F = 7.090, p =0.0022), Tukey-Kramer post-hoc test, p =0.0293) demonstrating defasciculation and disorganisation within the corpus callosum.

Nrp1/L1CAM ratio was not altered relative to the PBS group in Poly I:C or LPS non-responder groups, suggesting differing immune responses in these dams compared to LPS responders. Interestingly, mean L1CAM length was significantly higher (One-way ANOVA (F = 6.145, p =0.0042), Tukey-Kramer post-hoc test, p =0.0033) in the LPS non-responder group than the PBS group. This perhaps suggests some level of corpus callosum disruption in the LPS non-responder group, however some PBS data points in Figure 52B come close to LPS non-responder mean L1 length. A more likely explanation may therefore be the LPS non-responder groups differed in cutting angle or position within the corpus callosum than other groups.

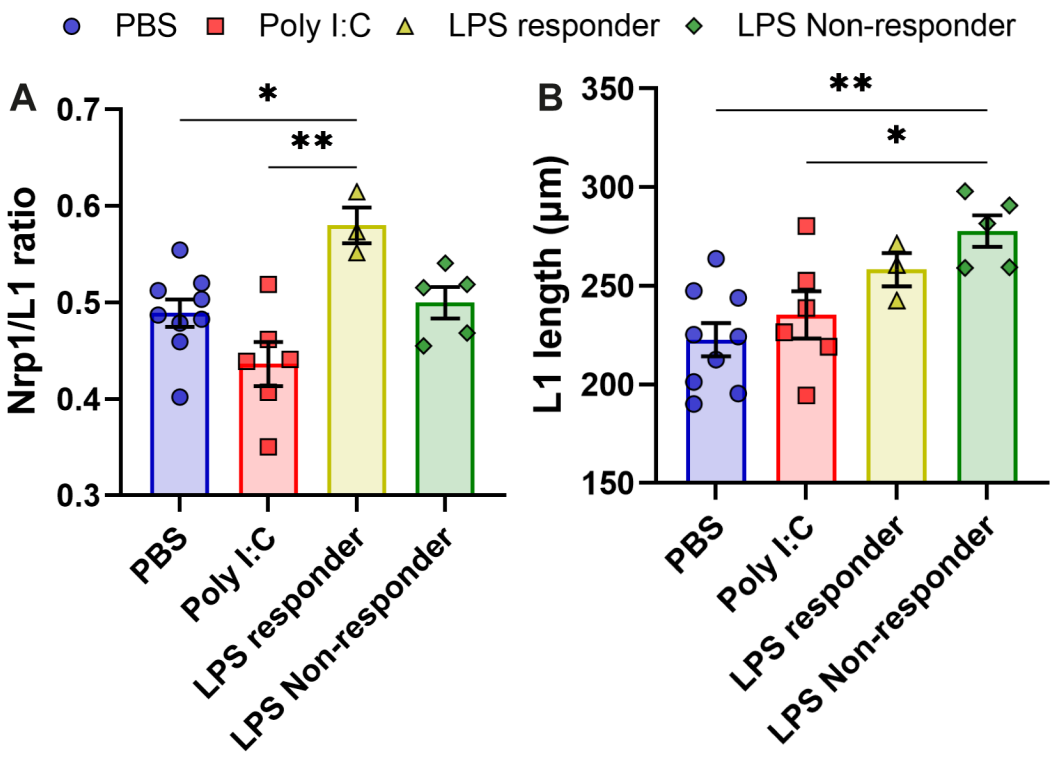

Figure 52: LPS responder foetuses were defasciculated whilst non-responders had a larger corpus callosum.

A) Ratio of fornix/caudal Nrp1 expression width at the midline relative to midline L1CAM expression (One-way ANOVA (F = 7.090, p =0.0022), Tukey-Kramer post-hoc test, ** = p =0.0011, * = p =0.0293). **B)** Length of fornix/caudal L1CAM expression width at the midline (One-way ANOVA (F = 6.145, p =0.0042), Tukey-Kramer post-hoc test, ** = p =0.0033, * = p =0.0418) **C-F)** Representative fluorescence images of the corpus callosum fornix region across maternal immune activation groups. PBS n=9; Poly I:C n=6; LPS responder n=3; LPS non-responder n=5.

LPS data for this figure was produced by Ashmee Almeida and Mayur Shetty.

5.3.4. Expression of Microglia Markers under MIA

As discussed in the introduction, microglia are affected by MIA in a variety of different ways. However, the impact of MIA on septal and glial wedge hotspot microglia has not yet been studied. As in chapter 4, the number of microglial cells was measured through iba1 immunohistochemistry to gauge changes in hotspot density and expression of dectin-1 was measured to assess changes in hotspot microglia differentiation. In Figure 53, values were excluded where the number of Iba1$^+$ cells fell below 10 in the glial wedges or 20 in the

septum as it was assumed that this was not a true representation of the microglial cluster. It was assumed that such low number of Iba1$^+$ cells arose through sub-optimal cutting angles failing to cut across the hotspot. This assumption is based on the high density of Iba1$^+$ observed in the glial wedge hotspots in chapter 3, which was higher still within the septum. The exception to this was in glial wedge LPS responders group, as mean Iba1$^+$ number was single digit for almost all measures taken. It was therefore assumed that rather than consistent alteration in cutting angle for 1 MIA group only, which seems unlikely, these differences were biologically relevant and all samples were included. Furthermore, data points were excluded where outside of 2 standard deviations from the mean. Again, it was assumed that technical variation accounted for this.

As shown in Figure 53, septal hotspot microglia were unaffected by MIA. There were no significant differences found between any groups for number of Iba1$^+$ cells, which varied by 27.05 between groups, or between proportion of dectin-1$^+$ labelled Iba1$^+$ cells, which varied by only 10.59% between groups. Glial wedge microglia did, however, vary based on MIA. Poly I:C MIA foetus mean Iba1+ cell number was 7.5 higher than the PBS group. Proportion of dectin-1$^+$ Iba1$^+$ cells was also higher than the PBS group by 14.83%. Although differences were not significant, they perhaps suggest some mild alteration in the glial wedge hotspot.

LPS responder foetuses had significantly fewer Iba1$^+$ cells in the glial wedge region than the PBS group by 12.4 (One-way ANOVA (F = 11.06, p =0.0005), Tukey-Kramer post-hoc test, * = p =0.0272). Proportion of dectin-1$^+$ microglia was also decreased although not significantly. These more consistent and extreme alterations in the LPS responder group indicates disruption to formation of the glial wedge microglia hotspot and differentiation of the specific subset of microglia found there. Interestingly, LPS non-responder foetuses had the same mean number of glial wedge Iba1+ cells as the Poly I:C group at 27.5. Proportion of dectin-1$^+$ Iba1$^+$ glial wedge cells was, however, relatively low at 17.69%. Taken together, Figure 53 results suggest Poly I:C and LPS MIA have differing effects on the presence and make-up of the glial wedge hotspots at E18.5.

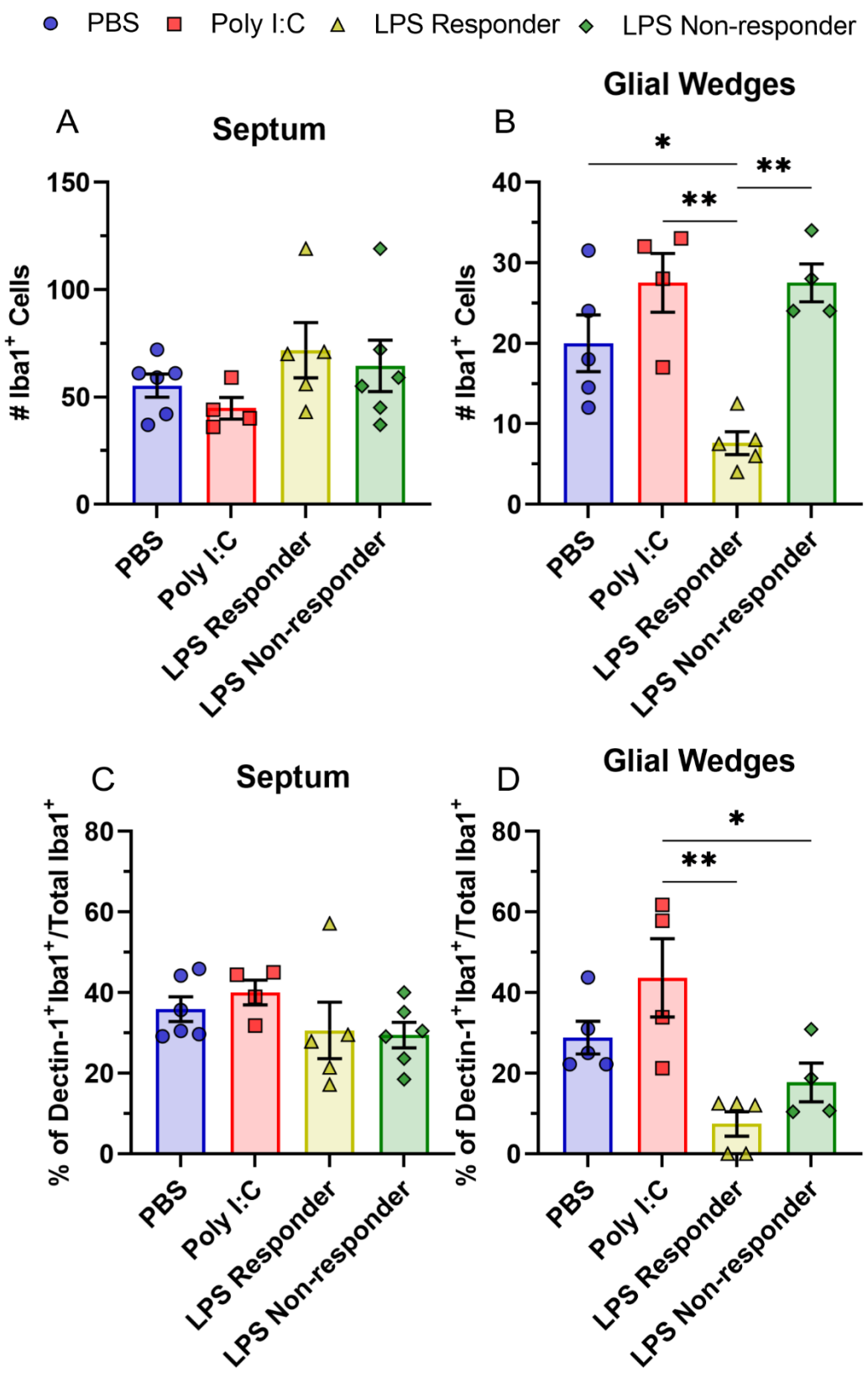
PBS
Poly I:C
LPS Responder
LPS Non-responder
A
Septum
Iba1+ Cells
150
100
50
0
B
Glial Wedges
Iba1+ Cells
40
30
20
10
0
*
**
**
C
Septum
% of Dectin-1+Iba1+/Total Iba1+
80
60
40
20
0
D
Glial Wedges
% of Dectin-1+Iba1+/Total Iba1+
80
60
40
20
0
*
**

Figure 53: Glial wedge microglia number and dectin-1 expression was affected by MIA unlike septal microglia.

A-B) Mean (+/- SEM) number of Iba1$^+$ cells in the septum and glial wedges of foetal brains from each maternal immune activation group (One-way ANOVA (F = 11.06, p =0.0005), Tukey-Kramer post-hoc test, ** = p =0.0012, * = p =0.0272). **C-D)** Mean (+/- SEM) percentage of Iba1$^+$ cells expressing dectin-1 in the septum or glial wedges (One-way ANOVA (F = 7.801, p =0.0027), Tukey-Kramer post-hoc test, ** = p =0.0020, * = p =0.0323). PBS n=6; Poly I:C n=4; LPS responder n=5; LPS non-responder n=6.

LPS data for this figure was produced by Ashmee Almeida and Mayur Shetty.

5.3.5. Microglial Transcription Profile under MIA

5.3.5.1. Cortical microglia expression profile

Further to the transcription profile data on microglia in control conditions covered in chapter 1, RNA sequencing experiments provided a complex pool of information from which to draw insights on the effects of MIA on microglia. As discussed previously, cortical and dissected brain samples self-segregate into two clear groups of clusters (Figure 54B). When comparing samples based on their MIA status, however, there is a less obvious separation of conditions. This is made clear from Figure 54D, where the majority of clusters show a predominant contribution from MIA litters, but 9 of these 22 clusters contain at least 10% of cells from control brains.

Cortical homeostatic clusters 2 and 3, contain at least 11% of cells from each MIA condition – Poly I:C and LPS. As discussed in chapter 1, these clusters share many similarities with homeostatic microglia in cluster 1, with the exception of having marginally increased expression of inflammation related genes. Cluster 1 is almost entirely composed of cells from control samples, at 94.2%, dropping to 11.7% and 24.2% of cells in clusters 2 and 3. Homeostatic cluster 1 could therefore represent the control cortical microglia subtype at E18.5. MIA could be increasing the differentiation of microglia into homeostatic clusters 2 and 3. LPS may be marginally more influential in this transition since clusters 2 and 3 were more composed of cells from LPS than PIC litters at 58.6% and 42.3% respectively. Only 31 genes were identified via differential expression analysis between clusters 3 and 1; however, MEA suggests cluster 3 expresses more inflammatory genes at the highest levels. The inflammatory gene enrichment score of cluster 3 was 10.76 higher than cluster 1 (Annex Table 3). Cluster 2 appears slightly more inflammatory than cluster 1 in MEA with a 1.13

higher enrichment score for inflammatory genes. Such a small number of differentially expressed genes suggests ORA may not be reliable and that clusters 1, 2 and 3 are related.

Homeostatic clusters 7 and 8 differ from other cortical clusters in that they are over 95% composed of cells from either PIC or LPS groups respectively. Differential expression analysis suggests that each of the homeostatic groups are highly similar to each other. There were only 189 genes differentially expressed between clusters 1 and 7 with a maximum of 0.333 log fold change. The GO terms 'phagocytosis' with enrichment ratio of 4.56, and 'ameboidal-type cell migration' at 3.43 were identified through ORA of genes differentially upregulated in cluster 1. Integrin subunit gene *Itgb2* was present in both of these terms. 'Interleukin-12 production' was enriched at a ratio of 6.20 in genes differentially upregulated in cluster 7, involving general cell signalling genes *Mapk14* and *Prkcd*. Between homeostatic clusters 1 and 8, there were 183 differentially expressed genes at a maximum of 4.5 log fold change. ORA identified GO terms involving metabolic processes, microtubule and actin cytoskeleton reorganisation as being enriched in both positive and negative sides of this differential expression dataset.

Interestingly, clusters 7 and 8 differ more from each other in expression profile than they do to control dominated cluster 1. 390 genes were differentially expressed over 0.25 log fold change between clusters 7 and 8 with a maximum of 0.565 log fold change. However, as when comparing clusters 1 and 8, the majority of these involved metabolic processes or cytoskeleton reorganisation. Response to stimulus GO terms such as 'response to fungus' and 'response to oxygen levels' featured amongst both sides of the differentially expressed genes. MEA also found that cluster 8 is more enriched for 'reactive' GO terms than cluster 7, amongst the most highly expressed genes (Annex Table 4). This perhaps indicates that clusters 7 and 8 have differentiated to react to different stimuli.

Clusters 15, 16, 17 and 20 contain small numbers of cells almost exclusively from one sample of LPS MIA exposed cortices. There are several explanations for small numbers of cells, less than 90 in each cluster, expressing genes associated with previously identified injury clusters. This may be due to LPS induced MIA or differences in the experimental technique affecting this particular sample differently from the others. Cells falling into the choroid plexus cluster may indicate differences in the dissection process perhaps including a larger region also containing choroid plexus material.

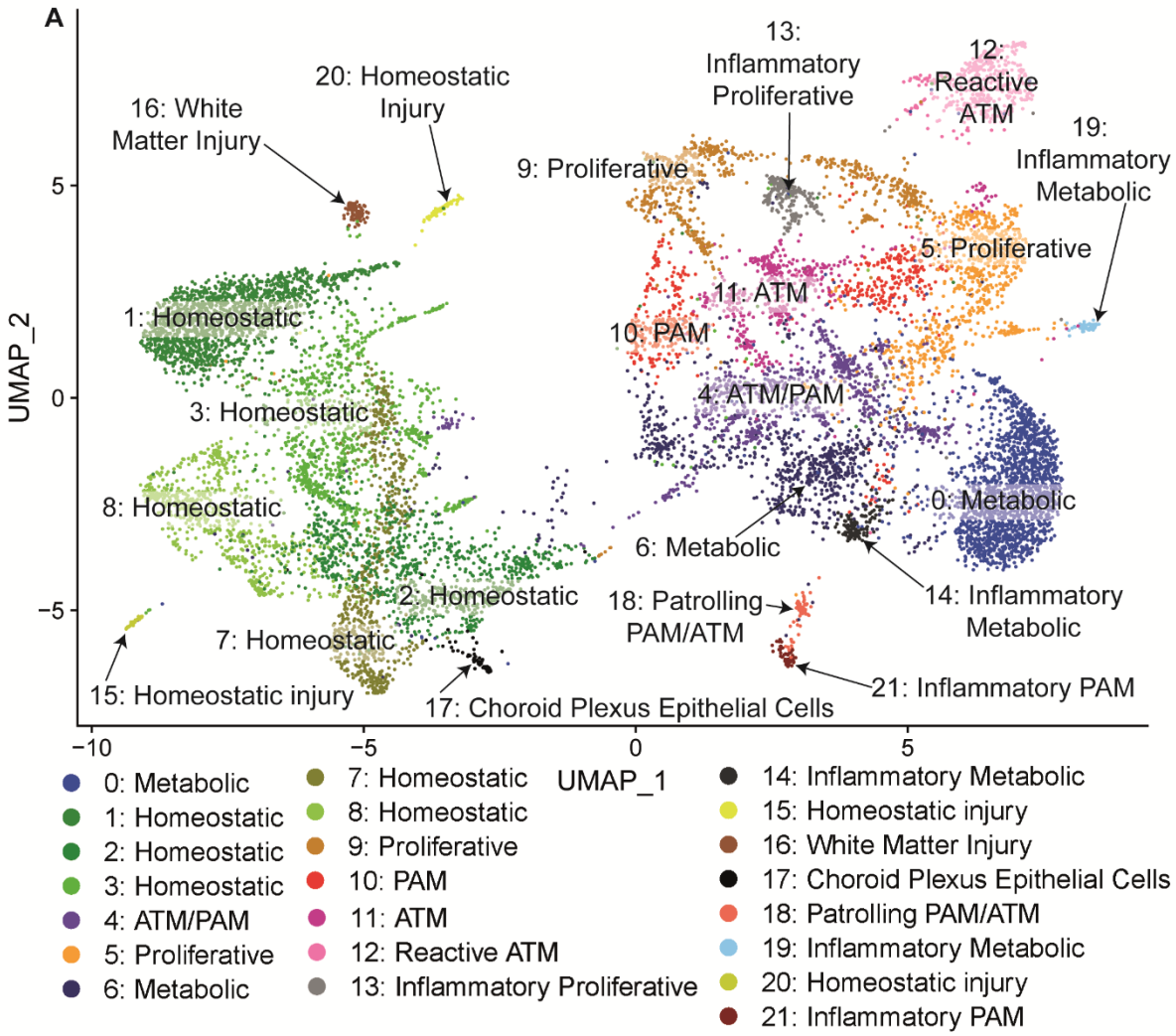
A
16: White Matter Injury
20: Homeostatic Injury
13: Inflammatory Proliferative
12: Reactive ATM
19: Inflammatory Metabolic
9: Proliferative
5: Proliferative
11: ATM
10: PAM
1: Homeostatic
3: Homeostatic
4: ATM/PAM
8: Homeostatic
0: Metabolic
6: Metabolic
2: Homeostatic
18: Patrolling PAM/ATM
14: Inflammatory Metabolic
7: Homeostatic
15: Homeostatic injury
17: Choroid Plexus Epithelial Cells
21: Inflammatory PAM
UMAP_2
UMAP_1
0: Metabolic
1: Homeostatic
2: Homeostatic
3: Homeostatic
4: ATM/PAM
5: Proliferative
6: Metabolic
7: Homeostatic
8: Homeostatic
9: Proliferative
10: PAM
11: ATM
12: Reactive ATM
13: Inflammatory Proliferative
14: Inflammatory Metabolic
15: Homeostatic injury
16: White Matter Injury
17: Choroid Plexus Epithelial Cells
18: Patrolling PAM/ATM
19: Inflammatory Metabolic
20: Homeostatic injury
21: Inflammatory PAM

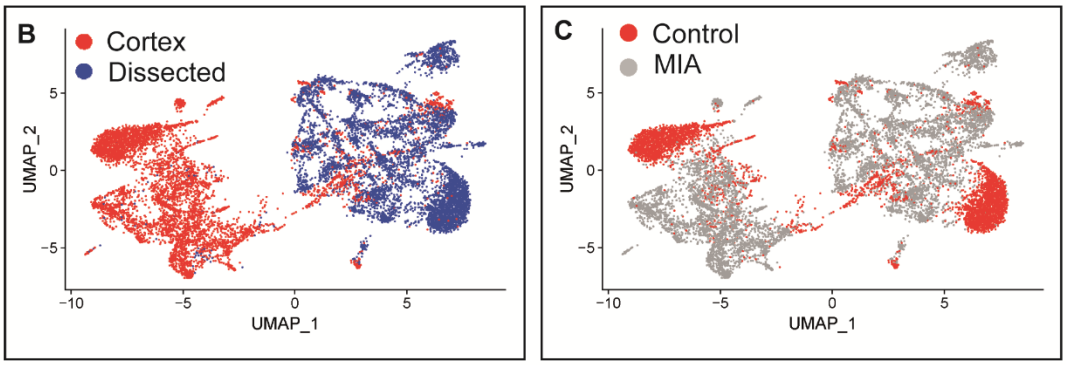
B
Cortex
Dissected
C
Control
MIA
UMAP_2
UMAP_1

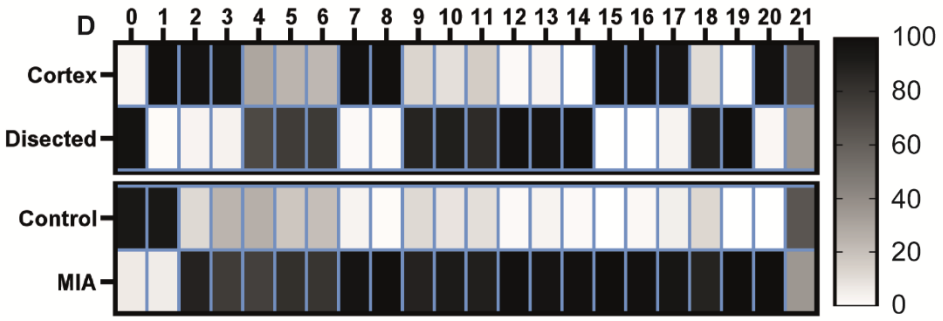
D
0 1 2 3 4 5 6 7 8 9 10 11 12 13 14 15 16 17 18 19 20 21
Cortex
Disected
Control
MIA
100
80
60
40
20
0

Figure 54: There are shifts in microglial populations following maternal immune activation.

A) UMAP plot showing 21 clusters identified through single cell sequencing of cells isolated from E18.5 brain samples. Clusters were labelled using ScType automated labelling system, previous single cell sequencing data and results of up-regulated gene over-representation analysis. **B)** UMAP plot from A highlighting cells taken from cortical (red) or dissected (blue) samples. **C)** UMAP plot from A highlighting cells taken from control (red) or MIA (grey) samples. **D)** Heatmap of the normalised percentage of cells assigned to each cluster from each sample type. *ATM – Axon Tract associated Microglia; MIA – Maternal Immune Activation; PAM – Proliferative-region Associated Microglia*

5.3.5.2. Metabolically active microglia expression profile

Clusters predominantly composed of cells from dissected midline regions had varying proportions of cells from each MIA condition. As for cortical clusters, one cluster was over 93% composed of control cells; this was metabolic cluster 0. Metabolic cluster 6, on the other hand, is split between each of the MIA conditions but totals far fewer cells than cluster 0. This suggests that MIA induces a shift away from the metabolically active microglia phenotype, and those metabolically active microglia that are present during MIA differ from those under control conditions.

Although both metabolically active clusters 0 and 6 appear similar in their MEA scores, according to Annex Table 4, these groups differentially expressed 281 genes with a maximum log fold change of 0.469. ORA suggests that cluster 6 may be more inflammatory, as the GO term ‘cell activation involved immune response’ was over represented with an enrichment ratio of 3.3 in cluster 6. This includes the toll-like receptor gene *CD180* and interleukin 4 receptor gene *Il4ra*. Increased inflammatory gene expression is unsurprising in microglia exposed to MIA, more of which are found in cluster 6. This inflammatory reaction does not appear to interfere with the most highly expressed developmental genes, which are expressed in similar numbers across clusters according to the MEA score in Annex Table 4.

Inflammatory metabolic cluster 14 was composed almost entirely of cells from MIA brains with 49.2% from PIC brains and 50% from LPS exposed brains. Comparing both metabolic clusters 0 and 6 with inflammatory metabolic cluster 14 reveals, there was an increased level

of inflammatory gene expression in cluster 14. MEA reveals a higher number of inflammation related genes, and a higher level of inflammatory gene enrichment score in cluster 14 than in both clusters 0 and 6. This analysis also showed cluster 14 had a much lower level of metabolism and development related gene expression than clusters 0 and 6, but higher levels of migratory gene expression.

Differential expression analysis identified 1918 differentially expressed genes up to 0.829 log fold change between clusters 0 and 14. The GO term 'cell cycle phase transition' was significantly overrepresented (Hypergeometric testing, p =0.00026) amongst genes differentially expressed in cluster 0 compared to cluster 14. 'Regulation of mitotic cell cycle' was also enriched in these genes. This could indicate higher levels of proliferation amongst cluster 14 cells. The higher number of differentially expressed genes between clusters 0 and 14 warrants GSEA. This analysis identified 3 of the top 20 GO terms involving 'development' amongst cluster 0 upregulated genes and 4 'metabolic process' GO terms of the top 20 upregulated in cluster 14. Interleukin-6 and -12 production GO terms were upregulated for cluster 0. Findings indicate that cluster 0 may be more effective at developmental processes than cluster 14, this is supported by MEA (Annex Table 4). MEA does not, however, support GSEA findings that cluster 14 may express more metabolism associated genes.

When comparing cluster 6 and cluster 14, there were 1850 differentially expressed genes between these clusters. Whilst ORA on this dataset identified microtubule and actin organisation GO terms, GSEA provided similar results to cluster 0 and 14 comparisons. Increased development associated GO terms were identified in cluster 6 as well as IL-6 and IL-12 production GO terms. The 'interleukin-2 production' GO term was, however, increased in cluster 14 with an enrichment score of 1.83.

5.3.5.3. ATM/PAM expression profile

Unlike metabolically active microglial clusters, ATM or PAM labelled clusters are composed of a more mixed set of cells across the various MIA conditions. Cluster 4 for example, labelled as ATM/PAM because of high levels of both ATM and PAM associated gene expression (Annex Table 3), was 26.1% control, 29.1% LPS and 44.8% PIC. Amongst the most highly expressed genes in the cluster, relatively few of them are related to inflammation, development, metabolism or migration in comparison to other clusters (Annex Table 4).

Comparing ATM/PAM cluster 4 with PAM cluster 10 reveals 644 differentially expressed genes with a maximum log fold change of 0.593. GSEA analysis of these genes mirrors MEA in that cluster 10 appears to express more genes associated with development and metabolism. Of the top 20 GO terms enriched in cluster 10 expressed genes, 5 involve 'development' and 3 include 'metabolic'.

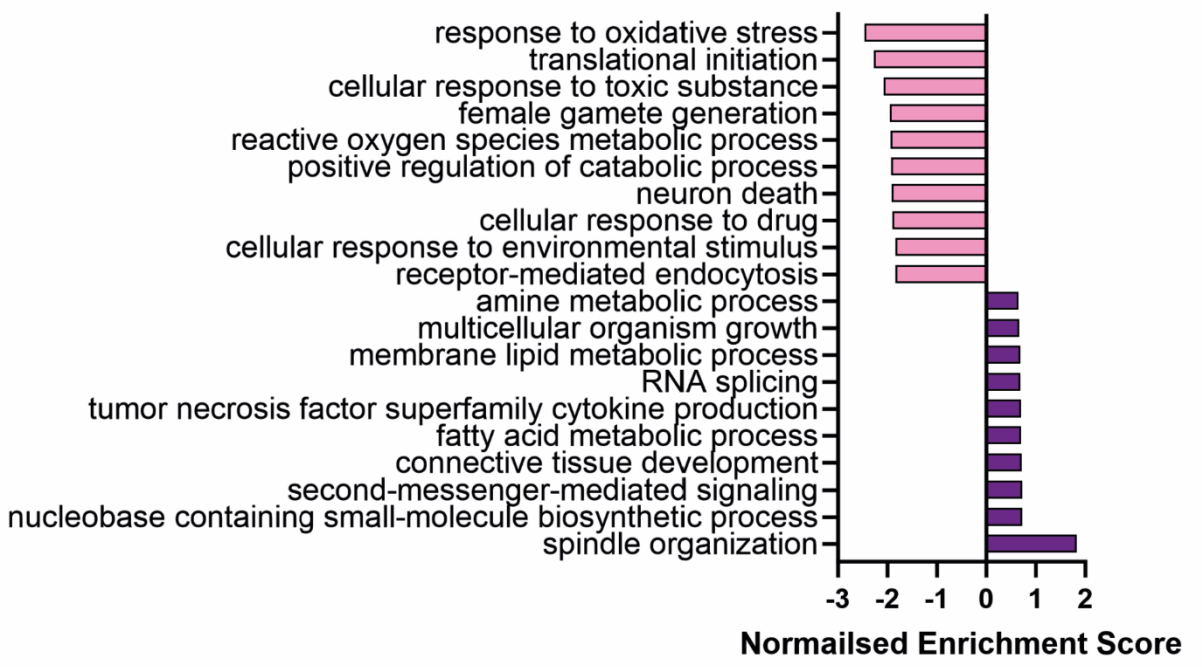

Figure 55: GSEA found 'response to oxidative stress' as most differentially expressed by cells in cluster 11 compared with cluster 4.
Bar chart showing top 10 GO terms identified through gene set enrichment analysis of genes differentially expressed between cluster 4 (positive values) and cluster 11 (negative values).

Comparing ATM/PAM cluster 4 with ATM cluster 11 produced 714 differentially expressed genes up to 0.69 log fold change. GSEA found 'response to oxidative stress' significantly enriched amongst cluster 11 cells in Figure 55 (Hypergeometric testing, p <0.0001). Other GO terms included in the 'reactive' group for MEA (Annex Table 4) were amongst the top 20 GO terms enriched in cluster 11 according to ORA results. Whilst this could mean ATM are more responsive to stimuli *in vivo*, one of the top 20 GO terms enriched in cluster 11 was 'response to mechanical stimulus'. This could be an artefact of tissue dissociation during the

experiment. The significantly upregulated (Hypergeometric testing, p =0.0001175) 'regulation of apoptotic signalling pathway' in ORA of genes differentially expressed by ATM cluster cells supports this hypothesis.

Differential expression analysis between PAM cluster 10 and ATM cluster 11 found 787 differentially expressed genes up to 0.577 log fold change. This suggests ATM and PAM clusters 4, 10 and 11 are almost equally different. GSEA and ORA of these differentially expressed genes identified GO terms describing a broad range of biological processes. Of the top 40 GO terms enriched on either side of GSEA, 26 had enrichment scores of below 1. This suggests there is no clear organised process of differentiation between these two clusters focused on a specific set of biological processes. The GO term 'response to alcohol' was marginally enriched in cluster 11 cells at 0.56 enrichment score, suggesting experimental manipulation may be a source of differences in gene expression between clusters 10 and 11.

Reactive ATM cluster 12 was labelled due to high expression of genes falling into response to stimulus GO terms amongst the most highly expressed genes. The UMAP plot shown in Figure 54A suggests reactive ATM segregate from other ATM and PAM populations. This cluster is 98.2% composed of cells from one LPS MIA sample and is amongst the top 6 clusters in MEA for enrichment of apoptotic GO terms (Annex Table 4). This could mean that cluster 12 is composed of experimentally activated or apoptotic ATM cells. GSEA of genes differentially expressed between reactive ATM cluster 12 and ATM/PAM cluster 4 found 'protein localization to nucleus' was enriched in cluster 12, with enrichment score of 1.74. Of the top 20 GO terms enriched in cluster 4 cells, 8 relate to development. ORA of genes differentially expressed in cluster 12 found 'ATP hydrolysis coupled transmembrane transport' highly, with enrichment ratio of 5.24, although not significantly enriched. Given that ATP hydrolysis and protein transport to the nucleus are involved in apoptosis (Yuanming et al. 1999; Daugas et al. 2000), gene expression changes in cluster 12 cells may relate to apoptosis. In support of this, 'intrinsic apoptotic signaling pathway' was enriched in differentially expressed genes analysed through ORA with enrichment ratio of 2.01 in reactive ATM cluster 12 cells.

Patrolling PAM, so labelled due to similarities with PAM/ATM and patrolling monocyte populations, form a small cluster of 59 cells which appear distant from most other PAM or ATM clusters in UMAP plot Figure 54A. This cluster expresses slightly higher levels of

inflammation related genes at over log 5 fold change in MEA (Annex Table 4). However, apoptosis related GO terms were also enriched in MEA at a 5.63 enrichment ratio. Further to this, 'response to acid chemical' was found to be enriched through GSEA amongst the 2223 genes differentially expressed by cluster 18 compared to cluster 4. This suggests experimental manipulation may responsible to gene expression changes amongst cluster 18 cells.

Inflammatory PAM are another small cluster composed of 53 cells predominantly (64.2%) of cells from control samples. MEA puts this cluster amongst the highest levels of inflammatory gene expression, hence the inflammatory PAM label, and the lowest levels of developmental, metabolic and migratory go terms. 5327 genes were found to be differentially expressed between inflammatory PAM in cluster 21 and PAM/ATM cluster 4 up to 2.03 log fold change. GSEA revealed response to alcohol and osmotic stress were both upregulated in cluster 21, suggesting the gene expression profile of this cluster may also be as a result of the isolation and sequencing process.

5.3.5.4. Proliferative microglia expression profile

Proliferative clusters 5 and 9 contain at least 11% of cells from all three MIA conditions. Differential expression analysis between these two groups produced 1064 differentially expressed genes up to 0.690 log fold change. However, GSEA found all of the top 40 GO terms with the exception of 'fatty acid derivative metabolic process' in cluster 5, have an enrichment score less than 1.0 (Figure 56). This suggests differentially expressed genes are fairly evenly split across a broad range of unrelated functions. When considering the most highly expressed genes in MEA, cluster 5 is more enriched for genes involved in inflammation, whereas cluster 9 appears to express a low number of metabolism associated genes at the highest levels. Development and migration associated genes however, appear to be similarly expressed at the highest levels. Taken together this data suggests the two proliferative clusters are similar in their expression profile.

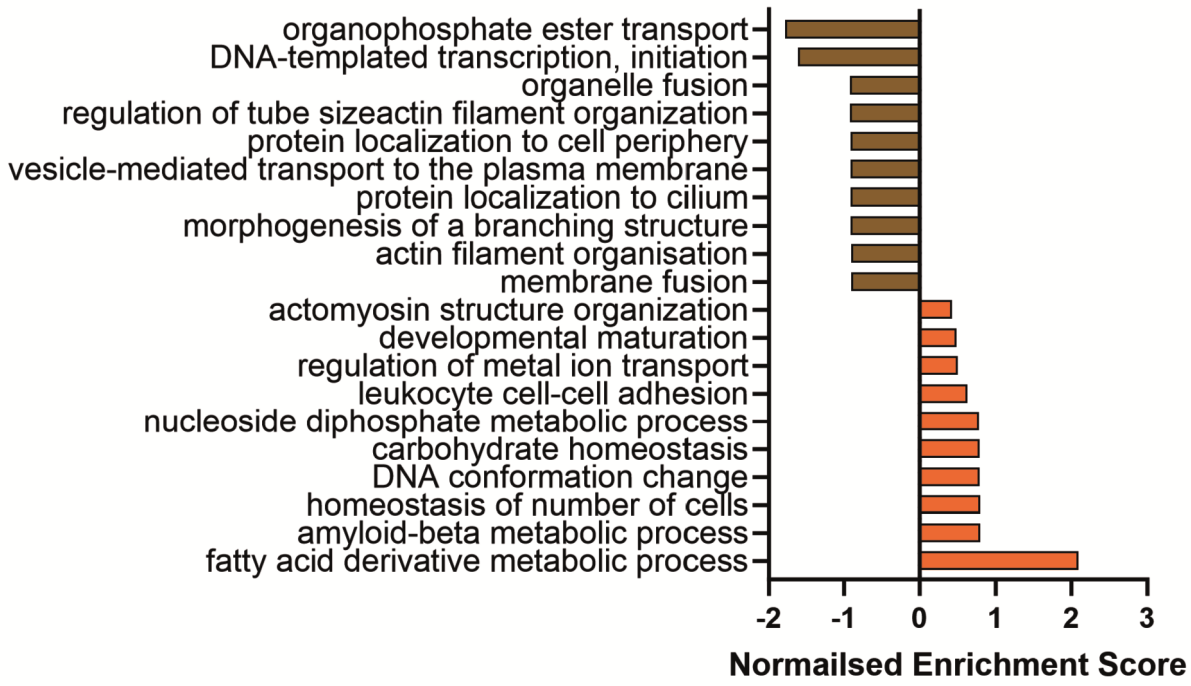

Figure 56: GSEA found most GO terms had an enrichment score below 1 when performed on genes differentially expressed between cluster 5 and 9.

Bar chart showing top 10 GO terms identified through gene set enrichment analysis of genes differentially expressed between cluster 5 (positive values) and cluster 9 (negative values).

5.3.5.5. Control, LPS and PIC comparison

Differential expression analysis found very few differences when comparing each MIA condition as a whole. However, the single cell sequencing technique allows more subtle differences between conditions to be detected, such as transitions between different microglial populations. Within the dissected septal region under control conditions 76.29% of cells were labelled as metabolically active. This proportion dropped to 24.54% in LPS MIA samples and 16.78% in PIC groups. Additionally, the inflammatory metabolic group contained only 1 control cell, but 124 LPS and 64 PIC cells. This amounts to 0.05%, 21.26% and 18.36% of CTL, LPS and PIC metabolically active groups respectively.

Table 6: Percentage of cells in each cluster belonging to each MIA condition

Cluster	0	1	2	3	4	5	6	7	8	9	10
Control	93.7	94.2	11.7	24.2	26.1	17.8	20.6	3.1	0.6	11.6	8.0
LPS	4.8	3.8	29.7	33.5	29.1	27.4	46.8	11.0	99.2	37.6	56.5
PIC	1.4	2.0	58.6	42.3	44.8	54.8	32.6	85.8	0.2	50.8	35.5

Cluster	11	12	13	14	15	16	17	18	19	20	21
Control	10.0	0.9	2.9	0.8	0.0	1.2	4.3	11.9	0.0	0.0	64.2
LPS	36.1	98.7	35.6	50.0	100.0	96.4	95.7	88.1	96.8	98.2	35.8
PIC	53.9	0.4	61.5	49.2	0.0	2.4	0.0	0.0	3.2	1.8	0.0

Shifts in microglial subtypes can also be seen amongst proliferative populations. Proliferative microglial cells make up 9.13% of control samples, 22.43% of LPS samples and 42.91% of PIC samples. Within the proliferative microglial subtype only 6 control cells were inflammatory proliferative whilst 73 were LPS and 126 were PIC reaching 2.66%, 13.69% and 14.14% of proliferative CTL, LPS and PIC clusters respectively.

ATM and PAM clusters appear to increase in prevalence as a result of both forms of MIA tested. These clusters formed 14.59% of control dissected region cells, 53.03% of LPS dissected region cells and 40.31% of PIC dissected region cells. Only 2 PIC cells fall into reactive, patrolling or inflammatory PAM/ATM groups whilst 46 are part of the control group and 524 were exposed to LPS MIA. Bringing these trends together, it appears as though either LPS or PIC MIA lead to a drastic shift in septal region microglial cells away from the metabolically active phenotype.

In cortical samples, MIA also had an effect on the prevalence of different microglial subtypes. 80.46% of cells isolated from control cortices clustered into homeostatic cluster 1, a cluster which itself contained very few cells, only 6.2%, from either MIA group. All other homeostatic clusters were predominantly composed of cells from MIA samples, as is clear from the heatmap in Figure 54D. With regard to homeostatic clusters 2 and 3, this may represent a shift to more inflammatory phenotypes, mentioned previously, as a result of MIA. Whilst clusters 2 and 3 contain a considerable number of cells from each MIA condition, cluster 7 is 85.8% PIC and cluster 8 is 99.2% LPS. This highlights the divergent effect of each inducer of MIA tested, not observed in the midline region. The remaining cortical clusters - homeostatic injury, white matter injury and choroid plexus epithelial cells, were each over 95% composed

of cells from LPS samples. Perhaps indicating a more detrimental effect of LPS MIA on cortical microglia differentiation than PIC, although each of these clusters contain fewer than 87 cells.

5.3.6. Establishing a Two Hit Model for Maternal Obesity and Immune Activation

As discussed, there is ample evidence associating maternal inflammation, both chronic and acute, with neurodevelopmental disorders (Han et al. 2021). Following on from the "three-hit hypothesis", the stacking of inflammatory insults to the maternal environment was studied here to examine whether this would result in worse outcome for offspring (Kim et al. 2015). Data shown in chapter 4 suggested high fat diet exposure may have been somewhat detrimental to offspring neurodevelopment. Prior to the study, it was anticipated that high fat diet combined with n-3 PUFA deficiency, as in 233HF/292HF diets, would be more detrimental than high fat diet with higher levels of n-3 PUFAs, as in 260HF diet. Indeed, n-3 PUFAs have been shown to attenuate the effects of MIA postnatally (Basil et al. 2018). In order to reduce the likelihood of all offspring failing to survive to E18.5, the least detrimental of these high fat diets: 260HF diet, was selected for combination with MIA. Mice were kept on the diet for 8 weeks prior to breeding. Poly I:C injection was selected to induce MIA due to the more consistent effects demonstrated on both dam and offspring In this chapter as well as the higher prevalence of this method in previous literature. The C57BL/6J strain is also more frequently used in MIA studies, with poly I:C injection often taking place at E12.5. This protocol was therefore applied to mice in this chapter alongside 260HF diet feeding. Embryos were then collected for analysis 24 hours after injection at E13.5 or at the end of gestation at E18.5. This cohort was name Maternal Obesity Maternal Infection (MOMI).

Following 8 weeks of *ad libitum* access to 260HF diet, dams had on average gained significantly more weight than those consuming control diet (Unpaired t-test: $t(3.048) = 29$, $p = 0.0049$). Interestingly, HFD exposed dams divided into two groups: those that gained 3g or less, similar to the MCD group, and those that gained 6g or more (Figure 57A). This highlights the metabolic differences across different dams even despite their high genetic similarity and same origin. Mice that gained more weight were divided equally alongside mice that gained less weight between each MIA or PBS group, as shown in Figure 57A. Fat weight as a proportion of total dam weight followed a similar pattern to overall dam weight gain, with

260HF dam mean significantly higher than MCD dam mean (Unpaired t-test: $t(2.842) = 28$, $p = 0.0083$). As previously, dams failed to maintain any significant differences in weight to sacrifice. This was even the case where mice were sacrificed earlier at E13.5. Similar restoration of dam weight during pregnancy has been reported in MIA literature (Arsenault et al. 2014).

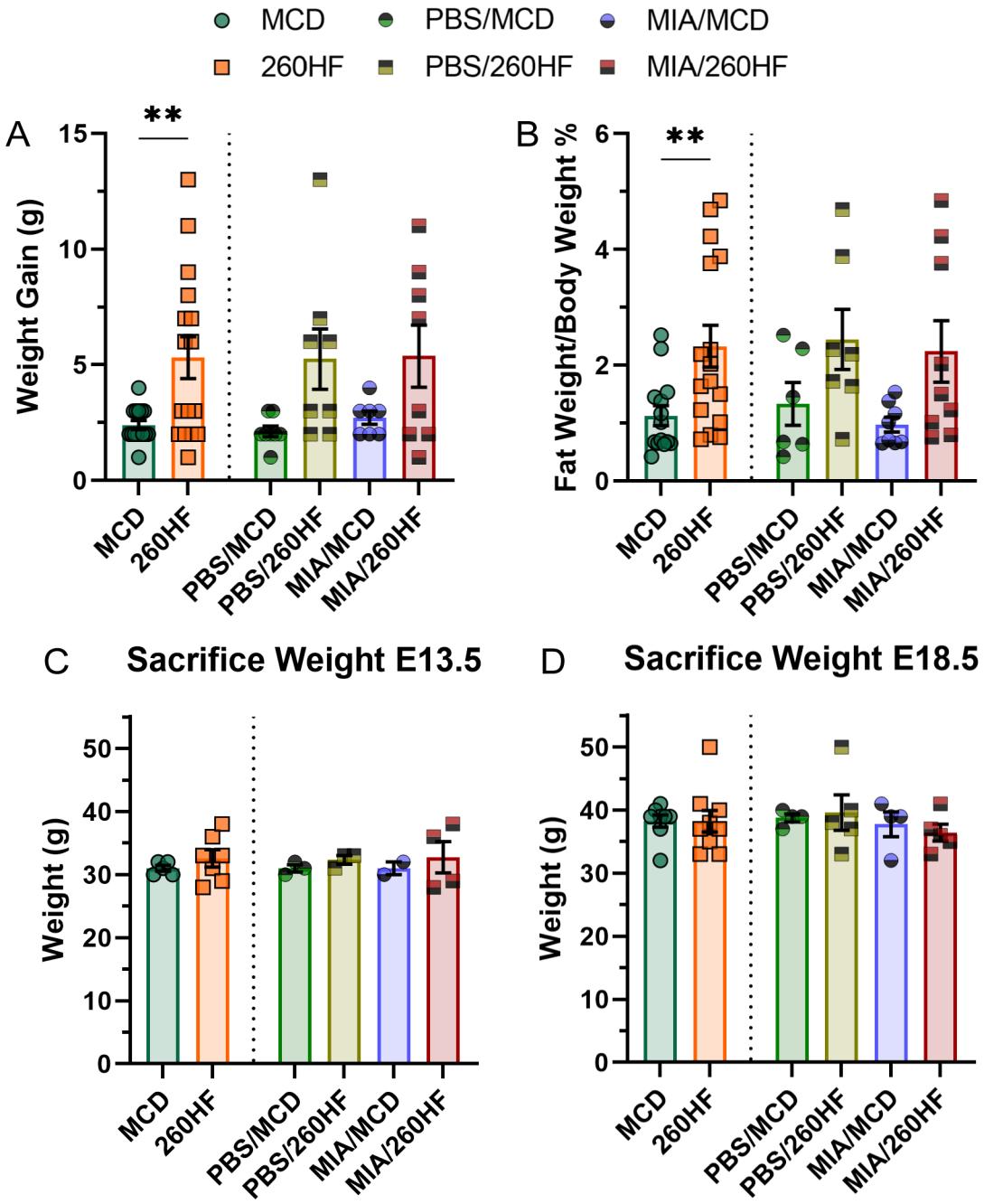

Figure 57: High fat diet mice gained more weight and fat weight proportion but weight differences did not remain to sacrifice.

A) Mean (+/- SEM) dam weight gain during high fat diet feeding for 260HF and MCD mice and those in each respective MIA groups (** = Unpaired t-test: $t(3.048) = 29$, $p = 0.0049$). **B)** Mean (+/- SEM) fat weight as proportion of body weight for 260HF and MCD mice and those in each respective MIA groups (** = Unpaired t-test: $t(2.842) = 28$, $p = 0.0083$). **C-D)** Mean (+/- SEM) dam sacrifice weight at E13.5 or E18.5 for 260HF and MCD mice and those in each respective MIA groups. MCD n=14, E13.5 n=6, E18.5 n=8; 260HF n=16, E13.5 n=7, E18.5 n=9; PBS/MCD n=7, E13.5 n=3, E18.5 n=4; PBS/260HF n=8, E13.5 n=3, E18.5 n=5; MIA/MCD n=6, E13.5 n=2, E18.5 n=4; MIA/260HF n=7, E13.5 n=3, E18.5 n=4.

With regards to MIA, high fat diet appeared to also modulate inflammatory response in Figure 58. MIA dams had on average a 1.36° temperature drop relative to PBS injected dams, demonstrating an inflammatory response to the viral mimetic. Again, there was some variation in response to injection with 260HF dams displaying a more extreme drop in temperature than MCD mice, even in those injected with PBS. This perhaps suggests some immune dysregulation as a result of the high fat diet feeding which was then further exacerbated by MIA.

Following the same pattern as temperature change 3 hours post injection, weight change 24 hours post injection was most negative in MIA/260HF dams at -0.88g. This was significantly lower than PBS/MCD mean weight change (One-way ANOVA ($F = 5.460$, $p = 0.0048$), Tukey-Kramer post-hoc test, $p = 0.0049$). Increasing severity of inflammatory reaction is clearly suggested by both temperature change and weight change in Figure 58, with PBS/MCD and MIA/260HF at the extremes of this trend. PBS/260HF and MIA/MCD groups form intermediates, with the former displaying a less inflammatory reaction than the latter.

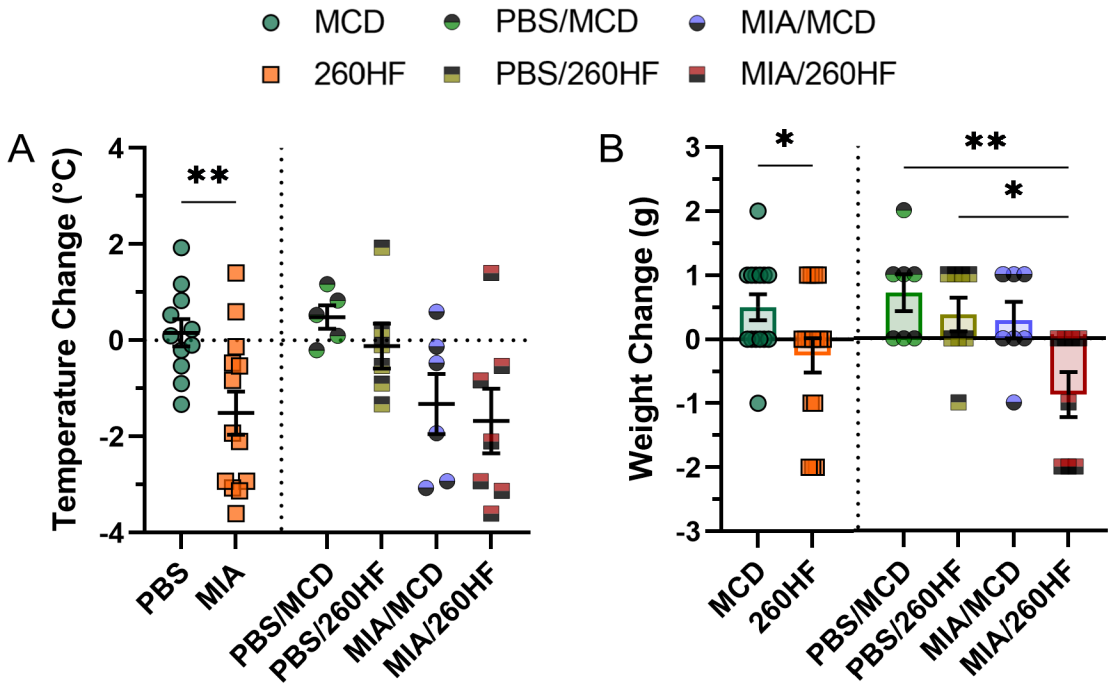

Figure 58: Poly I:C injected mice displayed more signs of MIA when combined with high fat diet feeding.

A) Mean (+/- SEM) maternal temperature change 3 hours post injection (** = Unpaired t-test: $t(2.191) = 28$, $p = 0.0369$). **B)** Mean (+/- SEM) maternal weight change 24 hours post injection (For MCD/260HF: * = Unpaired t-test: $t(2.191) = 28$, $p = 0.0369$) (For MIA groups: One-way ANOVA ($F = 5.460$, $p = 0.0048$), Tukey-Kramer post-hoc test, ** = $p = 0.0049$, * = $p = 0.0259$). MCD n=14; 260HF n=16; PBS/MCD n=7; PBS/260HF n=8; MIA/MCD n=6; MIA/260HF n=7.

5.3.7. MOMI Offspring Gross Measurements

Examination of impacts on offspring development was carried out as described previously with E13.5 embryos and E18.5 foetuses separated. There were no significant differences in litter size observed between groups in Figure 59. Number of necrotic foetuses, whilst also not differing significantly between groups, does show some indication of differing offspring effects on survival between groups. PBS groups had similarly low levels of mean number of necrotic foetuses at less than 1 in each. MIA/MCD dams had more necrotic foetuses on average at 2.29 with MIA/260HF litters most necrotic at 3 necrotic foetuses on average per litter. This pattern follows those described previously for dam inflammatory response measurements.

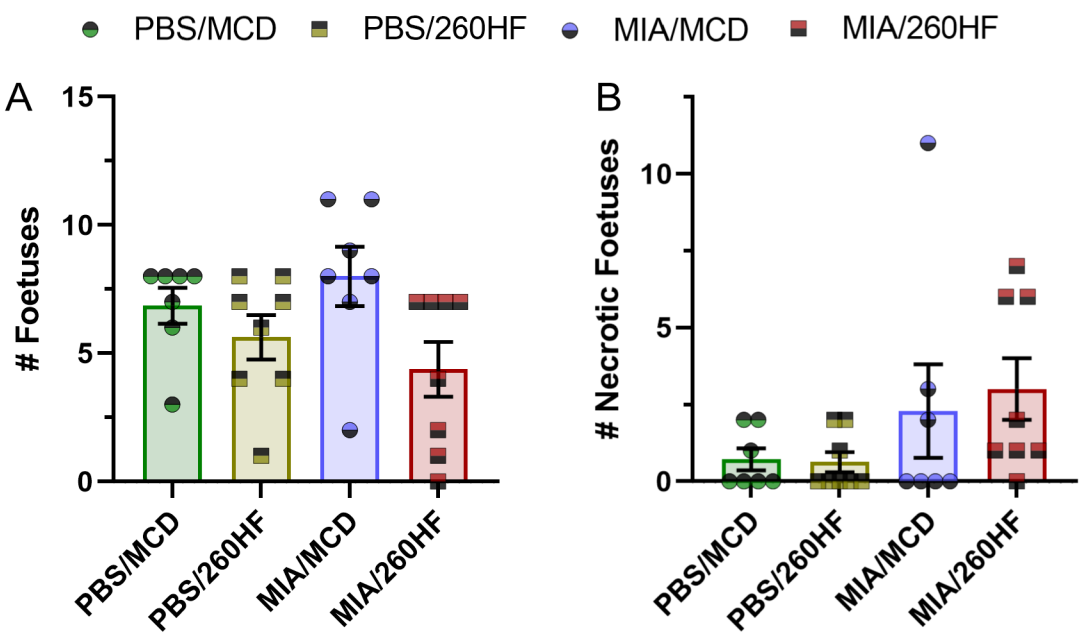

Figure 59: Number of necrotic foetuses differed between groups although not significantly like litter size.

A) Mean (+/- SEM) number of foetuses per litter. **B)** Mean (+/- SEM) number of necrotic foetuses per litter. MCD n=14; 260HF n=16; PBS/MCD n=7; PBS/260HF n=8; MIA/MCD n=6; MIA/260HF n=7.

Each group in this MOMI cohort displayed some signs of underdevelopment relative to PBS/MCD controls. Offspring exposed to either MIA or maternal 260HF all had lower mean body weight than PBS/MCD controls by 0.09-0.2g (Figure 60A). Only the high fat diet groups reached significance for decreased body weight (One-way ANOVA (F = 5.846, p =0.0011), Tukey-Kramer post-hoc test, $p \leq 0.0130$). MIA and maternal high fat diet offspring also had significantly reduced brain weight relative to controls grams (One-way ANOVA (F = 21.05, p <0.0001), Tukey-Kramer post-hoc test, $p \leq 0.0073$). Across both body weight and brain weight measurements, maternal high fat diet appeared to have a stronger effect on development than MIA. PBS/260HF and MIA/260HF group offspring fall 15.9% and 16.5% below control mean body weight compared to 7.5% for MIA/MCD offspring. Mean brain weight fell 19.1% and 21.5% below control in respective 260HF groups but only 11.9% in MIA/MCD offspring. These results also indicate that MIA combined with 260HF is more detrimental than 260HF alone, although only slightly.

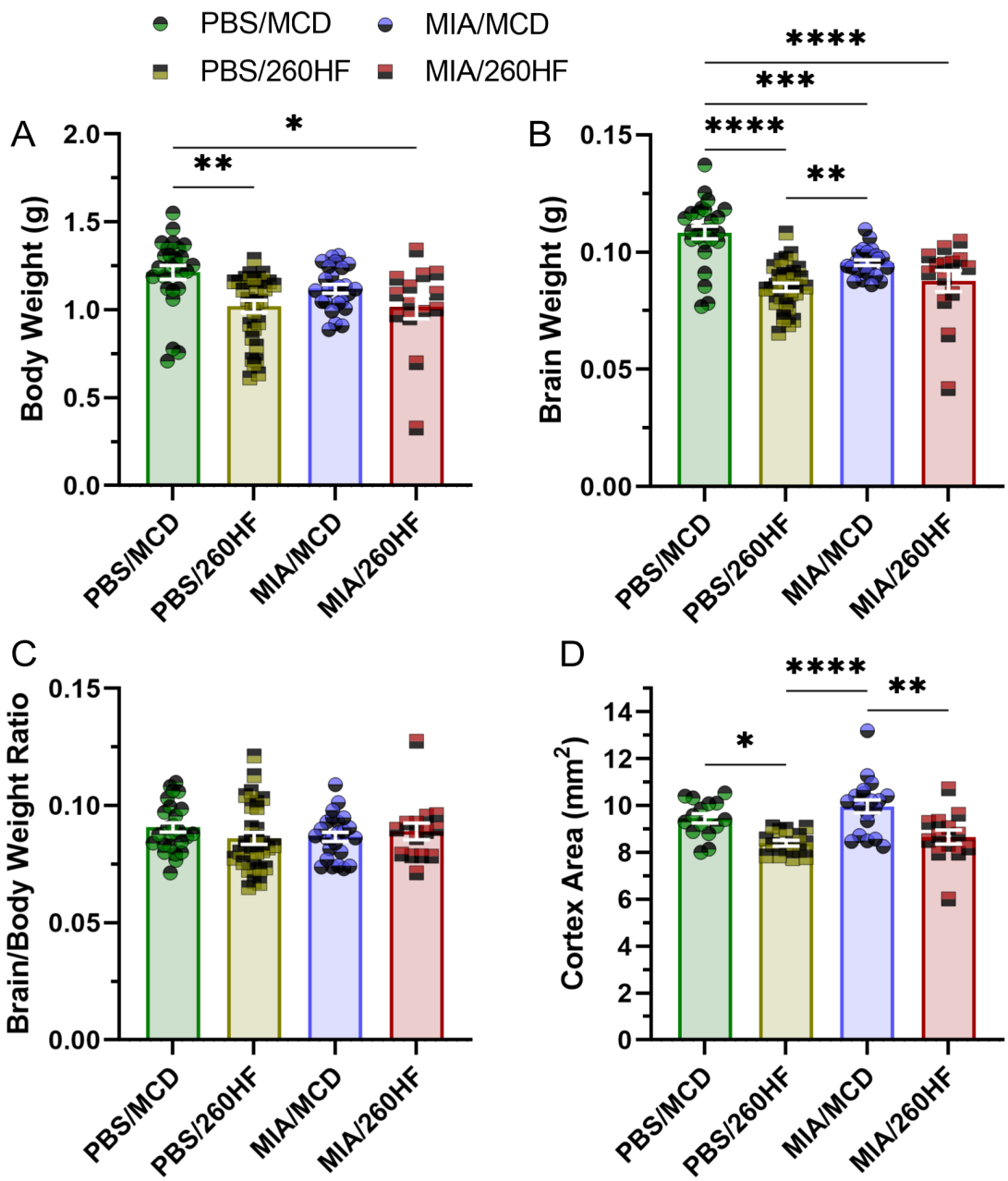

Figure 60: Offspring from each MOMI group appeared underdeveloped relative to control offspring. A) Mean (+/- SEM) E18.5 foetus body weight in grams (One-way ANOVA (F = 5.846, p =0.0011), Tukey-Kramer post-hoc test, ** = p =0.0014, * = p =0.0130). **B)** Mean (+/- SEM) E18.5 foetus brain weight in grams (One-way ANOVA (F = 21.05, p <0.0001), Tukey-Kramer post-hoc test, **** = p <0.0001, *** = p =0.0008, ** = p =0.0073). **C)** Mean (+/- SEM) E18.5 foetus brain to body weight ratio. **D)** Mean (+/- SEM) E18.5 foetus cortex area in mm^2. (One-way ANOVA (F = 9.559, p <0.0001), Tukey-Kramer post-hoc test, **** = p <0.0001, ** = p =0.0016, * = p =0.0177) PBS/MCD n=33; PBS/260HF n=31; MIA/MCD n=25; MIA/260HF n=14.

Ashmee Almeida and Mayur Shetty contributed towards data in this figure.

Mean cortex area measurements showed no significant difference between PBS/MCD and MIA/MCD groups whilst PBS/260HF mean cortex area was significantly lower than control (One-way ANOVA ($F = 9.559$, $p < 0.0001$), Tukey-Kramer post-hoc test, $p = 0.0177$). Despite differing from PBS/260HF mean cortex area by only 0.26mm^2, MIA/260HF offspring were not significantly lower than control. Again, this data suggests a more detrimental impact of high fat diet than MIA on this measure of brain development, although the stacking influence of both insults was not present. Brain to body weight ratio, shown in Figure 60C, remained comparable between groups suggesting any defects in offspring development were equally impactful on both brain and body.

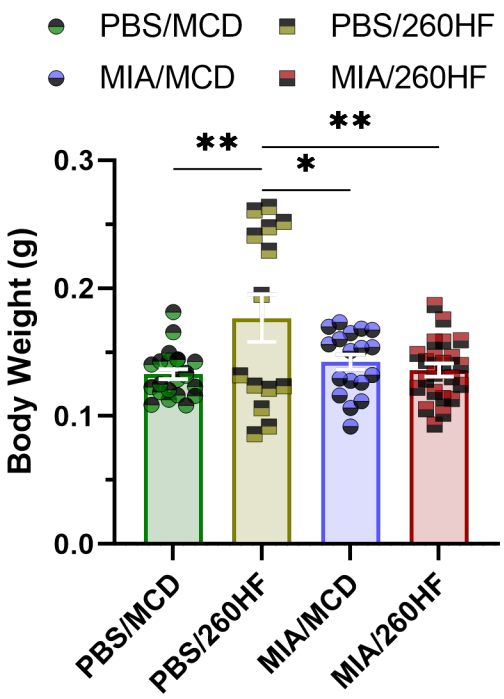

Figure 61: Embryo Body weight at E13.5 was significantly higher under maternal high fat diet alone.
Mean (+/- SEM) E13.5 foetus body weight in grams (One-way ANOVA ($F = 4.956$, $p = 0.0035$), Tukey-Kramer post-hoc test, ** = $p = 0.0035$, * = $p = 0.0430$). PBS/MCD n=34; PBS/260HF n=24; MIA/MCD n=32; MIA/260HF n=22.

Body weight measurements taken at E13.5 are in contrast to those at E18.5 and previous literature in that those exposed to maternal high fat diet appeared heavier than all other groups (Jungheim et al. 2010). The remaining groups of embryos all fall within 0.0094g of each other for mean body weight (Figure 61). All embryos weighing 0.2g and above came from one litter, suggesting either unusual overdevelopment in this maternal environment or perhaps a technical error meaning that these embryos were allowed to develop for longer than others. Upon removal of these data points PBS/260HF mean E13.5 body weight is no longer significantly heavier than other groups and at 0.12g, mean body weight is comparable to control. This data suggests that body weight measurements are not precise enough to detect the more subtle manifestations of underdevelopment that may be present at E13.5, although decreased body weight as a results of high fat diet has been reported at E14.5 (Jungheim et al. 2010).

5.3.8. MOMI Offspring Corpus Callosum Defasciculation

Although gross foetal measurements suggested some disruption to development within the MOMI cohort, this disruption was not carried through to measures of axon organisation. Corpus callosum Nrp1/L1CAM ratio, which functions as a measure of axon organisation within the corpus callosum, displayed no significant differences between any MOMI groups in Figure 62. Mean Nrp1/L1CAM ratio had a range of just 0.082 between groups. Similarly L1CAM length, acting as a measures of corpus callosum width, did not vary between groups.

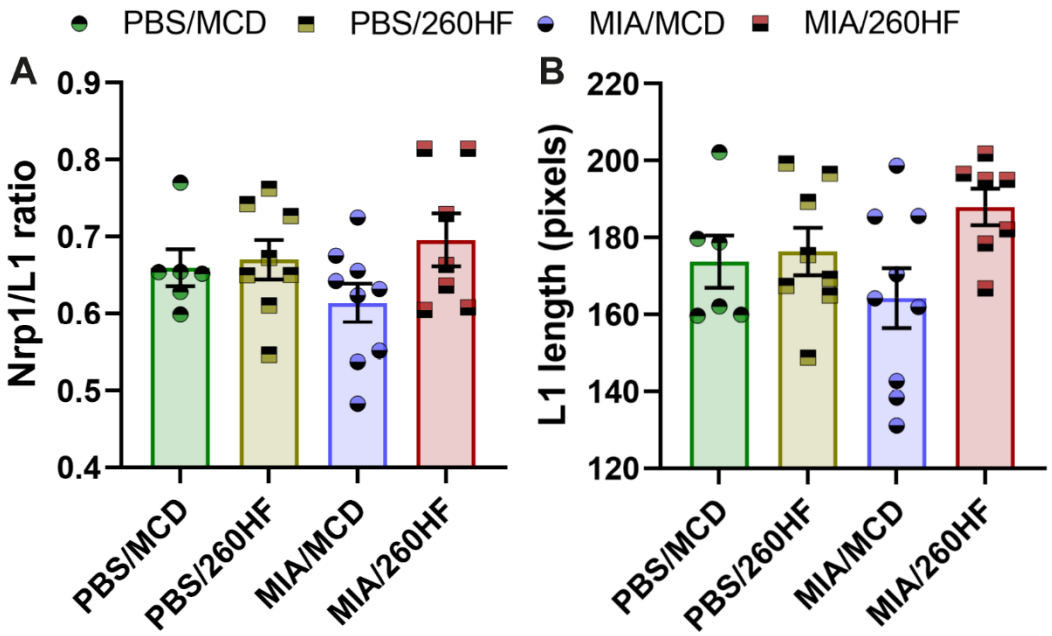

Figure 62: There were no differences between MOMI groups for any corpus callosum measurements taken.

A) Ratio of fornix/caudal Nrp1 expression width at the midline relative to midline L1CAM expression **B)** Length of fornix/caudal L1CAM expression width at the midline **C-F)** Representative fluorescence images of the corpus callosum fornix region across MOMI groups. PBS/MCD n=6; PBS/260HF n=8; MIA/MCD n=9; MIA/260HF n=7.

All data for this figure was produced by Ashmee Almeida and Mayur Shetty.

Nrp1/L1CAM ratio differs from all previous defasciculation measurements taken in that values vary around 0.65 rather than 0.5. This can be explained by differences in technique. Since cryosectioning and was used to obtain sections for the MOMI cohort, in order to maximise usage from each brain, rather than vibroslicing; brain morphology was likely more disrupted in the MOMI cohort.

5.3.9. Expression of Microglia Markers under MOMI

Perhaps unsurprisingly given there was no disruption to the corpus callosum in the cohort, there were few differences between groups for microglial markers surrounding the corpus callosum. As shown in Figure 63, the only significant differences between groups in this cohort were found within the septum. Each MIA or 260HF exposed group had significantly fewer iba1$^+$ cells in the septum relative to control (One-way ANOVA (F = 11.05, p =0.0006). Interestingly, here MIA appeared to be marginally more detrimental than maternal high fat diet since both MIA groups had at least 5 fewer iba1$^+$ cells in the septal region on average. This may have been due to chance however, since these differences were not significant. Septal expression of dectin-1 by Iba1$^+$ cells did not differ significantly but trended towards a decrease in MIA/260HF offspring expression by approximately 20% of septal Iba1$^+$ cells. MIA/MCD mice differed less from control offspring and PBS/260HF differed less still. It may be that a higher number of repeats would be required to tease apart what appear to be subtle differences in expression between groups in this cohort.

The microglia within the glial wedges were more similar between groups than those within the septum. No differences in number of Iba1$^+$ cells were found, although in a reversal of the septal pattern of microglial density, MIA/260HF mice trended towards a higher glial wedge Iba1$^+$ cell number than control. The high variability within the control group of glial wedge microglial measurements perhaps disguises some inter-group differences in this cohort. This may reflect the difficulty in obtaining a good cross-sectional view of the glial wedge hotspot when cryosectioning foetal mouse brains. Mean dectin-1 expression within the glial wedge hotspot was highly comparable between groups, varying by only 4.66% of total Iba1$^+$ cells.

Microglial results for this cohort suggest formation of the septal hotspot is somewhat disrupted under MIA and maternal high fat diet, but more so when both insults are combined. The differentiation of microglia within this cluster is less affected however, like the nearby glial wedge cluster which appears largely unaffected by these inflammatory conditions.

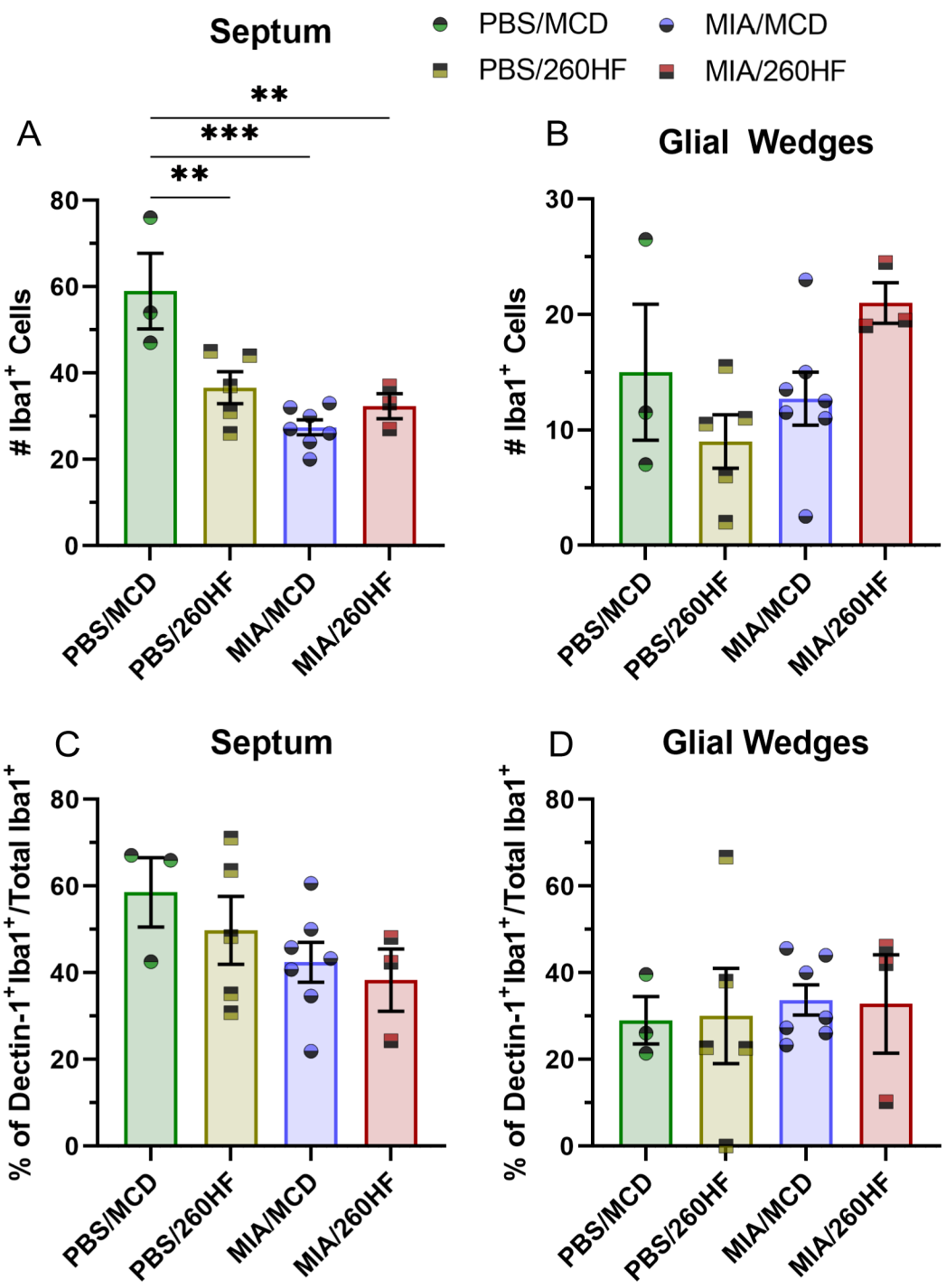

Figure 63: Corpus callosum adjacent microglial hotspots differed only in septal density within the MOMI cohort. A-B) Mean (+/- SEM) number of Iba1$^+$ cells in the septum and glial wedges of E18.5 brains from each MOMI group (One-way ANOVA (F = 11.05, p =0.0006), Tukey-Kramer post-hoc test, *** = p =0.0003, ** = $p \leq 0.0091$). **C-D)** Mean (+/- SEM) percentage of Iba1$^+$ cells expressing dectin-1 in the septum or glial wedges. PBS/MCD n=3; PBS/260HF n=5; MIA/MCD n=7; MIA/260HF n=3.

All data for this figure was produced by Ashmee Almeida and Mayur Shetty.

5.4. Discussion

5.4.1. The Impact of Maternal Immune Activation on Foetal Development

A key theme running through the data presented in this chapter is in variation between groups within cohorts presented here and variation from and within previous literature. The first unanticipated source of variation was in response to LPS, as measured by temperature or weight change following injection. Although the CD1 mice used in the MIA cohort presented here are highly genetically similar due to inbreeding, and were purchased from the same supplier and housed under the same conditions, some responded to LPS and others did not. This phenomenon has also been reported in rodent models under similar conditions (Bronson et al. 2011; Missault et al. 2014). Importantly, it was shown that 'responder' dams had increased expression of key inflammatory cytokines and 'responder' offspring displayed behavioural deficits not found in 'non-responders' (Missault et al. 2014). This variation likely derives from individual variability between mice which could become apparent through a variety of means: differing microbiomes, variable exposure to social stressors, distinct exposure to previous infection (Satija and Shalek 2014; Abolins et al. 2017).

A further difference in response was found between Poly I:C and LPS groups, both for dam and offspring measurements. Differences in response to these immune activators has been reported extensively in the literature, and likely reflects the differing targets of these molecules (Arsenault et al. 2014; Bao et al. 2022b). It has been shown for example that IL-6 is a key mediator of Poly I:C induced behavioural deficits (Smith et al. 2007). Data presented here suggests a stronger response to Poly I:C injection in terms of maternal weight change; number of necrotic embryos per litter; and offspring body weight. However, this does not carry through to measurements taken around the corpus callosum where the LPS-responder group appeared more defasciculated and showed more disruption to glial wedge hotspot formation. Such a combination of corpus callosum defects suggests formation of the glial wedge hotspots may be necessary for correct positioning of axons within the corpus callosum. This hypothesis is loosely supported by previous literature in that 'guide-post' structures composed of astrocytes are found at the glial wedges, which influence corpus callosum formation (Richards et al. 2004a; Piper et al. 2009). Microglia could interact with these glial wedge astrocytes, either supporting there differentiation and survival or assisting in their timely

removal, both of which microglia have been shown to carry out elsewhere (Thion et al. 2018b). Further experiments would be required to demonstrate this, perhaps through ablation of glial wedge microglia via timed ventricular clodronate injection or through genetic manipulation if more sophisticated tools are generated to target this specific developmental population.

If microglia were found to be the mediators of the impact of LPS MIA on corpus callosum defasciculation, it is likely that differing inflammatory responses between Poly I:C and LPS drive corpus callosum differences between respective groups. This is because microglia are highly responsive to various cytokines. However, several other processes common to acute immune reaction are able to disrupt foetal brain development. These include glucocorticoid elevation, hyperthermia and decreased food intake (Bronson et al. 2011). These alternative explanations seem less likely since Poly I:C dams displayed the same temperature changes and much higher weight change, indicative of modified food intake, than LPS injected dams. Previous authors have also suggested microglia may be involved in inducing corpus callosum defasciculation and demonstrated that microglia downregulated genes associated with nervous system development (Pont-Lezica et al. 2014). If, as hypothesised, dectin-1^{+} microglia are involved in promoting nervous system development, this finding may be reflected in the observed decreases in dectin-1 expression under LPS MIA.

Some previous studies contrast findings presented here. For example, others have found: a decrease in foetal body weight under LPS MIA and not poly I:C MIA; decreased LPS dam food intake not in poly I:C dams; decreased pup survival due to LPS MIA but not poly I:C MIA (Arsenault et al. 2014; Li et al. 2018). In fact, extensive variation can be found between many different studies (Bao et al. 2022b). This is thought to occur through varying study designs; differences in animal responses to immune challenge, for example the reaction of different mouse strains differs to the same LPS insult (Kato et al. 2000); and also differences in inflammatory substance. Poly I:C has been shown to be particularly variable with three batches of Poly I:C from the same vendor having significantly different abilities to induce an immune response (Harvey and Boksa 2012; Careaga et al. 2018). The source of this variation may be differences in Poly I:C length among manufacturers and even between batches from the same manufacturer, as shown by in vitro data (Mian et al. 2013; Kowash et al. 2019). This variability is known to affect the magnitude of immune responses (Zhou et al. 2013b).

5.4.2. The Impact of Maternal Immune Activation on Microglial Transcription

As covered in the results section, MIA appeared to result in a shift in midline region microglia away from a metabolically active transcription profile towards ATM/PAM or proliferative microglia. Forms of MIA differ in that LPS MIA increased the proportion of ATM/PAM-like cells more than PIC MIA, which preferentially induced an increase in proliferative microglial subtypes. Furthermore, within each microglial subtype found in the midline region, MIA appears to increase the likelihood of cells entering an inflammatory version. This is with the exception of PIC MIA, which did not induce a shift towards inflammatory PAM/ATM clusters. PAM and ATM clusters express many markers associated with 'activated' microglia, so it is perhaps unsurprising that MIA shifted microglial expression profile in this direction within the midline region.

Single-cell RNA sequencing findings somewhat contradict cell counting findings in that fewer Dectin-1$^+$ microglia were observed within the glial wedges of LPS exposed samples. However, as discussed in chapter 1 many ATM/PAM-like cells do not express Dectin-1, particularly inflammatory or patrolling PAM clusters predominantly composed of LPS exposed cells. The higher number of Iba1$^+$ cells counted under PIC supports the presence of more proliferative microglia identified through transcription analysis in the midline region. Increase in Dectin-1$^+$ cells in the glial wedge could be explained by the higher numbers of ATM/PAM cells under PIC identified through single-cell sequencing.

Microglia in the cortical region displayed divergent transcription changes when exposed to each respective form of MIA. Microglia appeared to transition away from homeostatic cluster 1 towards more inflammatory homeostatic clusters, with PIC preferentially inducing transition into cluster 7 and LPS inducing transition into cluster 8. Remaining cortical clusters were also almost exclusively from LPS samples, highlighting further differences between these stressors in the cortex. As mentioned in the results section, it may be that clusters 7 and 8 have differentiated to react to different stimuli.

There is limited and contrasting previous research on the effect of MIA on developmental microglia populations. One study found that MIA altered microglial motility and IL-6

expression, with differing results dependent upon developmental stage of injection – either E12 or E15 (Ozaki et al. 2020). Another study found no effect on microglial cell density or expression of IL-1β or Mac-2/Galectin-3 at E11.5, E12.5 or E17.5 following double poly I:C MIA at E11.5 and E15.5 (Smolders et al. 2015). In the adult brain, the injection of LPS was shown to induce a pro-inflammatory shift in microglial expression profile in the following 24 hours (Sousa et al. 2018). This shift towards an 'activated' microglial phenotype decreased expression of classical microglia makers and increased adult microglia heterogeneity. Interestingly, the expression profile of these cells appears to share some similarities with ATM but less similarities with PAM, as shown in Figure 64. As discussed in the paper, LPS activated microglia have some overlap with DAM.

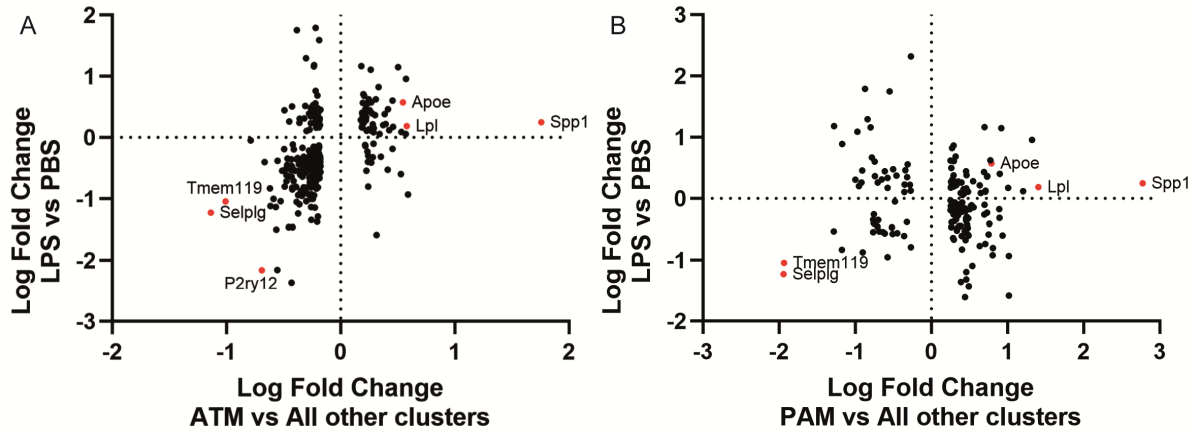

Figure 64: Expression profile of ATM and PAM microglia differs from adult microglia exposed to LPS.

A-B) Plots showing genes differentially expressed between PAM or ATM and other microglia examined in each respective study plotted against genes differentially expressed between adult brains exposed to LPS and adult control brains. Genes of interest are highlighted in red. *ATM – Axon-Tract associated Microglia; LPS – Lipopolysaccharide; PAM – Proliferative region Associated Microglia; PBS – Phosphate Buffered Saline.*

In a more recent study, dams were injected with LPS at E12.5 and microglia were shown to have retracted processes by E15.5, persisting to P1 where increased density of microglia was observed within the SVZ (Loayza et al. 2022). MIA exposed microglia increased expression of a range of cytokines at E15.5 and P4, one of which was PAM and ATM marker osteopontin, coded for by the *Spp1* gene. Overproduction of NPCs and disruption to cortical interneuron migration was also reported in MIA mice, as has been observed previously (Cunningham et al. 2013; Squarzoni et al. 2014). Although increased Spp1 expression was

not observed here (Figure 15) examining migration of cortical interneurons and NPC proliferation in MIA samples presented in this thesis could help improve understanding of the level and type of MIA that may be required to cause developmental disruption to these processes. Given that different injection time points and the viral mimetic Poly I:C was used here. Immunohistochemical staining could be used to for this purpose.

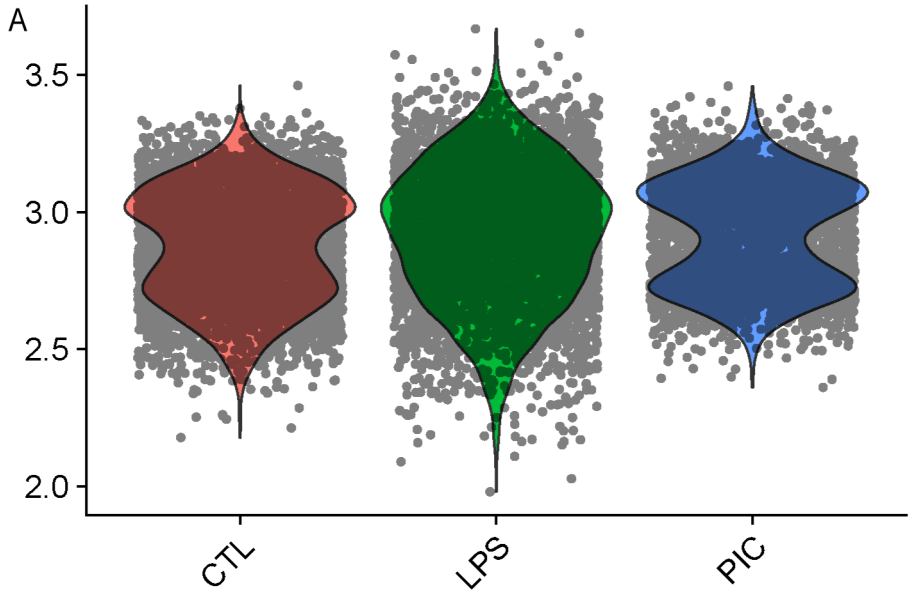

Figure 65: Spp1 expression was consistent across MIA groups.
Expression of *Spp1* across each respective MIA sample type displayed in violin plots. Expression level in log-transformed counts per 10,000 transcripts.
CTL – Control; LPS – Lipopolysaccharide; PIC - Polyinosinic:polycytidylic acid

Whilst single-cell sequencing results provide some insight into the differing effects of PIC and LPS, differential expression analysis produced a distinct lack of significant differences between clusters of microglia. In particular differential expression analysis comparing 1 cluster to all others often produced very few markers. This limitation and the lack of novel marker genes identified may reflect the technical limitations encountered during lab work. As discussed in chapter 2, a key control sample failed quality control check, limiting the reliability of comparisons to the control condition. Furthermore, extensive modifications to the transcription data was required to reduce noise and remove transcripts strongly affected by *ex vivo* activation (Section 2.2.5.9). This necessary process alongside technical activation is likely to have strongly reduced sensitivity of the assay, preventing the detection of meaningful differences between subtypes of microglia. Repetition of this protocol with a higher number of samples and a cytometer capable of sorting cells at a faster rate may yield more useful data.

5.4.3. The Impact of Two Inflammatory Hits on Foetal Development

The two sources of inflammation selected to study the combined influence of inflammatory insults during in utero development were obesity: a condition of chronic inflammation; and poly I:C induced MIA; inducing an acute inflammatory reaction. 260HF diet feeding for 8 weeks successfully induced obesity, as measured by a significant increase in weight relative to control. However, only half of the 260HF fed mice were heavier than control dams. This provided the opportunity to contrast the impact of high fat diet and obesity in combination with MIA or obesity alone.

Measures of dam immune activation following poly I:C injection nicely follow expected responses. Dams anticipated to be experiencing chronic inflammation following 260HF feeding displayed the largest drop in temperature and weight after injection. This suggests a stronger immune response than those injected with poly I:C alone. Dams injected with PBS and fed a high fat diet appear to have had a minor immune response to the injection itself, perhaps evident aberrant inflammatory response not experienced in those on control diet. This is to be expected during chronic inflammation when the immune system is pre-prepared to respond, or over respond, to any threat.

C57BL/6 are often used in MIA studies unlike the CD1 mice used here. This may also contribute to discrepancy between data presented her and in previous literature. Notably, C57BL/6 have been shown to have a specific kind of intestinal bacteria also found in CD1 mice which prevent an immune response from occurring. Data presented here however, suggests that an immune reaction may still occur in CD1 mice.

To conclude, this chapter highlights the huge array of sources of variation when considering development of neurodevelopmental disorders. Inflammatory prenatal stressors may differ from each other dependant on source of inflammation and interact with each other in unexpected ways, as in the MOMI cohort. Furthermore, time point of inflammatory insult likely plays a vital role in determining which systems will be affected, for example MOMI e12.5 vs e15.5. In addition to this, each specific stressor may interact with an individual differently dependent on genetic background, microbiome or a number of unknown factors. These factors make the study of developmental neuroinflammation particularly difficult. Solutions to

study these issues would involve tightly controlled environment, animal and inflammatory mediator supplier coupled with high number of repeats to account for individual variability by dividing each into a specific group. However this moves the mouse model yet further from the human environment where there is exposure to a broad range of different pathogens important for modifying the immune response (Tao and Reese 2017). These factors also provide clues as to why there is such great heterogeneity in response to prenatal insult in the human condition where vastly differing pre and postnatal environments are experienced and many different types of stressor can accumulate either in early or later life. Such heterogeneity points towards personalised medicine as a potential solution specific to each individuals insult and make up.

Chapter 6: Discussion

6.1. Main Findings

6.1.1. Transcription profile of septal microglia

Chapter 2 sought to demonstrate the presence of dense corpus callosum associated microglia hotspots during development of the structure and then characterise the transcription profile of said microglia. The E18.5 mouse glial wedges and septal region were shown to be home to dense clusters of microglia not seen within neighbouring regions or the cortex. The transcription profile of a proportion of these hotspot microglia were shown to be similar to previously identified Proliferative-region Associated Microglia (PAM) and Axon Tract-associated Microglia (ATM). Corpus callosum hotspot microglia were also shown to differ from cortical microglia in the same brains and dopaminergic axon tract associated microglia at E14.5. Single-cell RNA sequencing provided deeper examination of the E18.5 microglia transcription profile. This corroborated the transcription differences observed between cortical and midline microglia, and suggested that the majority of midline region microglia are in fact metabolically active microglia in association with ATM, PAM and proliferative microglia. In summary, this chapter demonstrated for the first time that PAM/ATM are present in hotspots surrounding the corpus callosum during its formation. This suggests that the developmental roles of PAM/ATM extend beyond those previously described in postnatal myelination to include prenatal corpus callosum development.

6.1.2. Characterising a unique microglial population within the developing forebrain

Chapter 3 built upon the findings of chapter 2 to explore the characteristics of corpus callosum associated microglia and further differentiate them from cortical microglia. The time-point at which corpus callosum microglia begin to differentiate and form hotspots was established. This provided further support for the hypothesis that these cells are involved in corpus callosum formation. The birthdate and proliferation rate of septal and glial wedge microglia was also explored, suggesting higher rates of proliferation relative to the cortex. Finally, migration data suggested septal and glial wedge microglia are mobile. Data presented here may be useful in understanding the function of and developing intervention strategies for

corpus callosum associated microglia, which appear to be unique within the developing late prenatal forebrain.

6.1.3. The effects of maternal high fat diet on development and corpus callosum formation

Chapter 4 focused on developing a model for maternal obesity in order to examine the effects on corpus callosum development and associated microglia. Although maternal obesity was not consistently induced, maternal high fat diet appeared to detrimentally impact foetal brain development and in some cases foetal body development and survival. The availability of n-3 or n-6 Poly-Unsaturated Fatty Acids (PUFAs) appeared to influence prenatal development, although not consistently. The corpus callosum and associated microglia were unaffected by exposure to maternal high fat diet. These findings suggest that corpus callosum formation and any roles associated microglia may have, are not sufficiently disrupted by maternal high fat diet to induce developmental defects.

6.1.4. The Effect of Maternal Immune Activation on development and corpus callosum formation

Chapter 5 aimed to characterise the impact of different forms of Maternal Immune Activation (MIA) on foetal neurodevelopment, corpus callosum formation and development as a whole, in addition to effects on septal and glial wedge microglia. Whilst Poly I:C MIA offspring had altered overall foetal development, the response to LPS group displayed corpus callosum disorganisation. This response to LPS group also had reduced number of glial wedge microglia and reduced microglia expressing PAM/ATM marker Dectin-1. Poly I:C MIA offspring on the other hand had the opposite effect, with increased total microglia number and proportion of cells expressing Dectin-1 in the glial wedges. When studying the impact of MIA in combination with maternal high fat diet, overall brain and body development appeared to be disrupted by both conditions with an additive effect observed only in decreased foetal survival. None of the groups displayed disruption to corpus callosum formation, despite each having reduced number of microglia within the septal hotspot. This chapter highlights the complex nature of environmental insults during development and suggests that specific disruption is required to induce corpus callosum defects. In addition to specific forms of MIA being required to induce corpus callosum defects, these appear also to be necessary during a specific developmental window.

6.2. Limitations

6.2.1. Transcription Profiling

Technical limitations involved in *in-situ* hybridisation and single-cell RNA sequencing reduce comparability between techniques. Whilst *in-situ* hybridisation is performed on a 20µm thick brain slice from a specific region of that brain, the single-cell RNA sequencing method I developed examined a much larger region of tissue across the midline. This results in thousands of cells from a large approximate region being compared with tens of cells from a specific small area of the brain. Combining this with the quality control failure of one of two control RNA sequencing samples means that there is reduced certainty of the size of PAM/ATM populations in the corpus callosum associated region under normal conditions. This is because control midline microglia were primarily metabolically active, according to single-cell sequencing results, which cannot be corroborated with a repeat control sample. MIA samples provide some indication that midline PAM/ATM population size may be larger than it appears in control samples; however, maternal inflammation could have influenced this.

A further limitation of single-cell RNA sequencing data presented here is that transcription changes in microglia as a result of technical activation generated 'noise' which had to be controlled for. This process involved removing expression data for many genes that had been strongly impacted by the experimental and transforming expression of other genes that were less impacted. Whilst this method was necessary to permit comparison between cells of different samples, it reduced the power of comparisons between all cells, as there was less expression data in which to look for differential expression and the level of differential expression was dampened. This resulted in far fewer significantly differentially expressed genes being detected between clusters. Additionally, this could have contributed to the homogeneity of control midline samples where, with more expression data, subtle differences between cells might have been detected. This could have resulted in more clusters, closely related to but distinguished from metabolically active microglia, being detected. Such limitations could be overcome by repeating the experiment with more samples utilising more advanced cell sorting equipment to minimise sorting time and therefore microglial activation.

6.2.2. The Mouse Model

6.2.2.1. Mouse Strain Differences

A number of different inbred mouse strains are used in scientific studies. The CD1 strain, selected for the majority of experiments in this thesis, is often used to study prenatal development due to the large litter size produced by this strain. Large litter sizes mean fewer animals can be used to obtain a large number of prenatal brains. The C57BL/6 strain is frequently used, as its genetic makeup is very well understood meaning that there are a variety of genetic tools available. Microglia have been shown to differ by mouse strain, with different numbers of Disease-Associated Microglia (DAM) observed and differences in expression of many genes (Kim et al. 2018; Yang et al. 2021). *Clec7a*, *Spp1* and *Lpl* are examples of genes differentially expressed between strains, including wild-derived and C57BL/6, which are also highly expressed by PAM/ATM (Yang et al. 2021). There may therefore be differences in microglia from CD1 mice, primarily examined in this thesis, relative to C57BL/6 mice, often investigated in other studies. Other studies, however, find few expression differences between mouse strains making comparison with previous still valid to some extent (Geirsdottir et al. 2019).

Mouse strains are also known to differ by their immune response (Sellers et al. 2012). This is because of both background strain, and other factors such as microbial milieu. Even within a mouse strain, during MIA, there is significant individual variation in immune response (Estes et al. 2020). In addition to variation in mouse strain there are also known differences in reagents, with Poly I:C shown to vary by batch both within and between vendors (Mueller et al. 2019). Differences such as these have led to heterogeneous and opposing findings in the study of MIA (Estes and McAllister 2016b; Kentner et al. 2019). Comparing findings presented here with previous studies on different mouse strains, or even experiments on different mouse strains within this thesis (MOMI cohort vs other cohorts) is therefore challenging. It must also be noted that, due to the failure of planned Enzyme-linked immunosorbent assay (ELISA) experiments, maternal and foetal cytokine profiles were not investigated. Results from these experiments may have helped to make comparisons with previous literature and confirm the presence and characteristics of each maternal immune response and subsequent impact on offspring.

Mirroring studies on MIA, studies on obesity show similar variation by mouse strain. Different strains have been shown to vary by fat mass percentage, glucose intolerance, insulin resistance and circulating inflammatory cytokine levels, all of which could influence foetal development (Montgomery et al. 2013; Li et al. 2020; Siersbæk et al. 2020). Differences in environmental factors discussed in chapter 3, such as microbial milieu, only add to difficulties in establishing a reproducible model for comparisons between and within studies.

6.2.2.2. Relevance to the Human Condition

Given that microglia differ between mouse strains, it is unsurprising that there are also differences between species. Adult human microglia have been shown to be more heterogeneous than in rodent, containing additional inflammatory or senescent-like microglial populations (Geirsdottir et al. 2019). Rodents also displayed notable differences to humans in expression of complement, phagocytic and susceptibility to neurodegeneration related genes. Whilst these differences could make data displayed here less relevant to the human condition, all rodents and humans were found to express a conserved core gene programme associated with glia neuron interactions. These conserved genes are more likely to be relevant to development and microglia distribute in a similar way during mouse and human development; therefore rodent models still have value in understanding human microglia (Menassa and Gomez-Nicola 2018b).

The genetic homogeneity of inbred mouse strains differs from the diverse genetic heterogeneity of humans. Whilst this reduces potential responses to environmental challenge, such as MIA or high fat diet, it is necessary to control for genetic variation in order to understand the impact of environmental stressors.

Methods used to model maternal obesity in rodents also diverge from the human equivalent. The root cause of obesity varies from person to person but is thought to involve a combination of biological, psychosocial, and behavioural factors, which include genetic makeup, socioeconomic status, and cultural influences (Skelton et al. 2011). The high fat diet mouse model of obesity attempts to control for almost all of these factors to focus on the result of consuming excess calories and lipids. Despite its necessity for understanding specific elements of obesity, this approach limits comparability to the heterogeneous human environment. Results presented here also demonstrate the difficulty in controlling for

environmental and biological factors when studying obesity. Such limitations could be overcome either by putting more stringent controls in place to control for environmental factors, or by introducing more heterogeneity in condition and genetics in an attempt to mirror the human environment – requiring huge numbers of animals for suitable statistical power.

Similar to models of maternal obesity, mouse models of MIA differ from human infection during pregnancy. As discussed in the introduction, whilst animals have conserved reactions to infection there are species specific differences in immunology, with C-reactive protein for example having a limited role in mouse (Holub et al. 2013; Torzewski et al. 2014; Ander et al. 2019). The human condition also involves infection rather than 'clean' infection through injection of a viral or bacterial antigen, which may occur over a longer time period and involve further complications. As with maternal obesity, this approach is necessary to study the influence of MIA exclusive of infection. A variety of outcomes are observed in humans affected by MIA as well as in animal models, even when attempting to control for complicating factors (Careaga et al. 2017).

6.3. Future Directions

Working to understand the developmental function of corpus callosum associated hotspot microglia is an important direction for future study. Findings presented here have provided a good basis for further exploration. Establishing that corpus callosum associated hotspot microglia share similarities with PAM and ATM suggests that they may be involved in phagocytosis of developmental structures, as has been demonstrated for ATM in the postnatal brain (Hammond et al. 2019). Trophic support of early calosal axons is another mechanism by which corpus callosum hotspot microglia may assist in corpus callosum development, based on microglial support of other corpus callosum crossing axons (Ueno et al. 2013).

Depletion experiments could help to confirm the function of corpus callosum hotspot microglia. Although previous work has shown disruption to corpus callosum fasciculation under microglial depletion, this technique removed all microglia from the brain, opening the possibility that another microglial population is responsible for these defects (Pont-Lezica et al. 2014). The use of CD11c-targetted toxin regimes, such as those developed by

Wlodarczyk et al. (2017), for example may be able to specifically deplete septal and glial wedge microglia specifically if utilised prenatally. Subsequent defects in neonatal brain development could then be attributed to this population. One might expect CD11c expression in corpus callosum associated hotspot microglia given their similarity to fountain of microglia cells targeted in Wlodarczyk et al. (2017). Itgax expression, coding for the CD11c protein, was not however increased in midline or PAM/ATM-like clusters studied here. Supplementary data from previous studies show decreased Itgax expression in PAM relative to other clusters but slightly increased expression in ATM (Hammond et al. 2019; Li et al. 2019a). A novel genetic tool developed from data described in this thesis, targeting Spp1 or Clec7a for example, may instead be required to understand septal and glial wedge microglia function. Varying time point of toxin injection targeting corpus callosum associated microglia would also be useful to examine any changing roles of these cells from E15.5-P14.

Further depletion experiments where microglia are removed from cultured brain slices, using liposomal chlodronate for example, followed by the re-introduction of specific microglial populations distinguished by Fluorescence-Activated Cell Sorting (FACS) may be valuable. Using this method, introducing homeostatic microglia to the septal region or septal microglia to the cortex could help understand whether specific populations are required for specific developmental function through examination of corpus callosum structure. Additionally, examining marker expression in microglia could help determine whether local brain parenchyma signalling is necessary and sufficient to induce differentiation of regional microglial populations or whether their developmental phenotype is conserved. Validity of results for such experiments would depend upon the effect of slicing and culturing brain samples on corpus callosum development and microglia.

Culturing corpus callosum containing brain slices in the presence of fatty acids and/or cytokines could help improve our understanding of the effect of MIA and maternal obesity on development. Microglial behaviour and corpus callosum development could be examined in these brain slices. This in situ experiment would remove potential confounding factors relating to environmental factors such as bacterial milieu, individual differences in diet consumption or inflammatory response. Findings would need to be replicated in vivo to confirm relevance to the living brain but would provide information on specific fatty acid and/or cytokine profiles to explore further.

Migration experiments building upon those covered in this thesis would be helpful to better understand the relationship between septal, glial wedge and postnatal 'fountain of microglia' hotspots. Performing migration experiments in a 2D environment, such as using brain slices or explants, is less relevant to the 3D living brain. Using time-lapse bi-photon microscopy in combination with the CX3CR1-GFP zebrafish might provide a more relevant model for investigation of microglia migration. The translucent zebrafish brain should allow the tracing of microglia migration along all 3 planes in a method not possible in the mouse brain. Using this method in combination with cytokine and/or fatty acid culture could link findings to the maternally obese or inflamed state.

With the advent of the COVID-19 epidemic at a time when obesity is prevalent, it is likely that a number of SARS-CoV-2 infections occurred alongside obesity during pregnancy. Although an initial study has not found a combined effect of SARS-CoV-2 and obesity on offspring outcome, these factors combined may have more subtle effects on offspring neurodevelopment (Weschenfelder et al. 2023). Using a two-hit model of SARS-CoV-2 antigen injection and maternal high fat diet may be useful to understand the potential future impact of the COVID-19 epidemic on offspring. I would suggest using a large number of animals to distinguish obese from overweight and normal weight high fat diet dams and obtaining animals from one supplier, then housing in a sterile environment to avoid differences due to bacterial milieu. Injection should take place at E15.5 to study septal microglia and corpus callosum development although other time points would be important for other developmental processes.

6.4. Concluding Remarks

Recent advances in our understanding of the many microglia populations present in the developing brain have provided opportunities to investigate early mechanisms involved in neuropsychiatric and neurodevelopmental disorders. This thesis has provided novel insights to improve our understanding of corpus callosum associated developmental microglia in steady state and when exposed to maternal inflammatory stressors. Further investigations building upon this research may one day provide avenues to intervene in the development of neuropsychiatric and neurodevelopmental disorders.

References

Abolins, S. et al. 2017. The comparative immunology of wild and laboratory mice, Mus musculus domesticus. *Nature Communications 2017 8:1* 8(1), pp. 1–13. doi: 10.1038/ncomms14811.

Abuaish, S. et al. 2018. Perinatal high fat diet induces early activation of endocrine stress responsivity and anxiety-like behavior in neonates. *Psychoneuroendocrinology* 98, pp. 11–21. doi: 10.1016/J.PSYNEUEN.2018.08.003.

Aldinger, K.A. et al. 2009. Genetic variation and population substructure in outbred CD-1 mice: Implications for genome-wide association studies. *PLoS ONE* 4(3). doi: 10.1371/journal.pone.0004729.

Alliot, F. et al. 1999. Microglia derive from progenitors, originating from the yolk sac, and which proliferate in the brain. *Developmental Brain Research* 117(2), pp. 145–152. doi: 10.1016/S0165-3806(99)00113-3.

Alves, J.M. et al. 2020. Sex differences in the association between prenatal exposure to maternal obesity and hippocampal volume in children. *Brain and Behavior* 10(2), p. e01522. doi: 10.1002/brb3.1522.

Amoli, M.M. et al. 2019. Over-expression of TGF-β1 gene in medication free Schizophrenia. *Psychoneuroendocrinology* 99, pp. 265–270. doi: 10.1016/j.psyneuen.2018.10.009.

Ander, S.E. et al. 2019. Immune responses at the maternal-fetal interface. *Science Immunology* 4(31). doi: 10.1126/sciimmunol.aat6114.

Andersen, M.S. et al. 2021. Heritability Enrichment Implicates Microglia in Parkinson's Disease Pathogenesis. *Annals of neurology* 89(5), p. 942. doi: 10.1002/ANA.26032.

Arlotta, P. et al. 2005. Neuronal subtype-specific genes that control corticospinal motor neuron development in vivo. *Neuron* 45(2), pp. 207–221. doi: 10.1016/J.NEURON.2004.12.036/ATTACHMENT/279058E1-58BB-4216-B48D-AB1DEB2888F1/MMC1.PDF.

Arnò, B. et al. 2014. Neural progenitor cells orchestrate microglia migration and positioning into the developing cortex. *Nature Communications* 5(1), pp. 1–13. doi: 10.1038/ncomms6611.

Arnold, T. and Betsholtz, C. 2013. Erratum: The importance of microglia in the development of the vasculature in the central nervous system. *Vascular Cell* 5(1), p.

12. doi: 10.1186/2045-824X-5-12.
Arnoux, I. and Audinat, E. 2015. Fractalkine Signaling and Microglia Functions in the Developing Brain. *Neural Plasticity* 2015. doi: 10.1155/2015/689404.
Arsenault, D. et al. 2014. The different effects of LPS and poly I:C prenatal immune challenges on the behavior, development and inflammatory responses in pregnant mice and their offspring. *Brain, Behavior, and Immunity* 38, pp. 77–90. doi: 10.1016/J.BBI.2013.12.016.
Austin, C.P. and Cepko, C.L. 1990. Cellular migration patterns in the developing mouse cerebral cortex. *Development* 110(3), pp. 713–732. doi: 10.1242/DEV.110.3.713.
Balsevich, G. et al. 2016. Prenatal Exposure to Maternal Obesity Alters Anxiety and Stress Coping Behaviors in Aged Mice. *Neuroendocrinology* 103(3–4), pp. 354–368. doi: 10.1159/000439087.
Bao, M. et al. 2022a. LPS versus Poly I:C model: comparison of long-term effects of bacterial and viral maternal immune activation on the offspring. *American Journal of Physiology - Regulatory, Integrative and Comparative Physiology* 322(2), p. R99. doi: 10.1152/AJPREGU.00087.2021.
Bao, M. et al. 2022b. LPS vs. Poly I:C Model: Comparison of Long-Term Effects of Bacterial and Viral Maternal Immune Activation (MIA) on the Offspring. *American Journal of Physiology - Regulatory Integrative and Comparative Physiology* 322(2). doi: 10.1152/AJPREGU.00087.2021/ASSET/IMAGES/LARGE/AJPREGU.00087.2021_F002.JPEG.
Barker, D.J. and Osmond, C. 1988. Low birth weight and hypertension. *British Medical Journal* 297(6641), pp. 134–135. doi: 10.1136/BMJ.297.6641.134-B.
Basil, P. et al. 2018. Prenatal immune activation alters the adult neural epigenome but can be partly stabilised by a n-3 polyunsaturated fatty acid diet. *Translational Psychiatry* 8(1), p. 125. doi: 10.1038/S41398-018-0167-X.
Bellenguez, C. et al. 2022. New insights into the genetic etiology of Alzheimer's disease and related dementias. *Nature Genetics 2022 54:4* 54(4), pp. 412–436. doi: 10.1038/s41588-022-01024-z.
Ben-Yehuda, H. et al. 2019. Maternal Type-I interferon signaling adversely affects the microglia and the behavior of the offspring accompanied by increased sensitivity to stress. *Molecular Psychiatry 2019 25:5* 25(5), pp. 1050–1067. doi:

10.1038/s41380-019-0604-0.
Benaim, C. et al. 2018. Early pregnancy body mass index modifies the association of pre-pregnancy dietary patterns with serum polyunsaturated fatty acid concentrations throughout pregnancy in Brazilian women. *Maternal & Child Nutrition* 14(1). doi: 10.1111/MCN.12480.
Bennett, M.L. et al. 2016. New tools for studying microglia in the mouse and human CNS. *Proceedings of the National Academy of Sciences* 113(12), pp. E1738–E1746. doi: 10.1073/PNAS.1525528113.
Bernier, L.P. et al. 2020. Microglial metabolic flexibility supports immune surveillance of the brain parenchyma. *Nature Communications* 11(1), pp. 1–17. doi: 10.1038/s41467-020-15267-z.
Bertani, B. and Ruiz, N. 2018. Function and biogenesis of lipopolysaccharides. *EcoSal Plus* 8(1). doi: 10.1128/ECOSALPLUS.ESP-0001-2018.
Biber, K. et al. 2007. Neuronal 'On' and 'Off' signals control microglia. *Trends in Neurosciences* 30(11), pp. 596–602. doi: 10.1016/J.TINS.2007.08.007.
Bilbo, S.D. and Tsang, V. 2010. Enduring consequences of maternal obesity for brain inflammation and behavior of offspring. *The FASEB Journal* 24(6), pp. 2104–2115. doi: 10.1096/fj.09-144014.
Bina, R. et al. 2020. De novo variants in SUPT16H cause neurodevelopmental disorders associated with corpus callosum abnormalities. *Journal of medical genetics* 57(7), p. 461. doi: 10.1136/JMEDGENET-2019-106193.
Bohlen, C.J. et al. 2017. Diverse Requirements for Microglial Survival, Specification, and Function Revealed by Defined-Medium Cultures. *Neuron* . doi: 10.1016/j.neuron.2017.04.043.
Van den Bossche, J. et al. 2017. Macrophage Immunometabolism: Where Are We (Going)? *Trends in Immunology* 38(6), pp. 395–406. doi: 10.1016/j.it.2017.03.001.
Boulan, L. and Léopold, P. 2021. What determines organ size during development and regeneration? *Development (Cambridge)* 148(1). doi: 10.1242/DEV.196063/237420.
Brioschi, S. et al. 2020. Brain macrophages in development, homeostasis and disease. *Journal of immunology (Baltimore, Md. : 1950)* 204(2), p. 294. doi: 10.4049/JIMMUNOL.1900821.
Bronson, S.L. et al. 2011. Individual differences in maternal response to immune challenge predict offspring behavior: Contribution of environmental factors.

Behavioural brain research 220(1), p. 55. doi: 10.1016/J.BBR.2010.12.040.
Brown, A.S. and Meyer, U. 2018. Maternal immune activation and neuropsychiatric illness: A translational research perspective. *American Journal of Psychiatry* 175(11), pp. 1073–1083. doi: 10.1176/appi.ajp.2018.17121311.
Buffington, S.A. et al. 2016. Microbial Reconstitution Reverses Maternal Diet-Induced Social and Synaptic Deficits in Offspring. *Cell* 165(7), pp. 1762–1775. doi: 10.1016/j.cell.2016.06.001.
Butler, A. et al. 2018. Integrating single-cell transcriptomic data across different conditions, technologies, and species. *Nature Biotechnology 2018 36:5* 36(5), pp. 411–420. doi: 10.1038/nbt.4096.
Butovsky, O. et al. 2006. Microglia activated by IL-4 or IFN-γ differentially induce neurogenesis and oligodendrogenesis from adult stem/progenitor cells. *Molecular and Cellular Neuroscience* 31(1), pp. 149–160. doi: 10.1016/J.MCN.2005.10.006.
Butovsky, O. et al. 2014. Identification of a unique TGF-β-dependent molecular and functional signature in microglia. *Nature Neuroscience* 17(1), pp. 131–143. doi: 10.1038/nn.3599.
Canales, C.P. et al. 2021. Sequential perturbations to mouse corticogenesis following in utero maternal immune activation. *eLife* 10. doi: 10.7554/ELIFE.60100.
Careaga, M. et al. 2017. Maternal Immune Activation and Autism Spectrum Disorder: From Rodents to Nonhuman and Human Primates. *Biological Psychiatry* . doi: 10.1016/j.biopsych.2016.10.020.
Careaga, M. et al. 2018. Variability in PolyIC induced immune response: Implications for preclinical maternal immune activation models. *Journal of Neuroimmunology* 323, pp. 87–93. doi: 10.1016/J.JNEUROIM.2018.06.014.
Carpenter, K.C. et al. 2013. Considerations to maximize fat mass gain in a mouse model of diet-induced weight gain. *Laboratory Animals* 47(4), pp. 266–273. doi: 10.1177/0023677213501658.
Casano, A.M. et al. 2016. Developmental Apoptosis Mediates Entry and Positioning of Microglia in the Zebrafish Brain. *Cell Reports* 16(4), pp. 897–906. doi: 10.1016/j.celrep.2016.06.033.
Charles A Janeway, J. et al. 2001. Receptors of the innate immune system.
Chen, H. et al. 2008. Maternal and Postnatal Overnutrition Differentially Impact Appetite Regulators and Fuel Metabolism. *Endocrinology* 149(11), pp. 5348–5356. doi: 10.1210/en.2008-0582.

Chen, Q. et al. 2014. Maternal pre-pregnancy body mass index and offspring attention deficit hyperactivity disorder: a population-based cohort study using a sibling-comparison design. *International Journal of Epidemiology* 43(1), p. 83. doi: 10.1093/IJE/DYT152.
Chen, V.S. et al. 2017. Histology Atlas of the Developing Prenatal and Postnatal Mouse Central Nervous System, with Emphasis on Prenatal Days E7.5 to E18.5. *Toxicologic Pathology* 45(6), pp. 705–744. doi: 10.1177/0192623317728134.
Choi, J.S. et al. 2004. Transient expression of osteopontin mRNA and protein in amoeboid microglia in developing rat brain. *Experimental Brain Research* 154(3), pp. 275–280. doi: 10.1007/s00221-003-1657-4.
Chow, K.-H. et al. 2016. Induction of Maternal Immune Activation in Mice at Mid-gestation Stage with Viral Mimic Poly(I:C). *Journal of Visualized Experiments : JoVE* 2016(109), p. 53643. doi: 10.3791/53643.
Christian, L.M. and Porter, K. 2014. Longitudinal changes in serum proinflammatory markers across pregnancy and postpartum: Effects of maternal body mass index. *Cytokine* 70(2), pp. 134–140. doi: 10.1016/j.cyto.2014.06.018.
Christians, J.K. et al. 2019. Effects of high-fat diets on fetal growth in rodents: A systematic review. *Reproductive Biology and Endocrinology* 17(1). doi: 10.1186/s12958-019-0482-y.
Cormican, S. and Griffin, M.D. 2021. Fractalkine (CX3CL1) and Its Receptor CX3CR1: A Promising Therapeutic Target in Chronic Kidney Disease? *Frontiers in Immunology* 12, p. 664202. doi: 10.3389/FIMMU.2021.664202/BIBTEX.
Courchesne, E. et al. 2011. Neuron number and size in prefrontal cortex of children with autism. *JAMA* 306(18), pp. 2001–2010. doi: 10.1001/JAMA.2011.1638.
Crew, R.C. et al. 2016. Maternal obesity induced by a ‘cafeteria’ diet in the rat does not increase inflammation in maternal, placental or fetal tissues in late gestation. *Placenta* 39, pp. 33–40. doi: 10.1016/j.placenta.2016.01.002.
Cuadros, M.A. and Navascués, J. 2001. Early origin and colonization of the developing central nervous system by microglial precursors. *Progress in Brain Research* 132, pp. 51–59. doi: 10.1016/S0079-6123(01)32065-4.
Cunningham, C.L. et al. 2013. Microglia Regulate the Number of Neural Precursor Cells in the Developing Cerebral Cortex. *Journal of Neuroscience* . doi: 10.1523/jneurosci.3441-12.2013.
Currle, D.S. et al. 2005. Direct and indirect roles of CNS dorsal midline cells in

choroid plexus epithelia formation. *Development* 132(15), pp. 3549–3559. doi: 10.1242/DEV.01915.
Daskalakis, N.P. et al. 2013. The three-hit concept of vulnerability and resilience: towards understanding adaptation to early-life adversity outcome. *Psychoneuroendocrinology* 38(9), p. 1858. doi: 10.1016/J.PSYNEUEN.2013.06.008.
Daugas, E. et al. 2000. Mitochondrio-nuclear translocation of AIF in apoptosis and necrosis. *The FASEB Journal* 14(5), pp. 729–739. doi: 10.1096/FASEBJ.14.5.729.
Davalos, D. et al. 2005. ATP mediates rapid microglial response to local brain injury in vivo. *Nature Neuroscience 2005 8:6* 8(6), pp. 752–758. doi: 10.1038/nn1472.
Davis, C.D. 2016. The gut microbiome and its role in obesity. *Nutrition Today* 51(4), pp. 167–174. doi: 10.1097/NT.0000000000000167.
Davis, J. and Mire, E. 2021. Maternal obesity and developmental programming of neuropsychiatric disorders: An inflammatory hypothesis. *https://doi.org/10.1177/23982128211003484* 5, p. 239821282110034. doi: 10.1177/23982128211003484.
Debnath, M. et al. 2013. Lack of association of IL-6 (−174 G > C) and TNF-α (−238 G > A) variants with paranoid schizophrenia in Indian Bengalee population. *Cytokine* 61(2), pp. 455–458. doi: 10.1016/J.CYTO.2012.10.028.
Debost, J.-C.P.G. et al. 2017. Joint Effects of Exposure to Prenatal Infection and Peripubertal Psychological Trauma in Schizophrenia. *Schizophrenia Bulletin* 43(1), pp. 171–179. doi: 10.1093/schbul/sbw083.
Dennis, M. et al. 2013. Age, plasticity, and homeostasis in childhood brain disorders. *Neuroscience & Biobehavioral Reviews* 37(10), pp. 2760–2773. doi: 10.1016/J.NEUBIOREV.2013.09.010.
Desai, N. et al. 2013. Maternal metformin treatment decreases fetal inflammation in a rat model of obesity and metabolic syndrome. *American Journal of Obstetrics and Gynecology* 209(2), pp. 136.e1-136.e9. doi: 10.1016/j.ajog.2013.05.001.
Deverman, B.E. and Patterson, P.H. 2009. Cytokines and CNS Development. *Neuron* 64(1), pp. 61–78. doi: 10.1016/j.neuron.2009.09.002.
Divakaruni, A.S. et al. 2018. Etomoxir Inhibits Macrophage Polarization by Disrupting CoA Homeostasis. *Cell Metabolism* 28(3), pp. 490-503.e7. doi: 10.1016/j.cmet.2018.06.001.
Dobin, A. et al. 2013. STAR: ultrafast universal RNA-seq aligner. *Bioinformatics* 29(1), pp. 15–21. doi: 10.1093/BIOINFORMATICS/BTS635.

Dunn, G.A. et al. 2022. Maternal diet and obesity shape offspring central and peripheral inflammatory outcomes in juvenile non-human primates. *Brain, Behavior, and Immunity* 102, pp. 224–236. doi: 10.1016/J.BBI.2022.02.024.
Duque, A. and Rakic, P. 2015. Identification of proliferating and migrating cells by BrdU and other thymidine analogs: Benefits and limitations. In: *Immunocytochemistry and Related Techniques*. Springer New York, pp. 123–139. doi: 10.1007/978-1-4939-2313-7_7.
Edlow, A.G. et al. 2016. Males are from Mars, and females are from Venus: Sex-specific fetal brain gene expression signatures in a mouse model of maternal diet-induced obesity. *American Journal of Obstetrics and Gynecology* . doi: 10.1016/j.ajog.2016.02.054.
Edlow, A.G. 2017. Maternal obesity and neurodevelopmental and psychiatric disorders in offspring. *Prenatal Diagnosis* 37(1), pp. 95–110. doi: 10.1002/pd.4932.
Edlow, A.G. et al. 2019. Placental Macrophages: A Window Into Fetal Microglial Function in Maternal Obesity. *International Journal of Developmental Neuroscience* 77(August 2018), pp. 60–68. doi: 10.1016/j.ijdevneu.2018.11.004.
Ellacott, K.L.J. et al. 2010. Assessment of feeding behavior in laboratory mice. *Cell Metabolism* 12(1), pp. 10–17. doi: 10.1016/j.cmet.2010.06.001.
Erice, C. et al. 2019. Regional Differences in the Contributions of TNF Reverse and Forward Signaling to the Establishment of Sympathetic Innervation. *Developmental Neurobiology* 79(4), pp. 317–334. doi: 10.1002/dneu.22680.
Ericsson, A.C. and Franklin, C.L. 2021. The gut microbiome of laboratory mice: considerations and best practices for translational research. *Mammalian Genome 2021 32:4* 32(4), pp. 239–250. doi: 10.1007/S00335-021-09863-7.
Estes, M.L. et al. 2019. Enhancing rigor and reproducibility in maternal immune activation models: practical considerations and predicting resilience and susceptibility using baseline immune responsiveness before pregnancy. *bioRxiv* , p. 699983. doi: 10.1101/699983.
Estes, M.L. et al. 2020. Baseline immunoreactivity before pregnancy and poly(I:C) dose combine to dictate susceptibility and resilience of offspring to maternal immune activation. *Brain, Behavior, and Immunity* 88, pp. 619–630. doi: 10.1016/J.BBI.2020.04.061.
Estes, M.L. and McAllister, A.K. 2016a. Maternal immune activation: Implications for neuropsychiatric disorders. *Science* 353(6301), pp. 772–777. doi:

10.1126/science.aag3194.
Estes, M.L. and McAllister, A.K. 2016b. Maternal immune activation: Implications for neuropsychiatric disorders. *Science* . doi: 10.1126/science.aag3194.
Fame, R.M. et al. 2011. Development, Specification, and Diversity of Callosal Projection Neurons. doi: 10.1016/j.tins.2010.10.002.
Fang, W.Q. et al. 2014. Overproduction of upper-layer neurons in the neocortex leads to autism-like features in mice. *Cell reports* 9(5), pp. 1635–1643. doi: 10.1016/J.CELREP.2014.11.003.
Farkas, L.M. et al. 2003. Transforming growth factor-βs are essential for the development of midbrain dopaminergic neurons in vitro and in vivo. *Journal of Neuroscience* 23(12), pp. 5178–5186. doi: 10.1523/JNEUROSCI.23-12-05178.2003.
Ferguson, S.A. and Maier, K.L. 2013. A review of seasonal/circannual effects of laboratory rodent behavior. *Physiology & Behavior* 119, pp. 130–136. doi: 10.1016/J.PHYSBEH.2013.06.007.
Fernandes, C. et al. 2012. Prenatal exposure to maternal obesity leads to hyperactivity in offspring. *Molecular Psychiatry* 17(12), pp. 1159–1160. doi: 10.1038/mp.2011.164.
Fernandes, M.R. et al. 2016. Animal models of obesity in rodents. An integrative review. *Acta Cirurgica Brasileira* 31(12), pp. 840–844. doi: 10.1590/S0102-865020160120000010.
Filipello, F. et al. 2018. The Microglial Innate Immune Receptor TREM2 Is Required for Synapse Elimination and Normal Brain Connectivity. *Immunity* 48(5), pp. 979-991.e8. doi: 10.1016/j.immuni.2018.04.016.
Fortunato, J.J. et al. 2017. Effects of ω-3 fatty acids on stereotypical behavior and social interactions in Wistar rats prenatally exposed to lipopolysaccarides. *Nutrition* 35, pp. 119–127. doi: 10.1016/j.nut.2016.10.019.
Fricke, E.M. et al. 2018. Lipopolysaccharide-induced maternal inflammation induces direct placental injury without alteration in placental blood flow and induces a secondary fetal intestinal injury that persists into adulthood. In: *American Journal of Reproductive Immunology*. Blackwell Publishing Ltd, p. e12816. doi: 10.1111/aji.12816.
Fricker, M. et al. 2012. MFG-E8 mediates primary phagocytosis of viable neurons during neuroinflammation. *Journal of Neuroscience* 32(8), pp. 2657–2666. doi: 10.1523/JNEUROSCI.4837-11.2012.

Friis, C.M. et al. 2013. Adiposity-related inflammation: Effects of pregnancy. *Obesity* 21(1), pp. E124–E130. doi: 10.1002/oby.20120.
Frydecka, D. et al. 2013. Genetic variants in transforming growth factor-b gene (TGFB1) affect susceptibility to schizophrenia. *Molecular Biology Reports* 40(10), pp. 5607–5614. doi: 10.1007/s11033-013-2662-8.
Fuller, A.D. and Van Eldik, L.J. 2008. MFG-E8 regulates microglial phagocytosis of apoptotic neurons. *Journal of Neuroimmune Pharmacology* 3(4), pp. 246–256. doi: 10.1007/s11481-008-9118-2.
Galliano, E. et al. 2018. Embryonic and postnatal neurogenesis produce functionally distinct subclasses of dopaminergic neuron. *eLife* 7. doi: 10.7554/ELIFE.32373.
Gao, Y. et al. 2014. Hormones and Diet, but Not Body Weight, Control Hypothalamic Microglial Activity. *Glia* 62(1), pp. 17–25. doi: 10.1002/glia.22580.
Gao, Y. et al. 2018. Deficiency of leptin receptor in myeloid cells disrupts hypothalamic metabolic circuits and causes body weight increase. *Molecular Metabolism* 7, pp. 155–160. doi: 10.1016/j.molmet.2017.11.003.
Gaus, R. et al. 2022. Reduced cortical neuron number and neuron density in schizophrenia with focus on area 24: a post-mortem case–control study. *European Archives of Psychiatry and Clinical Neuroscience 2022* 1, pp. 1–15. doi: 10.1007/S00406-022-01513-6.
Geirsdottir, L. et al. 2019. Cross-Species Single-Cell Analysis Reveals Divergence of the Primate Microglia Program. *Cell* 179(7), pp. 1609-1622.e16. doi: 10.1016/J.CELL.2019.11.010.
Gillespie, S.L. et al. 2016. Adaptation of the inflammatory immune response across pregnancy and postpartum in Black and White women. *Journal of Reproductive Immunology* 114, pp. 27–31. doi: 10.1016/j.jri.2016.02.001.
Ginhoux, F. et al. 2010a. Fate mapping analysis reveals that adult microglia derive from primitive macrophages. *Science* 330(6005), pp. 841–845. doi: 10.1126/science.1194637.
Ginhoux, F. et al. 2010b. Fate Mapping Analysis Reveals That Adult Microglia Derive from Primitive Macrophages. doi: 10.1126/science.1194637.
Glass, R. et al. 2019. Maternal immune activation with staphylococcal enterotoxin A produces unique behavioral changes in C57BL/6 mouse offspring. *Brain, Behavior, and Immunity* 75, pp. 12–25. doi: 10.1016/j.bbi.2018.05.005.
Glebov, K. et al. 2015. Serotonin stimulates secretion of exosomes from microglia

cells. *Glia* 63(4), pp. 626–634. doi: 10.1002/GLIA.22772.
Gobius, I. et al. 2016. Astroglial-Mediated Remodeling of the Interhemispheric Midline Is Required for the Formation of the Corpus Callosum. *Cell Reports* 17(3), pp. 735–747. doi: 10.1016/j.celrep.2016.09.033.
El Gohary, T.M. et al. 2015. Plasma level of transforming growth factor β 1 in children with autism spectrum disorder. *Egyptian Journal of Ear, Nose, Throat and Allied Sciences* 16(1), pp. 69–73. doi: 10.1016/j.ejenta.2014.12.002.
Goldmann, T. et al. 2016. Origin, fate and dynamics of macrophages at central nervous system interfaces. *Nature Immunology* 17(7), pp. 797–805. doi: 10.1038/ni.3423.
Gorbalenya, A.E. et al. 2020. The species Severe acute respiratory syndrome-related coronavirus: classifying 2019-nCoV and naming it SARS-CoV-2. *Nature Microbiology* 5(4), p. 536. doi: 10.1038/S41564-020-0695-Z.
Götz, M. and Huttner, W.B. 2005. The cell biology of neurogenesis. *Nature Reviews Molecular Cell Biology 2005 6:10* 6(10), pp. 777–788. doi: 10.1038/nrm1739.
Graham, C. et al. 2017. In vivo immune signatures of healthy human pregnancy: Inherently inflammatory or anti-inflammatory? *PLoS ONE* 12(6). doi: 10.1371/journal.pone.0177813.
Gregor, M.F. and Hotamisligil, G.S. 2011. Inflammatory Mechanisms in Obesity. *Annual Review of Immunology* 29(1), pp. 415–445. doi: 10.1146/annurev-immunol-031210-101322.
Griffith, O.W. et al. 2017. Embryo implantation evolved from an ancestral inflammatory attachment reaction. *Proceedings of the National Academy of Sciences of the United States of America* 114(32), pp. E6566–E6575. doi: 10.1073/pnas.1701129114.
Gumusoglu, S.B. and Stevens, H.E. 2019. Maternal Inflammation and Neurodevelopmental Programming: A Review of Preclinical Outcomes and Implications for Translational Psychiatry. *Biological Psychiatry* 85(2), pp. 107–121. doi: 10.1016/J.BIOPSYCH.2018.08.008.
Hagemeyer, N. et al. 2017. Microglia contribute to normal myelinogenesis and to oligodendrocyte progenitor maintenance during adulthood. *Acta Neuropathologica* 134(3), pp. 441–458. doi: 10.1007/s00401-017-1747-1.
Hammond, T.R. et al. 2019. Single-Cell RNA Sequencing of Microglia throughout the Mouse Lifespan and in the Injured Brain Reveals Complex Cell-State Changes.

Immunity . doi: 10.1016/j.immuni.2018.11.004.
Han, V.X. et al. 2021. Maternal acute and chronic inflammation in pregnancy is associated with common neurodevelopmental disorders: a systematic review. *Translational Psychiatry 2021 11:1* 11(1), pp. 1–12. doi: 10.1038/s41398-021-01198-w.
Hanisch, U.K. and Kettenmann, H. 2007. Microglia: active sensor and versatile effector cells in the normal and pathologic brain. *Nature Neuroscience 2007 10:11* 10(11), pp. 1387–1394. doi: 10.1038/nn1997.
Harvey, L. and Boksa, P. 2012. A stereological comparison of GAD67 and reelin expression in the hippocampal stratum oriens of offspring from two mouse models of maternal inflammation during pregnancy. *Neuropharmacology* 62(4), pp. 1767–1776. doi: 10.1016/J.NEUROPHARM.2011.11.022.
Heikura, U. et al. 2008. Variations in Prenatal Sociodemographic Factors associated with Intellectual Disability: A Study of the 20-Year Interval between Two Birth Cohorts in Northern Finland. *American Journal of Epidemiology* 167(2), pp. 169–177. doi: 10.1093/AJE/KWM291.
Hermann, G.M. et al. 2010. Neonatal macrosomia is an independent risk factor for adult metabolic syndrome. *Neonatology* 98(3), pp. 238–244. doi: 10.1159/000285629.
Hevner, R.F. et al. 2004. Postnatal shifts of interneuron position in the neocortex of normal and reeler mice: evidence for inward radial migration. *Neuroscience* 124(3), pp. 605–618. doi: 10.1016/J.NEUROSCIENCE.2003.11.033.
Hicks, S.P. and D'Amato, C.J. 1968. Cell migrations to the isocortex in the rat. *The Anatomical Record* 160(3), pp. 619–633. doi: 10.1002/AR.1091600311.
Higa, T.S. et al. 2014. Comparison between cafeteria and high-fat diets in the induction of metabolic dysfunction in mice. *International Journal of Physiology, Pathophysiology and Pharmacology* 6(1), pp. 47–54.
Hiramatsu, L. et al. 2017. Maternal exposure to Western diet affects adult body composition and voluntary wheel running in a genotype-specific manner in mice. *Physiology & Behavior* 179, pp. 235–245. doi: 10.1016/J.PHYSBEH.2017.06.008.
Hoeffel, G. et al. 2015. C-Myb+ Erythro-Myeloid Progenitor-Derived Fetal Monocytes Give Rise to Adult Tissue-Resident Macrophages. *Immunity* 42(4), pp. 665–678. doi: 10.1016/J.IMMUNI.2015.03.011.
Holub, M. et al. 2013. Clinical Study Cytokines and Chemokines as Biomarkers of

Community-Acquired Bacterial Infection. *Mediators of Inflammation* 2013. doi: 10.1155/2013/190145.
Hoshiko, M. et al. 2012. Deficiency of the Microglial Receptor CX3CR1 Impairs Postnatal Functional Development of Thalamocortical Synapses in the Barrel Cortex. *Journal of Neuroscience* 32(43), pp. 15106–15111. doi: 10.1523/JNEUROSCI.1167-12.2012.
Hotamisligil, G.S. et al. 1993. Adipose expression of tumor necrosis factor-α: Direct role in obesity-linked insulin resistance. *Science* 259(5091), pp. 87–91. doi: 10.1126/science.7678183.
Huang, Y. et al. 2023. The gut microbiome modulates the transformation of microglial subtypes. *Molecular Psychiatry 2023 28:4* 28(4), pp. 1611–1621. doi: 10.1038/s41380-023-02017-y.
Hughes, P.M. et al. 2002. Expression of fractalkine (CX3CL1) and its receptor, CX3CR1, during acute and chronic inflammation in the rodent CNS. *Glia* 37(4), pp. 314–327. doi: 10.1002/GLIA.10037.
Ianevski, A. et al. 2022. Fully-automated and ultra-fast cell-type identification using specific marker combinations from single-cell transcriptomic data. *Nature Communications 2022 13:1* 13(1), pp. 1–10. doi: 10.1038/s41467-022-28803-w.
Inoubli, O. et al. 2018. Haplotypes of TNFα/β Genes Associated with Sex-Specific Paranoid Schizophrenic Risk in Tunisian Population. *Disease Markers* 2018. doi: 10.1155/2018/3502564.
Inta, D. et al. 2008. Neurogenesis and widespread forebrain migration of distinct GABAergic neurons from the postnatal subventricular zone. *Proceedings of the National Academy of Sciences of the United States of America* 105(52), pp. 20994–20999. doi: 10.1073/PNAS.0807059105/SUPPL_FILE/SM6.MPG.
Jansson, T. 2016. Placenta plays a critical role in maternal-fetal resource allocation. *Proceedings of the National Academy of Sciences of the United States of America* 113(40), pp. 11066–11068. doi: 10.1073/pnas.1613437113.
Jernberg, J.N. et al. 2017. Developmental regulation and localization of carnitine palmitoyltransferases (CPTs) in rat brain. *Journal of Neurochemistry* 142(3), pp. 407–419. doi: 10.1111/jnc.14072.
Jialal, I. et al. 2014. Toll-like Receptor Status in Obesity and Metabolic Syndrome: A Translational Perspective. *The Journal of Clinical Endocrinology & Metabolism* 99(1), pp. 39–48. doi: 10.1210/JC.2013-3092.

Jung, S. et al. 2000. Analysis of Fractalkine Receptor CX3CR1 Function by Targeted Deletion and Green Fluorescent Protein Reporter Gene Insertion. *Molecular and Cellular Biology* 20(11), pp. 4106–4114. doi: 10.1128/mcb.20.11.4106-4114.2000.
Jungheim, E.S. et al. 2010. Diet-Induced Obesity Model: Abnormal Oocytes and Persistent Growth Abnormalities in the Offspring. *Endocrinology* 151(8), p. 4039. doi: 10.1210/EN.2010-0098.
Jurga, A.M. et al. 2020. Overview of General and Discriminating Markers of Differential Microglia Phenotypes. *Frontiers in Cellular Neuroscience* 14, p. 198. doi: 10.3389/FNCEL.2020.00198/BIBTEX.
Kaminow, B. et al. 2021. STARsolo: accurate, fast and versatile mapping/quantification of single-cell and single-nucleus RNA-seq data. *bioRxiv* , p. 2021.05.05.442755. doi: 10.1101/2021.05.05.442755.
Kang, S.S. et al. 2014. Dietary intervention rescues maternal obesity induced behavior deficits and neuroinflammation in offspring. *Journal of Neuroinflammation* . doi: 10.1186/s12974-014-0156-9.
Kang, S.S. et al. 2018. Microglial translational profiling reveals a convergent APOE pathway from aging, amyloid, and tau. *Journal of Experimental Medicine* 215(9), pp. 2235–2245. doi: 10.1084/JEM.20180653.
Karperien, A. et al. 2013. Quantitating the subtleties of microglial morphology with fractal analysis. *Frontiers in Cellular Neuroscience* 7(JANUARY 2013), pp. 1–34. doi: 10.3389/fncel.2013.00003.
Kato, T. et al. 2000. Heterogeneity in the immune response to serotype b LPS of Actinobacillus actinomycetemcomitans in inbred strains of mice. *FEMS Immunology & Medical Microbiology* 28(1), pp. 67–70. doi: 10.1111/J.1574-695X.2000.TB01458.X.
Kaufman, M.H. and Bard, J.B.L. 1999. The Anatomical Basis of Mouse Development., p. 305.
Kawasaki, T. and Kawai, T. 2014. Toll-like receptor signaling pathways. *Frontiers in Immunology* 5(SEP), p. 461. doi: 10.3389/FIMMU.2014.00461/BIBTEX.
Kentner, A.C. et al. 2019. Maternal immune activation: reporting guidelines to improve the rigor, reproducibility, and transparency of the model. *Neuropsychopharmacology* 44(2), p. 245. doi: 10.1038/S41386-018-0185-7.
Keren-Shaul, H. et al. 2017. A Unique Microglia Type Associated with Restricting Development of Alzheimer's Disease. *Cell* 169(7), pp. 1276-1290.e17. doi:

10.1016/j.cell.2017.05.018.
Khaodhiar, L. et al. 2004. Serum levels of interleukin-6 and C-reactive protein correlate with body mass index across the broad range of obesity. *Journal of Parenteral and Enteral Nutrition* 28(6), pp. 410–415. doi: 10.1177/0148607104028006410.
Kierdorf, K. et al. 2013. Microglia emerge from erythromyeloid precursors via Pu.1- and Irf8-dependent pathways. *Nature Neuroscience* 16(3), pp. 273–280. doi: 10.1038/nn.3318.
Kim, D.R. et al. 2015. Prenatal Programming of Mental Illness: Current Understanding of Relationship and Mechanisms. *Current Psychiatry Reports* 17(2). doi: 10.1007/s11920-014-0546-9.
Kim, D.W. et al. 2014. Obesity During Pregnancy Disrupts Placental Morphology, Cell Proliferation, and Inflammation in a Sex-Specific Manner Across Gestation in the Mouse1. *Biology of Reproduction* 90(6). doi: 10.1095/biolreprod.113.117259.
Kim, H. et al. 2019. Decreased Neuron Number and Synaptic Plasticity in SIRT3-Knockout Mice with Poor Remote Memory. *Neurochemical Research* 44(3), pp. 676–682. doi: 10.1007/S11064-017-2417-3/METRICS.
Kim, J.W. et al. 2018. Strain-specific differential expression of astrocytes and microglia in the mouse hippocampus. *Brain and Behavior* 8(5). doi: 10.1002/BRB3.961.
Kim, S. et al. 2017. Maternal gut bacteria promote neurodevelopmental abnormalities in mouse offspring. *Nature* . doi: 10.1038/nature23910.
King, V. et al. 2013a. Maternal Obesity Has Little Effect on the Immediate Offspring but Impacts on the Next Generation. *Endocrinology* 154(7), pp. 2514–2524. doi: 10.1210/EN.2013-1013.
King, V. et al. 2013b. The effects of an obesogenic diet during pregnancy on fetal growth and placental gene expression are gestation dependent. *Placenta* 34(11), pp. 1087–1090. doi: 10.1016/J.PLACENTA.2013.09.006.
Köberlin, M.S. et al. 2015. A Conserved Circular Network of Coregulated Lipids Modulates Innate Immune Responses. *Cell* 162(1), pp. 170–183. doi: 10.1016/j.cell.2015.05.051.
Koester, S.E. and O'Leary, D.D.M. 1993. Connectional Distinction between Callosal and Subcortically Projecting Cortical Neurons Is Determined Prior to Axon Extension. *Developmental Biology* 160(1), pp. 1–14. doi: 10.1006/DBIO.1993.1281.

Kowash, H.M. et al. 2019. Poly(I:C) source, molecular weight and endotoxin contamination affect dam and prenatal outcomes, implications for models of maternal immune activation. *Brain, Behavior, and Immunity* 82, pp. 160–166. doi: 10.1016/J.BBI.2019.08.006.
Krakowiak, P. et al. 2012. Maternal Metabolic Conditions and Risk for Autism and Other Neurodevelopmental Disorders. *Pediatrics* 129(5), p. e1121. doi: 10.1542/PEDS.2011-2583.
Kwon, E.J. and Kim, Y.J. 2017. What is fetal programming?: A lifetime health is under the control of in utero health. *Obstetrics and Gynecology Science* 60(6), pp. 506–519. doi: 10.5468/ogs.2017.60.6.506.
Lai, Z.L. et al. 2018. Fecal microbiota transplantation confers beneficial metabolic effects of diet and exercise on diet-induced obese mice. *Scientific Reports* 8(1), pp. 1–11. doi: 10.1038/s41598-018-33893-y.
Lancaster, G.I. et al. 2018. Evidence that TLR4 Is Not a Receptor for Saturated Fatty Acids but Mediates Lipid-Induced Inflammation by Reprogramming Macrophage Metabolism. *Cell Metabolism* 27(5), pp. 1096-1110.e5. doi: 10.1016/j.cmet.2018.03.014.
Li, G. et al. 2018. The intervention effect of aspirin on a lipopolysaccharide-induced preeclampsia-like mouse model by inhibiting the nuclear factor-κB pathway. *Biology of Reproduction* 99(2), pp. 422–432. doi: 10.1093/BIOLRE/IOY025.
Li, J. et al. 2020. High fat diet induced obesity model using four strains of mice: Kunming,C57BL/6, BALB/c and ICR. *Experimental Animals* 69(3), p. 326. doi: 10.1538/EXPANIM.19-0148.
Li, Q. et al. 2019a. Developmental Heterogeneity of Microglia and Brain Myeloid Cells Revealed by Deep Single-Cell RNA Sequencing. *Neuron* 101(2), pp. 207-223.e10. doi: 10.1016/j.neuron.2018.12.006.
Li, Q. et al. 2019b. Developmental Heterogeneity of Microglia and Brain Myeloid Cells Revealed by Deep Single-Cell RNA Sequencing. *Neuron* . doi: 10.1016/j.neuron.2018.12.006.
Li, Q. et al. 2019c. Developmental Heterogeneity of Microglia and Brain Myeloid Cells Revealed by Deep Single-Cell RNA Sequencing. *Neuron* 101(2), pp. 207-223.e10. doi: 10.1016/j.neuron.2018.12.006.
Liao, Y. et al. 2019. WebGestalt 2019: gene set analysis toolkit with revamped UIs and APIs. *Nucleic Acids Research* 47(W1), pp. W199–W205. doi:

10.1093/NAR/GKZ401.
Van Lieshout, R.J. et al. 2013. Maternal Pre-Pregnancy Body Mass Index and Internalizing and Externalizing Problems in Offspring. *http://dx.doi.org/10.1177/070674371305800305* 58(3), pp. 151–159. doi: 10.1177/070674371305800305.
Lindwall, C. et al. 2007. Commissure formation in the mammalian forebrain. *Current Opinion in Neurobiology* 17(1), pp. 3–14. doi: 10.1016/j.conb.2007.01.008.
Lins, B.R. et al. 2019. Maternal Immune Activation during Pregnancy Alters the Behavior Profile of Female Offspring of Sprague Dawley Rats. *eNeuro* 6(2), pp. 437–455. doi: 10.1523/ENEURO.0437-18.2019.
Liu, J. et al. 2013. Interplay between human microglia and neural stem/progenitor cells in an allogeneic co-culture model. *Journal of Cellular and Molecular Medicine* 17(11), pp. 1434–1443. doi: 10.1111/JCMM.12123.
Lively, S. et al. 2018. Comparing effects of transforming growth factor β1 on microglia from rat and mouse: Transcriptional profiles and potassium channels. *Frontiers in Cellular Neuroscience* 12, p. 115. doi: 10.3389/fncel.2018.00115.
Loayza, M. et al. 2022. Maternal immune activation alters fetal and neonatal microglia phenotype and disrupts neurogenesis in mice. *Pediatric Research 2022 93:5* 93(5), pp. 1216–1225. doi: 10.1038/s41390-022-02239-w.
Lund, H. et al. 2018. Competitive repopulation of an empty microglial niche yields functionally distinct subsets of microglia-like cells. *Nature Communications* 9(1). doi: 10.1038/s41467-018-07295-7.
Luo, S.X. et al. 2016. TGF-β Signaling in Dopaminergic Neurons Regulates Dendritic Growth, Excitatory-Inhibitory Synaptic Balance, and Reversal Learning. *Cell Reports* 17(12), pp. 3233–3245. doi: 10.1016/j.celrep.2016.11.068.
Lutz, T.A. and Woods, S.C. 2012. Overview of animal models of obesity. *Current Protocols in Pharmacology* CHAPTER(SUPPL.58), p. Unit5.61. doi: 10.1002/0471141755.ph0561s58.
Luzzo, K.M. et al. 2012. High Fat Diet Induced Developmental Defects in the Mouse: Oocyte Meiotic Aneuploidy and Fetal Growth Retardation/Brain Defects. *PLoS ONE* 7(11). doi: 10.1371/journal.pone.0049217.
Ma, C. et al. 2018. The integrated landscape of causal genes and pathways in schizophrenia. *Translational Psychiatry* 8(1), p. 67. doi: 10.1038/S41398-018-0114-X.

Madore, C. et al. 2014. Nutritional n-3 PUFAs deficiency during perinatal periods alters brain innate immune system and neuronal plasticity-associated genes. *Brain, Behavior, and Immunity* . doi: 10.1016/j.bbi.2014.03.021.
Maejima, Y. et al. 2020. Early life high-fat diet exposure evokes normal weight obesity. *Nutrition and Metabolism* 17(1), pp. 1–8. doi: 10.1186/S12986-020-00464-W/FIGURES/2.
Maelfait, J. et al. 2008. Stimulation of Toll-like receptor 3 and 4 induces interleukin-1β maturation by caspase-8. *The Journal of Experimental Medicine* 205(9), p. 1967. doi: 10.1084/JEM.20071632.
Malandrino, M.I. et al. 2015. Enhanced fatty acid oxidation in adipocytes and macrophages reduces lipid-induced triglyceride accumulation and inflammation. *American Journal of Physiology - Endocrinology and Metabolism* 308(9), pp. E756–E769. doi: 10.1152/ajpendo.00362.2014.
Malatesta, P. and Götz, M. 2013. Radial glia - From boring cables to stem cell stars. *Development (Cambridge)* 140(3), pp. 483–486. doi: 10.1242/dev.085852.
Maldonado-Ruiz, R. et al. 2019. Priming of hypothalamic ghrelin signaling and microglia activation exacerbate feeding in rats' offspring following maternal overnutrition. *Nutrients* 11(6). doi: 10.3390/nu11061241.
Manti, M. et al. 2018. Maternal androgen excess and obesity induce sexually dimorphic anxiety-like behavior in the offspring. *The FASEB Journal* 32(8), pp. 4158–4171. doi: 10.1096/FJ.201701263RR.
Marín-Teva, J.L. et al. 2004. Microglia Promote the Death of Developing Purkinje Cells. *Neuron* 41(4), pp. 535–547. doi: 10.1016/S0896-6273(04)00069-8.
Marschallinger, J. et al. 2020. Lipid-droplet-accumulating microglia represent a dysfunctional and proinflammatory state in the aging brain. *Nature Neuroscience 2020 23:2* 23(2), pp. 194–208. doi: 10.1038/s41593-019-0566-1.
Marsh, S.E. et al. 2020. Single Cell Sequencing Reveals Glial Specific Responses to Tissue Processing & Enzymatic Dissociation in Mice and Humans. *bioRxiv* , p. 2020.12.03.408542. doi: 10.1101/2020.12.03.408542.
Marsh, S.E. et al. 2022. Dissection of artifactual and confounding glial signatures by single-cell sequencing of mouse and human brain. *Nature Neuroscience 2022 25:3* 25(3), pp. 306–316. doi: 10.1038/s41593-022-01022-8.
Massarali, A. et al. 2022. Virus-Induced Maternal Immune Activation as an Environmental Factor in the Etiology of Autism and Schizophrenia. *Frontiers in*

Neuroscience 16. doi: 10.3389/FNINS.2022.834058.
Masuda, T. et al. 2019. Spatial and temporal heterogeneity of mouse and human microglia at single-cell resolution. *Nature* 566(7744), pp. 388–392. doi: 10.1038/s41586-019-0924-x.
Matcovitch-Natan, O. et al. 2016. Microglia development follows a stepwise program to regulate brain homeostasis. *Science* . doi: 10.1126/science.aad8670.
Matsuzaki, F. and Shitamukai, A. 2015. Cell division modes and cleavage planes of neural progenitors during mammalian cortical development. *Cold Spring Harbor Perspectives in Biology* 7(9), p. a015719. doi: 10.1101/cshperspect.a015719.
Mattei, D. et al. 2017. Maternal immune activation results in complex microglial transcriptome signature in the adult offspring that is reversed by minocycline treatment. *Translational Psychiatry* 7(5), pp. e1120–e1120. doi: 10.1038/tp.2017.80.
Mazaheri, F. et al. 2014. Distinct roles for BAI1 and TIM-4 in the engulfment of dying neurons by microglia. *Nature Communications 2014 5:1* 5(1), pp. 1–11. doi: 10.1038/ncomms5046.
McArdle, M.A. et al. 2013. Mechanisms of obesity-induced inflammation and insulin resistance: Insights into the emerging role of nutritional strategies. *Frontiers in Endocrinology* 4(MAY). doi: 10.3389/fendo.2013.00052.
McKee, S.E. et al. 2017. Methyl donor supplementation alters cognitive performance and motivation in female offspring from high-fat diet – fed dams. *The FASEB Journal* 31(6), pp. 2352–2363. doi: 10.1096/FJ.201601172R.
Menassa, D.A. and Gomez-Nicola, D. 2018a. Microglial dynamics during human brain development. *Frontiers in Immunology* 9(MAY). doi: 10.3389/fimmu.2018.01014.
Menassa, D.A. and Gomez-Nicola, D. 2018b. Microglial dynamics during human brain development. *Frontiers in Immunology* 9(MAY), p. 1014. doi: 10.3389/FIMMU.2018.01014/BIBTEX.
Meyers, E.A. and Kessler, J.A. 2017. TGF-β family signaling in neural and neuronal differentiation, development, and function. *Cold Spring Harbor Perspectives in Biology* 9(8). doi: 10.1101/cshperspect.a022244.
Mian, M.F. et al. 2013. Length of dsRNA (poly I:C) drives distinct innate immune responses, depending on the cell type. *Journal of Leukocyte Biology* 94(5), pp. 1025–1036. doi: 10.1189/JLB.0312125.
Milanova, I. V. et al. 2019. Diet-induced obesity disturbs microglial

immunometabolism in a time-of-day manner. *Frontiers in Endocrinology* 10(JUN). doi: 10.3389/fendo.2019.00424.
Miller, A.M. and Stella, N. 2009. Microglial cell migration stimulated by ATP and C5a involve distinct molecular mechanisms: Quantification of migration by a novel near-infrared method. *GLIA* 57(8), pp. 875–883. doi: 10.1002/glia.20813.
Missault, S. et al. 2014. The risk for behavioural deficits is determined by the maternal immune response to prenatal immune challenge in a neurodevelopmental model. *Brain, Behavior, and Immunity* 42, pp. 138–146. doi: 10.1016/J.BBI.2014.06.013.
Miyamoto, A. et al. 2016. Microglia contact induces synapse formation in developing somatosensory cortex. *Nature Communications* . doi: 10.1038/ncomms12540.
Molnár, Z. et al. 2006. Comparative aspects of cerebral cortical development. *The European Journal of Neuroscience* 23(4), p. 921. doi: 10.1111/J.1460-9568.2006.04611.X.
Monier, A. et al. 2006. Distribution and differentiation of microglia in the human encephalon during the first two trimesters of gestation. *Journal of Comparative Neurology* 499(4), pp. 565–582. doi: 10.1002/CNE.21123.
Monier, A. et al. 2007. Entry and Distribution of Microglial Cells in Human Embryonic and Fetal Cerebral Cortex. *Journal of Neuropathology & Experimental Neurology* 66(5), pp. 372–382. doi: 10.1097/NEN.0B013E3180517B46.
Montgomery, M.K. et al. 2013. Mouse strain-dependent variation in obesity and glucose homeostasis in response to high-fat feeding. *Diabetologia* 56(5), pp. 1129–1139. doi: 10.1007/S00125-013-2846-8/FIGURES/6.
Moon, H.S. et al. 2022. Mouse Model of Small for Gestational Age Offspring with Catch-up Growth Failure and Dysregulated Glucose Metabolism in Adulthood. *Journal of Obesity & Metabolic Syndrome* 31(1), p. 81. doi: 10.7570/JOMES22013.
Morgese, M.G. and Trabace, L. 2016. Maternal malnutrition in the etiopathogenesis of psychiatric diseases: Role of polyunsaturated fatty acids. *Brain Sciences* 6(3). doi: 10.3390/brainsci6030024.
Mosser, C.A. et al. 2017. Microglia in CNS development: Shaping the brain for the future. *Progress in Neurobiology* 149–150, pp. 1–20. doi: 10.1016/j.pneurobio.2017.01.002.
de Moura e Dias, M. et al. 2021. Diet-induced obesity in animal models: points to consider and influence on metabolic markers. *Diabetology and Metabolic Syndrome*

13(1), pp. 1–14. doi: 10.1186/S13098-021-00647-2/TABLES/3.
Mueller, F.S. et al. 2019. Influence of poly(I:C) variability on thermoregulation, immune responses and pregnancy outcomes in mouse models of maternal immune activation. *Brain, Behavior, and Immunity* 80, pp. 406–418. doi: 10.1016/J.BBI.2019.04.019.
Nemes-Baran, A.D. et al. 2020. Fractalkine-Dependent Microglial Pruning of Viable Oligodendrocyte Progenitor Cells Regulates Myelination. *Cell Reports* 32(7). doi: 10.1016/j.celrep.2020.108047.
Niculescu, M.D. and Lupu, D.S. 2009a. High fat diet-induced maternal obesity alters fetal hippocampal development. *International journal of developmental neuroscience : the official journal of the International Society for Developmental Neuroscience* 27(7), p. 627. doi: 10.1016/J.IJDEVNEU.2009.08.005.
Niculescu, M.D. and Lupu, D.S. 2009b. High fat diet-induced maternal obesity alters fetal hippocampal development. *International Journal of Developmental Neuroscience* 27(7), pp. 627–633. doi: 10.1016/j.ijdevneu.2009.08.005.
Nimmerjahn, A. et al. 2005. Neuroscience: Resting microglial cells are highly dynamic surveillants of brain parenchyma in vivo. *Science* 308(5726), pp. 1314–1318. doi: 10.1126/SCIENCE.1110647/SUPPL_FILE/1110647S9.MOV.
Niquille, M. et al. 2009. Transient Neuronal Populations Are Required to Guide Callosal Axons: A Role for Semaphorin 3C. *PLOS Biology* 7(10), p. e1000230. doi: 10.1371/JOURNAL.PBIO.1000230.
Nolan, A.M. et al. 2014. The neurite growth inhibitory effects of soluble TNFα on developing sympathetic neurons are dependent on developmental age. *Differentiation* 88(4–5), pp. 124–130. doi: 10.1016/j.diff.2014.12.006.
Nutrition, N.R.C. (US) S. on L.A. 1995. Nutrient Requirements of the Mouse.
O'Neil, A. et al. 2014. Preventing mental health problems in offspring by targeting dietary intake of pregnant women. *BMC Medicine* 12(1). doi: 10.1186/s12916-014-0208-0.
Ocañas, S.R. et al. 2022. Minimizing the Ex Vivo Confounds of Cell-Isolation Techniques on Transcriptomic and Translatomic Profiles of Purified Microglia. *eNeuro* 9(2), p. ENEURO.0348-21.2022. doi: 10.1523/ENEURO.0348-21.2022.
Ohtani, K. et al. 1999. Cell growth-regulated expression of mammalian MCM5 and MCM6 genes mediated by the transcription factor E2F. *Oncogene 1999 18:14* 18(14), pp. 2299–2309. doi: 10.1038/sj.onc.1202544.

Olson, J.K. et al. 2001. Direct Activation of Innate and Antigen-Presenting Functions of Microglia following Infection with Theiler's Virus. *Journal of Virology* 75(20), p. 9780. doi: 10.1128/JVI.75.20.9780-9789.2001.
Olson, J.K. and Miller, S.D. 2004. Microglia Initiate Central Nervous System Innate and Adaptive Immune Responses through Multiple TLRs. *The Journal of Immunology* 173(6), pp. 3916–3924. doi: 10.4049/JIMMUNOL.173.6.3916.
Ou, X. et al. 2015. Maternal adiposity negatively influences infant brain white matter development. *Obesity* 23(5), pp. 1047–1054. doi: 10.1002/oby.21055.
Ozaki, H.S. and Wahlsten, D. 1992. Prenatal formation of the normal mouse corpus callosum: a quantitative study with carbocyanine dyes. *The Journal of comparative neurology* 323(1), pp. 81–90. doi: 10.1002/CNE.903230107.
Ozaki, K. et al. 2020. Maternal immune activation induces sustained changes in fetal microglia motility. *Scientific Reports 2020 10:1* 10(1), pp. 1–19. doi: 10.1038/s41598-020-78294-2.
Panchenko, P.E. et al. 2016. Expression of epigenetic machinery genes is sensitive to maternal obesity and weight loss in relation to fetal growth in mice. *Clinical Epigenetics* 8(1), pp. 1–19. doi: 10.1186/S13148-016-0188-3.
Paolicelli, R.C. et al. 2011. Synaptic pruning by microglia is necessary for normal brain development. *Science* 333(6048), pp. 1456–1458. doi: 10.1126/SCIENCE.1202529/SUPPL_FILE/PAOLICELLI.SOM.PDF.
Paolicelli, R.C. et al. 2014. Fractalkine regulation of microglial physiology and consequences on the brain and behavior. *Frontiers in Cellular Neuroscience* 8(MAY). doi: 10.3389/FNCEL.2014.00129.
Park, H.S. and Kim, T.W. 2017. Paternal physical exercise improves spatial learning ability by enhancing hippocampal neuroplasticity in male pups born from obese maternal rats. *Journal of Exercise Rehabilitation* 13(3), p. 266. doi: 10.12965/JER.1734998.499.
Parkhurst, C.N. et al. 2013. Microglia promote learning-dependent synapse formation through brain-derived neurotrophic factor. *Cell* . doi: 10.1016/j.cell.2013.11.030.
Patsopoulos, N.A. et al. 2019. Multiple Sclerosis Genomic Map implicates peripheral immune cells & microglia in susceptibility. *Science (New York, N.Y.)* 365(6460). doi: 10.1126/SCIENCE.AAV7188.
Paul, L.K. et al. 2007. Agenesis of the corpus callosum: genetic, developmental and

functional aspects of connectivity. *Nature reviews. Neuroscience* 8(4), pp. 287–99. doi: 10.1038/nrn2107.
Peleg-Raibstein, D. et al. 2016. Enhanced sensitivity to drugs of abuse and palatable foods following maternal overnutrition. *Translational Psychiatry* 6(10), p. e911. doi: 10.1038/TP.2016.176.
Pendeloski, K.P.T. et al. 2017. Maternal obesity and inflammatory mediators: A controversial association. *American Journal of Reproductive Immunology* 77(5). doi: 10.1111/aji.12674.
Perelson, S. et al. 2000. -deoxyuridine ′ Using 5-Bromo-2 Quantification of Cell Turnover Kinetics. *J Immunol References* 164, pp. 5049–5054. doi: 10.4049/jimmunol.164.10.5049.
Pfeiffer, B.E. et al. 2010. Fragile X mental retardation protein is required for synapse elimination by the activity-dependent transcription factor MEF2. *Neuron* 66(2), pp. 191–197. doi: 10.1016/J.NEURON.2010.03.017.
Pinto, L. and Götz, M. 2007. Radial glial cell heterogeneity-The source of diverse progeny in the CNS. *Progress in Neurobiology* 83(1), pp. 2–23. doi: 10.1016/j.pneurobio.2007.02.010.
Piper, M. et al. 2009. Neuropilin 1-sema signaling regulates crossing of cingulate pioneering axons during development of the corpus callosum. *Cerebral Cortex* . doi: 10.1093/cercor/bhp027.
Pont-Lezica, L. et al. 2011. Physiological roles of microglia during development. *Journal of Neurochemistry* . doi: 10.1111/j.1471-4159.2011.07504.x.
Pont-Lezica, L. et al. 2014. Microglia shape corpus callosum axon tract fasciculation: Functional impact of prenatal inflammation. *European Journal of Neuroscience* . doi: 10.1111/ejn.12508.
Prestoz, L. et al. 2012. Dopaminergic axon guidance: which makes what? *Frontiers in Cellular Neuroscience* 6(JULY 2012). doi: 10.3389/FNCEL.2012.00032.
Prinz, M. et al. 2019. Microglia Biology: One Century of Evolving Concepts. *Cell* 179(2), pp. 292–311. doi: 10.1016/J.CELL.2019.08.053.
Rash, B.G. et al. 2018. Metabolic regulation and glucose sensitivity of cortical radial glial cells. *Proceedings of the National Academy of Sciences of the United States of America* 115(40), pp. 10142–10147. doi: 10.1073/pnas.1808066115.
Rash, B.G. and Grove, E.A. 2006. Area and layer patterning in the developing cerebral cortex. *Current Opinion in Neurobiology* 16(1), pp. 25–34. doi:

10.1016/J.CONB.2006.01.004.
Raybaud, C. 2010. The corpus callosum, the other great forebrain commissures, and the septum pellucidum: Anatomy, development, and malformation. *Neuroradiology* 52(6), pp. 447–477. doi: 10.1007/s00234-010-0696-3.
Reemst, K. et al. 2016. The Indispensable Roles of Microglia and Astrocytes during Brain Development. *Frontiers in Human Neuroscience* 10. doi: 10.3389/fnhum.2016.00566.
Rey, C. et al. 2018. Maternal n-3 polyunsaturated fatty acid dietary supply modulates microglia lipid content in the offspring. *Prostaglandins Leukotrienes and Essential Fatty Acids* 133, pp. 1–7. doi: 10.1016/j.plefa.2018.04.003.
Rey, C. et al. 2019. Dietary n-3 long chain PUFA supplementation promotes a pro-resolving oxylipin profile in the brain. *Brain, Behavior, and Immunity* 76, pp. 17–27. doi: 10.1016/j.bbi.2018.07.025.
Rezaie, P. et al. 2005. Microglia in the Cerebral Wall of the Human Telencephalon at Second Trimester. *Cerebral Cortex* 15(7), pp. 938–949. doi: 10.1093/CERCOR/BHH194.
Richards, L. et al. 2004a. Mechanisms regulating the development of the corpus callosum and its agenesis in mouse and human. *Clinical Genetics* 66(4), pp. 276–289. doi: 10.1111/j.1399-0004.2004.00354.x.
Richards, L.J. et al. 2004b. Mechanisms regulating the development of the corpus callosum and its agenesis in mouse and human. *Clinical Genetics* 66(4), pp. 276–289. doi: 10.1111/j.1399-0004.2004.00354.x.
Rinaldi, S.F. et al. 2017. Immune cell and transcriptomic analysis of the human decidua in term and preterm parturition. *Molecular Human Reproduction* 23(10), pp. 708–724. doi: 10.1093/MOLEHR/GAX038.
Rivera, H.M. et al. 2015a. The role of maternal obesity in the risk of neuropsychiatric disorders. *Frontiers in Neuroscience* . doi: 10.3389/fnins.2015.00194.
Rivera, H.M. et al. 2015b. The role of maternal obesity in the risk of neuropsychiatric disorders. *Frontiers in Neuroscience* 9(MAY). doi: 10.3389/fnins.2015.00194.
Rodriguez, A. et al. 2007. Maternal adiposity prior to pregnancy is associated with ADHD symptoms in offspring: evidence from three prospective pregnancy cohorts. *International Journal of Obesity 2008 32:3* 32(3), pp. 550–557. doi: 10.1038/sj.ijo.0803741.
Rooijen, N. Van and Sanders, A. 1994. Liposome mediated depletion of

macrophages: mechanism of action, preparation of liposomes and applications. *Journal of immunological methods* 174(1–2), pp. 83–93. doi: 10.1016/0022-1759(94)90012-4.
Rubenstein, J.L.R. et al. 1998. Regionalization of the prosencephalic neural plate. *Annual Review of Neuroscience* 21, pp. 445–477. doi: 10.1146/ANNUREV.NEURO.21.1.445.
Sakayori, N. et al. 2016. Maternal dietary imbalance between omega-6 and omega-3 polyunsaturated fatty acids impairs neocortical development via epoxy metabolites. *Stem Cells* 34(2), pp. 470–482. doi: 10.1002/STEM.2246.
Samad, F. et al. 1997. Elevated expression of transforming growth factor-β in adipose tissue from obese mice. *Molecular Medicine* 3(1), pp. 37–48. doi: 10.1007/bf03401666.
Samatov, T.R. et al. 2016. L1CAM: Cell adhesion and more. *Progress in Histochemistry and Cytochemistry* 51(2), pp. 25–32. doi: 10.1016/j.proghi.2016.05.001.
Sanders, T.R. et al. 2014. Maternal obesity and IL-6 lead to aberrant developmental gene expression and deregulated neurite growth in the fetal arcuate nucleus. *Endocrinology* . doi: 10.1210/en.2013-1968.
Sanguinetti, E. et al. 2019. Microbiota signatures relating to reduced memory and exploratory behaviour in the offspring of overweight mothers in a murine model. *Scientific Reports 2019 9:1* 9(1), pp. 1–12. doi: 10.1038/s41598-019-48090-8.
Dos Santos, S.E. et al. 2020. Similar Microglial Cell Densities across Brain Structures and Mammalian Species: Implications for Brain Tissue Function. *The Journal of Neuroscience* 40(24), p. 4622. doi: 10.1523/JNEUROSCI.2339-19.2020.
Satija, R. and Shalek, A.K. 2014. Heterogeneity in Immune Responses – From Populations to Single Cells. *Trends in immunology* 35(5), p. 219. doi: 10.1016/J.IT.2014.03.004.
Schaefer, C.A. et al. 2000. Maternal Prepregnant Body Mass and Risk of Schizophrenia in Adult Offspring. *Schizophrenia Bulletin* 26(2), pp. 275–286. doi: 10.1093/OXFORDJOURNALS.SCHBUL.A033452.
Schafer, D.P. et al. 2012. Microglia Sculpt Postnatal Neural Circuits in an Activity and Complement-Dependent Manner. *Neuron* 74(4), pp. 691–705. doi: 10.1016/J.NEURON.2012.03.026.
Schlaepfer, I.R. and Joshi, M. 2020. CPT1A-mediated Fat Oxidation, Mechanisms,

and Therapeutic Potential. *Endocrinology (United States)* 161(2). doi: 10.1210/endocr/bqz046.
Scholzen, T. and Gerdes, J. 2000. The Ki-67 Protein: From the Known and the Unknown. doi: 10.1002/(SICI)1097-4652(200003)182:3.
Schulz, C. et al. 2012. A lineage of myeloid cells independent of myb and hematopoietic stem cells. *Science* 335(6077), pp. 86–90. doi: 10.1126/science.1219179.
Sellers, R.S. et al. 2012. Immunological variation between inbred laboratory mouse strains: Points to consider in phenotyping genetically immunomodified mice. *Veterinary Pathology* 49(1), pp. 32–43. doi: 10.1177/0300985811429314/ASSET/IMAGES/LARGE/10.1177_0300985811429314-FIG1.JPEG.
Sen, S. et al. 2014. Obesity during pregnancy alters maternal oxidant balance and micronutrient status. *Journal of Perinatology* 34(2), pp. 105–111. doi: 10.1038/jp.2013.153.
Sgritta, M. et al. 2019. Mechanisms Underlying Microbial-Mediated Changes in Social Behavior in Mouse Models of Autism Spectrum Disorder. *Neuron* 101(2), pp. 246-259.e6. doi: 10.1016/J.NEURON.2018.11.018/ATTACHMENT/DC78D625-A17C-403E-9BF6-D7723E642C09/MMC1.PDF.
Shen, W. Bin et al. 2006. Identification of candidate genes at the corticoseptal boundary during development. *Gene Expression Patterns* 6(5), pp. 471–481. doi: 10.1016/j.modgep.2005.11.004.
Shigemoto-Mogami, Y. et al. 2014. Microglia Enhance Neurogenesis and Oligodendrogenesis in the Early Postnatal Subventricular Zone. *Journal of Neuroscience* 34(6), pp. 2231–2243. doi: 10.1523/jneurosci.1619-13.2014.
Shu, T. et al. 2003a. Development of midline glial populations at the corticoseptal boundary. *Journal of Neurobiology* 57(1), pp. 81–94. doi: 10.1002/neu.10252.
Shu, T. et al. 2003b. The glial sling is a migratory population of developing neurons. *Development (Cambridge, England)* 130(13), p. 2929. doi: 10.1242/DEV.00514.
Sierra, A. et al. 2016. The “Big-Bang” for modern glial biology: Translation and comments on Pío del Río-Hortega 1919 series of papers on microglia. *GLIA* 64(11), pp. 1801–1840. doi: 10.1002/GLIA.23046.
Siersbæk, M.S. et al. 2020. C57BL/6J substrain differences in response to high-fat diet intervention. *Scientific Reports 2020 10:1* 10(1), pp. 1–15. doi: 10.1038/s41598-

020-70765-w.
Singh, K.P. et al. 2018. Role of IL-1β IL-6 and TNF-α cytokines and TNF-α promoter variability in Plasmodium vivax infection during pregnancy in endemic population of Jharkhand, India. *Molecular Immunology* 97, pp. 82–93. doi: 10.1016/j.molimm.2018.03.019.
Skelton, J.A. et al. 2011. Etiologies of Obesity in Children: Nature and Nurture. *Pediatric clinics of North America* 58(6), p. 1333. doi: 10.1016/J.PCL.2011.09.006.
Smith, S.E.P. et al. 2007. Neurobiology of Disease Maternal Immune Activation Alters Fetal Brain Development through Interleukin-6. doi: 10.1523/JNEUROSCI.2178-07.2007.
Smolders, S. et al. 2015. Maternal immune activation evoked by polyinosinic:polycytidylic acid does not evoke microglial cell activation in the embryo. *Frontiers in Cellular Neuroscience* 9(AUGUST). doi: 10.3389/FNCEL.2015.00301.
Sousa, C. et al. 2018. Single-cell transcriptomics reveals distinct inflammation-induced microglia signatures. *EMBO Reports* 19(11). doi: 10.15252/EMBR.201846171.
Speakman, J.R. 2019. Use of high-fat diets to study rodent obesity as a model of human obesity. *International Journal of Obesity* 43(8), pp. 1491–1492. doi: 10.1038/s41366-019-0363-7.
Squarzoni, P. et al. 2014. Microglia Modulate Wiring of the Embryonic Forebrain. *Cell Reports* 8(5), pp. 1271–1279. doi: 10.1016/j.celrep.2014.07.042.
Staszewski, O. and Hagemeyer, N. 2019. Unique microglia expression profile in developing white matter. *BMC Research Notes* 12(1), p. 367. doi: 10.1186/s13104-019-4410-1.
Stevens, B. et al. 2007. The Classical Complement Cascade Mediates CNS Synapse Elimination. *Cell* 131(6), pp. 1164–1178. doi: 10.1016/j.cell.2007.10.036.
Stough, J.M.A. et al. 2016. Functional Characteristics of the Gut Microbiome in C57BL/6 Mice Differentially Susceptible to Plasmodium yoelii. *Frontiers in Microbiology* 7(SEP). doi: 10.3389/FMICB.2016.01520.
Stratoulias, V. et al. 2019. Microglial subtypes: diversity within the microglial community. *The EMBO Journal* 38(17). doi: 10.15252/embj.2019101997.
Streit, W.J. and Kreutzberg, G.W. 1988. Response of endogenous glial cells to motor neuron degeneration induced by toxic ricin. *Journal of Comparative Neurology* 268(2), pp. 248–263. doi: 10.1002/CNE.902680209.

Stuart, T. et al. 2019. Comprehensive Integration of Single-Cell Data. *Cell* 177(7), pp. 1888-1902.e21. doi: 10.1016/J.CELL.2019.05.031/ATTACHMENT/2F8B9EBE-54E6-43EB-9EF2-949B6BDA8BA2/MMC3.PDF.
Suárez, R. et al. 2014. Balanced interhemispheric cortical activity is required for correct targeting of the corpus callosum. *Neuron* . doi: 10.1016/j.neuron.2014.04.040.
Subramanian, A. et al. 2005. Gene set enrichment analysis: A knowledge-based approach for interpreting genome-wide expression profiles. *Proceedings of the National Academy of Sciences of the United States of America* 102(43), pp. 15545–15550. doi: 10.1073/PNAS.0506580102/SUPPL_FILE/06580FIG7.JPG.
Sundaresh, A. et al. 2019. IL6/IL6R genetic diversity and plasma IL6 levels in bipolar disorder: An Indo-French study. *Heliyon* 5(1). doi: 10.1016/J.HELIYON.2019.E01124.
Sureshchandra, S. et al. 2019. Impact of pregravid obesity on maternal and fetal immunity: Fertile grounds for reprogramming. *Journal of Leukocyte Biology* 106(5), pp. 1035–1050. doi: 10.1002/JLB.3RI0619-181R.
Swinnen, N. et al. 2013. Complex invasion pattern of the cerebral cortex bymicroglial cells during development of the mouse embryo. *GLIA* 61(2), pp. 150–163. doi: 10.1002/glia.22421.
Tan, Y.L. et al. 2020. Microglial regional heterogeneity and its role in the brain. *Molecular Psychiatry* 25(2), pp. 351–367. doi: 10.1038/s41380-019-0609-8.
Tang, A. et al. 2018. Catch-up growth, metabolic and cardiovascular risk in post-institutionalized Romanian adolescents. *Pediatric research* 84(6), p. 842. doi: 10.1038/S41390-018-0196-4.
Tao, L. and Reese, T.A. 2017. Making Mouse Models That Reflect Human Immune Responses. *Trends in immunology* 38(3), pp. 181–193. doi: 10.1016/J.IT.2016.12.007.
Tay, T.L. et al. 2018. Microglia gone rogue: Impacts on psychiatric disorders across the lifespan. *Frontiers in Molecular Neuroscience* 10. doi: 10.3389/fnmol.2017.00421.
Thion, M.S. et al. 2018a. Microbiome Influences Prenatal and Adult Microglia in a Sex-Specific Manner. *Cell* 172(3), pp. 500-516.e16. doi: 10.1016/j.cell.2017.11.042.
Thion, M.S. et al. 2018b. Microglia and early brain development: An intimate journey. *Science* 362(6411), pp. 185–189. doi: 10.1126/science.aat0474.

Thompson, J.R. et al. 2017. Exposure to a high-fat diet during early development programs behavior and impairs the central serotonergic system in juvenile non-human primates. *Frontiers in Endocrinology* . doi: 10.3389/fendo.2017.00164.
Thompson, J.R. et al. 2018. Maternal diet, metabolic state, and inflammatory response exert unique and long-lasting influences on offspring behavior in non-human primates. *Frontiers in Endocrinology* 9(APR), p. 23. doi: 10.3389/FENDO.2018.00161/FULL.
Torzewski, M. et al. 2014. Animal Models of C-Reactive Protein. *Mediators of Inflammation* 2014. doi: 10.1155/2014/683598.
Tramontin, A.D. et al. 2003. Postnatal development of radial glia and the ventricular zone (VZ): a continuum of the neural stem cell compartment. *Cerebral cortex (New York, N.Y. : 1991)* 13(6), pp. 580–587. doi: 10.1093/CERCOR/13.6.580.
Tremblay, M.È. et al. 2015. From the Cajal alumni Achúcarro and Río-Hortega to the rediscovery of never-resting microglia. *Frontiers in Neuroanatomy* 9(APR), p. 45. doi: 10.3389/FNANA.2015.00045/BIBTEX.
Tu, T.H. et al. 2019. Linoleic acid rescues microglia inflammation triggered by saturated fatty acid. *Biochemical and Biophysical Research Communications* 513(1), pp. 201–206. doi: 10.1016/j.bbrc.2019.03.047.
Turrigiano, G.G. and Nelson, S.B. 2004. Homeostatic plasticity in the developing nervous system. *Nature Reviews Neuroscience 2004 5:2* 5(2), pp. 97–107. doi: 10.1038/nrn1327.
Ueno, M. et al. 2013. Layer v cortical neurons require microglial support for survival during postnatal development. *Nature Neuroscience* 16(5), pp. 543–551. doi: 10.1038/nn.3358.
Urbonaite, G. et al. 2022. The impact of maternal high-fat diet on offspring neurodevelopment. *Frontiers in Neuroscience* 16. doi: 10.3389/FNINS.2022.909762.
Utz, S.G. et al. 2020. Early Fate Defines Microglia and Non-parenchymal Brain Macrophage Development. *Cell* , pp. 1–17. doi: 10.1016/j.cell.2020.03.021.
Valdearcos, M. et al. 2014. Microglia Dictate the Impact of Saturated Fat Consumption on Hypothalamic Inflammation and Neuronal Function. *Cell Reports* 9(6), pp. 2124–2138. doi: 10.1016/j.celrep.2014.11.018.
Verdejo-Román, J. et al. 2019. Maternal prepregnancy body mass index and offspring white matter microstructure: results from three birth cohorts. *International Journal of Obesity* 43(10), pp. 1995–2006. doi: 10.1038/s41366-018-0268-x.

Verhoef, J. et al. 2019. Immune Response in Human Pathology: Infections Caused by Bacteria, Viruses, Fungi, and Parasites. *Nijkamp and Parnham's Principles of Immunopharmacology* , p. 165. doi: 10.1007/978-3-030-10811-3_10.
Vidakovic, A.J. et al. 2015. Body mass index, gestational weight gain and fatty acid concentrations during pregnancy: the Generation R Study. *European Journal of Epidemiology* 30(11), pp. 1175–1185. doi: 10.1007/s10654-015-0106-6.
Wahlsten, D. et al. 2006. Recombinant inbreeding in mice reveals thresholds in embryonic corpus callosum development. *Genes, Brain and Behavior* 5(2), pp. 170–188. doi: 10.1111/j.1601-183X.2005.00153.x.
Waisman, A. et al. 2015. Homeostasis of Microglia in the Adult Brain: Review of Novel Microglia Depletion Systems. *Trends in Immunology* 36(10), pp. 625–636. doi: 10.1016/J.IT.2015.08.005.
Weinhard, L. et al. 2018. Microglia remodel synapses by presynaptic trogocytosis and spine head filopodia induction. *Nature Communications* . doi: 10.1038/s41467-018-03566-5.
Weisberg, S.P. et al. 2003. Obesity is associated with macrophage accumulation in adipose tissue. *Journal of Clinical Investigation* 112(12), pp. 1796–1808. doi: 10.1172/jci19246.
Werling, D.M. et al. 2016. Gene expression in human brain implicates sexually dimorphic pathways in autism spectrum disorders. *Nature Communications* 7. doi: 10.1038/NCOMMS10717.
Weschenfelder, F. et al. 2023. Obesity during Pregnancy and SARS-CoV-2/COVID-19-Case Series of the Registry Study "COVID-19 Related Obstetric and Neonatal Outcome Study" (CRONOS-Network). *Journal of Clinical Medicine* 12(6), p. 2089. doi: 10.3390/JCM12062089.
WHO 2011. *Global burden of mental disorders and the need for a comprehensive, coordinated response from health and social sectors at the country level*.
WHO 2021. Obesity and overweight. Available at: https://www.who.int/news-room/fact-sheets/detail/obesity-and-overweight [Accessed: 28 September 2023].
De Wilde, J. et al. 2009. An 8-Week High-Fat Diet Induces Obesity and Insulin Resistance with Small Changes in the Muscle Transcriptome of C57BL/6J Mice. *Lifestyle Genomics* 2(6), pp. 280–291. doi: 10.1159/000308466.
Willment, J. et al. 2005. The human ?-glucan receptor is widely expressed and functionally equivalent to murine Dectin-1 on primary cells. *European Journal of*

Immunology 35(5), pp. 1539–1547. doi: 10.1002/eji.200425725.
Wlodarczyk, A. et al. 2017a. A novel microglial subset plays a key role in myelinogenesis in developing brain. *The EMBO Journal* 36(22), pp. 3292–3308. doi: 10.15252/embj.201696056.
Wlodarczyk, A. et al. 2017b. A novel microglial subset plays a key role in myelinogenesis in developing brain. *The EMBO Journal* . doi: 10.15252/embj.201696056.
Xu, J. et al. 2016. Microglia Colonization of Developing Zebrafish Midbrain Is Promoted by Apoptotic Neuron and Lysophosphatidylcholine. *Developmental Cell* 38(2), pp. 214–222. doi: 10.1016/j.devcel.2016.06.018.
Yamamiya, M. et al. 2019. Microglia promote the proliferation of neural precursor cells by secreting osteopontin. *Biochemical and Biophysical Research Communications* 513(4), pp. 841–845. doi: 10.1016/j.bbrc.2019.04.076.
Yan, Z. et al. 2017. Maternal Chronic Folate Supplementation Ameliorates Behavior Disorders Induced by Prenatal High-Fat Diet Through Methylation Alteration of BDNF and Grin2b in Offspring Hippocampus. *Molecular Nutrition & Food Research* 61(12), p. 1700461. doi: 10.1002/MNFR.201700461.
Yang, H.S. et al. 2021. Natural genetic variation determines microglia heterogeneity in wild-derived mouse models of Alzheimer's disease. *Cell reports* 34(6), p. 108739. doi: 10.1016/J.CELREP.2021.108739.
Yao, S. et al. 2021. Reduced Inter-hemispheric Resting State Functional Connectivity and Its Association With Social Deficits in Autism. *Frontiers in Psychiatry* 12, p. 244. doi: 10.3389/FPSYT.2021.629870/BIBTEX.
Yeh, H.R. et al. 2018. Neurodevelopmental outcomes in children with prenatally diagnosed corpus callosal abnormalities. *Brain & development* 40(8), pp. 634–641. doi: 10.1016/J.BRAINDEV.2018.04.012.
Yockey, L.J. and Iwasaki, A. 2018. Interferons and Proinflammatory Cytokines in Pregnancy and Fetal Development. *Immunity* 49(3), pp. 397–412. doi: 10.1016/j.immuni.2018.07.017.
Yoon, S. et al. 2020. TGF-β-Induced Phosphorylation of Usp9X Stabilizes Ankyrin-G and Regulates Dendritic Spine Development and Maintenance. *Cell reports* 31(8). doi: 10.1016/J.CELREP.2020.107685.
Yuanming, H. et al. 1999. Role of cytochrome c and dATP/ATP hydrolysis in Apaf-1-mediated caspase-9 activation and apoptosis. *The EMBO Journal* 18(13), p. 3586.

doi: 10.1093/EMBOJ/18.13.3586.
Zembala-Szczerba, M. et al. 2017. Low-Grade Metabolically-Induced Inflammation Mediators Interleukin-6, Adiponectin, and TNF-α Serum Levels in Obese Pregnant Patients in the Perinatal Period. *Medical science monitor basic research* 23, pp. 1–7. doi: 10.12659/msmbr.902273.
Zheng, K. et al. 2018. Molecular and Genetic Evidence for the PDGFRα-Independent Population of Oligodendrocyte Progenitor Cells in the Developing Mouse Brain. *Journal of Neuroscience* 38(44), pp. 9505–9513. doi: 10.1523/JNEUROSCI.1510-18.2018.
Zhou, J. et al. 2013a. Axon position within the corpus callosum determines contralateral cortical projection. *Proceedings of the National Academy of Sciences* 110(29), pp. E2714–E2723. doi: 10.1073/pnas.1310233110.
Zhou, Y. et al. 2013b. TLR3 activation efficiency by high or low molecular mass poly I:C. *Innate immunity* 19(2), p. 184. doi: 10.1177/1753425912459975.
Zhu, C. et al. 2018. A mouse model of pre-pregnancy maternal obesity combined with offspring exposure to a high-fat diet resulted in cognitive impairment in male offspring. *Experimental Cell Research* 368(2), pp. 159–166. doi: 10.1016/j.yexcr.2018.04.019.

Annex

Annex Table 1 Legend

Table containing all primary antibodies used throughout the thesis and the dilution at which they were used.

Annex Table 1: Primary antibodies.

Primary Antibodies			
Target	**Host**	**Company**	**Dilution**
Ki67	Rabbit	Abcam	1:500
Nrp1	Goat	Biotechne	1:300
BrdU	Sheep	Abcam	1:200
L1CAM	Rat	Abcam	1:100
Tuj1	Mouse	Biolegend	1:1000
GFP	Chicken	Abcam	1:500
Iba1	Rabbit	wako (alphalabs)	1:1000
Dectin-1	Rat	InvivoGen	1:50
CPT1a	Mouse	Abcam	1:500
CD68	Rat	Abcam	1:100
Spp1	Rabbit	LSBio	1:500
Iba1	Goat	Wako (alphalabs)	1:500
Conjugated Primary Antibodies			
CD45 (PE/Cy7 conjugated)	Rat	Biolegend	1:100
CD11b (AlexaFluor488 conjugated)	Rat	Biolegend	1:100
***In situ*hybridisation probes**			
gpnmb		Biotechne (ACDbio)	1:50
clec7a		Biotechne (ACDbio)	1:50
spp1		Biotechne (ACDbio)	1:50
f13a1		Biotechne (ACDbio)	1:50

Annex Table 2 Legend

Table containing all secondary antibodies used throughout the thesis and the dilution at which they were used.

Annex Table 2: Secondary antibodies.

Secondary antibodies			
Target species	Host	Fluorophore	Dilution
rat	donkey	alexa568	1:500
mouse	donkey	alexa568	1:500
rabbit	donkey	alexa594	1:500
chicken	donkey	alexa594	1:500
goat	donkey	alexa594	1:500
goat	donkey	alexa 488	1:500
sheep	donkey	alexa 488	1:500
chicken	donkey	alexa 488	1:500
rabbit	donkey	alexa 488	1:500
mouse	donkey	alexa 488	1:500
rabbit	donkey	alexa647	1:500
goat	donkey	alexa647	1:500

Annex Table 3 Legend

Seurat clusters were analysed using ScType automated cell-type identification system (Ianevski et al. 2022). Gene expression data from Seurat clusters identified here was compared with clusters identified in Hammond et al. (2019) and Li et al. (2019a). Calculated ScType scores reflect how similar Seurat clusters discussed here are in relation to those produced in previous literature.

Clusters were labelled based on 'ScType score' or 'change in ScType score' arbitrary cut-offs. Neutrophil scores were discounted due to the lack of neutrophil marker expression across all cells, as shown in Annex Figure 3. Many of the labels produced by this data set are closely related (as discussed by Hammond et al. (2019)) making differentiation between clusters difficult, especially where number of cells is low. Lower scoring cluster labels and webgestalt enrichment data (Annex Table 4) was therefore used to distinguish between different clusters where PCA plots show clear differences between clusters in transcription profile. Normalised ScType score of: 1+ is considered high (green); 0.5-1 considered medium (yellow); 0-0.5 considered low (red). Change in normalised ScType score of 0.2 or higher was considered enough to invalidate the cell type of all those with a lower score. These cut-offs were decided arbitrarily after visualising the range of scores measured across all clusters in my data set. Bold cell types were used to label the cluster.

Cluster refers to the Seurat produced cluster number for my data. Cell type is the name of cell type or cluster given in either Hammond et al. (2019) or Li et al. (2019a). ScType score is the similarity measure given by ScType automated labelling system. # cells is the number of cells in each cluster. Normalised by # cells refers to the ScType score when divided by the number of cells within a cluster. Change in normalised refers to the change in normalised ScType score from the score given in the row above. The explanation column contains an explanation as to why each cluster was named using the selected cell type.

Annex Table 3: Seurat single cell sequencing clusters.

Cluster	Cell type	Sctype scores	# cells	Normalised by # cells	Change in normalised	Explanation
0	**Metabolically active microglia**	3120.18	1817	1.72		There was a change in normalised score of over 0.20 after the metabollically active microglia type.
0	Neutrophils	2756.04	1817	1.52	0.20	
0	Axon-tract microglia	2749.36	1817	1.51	0.01	
1	**Homeostatic microglia b**	2241.27	1612	1.39		Two of 3 cell types above the score quality and change in score cut off are homeostatic. Injury was considered an indication of inflammation.
1	White matter injury microglia	2164.03	1612	1.34	0.05	
1	**Homeostatic microglia**	2132.94	1612	1.32	0.02	
1	IEG+ microglia	1297.92	1612	0.81	0.52	
2	**Homeostatic microglia**	1330.42	952	1.40		Both cell types above the change in normalised score are homeostatic.
2	**Homeostatic microglia b**	1221.28	952	1.28	0.11	
2	Injury cluster 1	697.15	952	0.73	0.55	
3	**Homeostatic microglia**	1191.57	948	1.26		Cell type above change in normalised score and immediatley below are homeostatic.
3	**Homeostatic microglia b**	842.34	948	0.89	0.37	
4	**Axon-tract microglia**	1227.50	832	1.48		ATM, PAM and metabolic microglia are closely related and above the normalised score cut off. ATM/PAM are considered almost identical cell types.
4	**Postnatal PAM**	1050.34	832	1.26	0.21	
4	Metabolically active microglia	872.74	832	1.05	0.21	
4	Inflammatory monocytes	702.80	832	0.84	0.20	
5	**Proliferative microglia c**	1111.45	807	1.38		Metabolically active microglia are closely related to proliferative microglia, all proliferative microglia could be considered proliferative/metabolic.
5	Metabolically active microglia	964.89	807	1.20	0.18	
5	Brain border microglia	786.26	807	0.97	0.22	
6	**Metabolically active microglia**	924.62	795	1.16		Metabolic microglia are above both normalised sctype score and change in score cutoff.
6	Proliferative microglia c	749.23	795	0.94	0.22	
7	**Homeostatic microglia**	1105.26	671	1.65		Homeostatic microglia are both above and below change in score cutoff.
7	**Homeostatic microglia b**	840.31	671	1.25	0.39	

Cluster	Cell type	Sctype scores	# cells	Normalised by # cells	Change in normalised	Explanation
8	**Homeostatic microglia b**	1458.63	666	2.19		Homeostatic microglia are above change in score cutoff.
8	**Homeostatic microglia**	1432.35	666	2.15	0.04	
8	White matter injury microglia	1020.21	666	1.53	0.62	
9	**Proliferative microglia a**	868.30	636	1.37		Proliferative microglia are above the change in score cut off.
9	Metabolically active microglia	700.90	636	1.10	0.26	
10	**Postnatal PAM**	615.19	563	1.09		PAM and aged microglia are above sctype score cut off but aged was considered a marker of inflammation given that samples were prenatal.
10	Aged microglia	587.49	563	1.04	0.05	
10	Metabolically active microglia	488.33	563	0.87	0.18	
11	**Axon-tract microglia**	913.51	488	1.87		0.19 was the highest change in score in the top 10 scores so was used as a cutoff to label the cluster as ATM.
11	Metabolically active microglia	819.69	488	1.68	0.19	
11	Early/Postnatal microglia	730.27	488	1.50	0.18	
12	**Axon-tract microglia**	834.64	452	1.85		As the highest change in score in the top 10, 0.18 was used as a cutoff. Metabolic, PAM and early/postnatal microglia scores were discounted due to their close relationship with ATM. The Inflammatory monocytes label was used to inform the 'reactive' name given. Reactive was selected over inflammatory due to low levels of inflammatoion in webgestalt analysis.
12	Metabolically active microglia	780.98	452	1.73	0.12	
12	**Inflammatory monocytes**	711.14	452	1.57	0.15	
12	Early/Postnatal microglia	694.07	452	1.54	0.04	
12	Postnatal PAM	643.48	452	1.42	0.11	
12	Proliferative microglia c	563.51	452	1.25	0.18	
13	**Proliferative microglia c**	408.20	205	1.99		As the highest change in score in the top 5, 0.18 was used as a cutoff and metabollically active label was discounted due to it's close relationship with proliferative microglia.
13	Metabolically active microglia	386.49	205	1.89	0.11	
13	Aging cluster 2	349.52	205	1.70	0.18	

Cluster	Cell type	Sctype scores	# cells	Normalised by # cells	Change in normalised	Explanation
14	Neutrophils	249.49	126	1.98		As the highest change in score in the top 10, 0.15 was used as a cutoff and neutrophils was discounted due to lack of marker expression.
14	**Metabolically active microglia**	235.73	126	1.87	0.11	
14	Axon-tract microglia	216.77	126	1.72	0.15	
15	**Homeostatic microglia**	84.08	87	0.97		Injury cluster was used to distinguish this homeostatic cluster from others.
15	**Injury cluster 1**	65.35	87	0.75	0.22	
16	**White matter injury microglia**	210.25	84	2.50		Change in score cut off leaves white matter injury as the only viable label.
16	Homeostatic microglia	172.77	84	2.06	0.45	
17	**Choroid plexus epithelial cells**	183.32	69	2.66		Change in score cut off leaves choroid plexus epithelial cell as the only viable label.
17	White matter injury microglia	76.56	69	1.11	1.55	
18	**Postnatal PAM**	107.36	67	1.60		Patrolling was used with high score labels to distinguish this population from ATM/PAM and due to support from webgestalt analysis.
18	**Axon-tract microglia**	83.13	67	1.24	0.36	
18	**Patrolling monocytes**	49.61	67	0.74	0.50	
19	**Metabolically active microglia**	154.22	63	2.45		Metabolic is above the change in score cut off. Webgestalt inflammatory status was used to distinguish from other metabolic clusters.
19	Axon-tract microglia	129.36	63	2.05	0.39	
20	**Homeostatic microglia**	175.81	57	3.08		Homeostatic is above the change in score cut off with injury used to distinguish from other homeostatic clusters.
20	**Injury cluster 1**	102.83	57	1.80	1.28	
21	**Postnatal PAM**	94.19	53	1.78		PAM is above the change in score cutoff with the inflammatory label taken from webgestalt.
21	Hammond Cluster 5	70.57	53	1.33	0.45	

Annex Table 4 Legend

Table 4

Data displayed in the tables below are from over representation analysis carried out on genes which reached an expression level of at least 5 Seurat determined arbitrary units. Significant GO terms, as calculated by hypergeometric testing and Benjamini-Hochberg multiple testing correction, were then manually grouped into the broad biological processes displayed below: inflammatory, reactive, developmental, metabolic, migratory, apoptotic. Cluster relates to the Seurat produced cluster number. Enrichment is a measure of the number of genes expressed over the number of genes expected from the Illumina *Mus musculus* reference set and the level of expression of each of these genes. # GO terms is the number of significantly enriched GO terms found during over representation analysis, which fall into each respective category of biological process. Data is displayed in descending order with those most enriched in each category at the top. The grouping of clusters formed predominantly of cells from dissected region samples are coloured blue and those from the predominantly cortex sample clusters are coloured green with the smaller satellite clusters coloured in black.

Table 5

Examples of GO terms in each category

Annex Table 4: Manual Expression Analysis Results.

Inflammatory			Reactive			Developmental		
Cluster	Enrichment	# GO Terms	Cluster	Enrichment	# GO Terms	Cluster	Enrichment	# GO Terms
19	38.65	7	12	22.17	6	8	20.48	7
3	34.72	7	8	20.85	6	17	19.65	7
21	34.72	6	0	16.27	5	12	17.89	6
13	34.53	6	11	16.23	5	7	17.87	6
5	29.51	5	6	15.89	5	0	17.59	6
18	26.64	4	19	14.36	4	10	17.39	6
14	25.95	5	13	13.87	4	2	17.36	6
20	25.14	5	17	13.65	4	11	17.34	6
2	25.09	4	3	13.29	4	6	17.18	6
11	25.09	4	21	13.29	4	9	16.98	6
9	24.80	4	9	13.23	4	16	16.94	6
17	24.19	4	10	13.11	4	5	16.23	6
12	24.16	4	4	13.03	4	19	16.12	5
1	23.96	4	5	10.79	3	15	15.73	6
7	23.38	4	1	10.28	3	1	14.20	5
0	23.24	4	18	10.22	3	4	13.94	5
10	23.24	4	2	10.05	3	18	13.83	5
6	23.16	4	14	9.99	3	14	10.83	4
4	23.10	4	16	9.49	3	13	10.83	4
8	22.56	4	20	9.32	3	3	8.07	3
16	22.17	4	7	6.82	2	21	8.07	3
15	21.43	4	15	6.26	2	20	5.45	2

Metabolic			Migratory			Apoptotic		
Cluster	Enrichment	# GO Terms	Cluster	Enrichment	# GO Terms	Cluster	Enrichment	# GO Terms
8	20.87	5	13	14.53	4	20	12.88	3
6	15.04	4	14	12.96	4	14	10.27	2
0	15.02	4	8	12.69	4	13	8.23	1
7	14.68	4	20	10.88	4	2	5.72	2
2	14.63	4	19	10.16	3	21	5.72	2
16	14.55	4	9	10.08	3	12	5.64	2
11	14.03	4	10	9.95	3	18	5.63	2
10	12.29	3	0	9.74	3	19	2.84	1
12	11.78	3	7	9.54	3	6	2.68	1
20	11.59	3	6	9.51	3	11	2.68	1
1	11.53	3	11	9.51	3	9	2.65	1
5	10.95	3	15	9.37	3	17	2.56	1
18	10.85	3	18	9.33	3	0	2.55	1
13	10.76	3	12	9.15	3	10	2.55	1
17	8.45	2	5	9.03	3	3	2.53	1
4	8.40	2	4	8.93	3	1	2.49	1
3	8.34	2	3	8.48	3	8	2.47	1
21	8.34	2	21	8.48	3	4	2.45	1
19	8.34	2	17	6.91	2	5	0.00	0
9	8.15	2	1	6.91	2	7	0.00	0
14	7.81	2	2	6.75	2	15	0.00	0
15	7.79	2	16	6.40	2	16	0.00	0

Annex Table 5: Manual Expression Analysis Category Table

Inflammatory	Metabolic
antigen processing and presentation	regulation of cellular amide metabolic process
humoral immune response	regulation of protein catabolic process
response to molecule of bacterial origin	response to nutrient
Reactive	**Migratory**
cellular response to biotic stimulus	leukocyte migration
cellular response to drug	ameboidal-type cell migration
positive regulation of response to external stimulus	tissue migration
Developmental	**Apoptotic**
developmental growth involved in morphogenesis	regulation of apoptotic signaling pathway
positive regulation of growth	intrinsic apoptotic signaling pathway
positive regulation of neuron differentiation	myeloid cell apoptotic process

Annex Figure 1: All clusters of microglia express some level of pre-microglia markers.

A) UMAP plot coloured for expression of pre-microglia markers identified by (Masuda et al. 2019)

B) Expression of pre-microglia markers across cortical and dissected samples displayed in violin plots. Expression level in log-transformed counts per 10,000 transcripts.

Dis – Dissected.

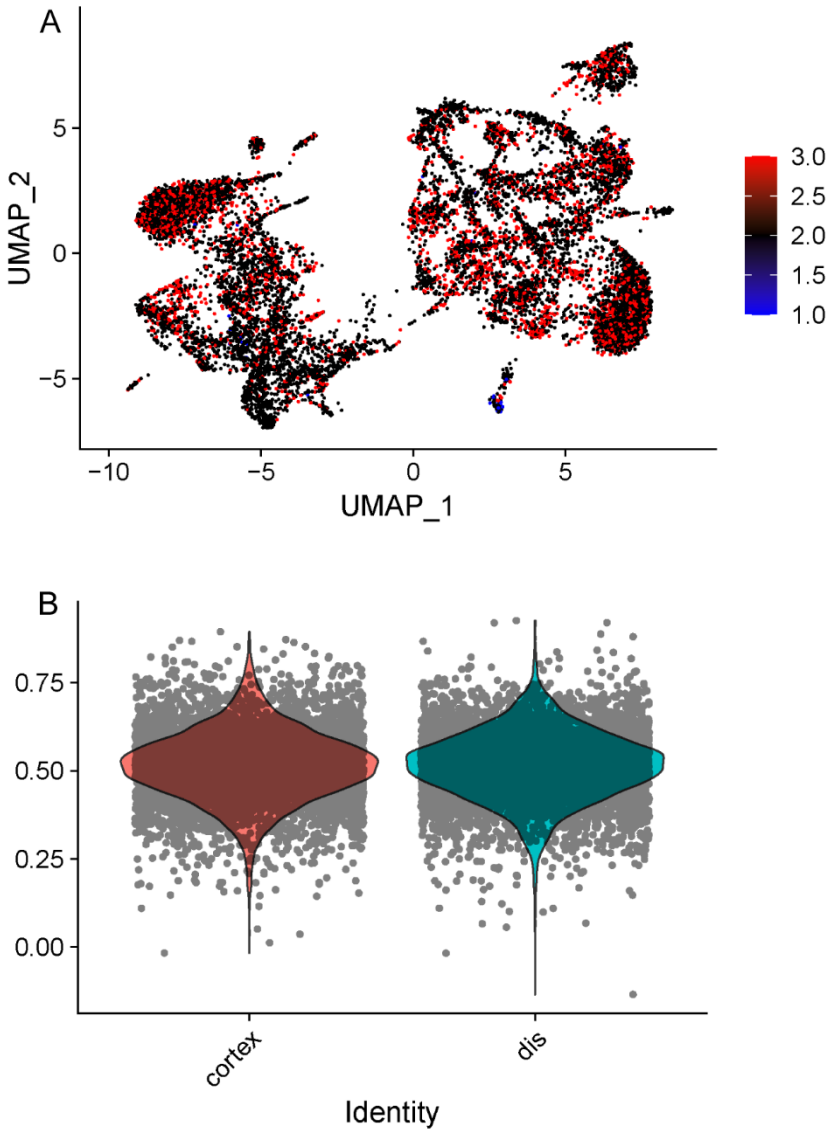

Annex Figure 2: Macrophage markers are not expressed by all clusters identified.

A) UMAP plot coloured for expression of macrophage markers identified by (Hammond et al. 2019).

B) Expression of macrophage markers across all clusters displayed in violin plots. Expression level in log-transformed counts per 10,000 transcripts.

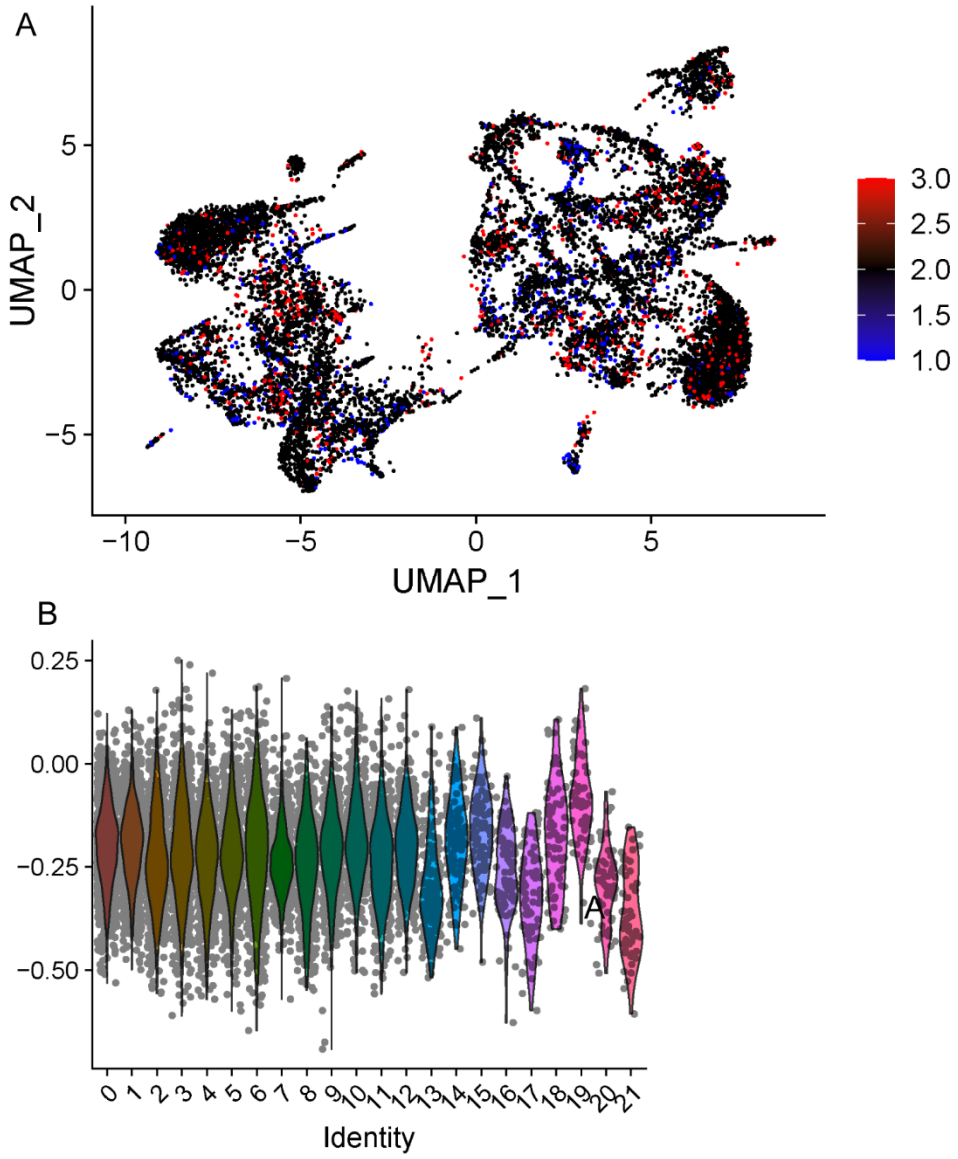

Annex Figure 3: Neutrophil marker *Itgax* is expressed at low levels by many clusters.

A) UMAP plot coloured for expression of Itgax, the gene coding for neutrophil marker CD11c. **B)** Expression of *Itgax* across all clusters displayed in violin plots. Expression level in log-transformed counts per 10,000 transcripts.

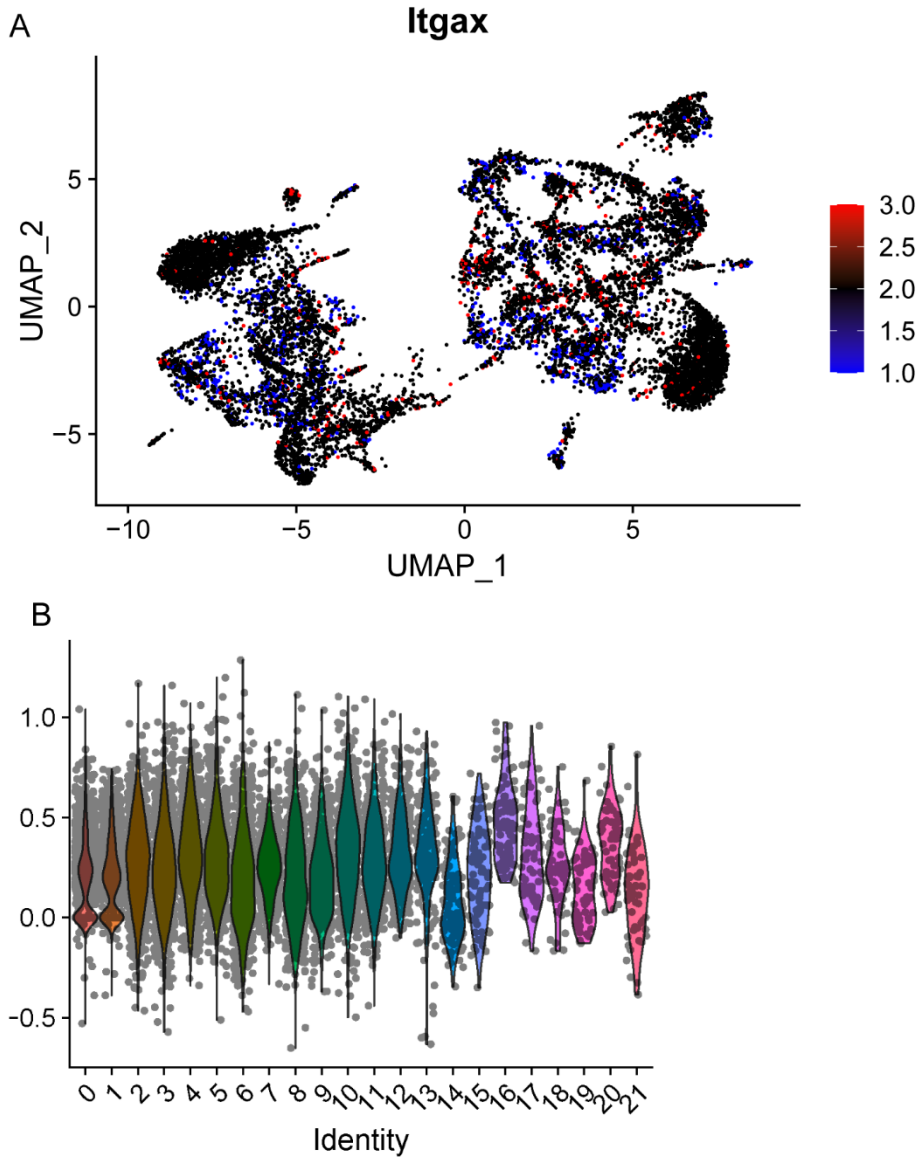

Annex Figure 4: Corpus callosum associated microglia hotspots wrap around in close proximity to the corpus callosum.

A) Video showing of a cleared E18.5 mouse brain immuno-labelled with anti-iba1 (red) and anti-nrp1 (green) and visualised using a light sheet microscope and Imaris as described below.
1-4 seconds: Outer surface of the E18.5 mouse brain using a non-labelled channel.
4-7 seconds: The brain in 3D with Iba1 (microglia marker) in red and Nrp1 (axon subset marker) in green.
8-14 seconds: A slice through the brain as depicted in standard epi-fluorescence microscope figures.
14-27 seconds: Midline corpus callosum region is highlighted showing how dense corpus callosum associated microglia hotspots wrap around the nrp1 labelled corpus callosum.
27+ seconds: The position of the highlighted midline corpus callosum region is shown relative to the rest of the brain.

Method

E18.5 brains were fixed in 4% PFA for 2 hours at room temperature then 24 hours at 4°C before washing in PBS for 24 hours at 4°C. Hydrogel solution (Logos Biosystems, C1310X) was prepared according to manufacturer instructions and brains were incubated in this solution for 24 hours at 4°C. Brains were placed in a Logos Biosystems polymerization system for 2h at 37 and -90kPa. Hydrogel embedded brains were rinsed in electrophoretic tissue clearing solution (Logos Biosystems, C13001) then left in fresh electrophoretic tissue clearing solution for 3 days at room temperature, changing the solution daily.

Brains were then washed in PBS at room temperature for 24 hours then incubated in PBSGT (PBS, Gelatine 0.2%, Triton 0.5%, Saponine 0.1%, Thymerosal 0.01%) at room temperature for 24 hours. Brains were then incubated in Iba1 and Nrp1 antibody solutions diluted in PBSGT, as set out in Annex Table 1, for 5 days at room temperature followed by incubation in corresponding secondary antibody solution for 24 hours at room temperature. Brains were washed in PBS and incubated in RIMS (histodenz) for an hour before imaging in RIMS on a lightsheet microscope (Leica).